

THESE DE DOCTORAT DE

L'UNIVERSITE DE RENNES 1

ECOLE DOCTORALE N° 596

Matière, Molécules, Matériaux

Spécialité : Physique

Par

Eszter DUDÁS

Non-LTE spectroscopy of methane in hypersonic flow for the characterisation of hot Jupiters

Thèse présentée et soutenue à Rennes, le 2 juillet 2021

Unité de recherche : Institut de Physique de Rennes (IPR UMR 6251)

Rapporteurs avant soutenance :

Alain CAMPARGUE
Séverine BOYE-PERONNE

Chercheur - LIPHY, Université Grenoble-Alpes
Professeur - ISMO, Université Paris-Saclay

Composition du Jury :

Président :	Alain CAMPARGUE	Directeur de recherche	Université Grenoble-Alpes
Examineurs :	Robert GAMACHE	Professeur émérite	University of Massachusetts Lowell
	Michaël REY	Chargé de recherche	Université Reims Champagne Ardenne
	Séverine BOYE-PERONNE	Professeur	Université Paris-Saclay
	Manuel GOUBET	Maître de conférences	Université de Lille
	Ludovic BIENNIER	Chargé de recherche	Université de Rennes 1
Dir. de thèse :	Robert GEORGES	Professeur	Université de Rennes 1

Abstract

A state-of-art experimental system, SMAUG has been developed to produce unprecedented infrared spectroscopic reference data that will help planetologists to detect new molecules and reconstruct the vertical structure of the atmosphere of exoplanets.

A specially designed small dimension Laval nozzle connected to a compact high enthalpy source equipped with cavity ringdown spectroscopy (CRDS) is used to produce high-resolution infrared spectra of polyatomic molecules in the 1.67 μm region. The experimental setup can operate according to two complementary working regimes to interpret the complex pattern of highly-excited vibrational states of methane.

The hypersonic jet delivers strong out-of-equilibrium state, in which vibrationally hot and rotationally cold high-resolution infrared spectra were recorded. The obtained non-LTE (Local Thermodynamic Equilibrium) spectrum of methane provides accurate positions of the upper energy levels to refine the potential energy surface on which *ab initio* variational theoretical models are based.

A new post-shock CRDS technique results in close to local thermodynamic equilibrium conditions which contribute to the analysis of a more complex rotational structure and complete the information on the excited hot vibrational energy levels.

Parallely, through a collaboration, a transformed Pocket Rocket plasma source was developed and implanted to SMAUG to investigate an alternative heating system and more elevated vibrational energy levels. This work was done in the frame of the e-PYTHEAS ANR project that focuses on high-temperature spectroscopy of small hydrocarbons.

Résumé

Le système expérimental de pointe SMAUG a été développé pour produire des données de référence spectroscopiques infrarouges inédites pour la détection de nouvelles molécules et la reconstruction de la structure verticale de l'atmosphère d'exoplanètes de type Jupiter chaud.

Une mini-tuyère de Laval en graphite, connectée à une source de haute enthalpie et couplée à un spectromètre par temps de déclin d'une cavité optique (CRDS), a été développée afin de produire des spectres infrarouges à haute résolution et haute température du méthane dans la région à 1,67 μm . Le dispositif expérimental fonctionne dans deux configurations complémentaires pour accéder aux signatures infrarouges complexes du méthane dans ses états vibrationnels fortement excités.

Une détente hypersonique produit un état de très fort déséquilibre thermodynamique moléculaire, associé à des températures vibrationnelles élevées et une température rotationnelle très basse. Du spectre hors équilibre sont extraites les positions précises des niveaux d'énergie vibrationnels excités qui affinent la surface d'énergie potentielle du méthane et améliorent la précision des modèles théoriques variationnels *ab initio* qui fournissent les listes de raies spectroscopiques à haute température à la communauté des planétologues.

Une nouvelle technique CRDS post-choc conduit à des conditions proches de l'équilibre thermodynamique local. Les températures vibrationnelle et rotationnelle élevées atteintes donnent accès à la structure rotationnelle complète des différentes bandes observées, de même qu'aux bandes chaudes vibrationnelles issues des états les plus excités de chaque polyade du méthane.

En parallèle, une source plasma radiofréquence de type Pocket Rocket a été adaptée et utilisée comme moyen de chauffage alternatif. Ce travail de thèse a été réalisé dans le cadre du projet ANR e-PYTHEAS qui vise à mieux connaître la formation des exoplanètes et leur évolution.

Acknowledgements

This thesis would not exist if it were not for Robert GEORGES and his much-appreciated support during these years we worked together. You gave me the opportunity to discover academic research through an internship and then you trusted me to come back to carry out this thesis. You showed me the crazy world of physicists and to trust that there is always something valuable in every ugly spectrum. I could not wish for a better thesis supervisor, although I know you hated reading through all this text written in English.

Christine CHARLES, I warmly thank you for introducing me to the field of space propulsion and to show me how interesting and adventurous the life of a researcher can be. Your personality and the success you achieved in your domain is a true inspiration for me.

I very much appreciated the helpful discussions with Robert GAMACHE and Michael REY which allowed me to slowly digest the complexity of the methane molecule and who provided help to analyse the recorded spectra. A special thanks goes to Vinayak KULKARNI and his helping hand in the fluid dynamic questions. Thank you, Samir KASSI, the master of the CRDS for keeping it alive.

I would like to say thank you to my colleagues in the Laboratory Astrophysics group at the IPR who helped me and guided me throughout these years. I am grateful for the tips and tricks of Abdessamad BENIDAR which guaranteed the convergence of those CFD simulations. I would not even last a day in my “teaching role” without the guidance of Sophie CARLES and her moral support after a more difficult class. The “two Jonathans”, Jonathan COURBE and Jonathan THIEVIN are welcomed for their assistance in operating SMAUG. The technical staff of the IPR, especially Ewen GALLOU and Didier BIET is recognised for their instantaneous support no matter if it was about drilling another hole or fabricating a new piece for SMAUG.

The social life would not be the same without the After-work football games and the “non-permanents” who ensured an enjoyable student-life part of these years. To my fellow comrades, Raghed BEJJANI and Olivier DURIF, it was nice to share the office with you and I really appreciated our long conversations during and after working hours. I will never forget that trip to Morocco Asma RAMZI and I am happy we walked together along the rocky road of thesis.

My dear BROTHER, it was reassuring to know I have a Matlab help center on my speed dial 24/24h. MAMA, PAPA and my family, thank you for always encouraging and supporting me and pretending that you enjoyed reading my article.

And last but not least, Thomas HEARNE, I even looked for another synonym of acknowledgement here, maybe a more Shakespearean way to express how grateful I am for everything you have done for me, but my two-legged dictionary was not available. Your proof readings, our scientific discussions and your continuous kind encouragement were what helped me through many of complicated phases of the past years. Having you by my side gave me very happy years in Rennes.

*“Only I have left to say,
More is thy due than more than all can pay.”*
William Shakespeare – Macbeth

The graphics at the front of each chapter were made in the frame of the « *Fête de la science 2019* » as the 2019 edition of *My thesis in comics*: « *Science en Bulles* ».

Comics scenario: peb

Drawings: fox

Colourisation: peb & fox

Artistic direction: Guillaume Prieur

Editing and publishing: Cathrine Cornu

Proof-reader: Valérie Poge

© 2019, groupe Sciences pour tous,
Syndicat national de l'édition
ISBN : 978-2-909 677-01-9



Contents

Introduction	11
Brief history of the theory of solar systems and the exoplanets	13
Detection of exoplanets	14
Types of exoplanets	15
Origin of the hot Jupiters	17
Confirmed species in the atmosphere of hot Jupiters	18
E-PYTHEAS project	18
References	19
Infrared spectroscopy of methane	25
1.1 Target molecule: methane	27
1.2 IR Rovibrational spectroscopy of methane	29
1.2.1 Vibration of methane	29
1.2.2 Rotation of methane	30
1.3 LTE vs non-LTE	34
1.4 Partition function	36
1.5 Line intensity	39
1.6 Boltzmann plot method	43
1.7 Databases of methane	44
1.7.1 Effective Hamiltonian extrapolation	44
1.7.2 Ab initio calculation	44
1.8 Previous IR spectroscopic studies of methane	46
1.8.1 LTE spectroscopy	46
1.8.2 Non-LTE spectroscopy	48
2.9 SMAUG	49
References	50
SMAUG experimental setup and its operation	57
2.1 Hypersonic flows	59
2.1.1 Knudsen number	59
2.1.1 Mach number	59
2.1.2 Compressibility	60
2.1.3 Viscosity	60
2.1.4 Isentropic expansion and ideal gas	61
2.1.5 Governing equations	61
2.2 Laval nozzle design	63
2.2.1 Nozzle profile calculation	64
2.2.2 CFD simulations and flow field analysis	68
2.2.3 Isentropic core vs shear-layer	72
2.2.4 2D Pitot probe	74
2.3 SMAUG experimental setup	79

2.3.1 High enthalpy source	80
2.3.2 Cavity Ring-Down Spectrometer	82
2.3.3 Determination of the reservoir temperature	84
2.4 Preliminary study on carbon monoxide	91
2.4.1 Vibrational relaxation	91
2.4.2 Rotational relaxation	92
References	93

Non-LTE CH₄ spectroscopy 99

3.1 The tetradecad spectral region	101
3.2 Recorded spectrum	102
3.2.1 Comparison between LTE and non-LTE experimental spectra	103
3.2.2 Line broadening	105
3.3 Simulated spectrum	108
3.4 Temperature extraction	110
3.4.1 Rotational temperatures	110
3.4.2 Vibrational temperatures	111
3.5 Line identification	116
3.6 Conclusion	119
References	120

Post-shock spectroscopy 125

4.1 Status report	127
4.2 Normal shock waves	128
4.2.1 Hugoniot equation	130
4.2.2 Experimental flow field for post-shock spectroscopy	131
4.3 Experimental setup	132
4.4 CFD simulations and flow field analysis of the shock layer	134
4.5 Experimental characterisation of the shock	137
4.5.1 Location of the shock front	137
4.5.2 Evolution of the rotational and vibrational temperatures trough the shock	138
4.6 Methane post-shock spectroscopy	143
References	146

Platypus project	149
5.1 Platypus project	151
5.2 Plasma	152
5.3 RF plasma source	153
5.3.1 RF Impedance matching network	153
5.4 Implantation into SMAUG	156
5.5 Visualisation of the plasma expansion	157
5.6 Preliminary study with carbon monoxide	158
5.6.1 Rotational and vibrational temperatures	159
5.7 Conclusion	162
References	163
Conclusions and perspectives	165
Conclusions	166
Perspectives	168
Annexes	171
High-temperature hypersonic Laval nozzle for non-LTE cavity ringdown spectroscopy	173
Exoplanètes : ça chauffe au labo	187
Poster: Out-of-equilibrium hypersonic jet spectroscopy	189
Poster: The Platypus exoplanet project	191
Résumé français détaillé	193

Introduction

“Ad astra per aspera.”⁵

LES EXOPLANÈTES TOURNENT AUTOUR D'AUTRES ÉTOILES QUE LE SOLEIL. LE PLUS SOUVENT, CELLES QU'ON PEUT OBSERVER SONT DES GÉANTES GAZEUSES COMME JUPITER, SAUF QU'ELLES SONT TOUTES PROCHES DE LEUR ÉTOILE ET DONC TRÈS CHAUDES, D'OÙ LEUR NOM DE « JUPITERS CHAUDS ».



⁵To the stars through difficulties¹

Contents

Brief history of the theory of solar systems and the exoplanets	13
Detection of exoplanets	14
Types of exoplanets	15
Origin of the hot Jupiters	17
Confirmed species in the atmosphere of hot Jupiters	18
E-PYTHEAS project	18
References	19

Brief history of the theory of solar systems and the exoplanets

The first heliocentric model in which the planets orbited around a centre star dates back to the ancient Greeks. Aristarchus of Samos, an astronomer and mathematician c.310 – c.230 BC, presented his observations and placed the Sun in the center of the universe with the Earth orbiting around it, meanwhile rotating around its own axis.²

In the 16th century, the Polish polymath Copernicus described the outline of the heliocentric model in a handwritten manuscript titled *Commentariolus*³ and later sums up his observations and calculations regarding to an alternative model of the universe in his printed book: *De revolutionibus orbium coelestium*.⁴ His work was followed by his tragically fated student, Giordano Bruno, who raised the interesting parallelism between the Sun and the other stars, as he wrote in *De l'Infinito, Universo, e Mondi*⁵ in 1584:

“In space there are countless constellations, suns and planets; we see only the suns because they give light; the planets remain invisible, for they are small and dark. There are also numberless Earths circling around their suns, no worse and no less than this globe of ours. For no reasonable mind can assume that heavenly bodies that may be far more magnificent than ours would not bear upon them creatures similar or even superior to those upon our human Earth.”

Nevertheless, more than another three centuries passed before the first observational proof of exoplanets was delivered. In 1917, calcium and other heavy-element absorption features were recorded by the Mount Wilson 60-inch telescope. Named after its discoverer as the van Maanen 2 Star⁶, the spectral features of the object could not be completely explained back in time and today this spectrum, captured on a small glass plate, can be considered as the first observational evidence of an exoplanet.

Another seven decades went by until in 1988 E. E. Becklin and B. Zuckerman reported an infrared object near a white dwarf.^{7,8} However, this was later revealed to be merely a dusty disk. The same year, Cambell *et al.* reported a probable stellar companion around the Chi1 Ori A and Gamma Cep stars after the observation of their large velocity variations.⁹ However, the quality of the recorded data was regarded insufficient to definitively label it an exoplanet discovery, although the presence of an exoplanet was confirmed in 2002.¹⁰ Finally, in 1995, Michel Mayor and Didier Queloz announced the definitive detection of the 51 Pegasi b exoplanet orbiting in the Pegasus constellation, for which they were awarded the 2019 Nobel prize for physics.^{11,12}

Detection of exoplanets

Exoplanets can be detected by using ground based telescopes, for example: HARPS - High Accuracy Radial velocity Planet Searcher¹³ as well as spatial telescopes, like Hubble Space Telescope,¹⁴ Spitzer Space Telescope¹⁵ and the Kepler mission.¹⁶ Five different methods have been successfully used to detect a planet beyond our solar system to date.

Most of the discovered exoplanets have been spotted using the so-called transit method.¹⁷ While orbiting around its star a primary eclipse can occur when the exoplanet passes between the star and the observing telescope. At this time an absorption spectrum of its surface can be recorded. When the exoplanet arrives behind its star, a secondary eclipse takes place and a corresponding emission spectrum of the atmosphere of the planet can be observed. This is a very powerful detection method and is considered to be an exoplanet gold mine by scientist as it delivers an insight of the composition of the atmosphere of the exoplanet as a bonus. However, there are limitations of this method to be outlined as well. First of all, the transit has to be observable, meaning that the plane of the event has to line up with the observer, otherwise it will not be detected. On the other hand, the method is heavily biased towards planets orbiting close to their stars, as their orbital duration is shorter, providing more eclipses and therefore observation opportunities per Earth year.

The radial velocity method¹⁸ was used to detect the first exoplanet and remains a very powerful tool up to date. In this approach, as was mentioned in case of the discovery of Pegasi b, the orbiting planet makes its star wobble, which cause a Doppler shift in the light arriving from the star. This technique is often used to confirm exoplanets found by other means as well.

A relatively new approach is the so-called direct imaging technique where a picture of the exoplanet is captured by blocking the much brighter light of its star.^{19,20} A fourth approach is gravitational microlensing, where the exoplanet orbiting around a star bends the starlight with its gravity.²¹ The change of direction of the starlight can cause a brightening and fade away which contains information of the size of the exoplanet. To be able to detect such an event, the astronomers have to observe a large part of the sky.

Finally, to date only one planet has been discovered by the means of astrometry.²² In this technique, the wobbling motion of the star caused by an exoplanet orbit causes a change in the position of the star with respect to other stars. Using this approach to detect exoplanets requires extremely precise optics and it is hard to carry out such measurements from the Earth as its atmosphere distorts the arriving starlight.

Types of exoplanets

The Milky Way contains at least 100 billion stars and the Sun is only one of them. Like Giordano Bruno, scientists today believe that each of those stars have their own planetary system. Also, similarly to our solar system, the discovered exoplanets represent a variety of different types and sizes. Up to May 2021, more than four thousand exoplanets have been detected and confirmed, and several thousand more candidates await confirmation.

A group of exoplanets, called Super-Earths, has a misleading name, as it does not refer to a direct similarity to our home. The Super-Earth notation only reflects the size of the discovered exoplanets in relation to our habitable one. Precisely, this group contains planets more massive than Earth but smaller than Neptune. Considering their nature, it is hard to compare it to anything around us as no similar planet can be found in our solar system. This is rather interesting, knowing that more than 1000 of this kind of planet have been detected around distant stars. In the contest of finding the doppelganger of the Earth several constraints were introduced, such as the presence of a Sun like star, a close to rocky surface and an orbiting distance comparable to the one we follow. The first Super-Earth exoplanet was discovered in 2015, and was baptised Kepler-452b.^{23–25}

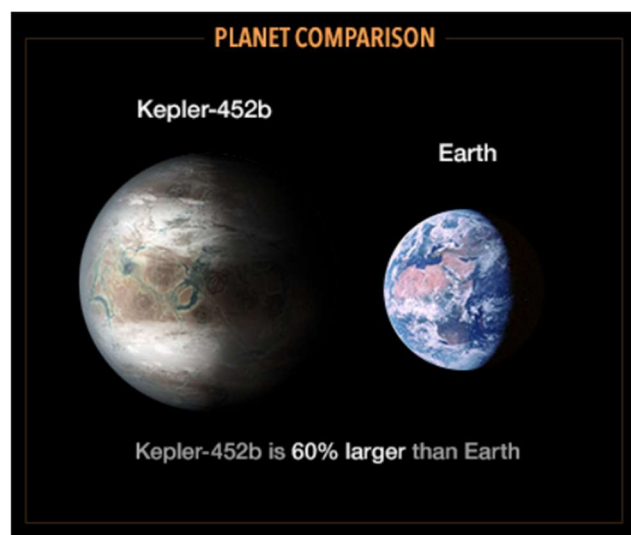


Figure 0.1: Comparison of the Super-Earth type Kepler-452b exoplanet to the Earth. Credit: NASA/JPL-Caltech

Exoplanets of a size comparable to Neptune or Uranus in our solar system are called Neptune-like exoplanets. In 2010, HAT-P-11b²⁶, an icy giant Neptune-like exoplanet, was discovered. However, studying the atmosphere of icy giants and determining their composition remains challenging as they are often surrounded by dense clouds which block any light from passing through. Nevertheless, in 2014, water vapour absorption was detected in the transmission spectrum of HAT-P-11b.²⁷

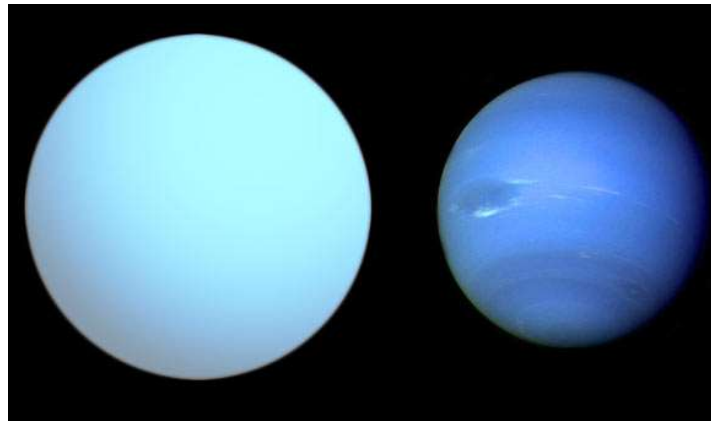


Figure 0.2: Comparison of HAT-P-11b (left) to Neptune (right). Credit: Aldaron / CC BY-SA 3.0

In a smaller number, some terrestrial exoplanets have been found. These are composed of rock, silicate water, or carbon. Kepler-11b²⁸ was detected in 2011 and, along with other members of this group, was investigated for an atmosphere, oceans, liquid water on its surface or any other sign that might suggest clues as to its habitability.

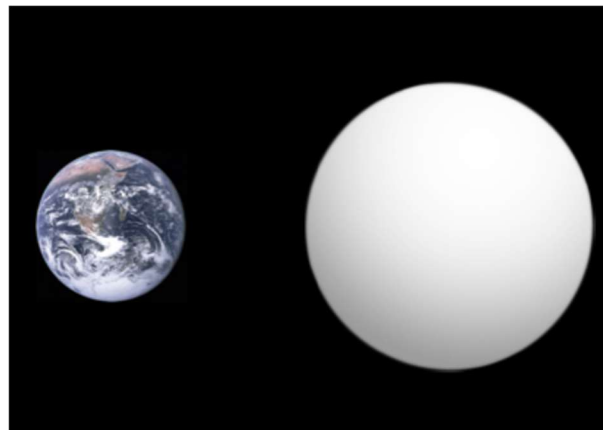


Figure 0.3: Comparison of Kepler-11b (right) to Earth (left). These rocky terrestrial exoplanets are considered the most probable to provide a habitable climate. Credit: Aldaron / CC BY-SA 3.0

Finally, and most importantly, almost one quarter of the discovered planets fall into the gas-giant type exoplanets which are alike to Jupiter and Saturn in our own solar system. This is to say that these large planets are mainly composed of large quantities of gases over a solid core. A special group of the gas giants are the so-called hot Jupiters, which orbit so close to their star that their atmosphere can reach up to several thousands of kelvins. Furthermore, being the size of Jupiter, or larger, and with a very close orbit, they can make their star wobble, which can be measured as a shift in the spectrum of the light of the star. This makes hot Jupiters relatively easy to detect. A famous representation of this exoplanet type is 51 Pegasi b¹², the first ever confirmed exoplanet. This planet orbits its star so fast that only four Earth days makes an entire year for this planet, which can be found a mere 50 light years from Earth.

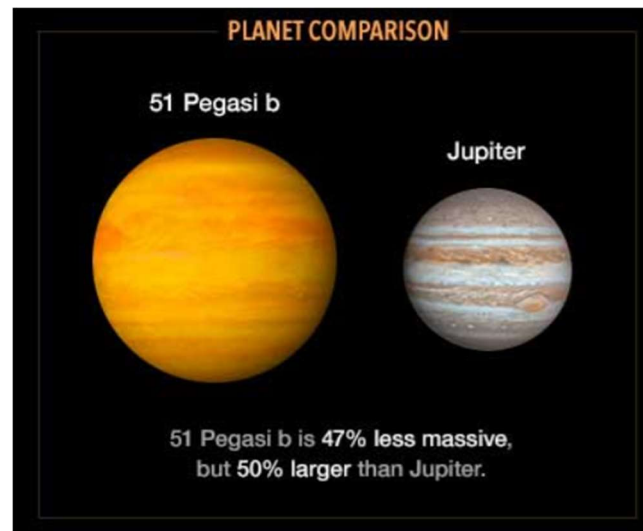


Figure 0.4: Comparison of the hot-Jupiter type 51 Pegasi b exoplanet to Jupiter. Credit: NASA/JPL-Caltech

Origin of the hot Jupiters

The question of how the hot Jupiters could live so close to their host stars fascinated astronomers since the detection of the first exoplanet. General agreement thought that giant planets either form by core accretion^{29–31} or gravitational instability^{32,33} however, this latter case is not possible given the gas conditions close to the star.³⁴ Conversely, core accretion could happen close to a star but it is questionable if such a large core could form.^{35,36}

To overcome this ambiguity three hypotheses, presented in figure (0.5), have emerged to explain the existence of gas giant planets orbiting close their star. The theory of *in situ* formation assumes that the hot Jupiters are accelerated gaseous envelopes that were grown or assembled at their actual position around the star.³⁷ A second presumption is disk migration^{38–40} which considers that the hot Jupiters were formed further out and travelled with a gaseous disk surrounding the young star to their current position. A third approach is the formation by a tidal migration.⁴¹ Once the gas disk cleared away from the star, the hot Jupiter could be pushed to a highly elliptical orbit and approach a star by tidal dissipation.

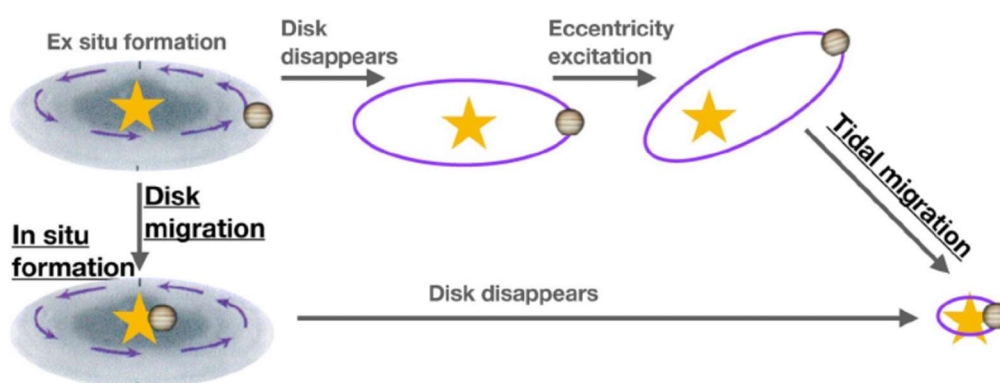


Figure 1. Origins hypotheses for hot Jupiters: in-situ formation, disk migration, and high eccentricity tidal migration.

Figure 0.5: Three hypotheses destined to explain the origin and orbital evolution of the hot Jupiters⁴²

Confirmed species in the atmosphere of hot Jupiters

Following the prodigious progress of infrared (IR) astronomy, it is possible to probe the composition and find the conditions prevailing in the atmospheres of giant gaseous exoplanets located several tens of light years away. In fact, today, the challenge is linked to the interpretation of the infrared signals which reach us from their ultra-hot atmosphere. The exploitation of these complex signals relies on elaborate radiative transfer codes⁴³ which call upon spectroscopic molecular databases developed on the basis of both *ab initio* calculations and laboratory data obtained under well controlled conditions. Ultimately, experimental infrared spectroscopic reference data will help planetologists to detect new molecules and reconstruct the vertical structure of the atmosphere of exoplanets. The idea is to match a simulated spectrum generated using a presumption of the species present in the atmosphere and a code governing the way they transfer radiation to the observed spectrum. By tuning the different input parameters such as the species present, their temperature and density, *etc* a good estimate of the characteristics of the atmosphere can be achieved. So far, besides from hydrogen and helium, the presence of water vapour⁴⁴, carbon monoxide⁴⁵, carbon dioxide⁴⁶, hydrogen cyanide^{45,47,48}, ammonia⁴⁹, acetylene⁴⁹ and methane^{46,50–52} have been confirmed in the atmospheres of exoplanets.

E-PYTHEAS project

The acronym e-PYTHEAS stands for exo-Planetary high-Temperature Hydrocarbons by Emission and Absorption Spectroscopy⁵³ and is a collaboration led by the planetologist A. Coustenis (LESIA, Paris Observatory), between five French laboratories, bringing together molecular physicists, theoretical chemists and astrophysicists. The project aims to contribute to the interpretation and analysis of the data describing spatial hot gaseous media. In other words, hot Jupiters. Past and current spatial observations of exoplanets have already delivered a huge quantity of infrared spectroscopic data of the atmospheres of these exoplanets. Additionally, upcoming spatial missions as the American-European-Canadian James Webb Space telescope⁵⁴ and the European ARIEL mission⁵⁵ will produce an unprecedented quantity of high-temperature infrared spectral data.

This thesis was conducted in the frame of this project and aims to deliver the required high-temperature, high-resolution spectral data through laboratory studies of methane. At the beginning, chapter I portrays the theory behind the IR spectroscopy of methane and details the previous experimental studies which contributed to the development of theoretical databases. Thereafter, the development of a state-of-art experimental setup is described in chapter II. Following this, the results of the non-Local Thermodynamic Equilibrium (non-LTE) methane spectra are analysed in chapter III. To go beyond these results, a new post-shock experimental setup was developed and its operation and the obtained preliminary results are discussed in chapter IV. Last but not least, an alternative heating source was developed in collaboration with an Australian research group. The conception of the platypus cold plasma source and the preliminary results obtained by probing the plasma jet are exhibited in chapter V. Conclusions and perspectives are summed up in the last pages.

References

- (1) Hoyt, J. K. *The Cyclopaedia of Practical Quotationos, English and Latin: With an Appendix Containing Proverbs from the Latin and Modern Foreign Languages ...*; Funk & Wagnalls, 1889.
- (2) Heath, T. L.; Aristarchus, of S. O. the sizes and distances of the sun and moon E. & G. 1913. *Aristarchus of Samos, the Ancient Copernicus; a History of Greek Astronomy to Aristarchus, Together with Aristarchus's Treatise on the Sizes and Distances of the Sun and Moon*; Oxford: Clarendon press, 1913.
- (3) Koyré, A. *The Astronomical Revolution: Copernicus, Kepler, Borelli*; Courier Corporation, 1992.
- (4) Copernicus, N. *De Revolutionibus Orbium Coelestium*; 1543.
- (5) Sanasi, P. *De l'Infinito, Universo e Mondi*. 70.
- (6) Maanen, A. van. A very faint star of spectral type F. *PASP* **1919**, 31 (179), 42. <https://doi.org/10.1086/122810>.
- (7) Becklin, E. E.; Zuckerman, B. A Low-Temperature Companion to a White Dwarf Star. *Nature* **1988**, 336 (6200), 656–658. <https://doi.org/10.1038/336656a0>.
- (8) Graham, J. R.; Matthews, K.; Neugebauer, G.; Soifer, B. T. The Infrared Excess of G29-38 - A Brown Dwarf or Dust? *The Astrophysical Journal* **1990**, 357, 216–223. <https://doi.org/10.1086/168907>.
- (9) Campbell, B.; Walker, G. A. H.; Yang, S. A Search for Substellar Companions to Solar-Type Stars. *The Astrophysical Journal* **1988**, 331, 902–921. <https://doi.org/10.1086/166608>.
- (10) Hatzes, A. P.; Cochran, W. D.; Endl, M.; McArthur, B.; Paulson, D. B.; Walker, G. A. H.; Campbell, B.; Yang, S. A Planetary Companion to γ Cephei A. *ApJ* **2003**, 599 (2), 1383. <https://doi.org/10.1086/379281>.
- (11) The Nobel Prize in Physics 2019 <https://www.nobelprize.org/prizes/physics/2019/summary/> (accessed 2021 -05 -27).
- (12) Mayor, M.; Queloz, D. A Jupiter-Mass Companion to a Solar-Type Star. *Nature* **1995**, 378 (6555), 355–359. <https://doi.org/10.1038/378355a0>.
- (13) Mayor, M.; Pepe, F.; Queloz, D.; Bouchy, F.; Rupprecht, G.; Lo Curto, G.; Avila, G.; Benz, W.; Bertaux, J.-L.; Bonfils, X.; Dall, Th.; Dekker, H.; Delabre, B.; Eckert, W.; Fleury, M.; Gilliotte, A.; Gojak, D.; Guzman, J. C.; Kohler, D.; Lizon, J.-L.; Longinotti, A.; Lovis, C.; Megevand, D.; Pasquini, L.; Reyes, J.; Sivan, J.-P.; Sosnowska, D.; Soto, R.; Udry, S.; van Kesteren, A.; Weber, L.; Weilenmann, U. Setting New Standards with HARPS. *The Messenger* **2003**, 114, 20–24.
- (14) Prospects for astrometry with the Hubble Space Telescope | SpringerLink <https://link.springer.com/article/10.1007/BF02285054> (accessed 2021 -06 -03).
- (15) Werner, M. W.; Roellig, T. L.; Low, F. J.; Rieke, G. H.; Rieke, M.; Hoffmann, W. F.; Young, E.; Houck, J. R.; Brandl, B.; Fazio, G. G.; Hora, J. L.; Gehrz, R. D.; Helou, G.; Soifer, B. T.; Stauffer, J.; Keene, J.; Eisenhardt, P.; Gallagher, D.; Gautier, T. N.; Irace, W.; Lawrence, C. R.; Simmons, L.; Cleve, J. E. V.; Jura, M.; Wright, E. L.; Cruikshank, D. P. The Spitzer Space Telescope Mission. *ApJS* **2004**, 154 (1), 1–9. <https://doi.org/10.1086/422992>.
- (16) Borucki, W. J.; Koch, D. G.; Lissauer, J. J.; Basri, G. B.; Caldwell, J. F.; Cochran, W. D.; Dunham, E. W.; Geary, J. C.; Latham, D. W.; Gilliland, R. L.; Caldwell, D. A.; Jenkins, J. M.; Kondo, Y. The Kepler Mission: A Wide-Field-of-View Photometer Designed to Determine the Frequency of Earth-Size Planets around Solar-like Stars. In *Future EUV/UV and Visible Space Astrophysics Missions and Instrumentation*; International

- Society for Optics and Photonics, 2003; Vol. 4854, pp 129–140.
<https://doi.org/10.1117/12.460266>.
- (17) Borucki, W. J.; Koch, D.; Basri, G.; Batalha, N.; Brown, T.; Caldwell, D.; Caldwell, J.; Christensen-Dalsgaard, J.; Cochran, W. D.; DeVore, E.; Dunham, E. W.; Dupree, A. K.; Gautier, T. N.; Geary, J. C.; Gilliland, R.; Gould, A.; Howell, S. B.; Jenkins, J. M.; Kondo, Y.; Latham, D. W.; Marcy, G. W.; Meibom, S.; Kjeldsen, H.; Lissauer, J. J.; Monet, D. G.; Morrison, D.; Sasselov, D.; Tarter, J.; Boss, A.; Brownlee, D.; Owen, T.; Buzasi, D.; Charbonneau, D.; Doyle, L.; Fortney, J.; Ford, E. B.; Holman, M. J.; Seager, S.; Steffen, J. H.; Welsh, W. F.; Rowe, J.; Anderson, H.; Buchhave, L.; Ciardi, D.; Walkowicz, L.; Sherry, W.; Horch, E.; Isaacson, H.; Everett, M. E.; Fischer, D.; Torres, G.; Johnson, J. A.; Endl, M.; MacQueen, P.; Bryson, S. T.; Dotson, J.; Haas, M.; Kolodziejczak, J.; Van Cleve, J.; Chandrasekaran, H.; Twicken, J. D.; Quintana, E. V.; Clarke, B. D.; Allen, C.; Li, J.; Wu, H.; Tenenbaum, P.; Verner, E.; Bruhweiler, F.; Barnes, J.; Prsa, A. Kepler Planet-Detection Mission: Introduction and First Results. *Science* **2010**, 327, 977.
<https://doi.org/10.1126/science.1185402>.
 - (18) Hatzes, A. P. The Radial Velocity Method for the Detection of Exoplanets. In *Methods of Detecting Exoplanets: 1st Advanced School on Exoplanetary Science*; Bozza, V., Mancini, L., Sozzetti, A., Eds.; Astrophysics and Space Science Library; Springer International Publishing: Cham, 2016; pp 3–86. https://doi.org/10.1007/978-3-319-27458-4_1.
 - (19) Lagrange, A.-M. Direct Imaging of Exoplanets. *Philosophical Transactions of the Royal Society A: Mathematical, Physical and Engineering Sciences* **2014**, 372 (2014), 20130090. <https://doi.org/10.1098/rsta.2013.0090>.
 - (20) Seager, S. *Exoplanets*; University of Arizona Press, 2010.
 - (21) Mao, S. Astrophysical Applications of Gravitational Microlensing. *Res. Astron. Astrophys.* **2012**, 12 (8), 947–972. <https://doi.org/10.1088/1674-4527/12/8/005>.
 - (22) Xu, W.; Liao, X.; Zhou, Y.; Xu, X. Exoplanet Detection by Astrometric Method. *Chinese Astronomy and Astrophysics* **2017**, 41 (3), 381–398.
<https://doi.org/10.1016/j.chinastron.2017.08.007>.
 - (23) Jenkins, J. M.; Twicken, J. D.; Batalha, N. M.; Caldwell, D. A.; Cochran, W. D.; Endl, M.; Latham, D. W.; Esquerdo, G. A.; Seader, S.; Bieryla, A.; Petigura, E.; Ciardi, D. R.; Marcy, G. W.; Isaacson, H.; Huber, D.; Rowe, J. F.; Torres, G.; Bryson, S. T.; Buchhave, L.; Ramirez, I.; Wolfgang, A.; Li, J.; Campbell, J. R.; Tenenbaum, P.; Sanderfer, D.; Henze, C. E.; Catanzarite, J. H.; Gilliland, R. L.; Borucki, W. J. Discovery and validation of Kepler-452b: A $1.6R_{\oplus}$ Super Earth exoplanet in the habitable zone of a G2 star. *AJ* **2015**, 150 (2), 56. <https://doi.org/10.1088/0004-6256/150/2/56>.
 - (24) Silva, L.; Vladilo, G.; Murante, G.; Provenzale, A. Quantitative Estimates of the Surface Habitability of Kepler-452b. *Monthly Notices of the Royal Astronomical Society* **2017**, 470 (2), 2270–2282. <https://doi.org/10.1093/mnras/stx1396>.
 - (25) Hu, Y.; Wang, Y.; Liu, Y.; Yang, J. Climate and Habitability of Kepler 452b Simulated with a Fully Coupled Atmosphere–Ocean General Circulation Model. *ApJL* **2017**, 835 (1), L6.
<https://doi.org/10.3847/2041-8213/aa56c4>.
 - (26) Bakos, G. Á.; Torres, G.; Pál, A.; Hartman, J.; Kovács, G.; Noyes, R. W.; Latham, D. W.; Sasselov, D. D.; Sipőcz, B.; Esquerdo, G. A.; Fischer, D. A.; Johnson, J. A.; Marcy, G. W.; Butler, R. P.; Isaacson, H.; Howard, A.; Vogt, S.; Kovács, G.; Fernandez, J.; Moór, A.; Stefanik, R. P.; Lázár, J.; Papp, I.; Sári, P. HAT-P-11b: A Super-Neptune planet transiting

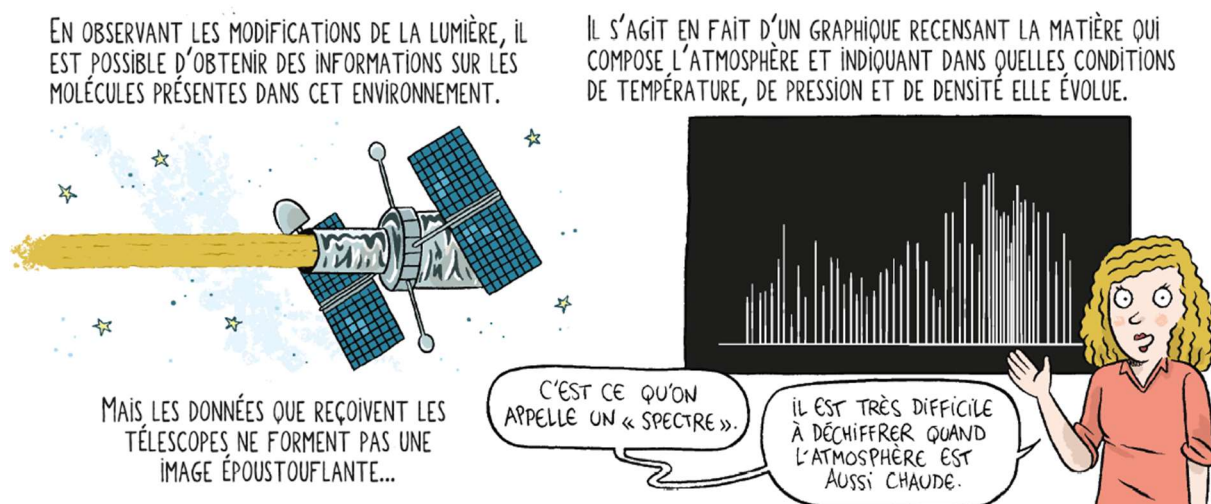
- a bright k star in the Kepler field. *ApJ* **2010**, 710 (2), 1724–1745.
<https://doi.org/10.1088/0004-637X/710/2/1724>.
- (27) Fraine, J.; Deming, D.; Benneke, B.; Knutson, H.; Jordán, A.; Espinoza, N.; Madhusudhan, N.; Wilkins, A.; Todorov, K. Water Vapour Absorption in the Clear Atmosphere of a Neptune-Sized Exoplanet. *Nature* **2014**, 513 (7519), 526–529.
<https://doi.org/10.1038/nature13785>.
- (28) Lissauer, J. J.; Fabrycky, D. C.; Ford, E. B.; Borucki, W. J.; Fressin, F.; Marcy, G. W.; Orosz, J. A.; Rowe, J. F.; Torres, G.; Welsh, W. F.; Batalha, N. M.; Bryson, S. T.; Buchhave, L. A.; Caldwell, D. A.; Carter, J. A.; Charbonneau, D.; Christiansen, J. L.; Cochran, W. D.; Desert, J.-M.; Dunham, E. W.; Fanelli, M. N.; Fortney, J. J.; Gautier Iii, T. N.; Geary, J. C.; Gilliland, R. L.; Haas, M. R.; Hall, J. R.; Holman, M. J.; Koch, D. G.; Latham, D. W.; Lopez, E.; McCauliff, S.; Miller, N.; Morehead, R. C.; Quintana, E. V.; Ragozzine, D.; Sasselov, D.; Short, D. R.; Steffen, J. H. A Closely Packed System of Low-Mass, Low-Density Planets Transiting Kepler-11. *Nature* **2011**, 470 (7332), 53–58.
<https://doi.org/10.1038/nature09760>.
- (29) Perri, F.; Cameron, A. G. W. Hydrodynamic Instability of the Solar Nebula in the Presence of a Planetary Core. *Icarus* **1974**, 22 (4), 416–425.
[https://doi.org/10.1016/0019-1035\(74\)90074-8](https://doi.org/10.1016/0019-1035(74)90074-8).
- (30) Pollack, J. B.; Hubickyj, O.; Bodenheimer, P.; Lissauer, J. J.; Podolak, M.; Greenzweig, Y. Formation of the Giant Planets by Concurrent Accretion of Solids and Gas. *Icarus* **1996**, 124 (1), 62–85. <https://doi.org/10.1006/icar.1996.0190>.
- (31) Project MUSE - Protostars and Planets VI <https://muse.jhu.edu/chapter/1386905> (accessed 2021 -06 -03).
- (32) Boss, A. P. Giant Planet Formation by Gravitational Instability. *Science* **1997**, 276 (5320), 1836–1839. <https://doi.org/10.1126/science.276.5320.1836>.
- (33) Durisen, R.; Boss, A.; Mayer, L.; Nelson, A.; Quinn, T.; Rice, K. Gravitational Instabilities in Gaseous Protoplanetary Disks and Implications for Giant Planet Formation. *arXiv:astro-ph/0603179* **2006**.
- (34) Rafikov, R. R. Can Giant Planets Form by Direct Gravitational Instability? *ApJ* **2005**, 621 (1), L69. <https://doi.org/10.1086/428899>.
- (35) Batygin, K.; Bodenheimer, P. H.; Laughlin, G. P. In situ formation and dynamical evolution of hot jupiter systems. *ApJ* **2016**, 829 (2), 114. <https://doi.org/10.3847/0004-637X/829/2/114>.
- (36) Lee, E. J.; Chiang, E.; Ormel, C. W. Make Super-Earths, not Jupiters: accreting nebular gas onto solid cores at 0.1 au and beyond. *ApJ* **2014**, 797 (2), 95.
<https://doi.org/10.1088/0004-637X/797/2/95>.
- (37) Bailey, E.; Batygin, K. The Hot Jupiter Period–Mass Distribution as a Signature of in Situ Formation. *ApJL* **2018**, 866 (1), L2. <https://doi.org/10.3847/2041-8213/aade90>.
- (38) Rasio, F. A.; Tout, C. A.; Lubow, S. H.; Livio, M. Tidal Decay of Close Planetary Orbits. *The Astrophysical Journal* **1996**, 470, 1187. <https://doi.org/10.1086/177941>.
- (39) Levrard, B.; Winisdoerffer, C.; Chabrier, G. Falling transiting extrasolar giant planets. *ApJ* **2009**, 692 (1), L9–L13. <https://doi.org/10.1088/0004-637X/692/1/L9>.
- (40) Hellier, C.; Anderson, D. R.; Cameron, A. C.; Miller, G. R. M.; Queloz, D.; Smalley, B.; Southworth, J.; Triaud, A. H. M. J. On the Orbit of the Short-Period Exoplanet WASP-19b. *ApJ* **2011**, 730 (2), L31. <https://doi.org/10.1088/2041-8205/730/2/L31>.

- (41) Nagasawa, M.; Ida, S.; Bessho, T. Formation of Hot Planets by a Combination of Planet Scattering, Tidal Circularization, and the Kozai Mechanism. *The Astrophysical Journal* **2008**, 678, 498–508. <https://doi.org/10.1086/529369>.
- (42) Fortney, J. J.; Dawson, R. I.; Komacek, T. D. Hot Jupiters: Origins, Structure, Atmospheres. *Journal of Geophysical Research: Planets* **2021**, 126 (3), e2020JE006629. <https://doi.org/10.1029/2020JE006629>.
- (43) Clough, S. A.; Shephard, M. W.; Mlawer, E. J.; Delamere, J. S.; Iacono, M. J.; Cady-Pereira, K.; Boukabara, S.; Brown, P. D. Atmospheric Radiative Transfer Modeling: A Summary of the AER Codes. *Journal of Quantitative Spectroscopy and Radiative Transfer* **2005**, 91 (2), 233–244. <https://doi.org/10.1016/j.jqsrt.2004.05.058>.
- (44) A continuum from clear to cloudy hot-Jupiter exoplanets without primordial water depletion - PubMed <https://pubmed.ncbi.nlm.nih.gov/26675732/> (accessed 2021 -05 -28).
- (45) The orbital motion, absolute mass and high-altitude winds of exoplanet HD209458b | Nature <https://www.nature.com/articles/nature09111> (accessed 2021 -05 -28).
- (46) Swain, M. R.; Tinetti, G.; Vasisht, G.; Deroo, P.; Griffith, C.; Bouwman, J.; Chen, P.; Yung, Y.; Burrows, A.; Brown, L. R.; Matthews, J.; Rowe, J. F.; Kuschnig, R.; Angerhausen, D. Water, Methane, and Carbon Dioxide Present in the Dayside Spectrum of the Exoplanet HD 209458b. *Nippon rinsho. Japanese journal of clinical medicine* **2009**, 704 (2), 1616–1621. <https://doi.org/10.1088/0004-637X/704/2/1616>.
- (47) Deming, D.; Wilkins, A.; McCullough, P.; Burrows, A.; Fortney, J. J.; Agol, E.; Dobbs-Dixon, I.; Madhusudhan, N.; Crouzet, N.; Desert, J.-M.; Gilliland, R. L.; Haynes, K.; Knutson, H. A.; Line, M.; Magic, Z.; Mandell, A. M.; Ranjan, S.; Charbonneau, D.; Clampin, M.; Seager, S.; Showman, A. P. Infrared transmission spectroscopy of the exoplanets HD 209458b and XO-1b using the wide field camera-3 on the Hubble space Telescope. *ApJ* **2013**, 774 (2), 95. <https://doi.org/10.1088/0004-637X/774/2/95>.
- (48) Hawker, G. A.; Madhusudhan, N.; Cabot, S. H. C.; Gandhi, S. Evidence for Multiple Molecular Species in the Hot Jupiter HD 209458b. *ApJ* **2018**, 863 (1), L11. <https://doi.org/10.3847/2041-8213/aac49d>.
- (49) Giacobbe, P.; Brogi, M.; Gandhi, S.; Cubillos, P. E.; Bonomo, A. S.; Sozzetti, A.; Fossati, L.; Guilluy, G.; Carleo, I.; Rainer, M.; Harutyunyan, A.; Borsa, F.; Pino, L.; Nascimbeni, V.; Benatti, S.; Biazzo, K.; Bignamini, A.; Chubb, K. L.; Claudi, R.; Cosentino, R.; Covino, E.; Damasso, M.; Desidera, S.; Fiorenzano, A. F. M.; Ghedina, A.; Lanza, A. F.; Leto, G.; Maggio, A.; Malavolta, L.; Maldonado, J.; Micela, G.; Molinari, E.; Pagano, I.; Pedani, M.; Piotto, G.; Poretti, E.; Scandariato, G.; Yurchenko, S. N.; Fantinel, D.; Galli, A.; Lodi, M.; Sanna, N.; Tozzi, A. Five Carbon- and Nitrogen-Bearing Species in a Hot Giant Planet's Atmosphere. *Nature* **2021**, 592 (7853), 205–208. <https://doi.org/10.1038/s41586-021-03381-x>.
- (50) Swain, M. R.; Vasisht, G.; Tinetti, G. The Presence of Methane in the Atmosphere of an Extrasolar Planet. *Nature* **2008**, 452 (7185), 329–331. <https://doi.org/10.1038/nature06823>.
- (51) Swain, M.; Vasisht, G.; Tinetti, G. Methane Present in an Extrasolar Planet Atmosphere. **2008**.
- (52) Swain, M. R.; Deroo, P.; Griffith, C. A.; Tinetti, G.; Thatte, A.; Vasisht, G.; Chen, P.; Bouwman, J.; Crossfield, I. J.; Angerhausen, D.; Afonso, C.; Henning, T. A Ground-Based near-Infrared Emission Spectrum of the Exoplanet HD 189733b. *Nature* **2010**, 463 (7281), 637–639. <https://doi.org/10.1038/nature08775>.

- (53) exo-Planetary high-Temperature Hydrocarbons by Emission and Absorption Spectroscopy <https://anr.fr/Project-ANR-16-CE31-0005> (accessed 2021-05-28).
- (54) James Webb Space Telescope - Webb/NASA <https://www.jwst.nasa.gov/> (accessed 2021-05-20).
- (55) Ariel Space Mission – European Space Agency M4 Mission <https://arielmission.space/> (accessed 2021-05-20).

Infrared spectroscopy of methane

*“Scientia nihil aliud est quam veritatis imago.”**



* Science is but an image of the truth.¹

Contents

1.1 Target molecule: methane	27
1.2 Energy structure.....	29
1.2.1 Vibration of methane.....	29
1.2.2 Rotation of methane.....	30
1.2.3 Nuclear spin isomers	31
1.3 Line intensity	34
1.4 LTE vs non-LTE.....	36
1.5 Partition function	39
1.6 Boltzmann plot method	43
1.7 Databases of methane	44
1.7.1 Effective Hamiltonian extrapolation	44
1.7.2 Ab initio calculation	44
1.8 Previous IR spectroscopic studies of methane.....	46
1.8.1 LTE spectroscopy	46
1.8.2 Non-LTE spectroscopy	48
1.9 SMAUG.....	49
References	50

1.1 Target molecule: methane

Infrared radiation was discovered by Sir William Herschel² in 1800. It concerns the electromagnetic spectrum between the $12800 - 4000 \text{ cm}^{-1}$ spectral range[†] and it is arbitrarily classified into three regions: near ($12800 - 4000 \text{ cm}^{-1}$), middle ($4000 - 1000 \text{ cm}^{-1}$) and far ($1000 - 100 \text{ cm}^{-1}$) IR. The energy of this radiation typically matches the energy of transitions between rotational states of different vibrational states of molecules in the gas phase, but within the original electronic state of those molecules. Infrared is thus of particular importance for the detection and characterisation of the so-called “cool” astrophysical bodies such as hot Neptunes and hot Jupiters, but also brown dwarfs or evolved red giant stars of the asymptotic giant branch stellar class. The typical temperature of these objects varies between 500 and 3000 K, leading to black body emission peaking in the infrared range. Infrared telescopes are therefore extensively used to measure the molecular opacities of these objects either by absorption or emission.

At the moment, as mentioned in the Introduction, methane is in the spotlight of numerous astrophysical investigations as a key molecule in the atmosphere of hot Jupiters³ and many exoplanets.^{4–7} It is also a powerful absorber and emitter in the infrared spectral region, and, as such, methane plays an important role in radiative transfer processes specific to the atmospheres in which it is present. In parallel, the radiative properties of methane can reveal interesting physical and chemical properties of planetary atmospheres sometimes subjected to extreme conditions. Being the simplest hydrocarbon, methane has been addressed in numerous investigations in various scientific fields. In the 19th century, its three-dimensional structure and its chemical bonding was investigated by the Dutch physical chemist Jacobus Henricus van't Hoff.⁸ Later, his investigations allowed physicists to study its potential energy surfaces for molecular dynamics purposes.^{9,10}

Methane (CH_4) is a spherical top hydrocarbon molecule. As figure (1.1) represents, it is a highly symmetrical molecule with a tetrahedral molecular geometry due to four equivalent C-H bonds. Examination of figure (1.1) shows it to be invariant (apart from atom numbering) under the following 24 point group operations: the identity; eight three-fold rotations; three two-fold rotations; six four-fold rotation-reflections; and six planar reflections. Methane therefore belongs to the tetrahedral point group T_d characterised by the five irreducible representations A_1 , A_2 , E , F_1 and F_2 (see table (1.1)).^{11–13}

[†] cm^{-1} unit, commonly referred to as a “wavenumber”, corresponds to the inverse of the wavelength of the light

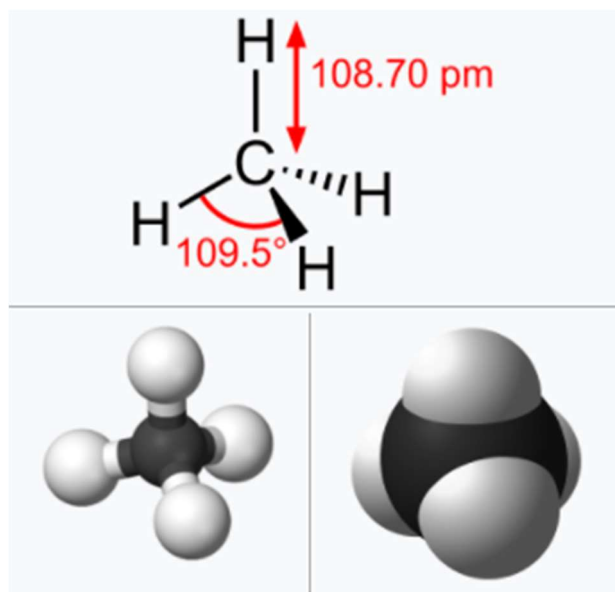
Figure 1.1: Structure of the methane molecule¹⁴

Table 1.1: Character Table for the T_d point group, where E =identity, C_3 =three-fold rotation, C_2 =two-fold rotation, S_4 =four-fold rotation and inversion, σ_d =planar reflection. The F_1 representation can be characterised as a rotation in Cartesian coordinates, while the F_2 representation can be characterised as a translation in Cartesian coordinates. ^{11–13}

T_d	E	$8C_3$	$3C_2$	$6S_4$	$6\sigma_d$	
A_1	1	1	1	1	1	
A_2	1	1	1	-1	-1	
E	2	-1	2	0	0	
F_1	3	0	-1	1	-1	$R_x R_y R_z$
F_2	3	0	-1	-1	1	$T_x T_y T_z$

The reducible representation for the displacement coordinates of the molecule is therefore $\Gamma_{3N} = A_1 + E + F_1 + 3F_2$, where N is the number of atoms in the molecule. In the Γ_{3N} representation, six of the irreducible representations correspond to translations and rotations of the molecule. The representation relative to atoms moving in the same direction at once is $\Gamma_T = F_2$, while the representation corresponding to rotation is $\Gamma_R = F_1$, the dimension of these irreducible representations is 3, as shown in the second column of table (1.1). Finally, the irreducible representation of vibrations is $\Gamma_V = \Gamma_{3N} - \Gamma_T - \Gamma_R = A_1 + E + 2F_2$.

1.2 Energy structure

The energy structure of the methane molecule is described by the molecular wavefunction. To simplify its determination, the Born-Oppenheimer approximation is employed, which decomposes the total wave function (ψ_{tot}) describing a molecule into the product of the separate electronic (ψ_{el}), vibrational-rotational ($\psi_{vib-rot}$), electron spin (ψ_{es}) and nuclear spin (ψ_{ns}) wavefunctions:

$$\psi_{tot} = \psi_{el}\psi_{vib-rot}\psi_{es}\psi_{ns} \quad 1.1$$

Moreover, in the rigid-rotor and harmonic-oscillator approximations, the vibrational rotational wavefunction can be further decomposed into the product of the vibrational (ψ_{vib}) and rotational (ψ_{rot}) wavefunctions:

$$\psi_{vib-rot} = \psi_{vib}\psi_{rot} \quad 1.2$$

Each of these five classifications of the energy of a methane molecular will be treated, separately, in detail in the following sections.

1.2.1 Vibration of methane

The vibration of methane is limited to certain modes, the so-called normal modes where each of these normal modes corresponds to a vibrational degree of freedom. Fundamentally, the normal modes describe the independent motion of atoms or groups of atoms that can be excited separately and without stimulating any other normal mode.¹¹ Concerning methane, the number of coordinates is $3N-6 = 9$, with $\Gamma_V = A_1 + E + 2F_2$. Using the T_d character table, the representation of the vibration can be decomposed on the basis of the internal stretching and bending of the molecule, leading to $\Gamma_V = \Gamma_{str} + \Gamma_{bend}$, with $\Gamma_{str} = A_1 + F_2$ and $\Gamma_{bend} = E + F_2$. This corresponds to four stretching modes and five bending modes (E and F_2 irreducible representations are twofold and threefold degenerated, respectively). The four C-H stretching modes can be reduced to one symmetrical stretch, A_1 , and a triply degenerate F_2 antisymmetric C-H stretch. Similarly, the five bending modes reduce to a pair of E modes along a triply degenerate F_2 bending mode. The result is four normal modes of vibration for the methane¹⁵:

Table 1.2: Four normal modes of methane

¹² CH ₄ normal vibrational mode	Type	Sym.	Deg.	Wavenumber (cm ⁻¹)
ν_1	symmetric C-H stretch	A_1	1	2916.433
ν_2	bend	E	2	1533.345
ν_3	antisymmetric C-H stretch	F_2	3	3019.418
ν_4	bend	F_2	3	1310.776

Note that only the ν_3 and ν_4 vibration modes are active in the infrared since these are the only modes that induce a non-zero dipole moment.

Observing the frequencies of the normal modes, it can be seen that mode ν_2 is quite close to ν_4 and that their frequency is about half of the stretching modes ν_1 and ν_3 . Therefore, the vibrational modes of methane form groups of vibrational levels with the following ratio: $\nu_1 \sim 2\nu_2 \sim \nu_3 \sim 2\nu_4$.

A group of methane vibrational energy levels is called a polyad (P), and the quantum number of the polyad could be obtained from:

$$n = 2(\nu_1 + \nu_3) + \nu_2 + \nu_4 \quad 1.3$$

The different polyads are displayed in table (1.3).

Table 1.3: Summary of the polyads concerned in this thesis, underlying the rising numbers of vibrational sublevels as energy increases

Polyad No. (P_x)	Name	Vibrational levels
P_0	Ground state	1
P_1	Dyad	2
P_2	Pentad	9
P_3	Octad	24
P_4	Tetradecad	60
P_5	Icosad	134
P_6	Triacontad	280
P_7	Tetracontad	538

1.2.2 Rotation of methane

The rotational energy levels of methane are given by:

$$E_{JK} = BJ(J+1) - D_J J^2(J+1)^2 \quad 1.4$$

Where the first term describes the rigid body rotational energy level, and the following terms are the corrections due to the centrifugal distortion. D_J is the centrifugal distortion constant. The rotational constant B is given by:

$$B = \frac{h^2}{8\pi^2 I} \quad 1.5$$

I – is the moment of inertia of the molecule, and as methane is a symmetrical top: $I_a = I_b = I_c = I$ and h is Planck's constant.

Remark: methane being a relatively light molecule, its moment of inertia is small and thus associated with a relatively large rotational constant $B = 5.2412 \text{ cm}^{-1}$. The rotational energy levels are therefore relatively far from each other and the vibrational bands therefore extend over several hundred wavenumbers (see figure (1.2)).

The symmetry of the rotational wave function is given in table (1.4), according to the different J values. The selection rules allow rovibrational transitions where $\Delta J = -1, 0, +1$, resulting in three branches P, Q, and R, respectively, as it is presented in panel (a) of figure (1.2).

Table 1.4: Symmetry of the rotational wave function of methane with varying J .

J	Γ_R
0	A_1
1	F_1
2	$E \oplus F_2$
3	$A_2 \oplus F_1 \oplus F_2$
4	$A_1 \oplus E \oplus F_1 \oplus F_2$
5	$E \oplus 2F_1 \oplus F_2$
6	$A_1 \oplus A_2 \oplus E \oplus F_1 \oplus 2F_2$

The Coriolis force causes a coupling between the vibration and the rotation of the molecule which results in interactions between vibrational states of same symmetry. The coupling occurs when the product of the vibrational symmetries of the two vibrational levels involved contains the rotational symmetry F_1 , which limits this type of interaction to the F_2 vibrational symmetry (because $F_1 \in F_2 \otimes F_2 = A_1 \oplus E \oplus F_1 \oplus F_2$, while $F_1 \notin E \otimes E$ and $F_1 \notin A_1 \otimes A_1$).^{16,17} The Coriolis interaction is therefore responsible for lifting degeneracy which results in a splitting of the energy levels of the rovibrational states involved, and therefore to a multiplication of the permitted transitions leading to a number of satellite transitions observable in the spectrum of methane with the same J -levels (see panel (b) of figure (1.2)).

1.2.3 Nuclear spin isomers

The methane molecule is composed of a carbon atom of zero nuclear spin (boson) and four hydrogen atoms of one-half nuclear spin (fermions), resulting in a total nuclear spin of $I = 0$, $I = 1$ or $I = 2$, corresponding to the *para*, *ortho* and *meta* nuclear spin isomers, respectively. The reducible representation relative to the nuclear spin of the molecule can be expressed on the basis of the irreducible representations of the T_d character table: $\Gamma_{NS} = 5A_1 + E + 3F_2$.

According to the Pauli exclusion principle, the construction of the total wave function of methane, ψ_{tot} , must be antisymmetric with respect to the permutation of two hydrogen atoms. Its symmetry must therefore be A_1 or A_2 . Considering methane molecule in its fundamental electronic state (A_1 symmetry) yields to:

$$\Gamma_{tot} = \Gamma_V \otimes \Gamma_R \otimes \Gamma_{NS}$$

Furthermore, considering the vibrational ground state (A_1 symmetry) as an example, yields:

$$\Gamma_{tot} = \Gamma_R \otimes \Gamma_{NS}$$

The possible combinations of Γ_R and Γ_{NS} are summarised in table (1.5), leading to the statistical weights (5 for A_1 and A_2 , 2 for E , and 3 for F_1 and F_2) responsible for the line intensities observed within a same- J cluster of rovibrational lines (see again panel (b) of figure (1.2)).

Finally, the complete energy structure of methane for the first four polyads is represented visually in figure (1.3).

Table 1.5: Statistical weights according to the nuclear spin state and the symmetry of the rotational wave function

Γ_R	Γ_{NS}	Γ_{tot}	Statistical weight (2I+1)
A ₁	A ₁ (I = 2)	A ₁	5
A ₂	A ₁ (I = 2)	A ₂	5
E	E (I = 0)	A ₁ ⊕ A ₂	2
F ₁	F ₂ (I = 1)	A ₂	3
F ₂	F ₂ (I = 1)	A ₁	3

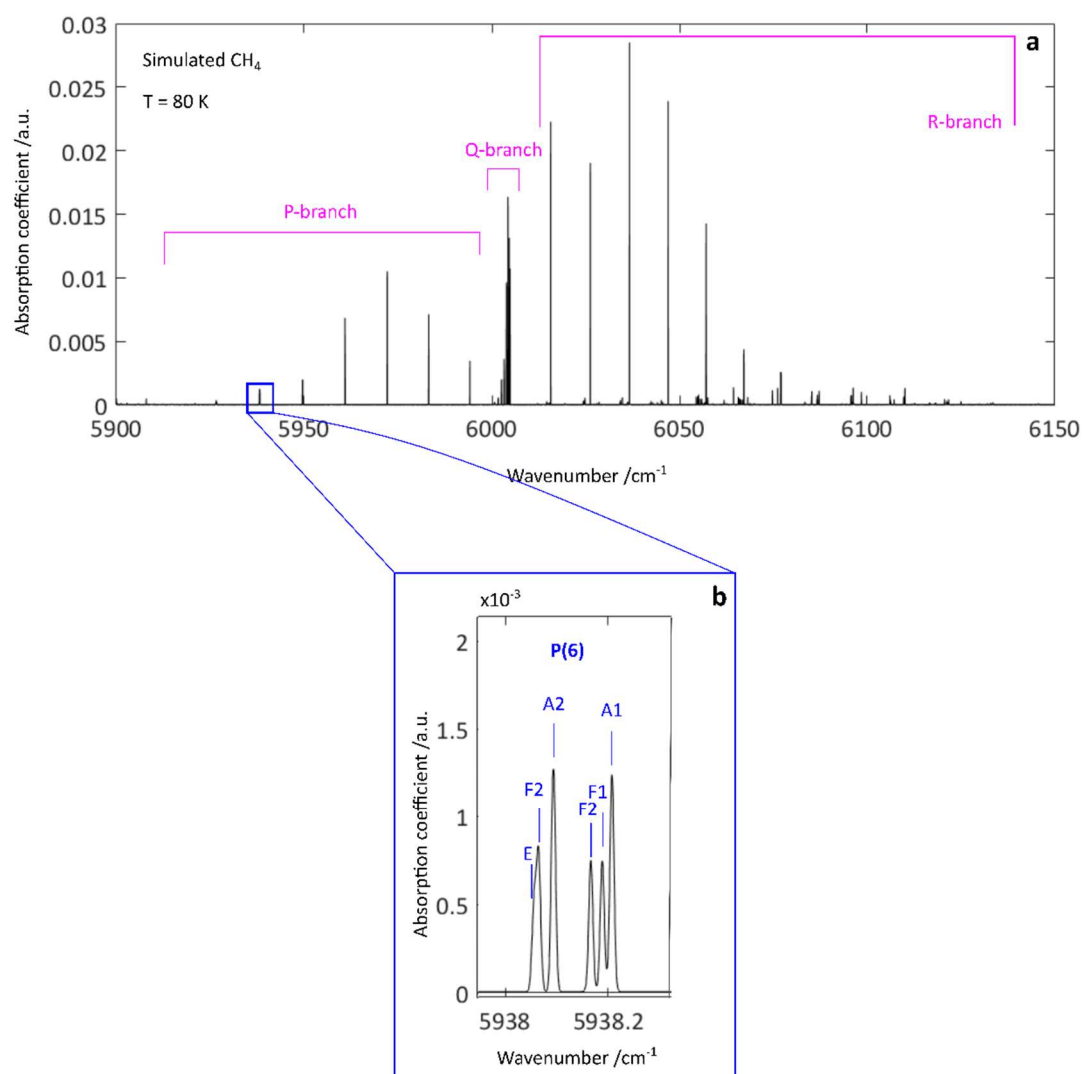


Figure 1.2: Simulated spectrum of methane at 80 K. Panel (a) exhibits the three P, Q and R branches. Panel (b) highlights the presence of the cluster splitting with the 5/2/3 ratio for rotational lines of A/E/F symmetry.

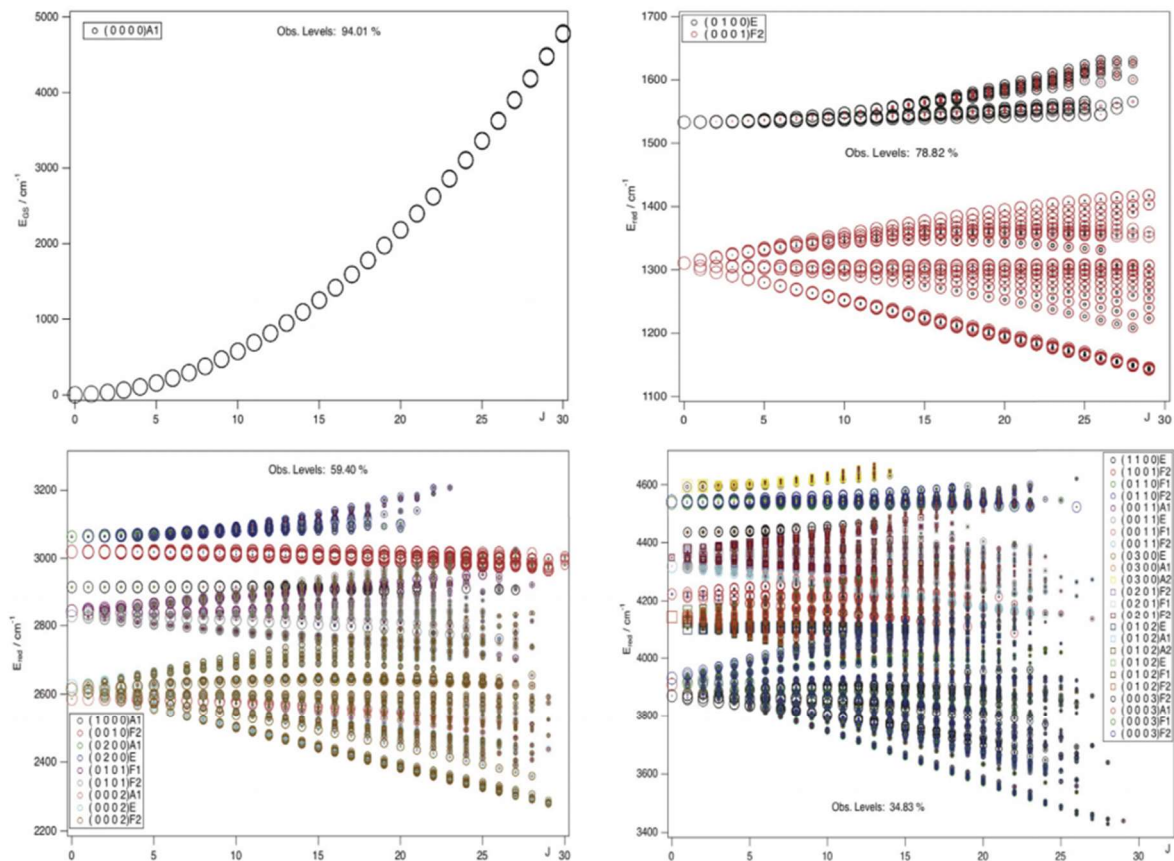


Fig. 4. Reduced energy levels of methane for P_0 to P_3 polyads. Sub-states are characterized using different symbols (circles or squares) and colors. For a given J -level the size of each marker defines the percentage of the zeroth-order states that composes the levels. (For interpretation of the references to colour in this figure, the reader is referred to the web version of this article.)

Figure 1.3: Representation of the methane energy structure by Amyay and Boudon¹⁸

1.3 Line intensity

A laser beam passing through a layer of homogenous gas loses a certain quantity of its initial intensity ($I(\nu)$) at a given wavenumber (ν). The variation of the intensity ($dI(\nu)$) can be described by the Beer-Lambert law¹⁹:

$$dI(\nu) = -\alpha(\nu)I(\nu)dl \quad 1.6$$

Where, $\alpha(\nu)$ - spectral absorption coefficient in cm^{-1} and dl - the pathlength of the studied layer of gas. By defining the integrated absorption coefficient (σ) of an isolated line centred at ν_0 :

$$\sigma = \int_{-\infty}^{\infty} \alpha(\nu - \nu_0) d(\nu - \nu_0) \quad 1.7$$

the spectral absorption coefficient can be determined using the integrated absorption coefficient as a proportionality constant and a normalized profile ($\Phi(\nu - \nu_0)$) whose integral over the entire spectral domain is unity.

$$\alpha(\nu - \nu_0) = \sigma \Phi(\nu - \nu_0) \quad 1.8$$

At the same time, the integrated absorption coefficient can be expressed proportionally to various conditions of the probed gas, such as pressure (p), volumetric density (ρ) and number of absorbing molecules per unit volume (N):

$$\sigma = \sigma_v^p p = \sigma_v^\rho \rho = \sigma_v^N N \quad 1.9$$

Following this equation, a relationship between the pressure and the number of absorbing molecules can be established which demonstrates the temperature dependence of the integrated absorption coefficient:

$$\sigma_v^N(T) = \frac{P}{N} \sigma_v^p \quad 1.10$$

Knowing that the integrated absorption coefficient depends on temperature calls for a relationship that describes the changes in intensity from some T_0 to T . This ratio depends on how the energy of the molecule is distributed across its different levels at the two temperatures (the partition functions) and the particular energies of the lower and upper states involved in the transition (or the energy of just the lower state along with the transition energy, which is the difference between the two states).²⁰ The effect of the partition functions, lower state energy and transition energy on the integrated absorption coefficient between different temperatures is given as:

$$\sigma_v^N(T) = \sigma_v^N(T_0) \frac{Q_{tot}(T_0)}{Q_{tot}(T)} e^{-c_2 E_i \left(\frac{1}{T} - \frac{1}{T_0} \right)} \left[\frac{1 - e^{-\frac{c_2 v}{T}}}{1 - e^{-\frac{c_2 v}{T_0}}} \right] \quad 1.11$$

Where, $Q_{tot}(T)$ – the total partition function sum (see next paragraph), E_i – lower state energy, ν – transition energy, $c_2 = \frac{hc}{k}$ – the second rotational constant, where k – Boltzmann constant, c – the speed of the light.

1.4 LTE vs non-LTE

Depending on the medium in which it is located (plasma, supersonic expansion, photosphere, planetary atmosphere, shock layer, etc.), a gas may no longer be in conditions corresponding to a Local Thermodynamic Equilibrium (LTE). LTE is achieved when there are sufficient collisions between the molecules to evenly distribute energy through the different degrees of freedom of the molecule. It usually occurs when the temperature and pressure values are not very low, and the population throughout the quantum energy states follows a Boltzmann distribution and at the same time, the molecular velocity remains Maxwellian.

Conversely, when there is a drop in the number of molecular collisions, the above-mentioned population distribution differs from a Boltzmann, while the molecular velocity still respects a Maxwellian distribution. This phenomenon is called a non-Local Thermodynamic Equilibrium (non-LTE) and it happens when the radiative lifetimes of certain vibrational energy states are in comparable scale to the mean time between incidents of molecular collisions.²¹ In this latter condition, the internal energy populations are not determined strictly by collisional energy exchange and other factors gain importance, such as radiative and chemical pumping as well as radiative losses.²²

The temperature of the gas is intimately related to the distribution of the molecules throughout their various energy levels and therefore the intensity of a transition is strongly dependent on the temperature of the gas. Given that vibrational energy spacing is generally larger than rotational energy spacing, a vibrational molecular state is normally associated with a series of rotational molecular states. A rovibrational transition connects two different vibrational energy levels to form a vibrational band, with P, Q, and R branches defined by their lower J -level (refer to figure (1.4)). If the initial vibrational energy level corresponds to the ground vibrational state (i.e. without any quanta of vibration) then the vibrational band is referred to as a “cold” band, mainly because at room or colder temperatures the population of the ground state is important and leads to an intense absorption band. If the initial vibrational energy level corresponds to an excited vibrational state, then the vibrational band is referred to as a “hot” band, because to be detectable such band requires a significant thermal population on its initial vibrational state. Of course, to achieve this, the temperature of the gas must be higher as the vibrational state is at high energy.

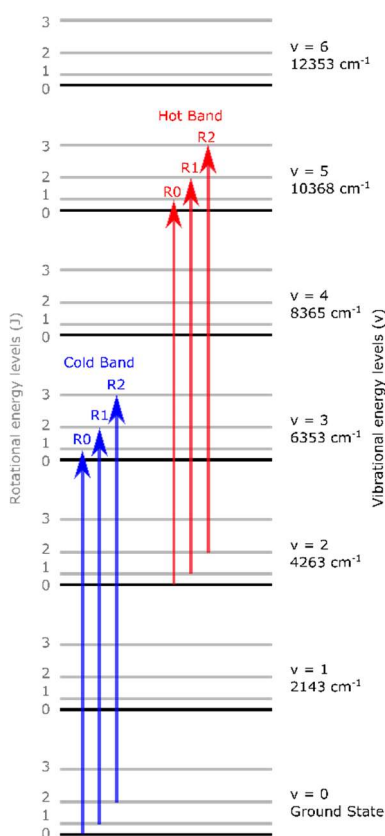


Figure 1.4: Schematic representation of rovibrational transitions of CO (blue: $3 \leftarrow 0$ cold band transitions and red: $5 \leftarrow 2$ cold band transitions)

In a hypersonic jet (a more detailed explanation of this concept follows in Chapter II) the non-LTE condition is based on a very efficient and quick rotational-translational (R-T) energy transfer, and a rather inefficient vibrational-translational (V-T) collisional energy transfer, throughout the adiabatic expansion. From a spectroscopic point of view, the spectra obtained in such extreme conditions expose a simplified rotational structure, as it can be seen in panel (c) of figure (1.5), meanwhile this energy structure permits a line-by-line analysis of the various hot bands that can be detected. The exact determination of the line positions would be impossible in high-temperature LTE conditions due to the vast number of overlapping transitions, as represented in panel (b) of figure (1.5). Finally, panel (a) of figure (1.5) demonstrates the case of a molecule in cold LTE conditions, missing information on the hot bands.

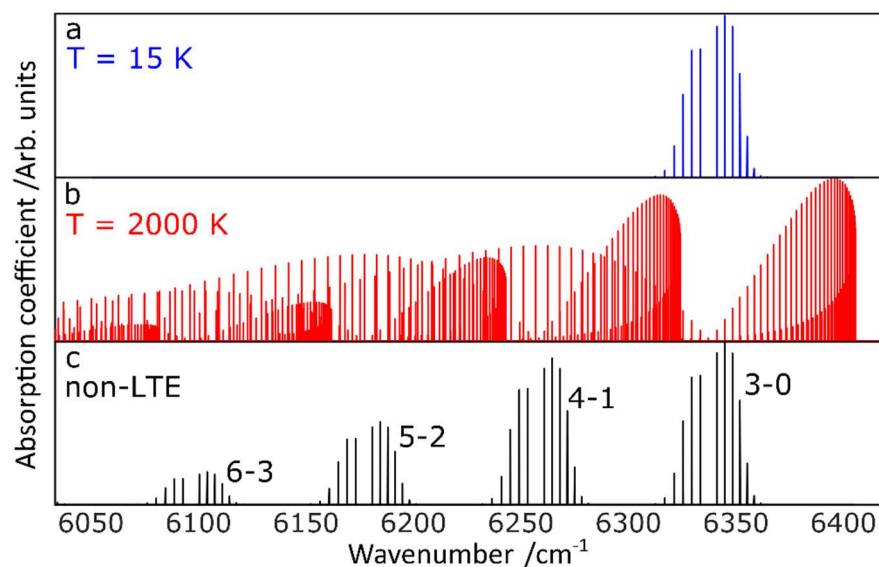


Figure 1.5: Simulated CO spectra at different conditions, underlining the advantage of non-LTE spectroscopy. Panel (a): simulated CO spectrum at 15 K, only the lines corresponding to the 3 \leftarrow 0 cold band appear. Panel (b): simulated CO spectrum at 2000 K in LTE conditions, revealing the 4 \leftarrow 1, 5 \leftarrow 2 and 6 \leftarrow 3 hot bands and the multiple overlapping lines. Panel (c): simulated non-LTE CO spectrum with vibrational temperature: $T_{\text{vib}} = 2000$ K and rotational temperature: $T_{\text{rot}} = 15$ K highlighting a simplified rotational structure and the presence of hot bands.

1.5 Partition function

The internal partition function allows the calculation of the probability of a system to occupy a given energy state. The total partition function sum is a direct summation of the population for all of the quantum states (s_i):

$$Q_{tot}(T) = \sum_{all\ s_i} g_i e^{\frac{-c_2 E_i}{T}} \quad 1.12$$

Where, g_i – is the statistical weight of level i and E_i – the energy of level i . Remark, equation (1.12) considers LTE conditions and subsequently a Maxwell-Boltzmann distribution characterised by a temperature T . Knowing the molecular density (N) as well allows the derivation of the density of molecules (n) present in a given quantum state at the given temperature:

$$n_i(T) = N \frac{g_i e^{\frac{-c_2 E_i}{T}}}{Q_{tot}(T)} \quad 1.13$$

Or, in case of no knowledge of the molecular density, the concept of the population probability (W_i) can be introduced:

$$W_i = \frac{g_i e^{\frac{-c_2 E_i}{T}}}{Q_{tot}(T)} \quad 1.14$$

Obviously, summing up the population probabilities over every quantum state results in unity.

The different quantum states can be considered as rovibrational states, and their energy level (E_i) can be represented as the sum of a vibrational energy (E_v) and a rotational energy (E_r):

$$E_i = E_v + E_r \quad 1.15$$

Henceforth, the partition function can be written as a product of the vibrational partition function ($Q_{vib}(T)$) summed over every vibrational state (v_i) times the rotational partition function ($Q_{rot}(T)$) summed over all the rotational levels (J_i)^{23–26}:

$$Q_{tot}(T) = Q_{vib}(T) \times Q_{rot}(T) \quad 1.16$$

This product approximation turns out to be very accurate for methane.²⁷

$$Q_{tot}(T) = \sum_{all\ v_i} g_{v_i} e^{\frac{-c_2 E_{v_i}}{T}} \times \sum_{all\ J_i} g_{J_i} e^{\frac{-c_2 E_{r_i}}{T}} \quad 1.17$$

Where, g_{v_i} – represents the statistical weight of the vibrational states and g_{j_i} – describes the statistical weight for every rotational level.

Accordingly, equation (1.11) can be modified to:

$$\sigma_v^N(T) = \sigma_v^N(T_0) \frac{Q_{tot}(T_0)}{Q_{vib}(T) \times Q_{rot}(T)} e^{-c_2 E_i \left(\frac{1}{T} - \frac{1}{T_0} \right)} \left[\frac{1 - e^{-\frac{c_2 v}{T}}}{1 - e^{-\frac{c_2 v}{T_0}}} \right] \quad 1.18$$

Radiative transfer theory delivers a spectral line intensity which describes a rovibrational transition from a lower energy level (i) to an upper level (j) as a function of the center of the line (ν_{ij}), the Einstein coefficient^{20,28} (B_{ij}) for absorption and the corresponding lower (g_i) and upper (g_j) statistical weights and the lower (n_i) and upper (n_j) populations:

$$\sigma_{ij} = \frac{h\nu_{ij}}{c} B_{ij} n_i \left(1 - \frac{g_i n_j}{g_j n_i} \right) \quad 1.19$$

Considering LTE conditions, the Boltzmann factor Γ represents the ratio of the population regarding the upper and lower levels:

$$\Gamma = \frac{g_i n_j}{g_j n_i} = e^{\frac{-c_2 \nu_{ij}}{T}} \quad 1.20$$

Until now, the molecules were considered in LTE conditions and the above-mentioned equations are adequate assuming this criterion. However, when non-LTE conditions occur, these equations have to be modified to respect the fact that the population levels differ from the Boltzmann distribution, while they maintain a Maxwellian molecular velocity distribution.

To describe the integrated absorption coefficient in non-LTE conditions, additional temperatures have to be introduced next to the base kinetic temperature (T). The rotational temperature (T_r) describes the population distribution across rotational levels and the vibrational temperature (T_v) defines the populations across vibrational levels. In a hypersonic jet, in the adiabatic expansion, the kinetic temperature drops and the rotational temperature follows its value closely, meanwhile, due to the lack of molecular collisions, the vibrational temperature cannot relax efficiently and this results in: $T < T_r \ll T_v$.

Furthermore, one rotational temperature is enough to describe the rotational structure among the rotational levels, on the other hand a set of vibrational temperatures is required to model the vibrational level population²¹. In fact, these vibrational temperatures express the population (n_{v_i}) on a given vibrational level with reference to the population of lowest vibrational level (n_0), namely the ground state:

$$T_{v_i} = \frac{hcE_{v_i}}{k \ln \left(\frac{g_{v_i} n_0}{g_0 n_{v_i}} \right)} \quad 1.21$$

Here, g_{v_i} and g_0 are the statistical weights of the v_i vibrational level and the ground state respectively.

Henceforth, the non-LTE partition function can be written as:

$$Q_{tot}(T_r, T_{v_i}) = \sum_{all v_i} g_{v_i} e^{\frac{-c_2 E_{v_i}}{T_{v_i}}} \times \sum_{all J_i} g_{J_i} e^{\frac{-c_2 E_{J_i}}{T_r}} \quad 1.22$$

Accordingly, the ratio of the population of the upper (n_j) and lower (n_i) levels in non-LTE conditions can be given as:

$$\frac{n_j}{n_i} = \frac{g_j}{g_i} \frac{e^{\frac{-c_2 E_{v_j}}{T_{v_j}}} \cdot e^{\frac{-c_2 E_r}{T_r}}}{e^{\frac{-c_2 E_i}{T_i}}} \quad 1.23$$

Finally, the non-LTE integrated absorption coefficient can be obtained:

$$\sigma_{ij}(T_r, T_{v_i}) = \sigma_{ij}(T_0) \frac{Q_0(T_0)}{Q_{rot}(T_r) \times Q_{vib}(T_{v_i})} \times e^{\frac{E_i}{kT_0} - \frac{1}{k} \left(\frac{E_i^{vib}}{T_{v_i}} + \frac{E_i^{rot}}{T_r} \right)} \quad 1.24$$

$$\times \left[\frac{1 - e^{-\left(\frac{E_j^{vib} - E_i^{vib}}{kT_{v_i}} + \frac{E_j^{rot} - E_i^{rot}}{kT_r} \right)}}{1 - e^{-\frac{hc\tilde{\nu}_{ij}}{kT_0}}} \right]$$

Remark, each vibrational state has its corresponding vibrational temperature which has to be applied depending on the characteristics of the transitions. Also, to obtain a non-LTE vibrational partition function every vibrational state has to be summed up by using the corresponding vibrational temperature for each vibrational level.

Figure (1.6) is a schematic representation of the methane energy structure. Panel (a) of figure (1.6) exhibits the lowest energy state, the ground state, and the first polyad, namely the dyad with its two vibrational energy levels. The panel also demonstrates the possible relaxation processes, between the rotational energy levels, between the vibrational levels within a polyad (intra-polyad vibrational relaxation) and relaxation between polyads (inter-polyad vibrational relaxation).

In panel (b) of figure (1.6) the degenerate vibrational levels of the pentad are shown; the panel aims to illustrate the close and occasionally overlapping rotational levels of the different vibrational levels. This is considered to be the reason why an efficient intra-polyad vibrational relaxation could occur, as the population could easily descend to lower vibrational levels through efficient relaxations within the polyad. However, due to the bigger energy gaps in-between the polyads, the inter-polyad relaxation is thought to be much less effective.^{29,30}

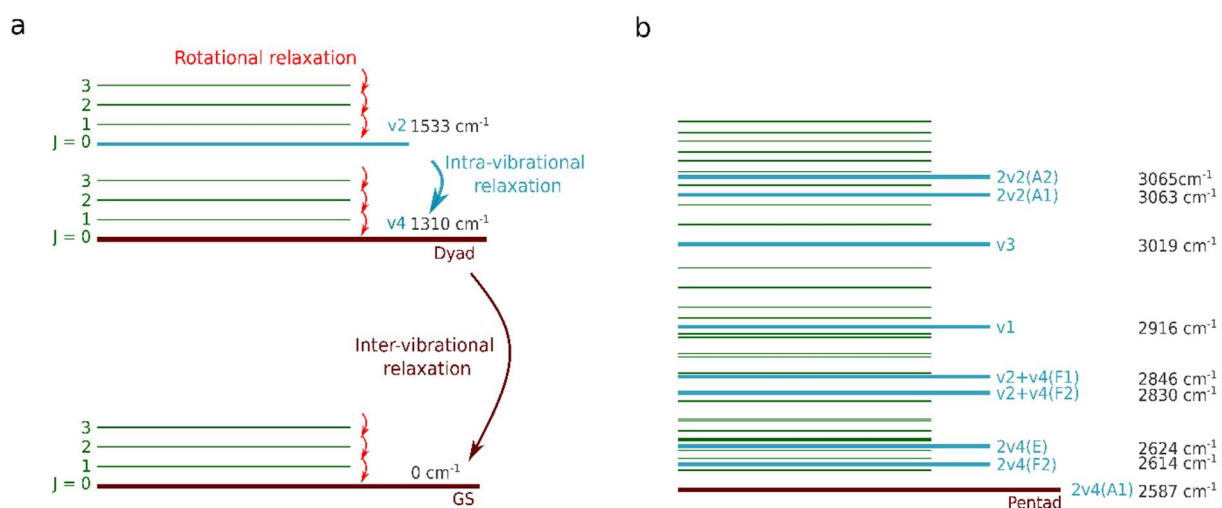


Figure 1.6: Schematic representation of the ro-vibrational energy structure of methane. Panel (a) represents the ground state and the first polyad (dyad), and the possible relaxation processes. Panel (b) highlights the degenerate vibrational modes and the energy structure of the pentad polyad.

1.6 Boltzmann plot method

The Boltzmann plot method is a commonly used technique to retrieve molecular temperatures by comparing the relative intensities of different energy levels, rotational or vibrational. It can characterise the population distribution in the rotational and vibrational energy levels as long as the population distribution can be considered Boltzmannian. The Boltzmann distribution gives the relationship of the populations between a lower energy state (N_i) and a higher (N_j) energy state:

$$\frac{N_j}{N_i} = \frac{g_j}{g_i} e^{-\frac{E_j - E_i}{k \cdot T}} \quad 1.25$$

Where, g_j and g_i – are the statistical weights of the upper (E_j) and lower (E_i) energy states respectively, k – is the Boltzmann constant and T – is the characteristic temperature.

The recorded absorption coefficient depends on:

$$\alpha_{ij}(v_{ij}, T) = \frac{g_j}{Q_{tot}(T)} \frac{A_{ji}}{8\pi c v_{ij}^2} e^{-\frac{c_2 E_i}{T}} \left(1 - e^{-\frac{c_2 v_{ij}}{T}}\right) \quad 1.26$$

Where, A_{ji} – is the corresponding Einstein coefficient for spontaneous emission. The term $\left(1 - e^{-\frac{c_2 v}{T}}\right)$ is neglected at the moment due to its value close to unity (~ 0.98) in the conditions of these experiments. Then, equation (1.26) can be rewritten:

$$\ln\left(\frac{\alpha_{ij}(v, T) \cdot Q_{tot}(T) \cdot 8\pi c v_{ij}^2}{g_j \cdot A_{ji}}\right) = -\frac{c_2 E_i}{T} \quad 1.27$$

This formula allows the determination of the characteristic rotational or vibrational temperature of a molecule depending on the substituted energy E_i , which can take the form of rotational or vibrational energy levels as well.

1.7 Databases of methane

More and more observational data arrive from the various spatial environments and extra-terrestrial atmospheres each day. In order to investigate and interpret these data it is vital to have accurate line lists that can be used as input files for radiative transfer codes^{31,32} which in turn are used to model the atmospheres being observed³³ or to carry out concentration measurements of these environments.^{34,35} In the following section, some different line list construction approaches are presented for the two databases that contain information relative to the infrared spectrum of methane.

1.7.1 Effective Hamiltonian extrapolation

In this approach, the line list is based on infrared experimental spectra and the calculated rovibrational line list results from an effective Hamiltonian constructed for one particular polyad. This approach is very precise as it can calculate rovibrational transitions with a precision equal to the experimental observations. The calculated transitions, however, are less precise for extrapolated transitions involving rotational or vibrational energy levels not yet determined experimentally.

1.7.1.1 MeCaSDa - methane calculated spectroscopic database

The MeCaSDa^{36,37} database provides a purely calculated line list that is based on the most recent fitted and assigned experimental spectra obtained by different research groups.^{38–40} This method constructs the effective Hamiltonian, dipole and polarizability parameters adaptively for every polyad scheme of methane.

1.7.1.2 HITRAN - high-resolution transmission molecular absorption database

The line list provided by HITRAN⁴¹ is based, in principle, on high-resolution experimental spectral data recorded under controlled laboratory conditions. However, in case of lack of experimental data, the experimental lines are complemented with theoretically calculations. The database aims to provide a theoretically self-consistent set of parameters with the highest accuracy possible.

These semi-empirical lines are widely used in the field of spectroscopy for their very accurate line parameters. However, the accuracy comes with the price of the slow progress of the extension of the database. Carrying out line-by-line analysis for polyatomic molecule like methane at higher energy levels suggests the study of millions of overlapping lines appearing in the recorded spectrum. Often, the limited numbers of rovibrational transitions in the HITRAN database do not fulfil the requirements raised by the current and upcoming astrophysical challenges.

For planetary and astrophysical applications, completeness is generally more important than accuracy on the individual lines, therefore the below discussed *ab initio* calculations are preferred.

1.7.2 Ab initio calculation

To respond the above-mentioned needs, a completely different approach is the so-called *ab initio* calculation. Instead of fitting a function over experimental data and then extrapolating it over a wider spectral and temperature domain, in case of an *ab initio* model the theoretical line

list is derived from molecular potential energy surface (PES) and dipole moment (DM) surfaces, constructed from physical first principles, thus considering all the polyads simultaneously.

1.7.2.1 TheoReTS - theoretical Reims–Tomsk spectral data

A very unique feature of TheoReTS⁴² database is the exhaustive line list of the hot bands of methane, which describe the rovibrational transitions issuing from highly excited vibrational levels to over 13000 cm⁻¹ in spectral range or corresponding to conditions of 3000 K.⁴³ In general, the results of the *ab initio* calculations match the experimentally recorded spectra very well at lower energy levels, however the discrepancy grows as the energy rises. Therefore, the vibrational band centres are corrected using the VSS procedure⁴⁴, nevertheless this procedure does not concern the rotational lines, nor the vibration-rotation interactions, they are always the result of pure *ab initio* surfaces.

1.7.2.2 ExoMol

The aim of the ExoMol^{45,46} database is to provide high temperature line lists for molecules which are considered to play a key role in hot spatial environments such as exoplanets and cool stars. Concerning methane, the line list YT10to10^{47,48} delivers calculated high temperature line list up to 12000 cm⁻¹ in transition energy.

In conclusion, spectroscopic databases are rapidly improving and expanding in terms of their accuracy as well as in their coverage of the spectral domain. However, as it has been pointed out, the correctness and therefore the utility of the theoretical line lists highly depends on the experimental verification of the spectral parameters. In the following chapter, the experimental work is presented, without the list being exhaustive, that has contributed to the validation of, or, where it was needed, to the correction of, the calculated lines.

1.8 Previous IR spectroscopic studies of methane

1.8.1 LTE spectroscopy

1.8.1.1 Dyad and pentad

Concerning studies on methane hot bands, an update on the existing line list⁴⁹ covering the dyad polyad, the ν_4 and ν_2 vibrational levels of methane, was reported by Amyay *et al.*⁵⁰ High resolution, high temperature emission spectra, up to 1400 K, were recorded using a Bruker IFS 125HR Fourier transform spectrometer (FTS) at the SOLEIL synchrotron facility, over the 1100-1500 cm^{-1} spectra range. This study resulted in the extension of the rotational assignments of transitions issuing from the P_1 - P_0 and the P_2 - P_1 polyads. Furthermore, 8512 new transitions contributed to the significant improvement, in terms of a more complete rotational structure, of the MeCaSDa database.

Following the investigation of the dyad polyad, a new data set concerning the pentad polyad was recorded in Rennes using the same technique by Amyay *et al.*¹⁵ A High Enthalpy Source⁵¹ generated a continuously renewing flow of high temperature methane, whose infrared emission was collected by a high resolution FTS.

1.8.1.2 Tetradecad and icosad

The absorption spectrum of methane in the 5852-6181 cm^{-1} spectral region was investigated using CRDS by Gao *et al.*⁵² probing cold (81 K) methane in a cryogenic cell with a series of distributed feedback (DFB) lasers. The investigated spectral domain concerns the tetradecad region where the $2\nu_3$ band is represented. As a result of the investigation, 845 low energy transitions were identified. In a direct continuation of the previous work, the obtained transitions at 81 K were compared to lines recorded at 296 K in frame of the GOSAT project⁵³ to explore the temperature dependence of the methane absorption spectrum and to retrieve additional transitions corresponding to the $2\nu_3$ band.⁵⁴

Afterwards, the same experimental system was used by Campargue *et al.* to record the absorption spectrum corresponding to the icosad polyad.⁵⁵ Cold spectral data was obtained in the 6717-7351 cm^{-1} spectral domain where the higher vibrational band of methane, the $\nu_2+2\nu_3$, dominates and where the theoretical line lists reported inaccurate rovibrational energies. An exhaustive lower energy line list, consisting of almost 13000 experimental lines, was established at 81 K.⁵⁶ The corresponding data is incorporated in the WKMC (Wang, Kassi, Mondelain & Campargue) empirical line list (from 5852-7919 cm^{-1}).

The tetradecad spectral region in the 5693-6257 cm^{-1} domain was investigated by Ghysels *et al.* at 964 K. Using the DAS high-temperature experimental setup^{57,58}, consisting of an absorption cell implanted into a single-zone tubular furnace, transitions were recorded by a set of DFB lasers.⁵⁹ This study derived a more complex rotational spectrum with the appearance of transitions issuing from $J = 21$ rotational level.

1.8.1.3 Tetradecad, icosad and triacontad

An absorption cross section atlas was delivered by Wong *et al.*⁶⁰ in the near-infrared, or 5200-9200 cm^{-1} region. Spectral data of methane were recorded at eight different temperatures, between 296 and 1000 K, using a Bruker IFS 120/125HR FTS. The registered transitions concern the tetradecad, icosad and triacontad polyads. The investigation validated the precise high-

resolution theoretical line list describing the tetradecad and icosad polyads, however, it also revealed the inaccuracy of the theoretical calculations at even higher energy levels.

1.8.1.4 Triacontad

The first recorded lines from the triacontad polyad dates back to 1980. Pierre *et al.* used a cooled multiple-reflection cell coupled with a FT spectrometer to measure the most intense lines around 9000 cm^{-1} and reported the first line assignments on the $3\nu_3$ vibrational band.⁶¹

An empirical line list in the $9028 - 10435\text{ cm}^{-1}$ spectral region was reported by Béguier *et al.* recording data with a Bruker IFS 120HR FT spectrometer and a 1.5 m long multipass cell. The cold bands recorded at 301 K explore the tetracontad and the high energy region of the triacontad and resulted 7212 and 574 lines respectively.⁶²

The transitions arriving to the $8900\text{--}9100\text{ cm}^{-1}$ spectral region were investigated by Foltynowicz *et al.*⁶³ by the mean of a high-power singly resonant continuous wave (cw) optical parametric oscillator (OPO) pump and a frequency comb probe.⁶⁴ The methane gas was placed into a 80 mm long single-pass cell and was cooled down by dint of liquid nitrogen. The study reports revolutionary experimental data on the previously unexamined $3\nu_3$ band region.

1.8.1.5 Tetracontad and pentacontakaipentad

The lowest rotational level, $J = 0$, was assigned for each excited vibrational state of methane up to 12000 cm^{-1} .⁶⁵ The significantly high energy tetracontad and pentacontakaipentad polyads were investigated in Zürich using a Bruker IFS 125HR prototype spectrometer. For recording cold spectra at 80 K, a multireflection collisional cooling cell⁶⁶ was used.

1.8.2 Non-LTE spectroscopy

1.8.2.1 Dyad, pentad and octad

The hot bands of methane were investigated by Hilico *et al.*²⁹ in a supersonic jet using a high-resolution pulsed infrared spectrometer which was based on a tunable diode laser. The preheated methane was injected into a slit-shaped pulsed nozzle. Non-LTE lines were recorded describing transitions between the pentad-dyad and the octad-pentad polyads. The authors pointed out that while a single 200(10) K rotational temperature could be used to characterise the rotational population on each vibrational state, multiple vibrational temperatures had to be introduced to explain the distribution of the vibrational population. Using the Boltzmann plot method, a global vibrational temperature of 830 K was delivered which took into account all the recorded lines. A more specific, partial vibrational temperature of 220 K was obtained focusing on the pentad-dyad lines and 360 K concerning the octad-pentad lines.

The same phenomena was observed by Bronnikov *et al.*³⁰ using the same slit-jet experimental setup as mentioned above. Non-LTE spectroscopy was performed on vibrationally excited, rotationally cooled, methane and the authors proposed a formalism to estimate the populations on the different vibrational polyads. Their observations confirmed an inefficient vibrational relaxation among the polyads (inter-polyad), whereas a significant redistribution of the population occurred within each polyad (intra-polyad).

1.8.2.2 Tetradecad

A continuous high temperature methane flow was generated by the High Enthalpy Source⁵¹ and probed by cw-CRDS. In the created hypersonic free-jet expansion⁶⁷, strong non-LTE conditions were obtained, and rotationally cold hot bands were recorded in the tetradecad region.

1.8.2.3 Icosad

The dataset was recorded by Hippler and Quack⁶⁸ at room temperature and in a supersonic slit-jet expansion using a Doppler-limited-resolution FTIR spectrometer and a cw-CRDS. A complex rovibrational spectrum was delivered describing the icosad polyad in the 6600-7700 cm⁻¹ spectral range. The low- J value transitions were investigated in the pulsed slit-jet expansion allowing a precise line assignment. The higher J transitions were searched for in the spectra obtained at room temperature.

1.9 SMAUG

This thesis presents the development of, and the results obtained, using a state-of-the-art experimental system christened Spectroscopy of Molecules Accelerated in Uniform Gas flow (SMAUG). Its name pays tribute to the dragon character imagined by J.R.R. Tolkien, since they both blow hot gas. In summary, as figure (1.7) represents, a small dimension Laval nozzle produces a continuous hypersonic flow which is probed by CRDS. The experimental system delivers vibrationally hot and rotationally cold high-resolution infrared spectroscopic reference data that will help planetologists to detect new molecules and reconstruct the vertical structure of the atmosphere of exoplanets.

In chapter II, the development and the operation of SMAUG is presented. Chapter III reveals the recorded non-LTE methane spectral data presenting transitions arriving up to the triacontad and presumably to the tetracontad polyad. The following chapter IV describes the novel post-shock CRDS technique that has been recently developed to deliver the rovibrational spectrum of high-temperature methane. Finally, chapter V exhibits a completely different, under-development approach using a high-temperature plasma plume generated by the “Platypus” source to overcome various limitations of the base SMAUG setup.

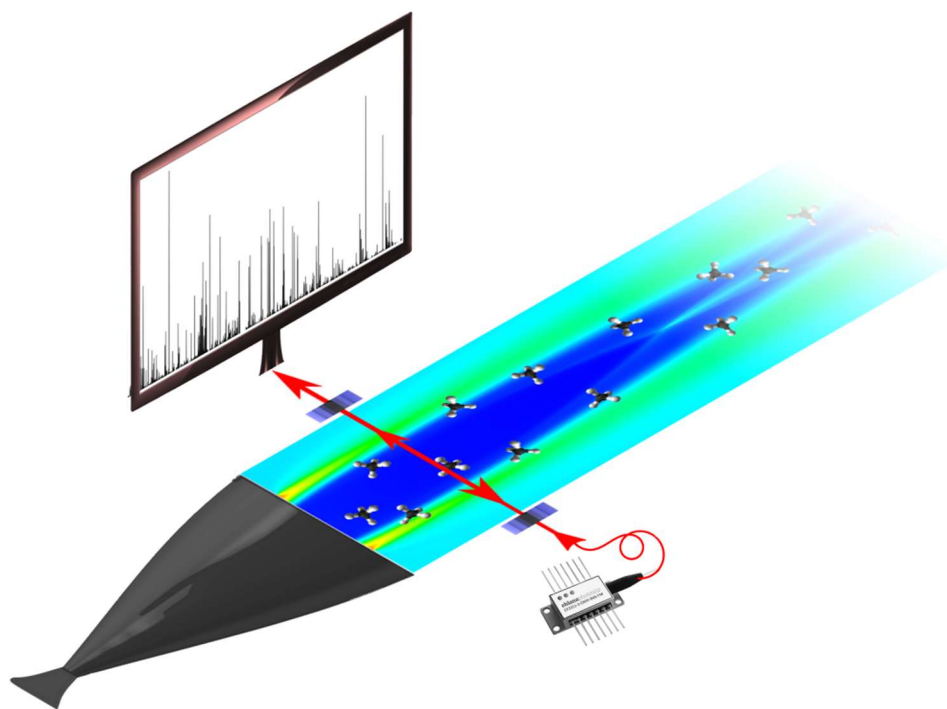


Figure 1.7: SMAUG experimental setup⁶⁹

References

- (1) Hoyt, J. K. The Cyclopaedia of Practical Quotationos, English and Latin: With an Appendix Containing Proverbs from the Latin and Modern Foreign Languages ...; Funk & Wagnalls, 1889.
- (2) Herschel, W. XIV. Experiments on the Refrangibility of the Invisible Rays of the Sun. Philosophical Transactions of the Royal Society of London **1800**, 90, 284–292. <https://doi.org/10.1098/rstl.1800.0015>.
- (3) Swain, M. R.; Vasisht, G.; Tinetti, G. The Presence of Methane in the Atmosphere of an Extrasolar Planet. Nature **2008**, 452 (7185), 329–331. <https://doi.org/10.1038/nature06823>.
- (4) Coustenis, A.; Achterberg, R. K.; Conrath, B. J.; Jennings, D. E.; Marten, A.; Gautier, D.; Nixon, C. A.; Flasar, F. M.; Teanby, N. A.; Bézard, B.; Samuelson, R. E.; Carlson, R. C.; Lellouch, E.; Bjoraker, G. L.; Romani, P. N.; Taylor, F. W.; Irwin, P. G. J.; Fouchet, T.; Hubert, A.; Orton, G. S.; Kunde, V. G.; Vinatier, S.; Mondellini, J.; Abbas, M. M.; Courtin, R. The Composition of Titan's Stratosphere from Cassini/CIRS Mid-Infrared Spectra. Icarus **2007**, 189 (1), 35–62. <https://doi.org/10.1016/j.icarus.2006.12.022>.
- (5) Swain, M. R.; Tinetti, G.; Vasisht, G.; Deroo, P.; Griffith, C.; Bouwman, J.; Chen, P.; Yung, Y.; Burrows, A.; Brown, L. R.; Matthews, J.; Rowe, J. F.; Kuschnig, R.; Angerhausen, D. Water, Methane, and Carbon Dioxide Present in the Dayside Spectrum of the Exoplanet HD 209458b. Nippon rinsho. Japanese journal of clinical medicine **2009**, 704 (2), 1616–1621. <https://doi.org/10.1088/0004-637X/704/2/1616>.
- (6) Swain, M. R.; Vasisht, G.; Tinetti, G.; Bouwman, J.; Chen, P.; Yung, Y.; Deming, D.; Deroo, P. Molecular Signatures in the Near-Infrared Dayside Spectrum of HD 189733b. The Astrophysical Journal Letters **2009**, 690, L114–L117. <https://doi.org/10.1088/0004-637X/690/2/L114>.
- (7) Swain, M. R.; Deroo, P.; Griffith, C. A.; Tinetti, G.; Thatte, A.; Vasisht, G.; Chen, P.; Bouwman, J.; Crossfield, I. J.; Angerhausen, D.; Afonso, C.; Henning, T. A Ground-Based near-Infrared Emission Spectrum of the Exoplanet HD 189733b. NATURE **2010**, 463 (7281), 637–639. <https://doi.org/10.1038/nature08775>.
- (8) Hoff, J. H. van't. Vorlesungen Über Theoretische Und Physikalische Chemie, Volumes 1-3; F. Vieweg und sohn, 1898; Vol. 1–3.
- (9) Marquardt, R.; Quack, M. Global Analytical Potential Hypersurface for Large Amplitude Nuclear Motion and Reactions in Methane II. Characteristic Properties of the Potential and Comparison to Other Potentials and Experimental Information. J. Phys. Chem. A **2004**, 108 (15), 3166–3181. <https://doi.org/10.1021/jp037305v>.
- (10) Schwenke, D. W.; Partridge, H. Vibrational Energy Levels for CH₄ from an Ab Initio Potential. Spectrochim Acta A Mol Biomol Spectrosc **2001**, 57 (4), 887–895. [https://doi.org/10.1016/s1386-1425\(00\)00451-0](https://doi.org/10.1016/s1386-1425(00)00451-0).
- (11) Herzberg, G. Infrared and Raman Spectra of Polyatomic Molecules; Van Nostrand: New York, 1945.
- (12) Herzberg, G. Electronic Spectra and Electronic Structure of Polyatomic Molecules; Van Nostrand: New York, 1966.
- (13) Wilson, E. B.; Decius, J. C.; Cross, P. C. Molecular Vibrations: The Theory of Infrared and Raman Vibrational Spectra; McGraw-Hill: New York, 1955.
- (14) Jynto, !Original:Benjah-bmm27Vector: Full Structural Formula of the Methane Molecule, the Simplest Alkane, and the Principal Component of Natural Gas, Showing the Bond Lengths and Angles.; 2010.

- (15) Amyay, B.; Gardez, A.; Georges, R.; Biennier, L.; Vander Auwera, J.; Richard, C.; Boudon, V. New Investigation of the ν_3 C–H Stretching Region of $^{12}\text{CH}_4$ through the Analysis of High Temperature Infrared Emission Spectra. *The Journal of Chemical Physics* **2018**, 148 (13), 134306. <https://doi.org/10.1063/1.5023331>.
- (16) Jahn, H. A.; null, null; Bragg, W. H.; null, null. A New Coriolis Perturbation in the Methane Spectrum I. Vibrational-Rotational Hamiltonian and Wave Functions. *Proceedings of the Royal Society A: Mathematical, Physical and Engineering Sciences* **1938**, 168 (935), 469–495. <https://doi.org/10.1098/rspa.1938.0187>.
- (17) Childs, W. H. J.; Jahn, H. A.; Bragg, W. L. A New Coriolis Perturbation in the Methane Spectrum III. Intensities and Optical Spectrum. *Proceedings of the Royal Society of London. Series A. Mathematical and Physical Sciences* **1939**, 169 (939), 451–463. <https://doi.org/10.1098/rspa.1939.0009>.
- (18) Amyay, B.; Boudon, V. Vibration-Rotation Energy Levels and Corresponding Eigenfunctions of $^{12}\text{CH}_4$ up to the TetradeCAD. *Journal of Quantitative Spectroscopy and Radiative Transfer* **2018**, 219, 85–104. <https://doi.org/10.1016/j.jqsrt.2018.08.002>.
- (19) Penner, S. S. *Quantitative Molecular Spectroscopy and Gas Emissivities*; Addison-Wesley Pub. Co.: Reading, Mass., 1959.
- (20) Šimečková, M.; Jacquemart, D.; Rothman, L. S.; Gamache, R. R.; Goldman, A. Einstein A-Coefficients and Statistical Weights for Molecular Absorption Transitions in the HITRAN Database. *Journal of Quantitative Spectroscopy and Radiative Transfer* **2006**, 98 (1), 130–155. <https://doi.org/10.1016/j.jqsrt.2005.07.003>.
- (21) Edwards, D. P.; López-Puertas, M.; Gamache, R. R. The Non-LTE Correction to the Vibrational Component of the Internal Partition Sum for Atmospheric Calculations. *Journal of Quantitative Spectroscopy and Radiative Transfer* **1998**, 59 (3), 423–436. [https://doi.org/10.1016/S0022-4073\(97\)00125-8](https://doi.org/10.1016/S0022-4073(97)00125-8).
- (22) Herzberg, G. *Molecular Spectra and Molecular Structure*. II, II,; 1945.
- (23) Laraia, A. L.; Gamache, R. R.; Lamouroux, J.; Gordon, I. E.; Rothman, L. S. Total Internal Partition Sums to Support Planetary Remote Sensing. *Icarus* **2011**, 215 (1), 391–400. <https://doi.org/10.1016/j.icarus.2011.06.004>.
- (24) Fischer, J.; Gamache, R. R. Total Internal Partition Sums for Molecules of Astrophysical Interest. *Journal of Quantitative Spectroscopy and Radiative Transfer* **2002**, 74 (3), 263–272. [https://doi.org/10.1016/S0022-4073\(01\)00234-5](https://doi.org/10.1016/S0022-4073(01)00234-5).
- (25) Gamache, R. R.; Rothman, L. S. Extension of the HITRAN Database to Non-LTE Applications. *Journal of Quantitative Spectroscopy and Radiative Transfer* **1992**, 48 (5), 519–525. [https://doi.org/10.1016/0022-4073\(92\)90117-M](https://doi.org/10.1016/0022-4073(92)90117-M).
- (26) Gamache, R. R.; Hawkins, R. L.; Rothman, L. S. Total Internal Partition Sums in the Temperature Range 70–3000 K: Atmospheric Linear Molecules. *Journal of Molecular Spectroscopy* **1990**, 142 (2), 205–219. [https://doi.org/10.1016/0022-2852\(90\)90178-S](https://doi.org/10.1016/0022-2852(90)90178-S).
- (27) Gamache, R. R.; Vispoel, B.; Rey, M.; Nikitin, A.; Tyuterev, V.; Egorov, O.; Gordon, I. E.; Boudon, V. Total Internal Partition Sums for the HITRAN2020 Database. *Journal of Quantitative Spectroscopy and Radiative Transfer* **2021**, 271, 107713. <https://doi.org/10.1016/j.jqsrt.2021.107713>.
- (28) Gamache, R. R.; Rothman, L. S. Extension of the HITRAN Database to Non-LTE Applications. *Journal of Quantitative Spectroscopy and Radiative Transfer* **1992**, 48 (5), 519–525. [https://doi.org/10.1016/0022-4073\(92\)90117-M](https://doi.org/10.1016/0022-4073(92)90117-M).
- (29) Hilico, J. C.; Baronov, G. S.; Bronnikov, D. K.; Gavrikov, S. A.; Nikolaev, I. I.; Rusanov, V. D.; Filimonov, Y. G. High-Resolution Spectroscopy of (Pentad-Dyad) and (Octad-Pentad)

- Hot Bands of Methane in a Supersonic Jet. *Journal of Molecular Spectroscopy* **1993**, 161 (2), 435–444. <https://doi.org/10.1006/jmsp.1993.1249>.
- (30) Bronnikov, D. K.; Kalinin, D. V.; Rusanov, V. D.; Filimonov, YU. G.; Selivanov, YU. G.; Hilico, J. C. SPECTROSCOPY AND NON-EQUILIBRIUM DISTRIBUTION OF VIBRATIONALLY EXCITED METHANE IN A SUPERSONIC JET. *Journal of Quantitative Spectroscopy and Radiative Transfer* **1998**, 60 (6), 1053–1068. [https://doi.org/10.1016/S0022-4073\(97\)00210-0](https://doi.org/10.1016/S0022-4073(97)00210-0).
- (31) Kempton, E. M.-R.; Lupu, R. E.; Owusu-Asare, A.; Slough, P.; Cale, B. Exo-Transmit: Radiative Transfer Code for Calculating Exoplanet Transmission Spectra. *Astrophysics Source Code Library* **2016**, ascl:1611.005.
- (32) Heng, K.; Marley, M. Radiative Transfer for Exoplanet Atmospheres. *arXiv:1706.03188 [astro-ph, physics:physics]* **2018**, 2137–2152. https://doi.org/10.1007/978-3-319-55333-7_102.
- (33) Fortney, J. J. Modeling Exoplanetary Atmospheres: An Overview. *arXiv:1804.08149 [astro-ph]* **2018**.
- (34) Payan, S.; de La Noë, J.; Hauchecorne, A.; Camy-Peyret, C. A Review of Remote Sensing Techniques and Related Spectroscopy Problems. *Comptes Rendus Physique* **2005**, 6 (8), 825–835. <https://doi.org/10.1016/j.crhy.2005.07.013>.
- (35) Thomas, B. Remote Sensing of Atmospheric Trace Gases by Optical Correlation Spectroscopy and Lidar. *phdthesis, Université Claude Bernard - Lyon I*, 2013.
- (36) Ba, Y. A.; Wenger, C.; Surleau, R.; Boudon, V.; Rotger, M.; Daumont, L.; Bonhommeau, D. A.; Tyuterev, V. G.; Dubernet, M.-L. MeCaSDa and ECaSDa: Methane and Ethene Calculated Spectroscopic Databases for the Virtual Atomic and Molecular Data Centre. *Journal of Quantitative Spectroscopy and Radiative Transfer* **2013**, 130, 62–68. <https://doi.org/10.1016/j.jqsrt.2013.05.001>.
- (37) MeCaSDa – Methane Calculated Spectroscopic Database | VAMDC Consortium, 2014.
- (38) Daumont, L.; Nikitin, A. V.; Thomas, X.; Régalia, L.; Von der Heyden, P.; Tyuterev, V. G.; Rey, M.; Boudon, V.; Wenger, Ch.; Loëte, M.; Brown, L. R. New Assignments in the 2 μ m Transparency Window of the 12CH₄ Octad Band System. *Journal of Quantitative Spectroscopy and Radiative Transfer* **2013**, 116, 101–109. <https://doi.org/10.1016/j.jqsrt.2012.08.025>.
- (39) Albert, S.; Bauerecker, S.; Boudon, V.; Brown, L. R.; Champion, J.-P.; Loëte, M.; Nikitin, A.; Quack, M. Global Analysis of the High Resolution Infrared Spectrum of Methane 12CH₄ in the Region from 0 to 4800cm⁻¹. *Chemical Physics* **2009**, 356 (1), 131–146. <https://doi.org/10.1016/j.chemphys.2008.10.019>.
- (40) Boudon, V.; Pirali, O.; Roy, P.; Brubach, J.-B.; Manceron, L.; Vander Auwera, J. The High-Resolution Far-Infrared Spectrum of Methane at the SOLEIL Synchrotron. *Journal of Quantitative Spectroscopy and Radiative Transfer* **2010**, 111 (9), 1117–1129. <https://doi.org/10.1016/j.jqsrt.2010.02.006>.
- (41) Gordon, I. E.; Rothman, L. S.; Hill, C.; Kochanov, R. V.; Tan, Y.; Bernath, P. F.; Birk, M.; Boudon, V.; Campargue, A.; Chance, K. V.; Drouin, B. J.; Flaud, J.-M.; Gamache, R. R.; Hodges, J. T.; Jacquemart, D.; Perevalov, V. I.; Perrin, A.; Shine, K. P.; Smith, M.-A. H.; Tennyson, J.; Toon, G. C.; Tran, H.; Tyuterev, V. G.; Barbe, A.; Császár, A. G.; Devi, V. M.; Furtenbacher, T.; Harrison, J. J.; Hartmann, J.-M.; Jolly, A.; Johnson, T. J.; Karman, T.; Kleiner, I.; Kyuberis, A. A.; Loos, J.; Lyulin, O. M.; Massie, S. T.; Mikhailenko, S. N.; Moazzen-Ahmadi, N.; Müller, H. S. P.; Naumenko, O. V.; Nikitin, A. V.; Polyansky, O. L.; Rey, M.; Rotger, M.; Sharpe, S. W.; Sung, K.; Starikova, E.; Tashkun, S. A.; Auwera, J. V.;

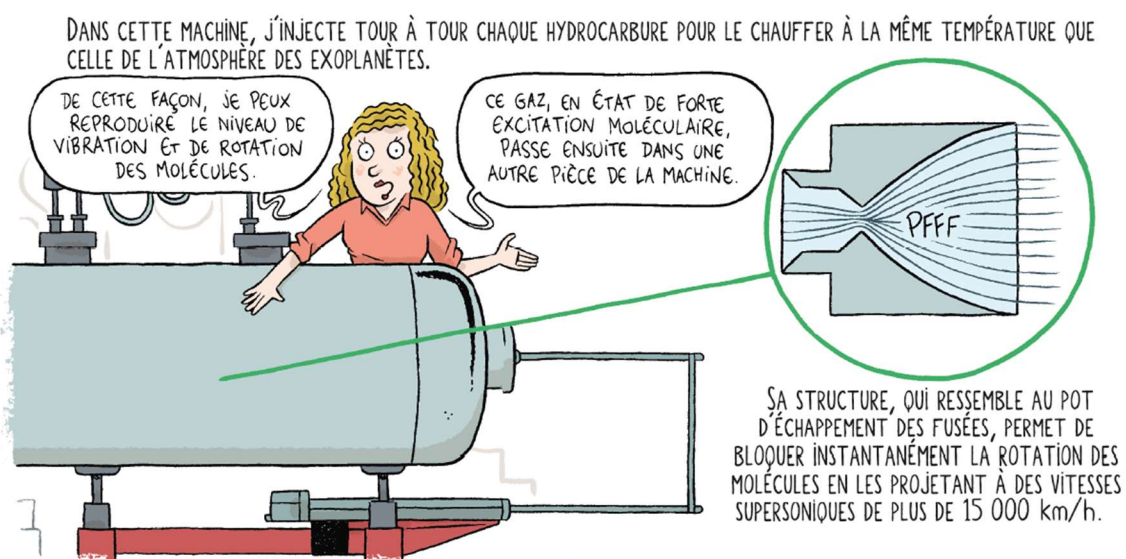
- Wagner, G.; Wilzewski, J.; Wcisło, P.; Yu, S.; Zak, E. J. The HITRAN2016 Molecular Spectroscopic Database. *Journal of Quantitative Spectroscopy and Radiative Transfer* **2017**, 203, 3–69. <https://doi.org/10.1016/j.jqsrt.2017.06.038>.
- (42) Rey, M.; Nikitin, A. V.; Babikov, Y. L.; Tyuterev, V. G. TheoReTS – An Information System for Theoretical Spectra Based on Variational Predictions from Molecular Potential Energy and Dipole Moment Surfaces. *Journal of Molecular Spectroscopy* **2016**, 327, 138–158. <https://doi.org/10.1016/j.jms.2016.04.006>.
- (43) Rey, M.; Nikitin, A. V.; Tyuterev, V. G. Accurate Theoretical Methane Line Lists in the Infrared up to 3000 K and Quasi-Continuum Absorption/Emission Modeling for Astrophysical Applications. *ApJ* **2017**, 847 (2), 105. <https://doi.org/10.3847/1538-4357/aa8909>.
- (44) Rey, M.; Chizhmakova, I. S.; Nikitin, A. V.; Tyuterev, V. G. Understanding Global Infrared Opacity and Hot Bands of Greenhouse Molecules with Low Vibrational Modes from First-Principles Calculations: The Case of CF₄. *Phys. Chem. Chem. Phys.* **2018**, 20 (32), 21008–21033. <https://doi.org/10.1039/C8CP03252A>.
- (45) Tennyson, J.; Yurchenko, S. N.; Al-Refaie, A. F.; Barton, E. J.; Chubb, K. L.; Coles, P. A.; Diamantopoulou, S.; Gorman, M. N.; Hill, C.; Lam, A. Z.; Lodi, L.; McKemmish, L. K.; Na, Y.; Owens, A.; Polyansky, O. L.; Rivlin, T.; Sousa-Silva, C.; Underwood, D. S.; Yachmenev, A.; Zak, E. The ExoMol Database: Molecular Line Lists for Exoplanet and Other Hot Atmospheres. *Journal of Molecular Spectroscopy* **2016**, 327, 73–94. <https://doi.org/10.1016/j.jms.2016.05.002>.
- (46) Tennyson, J.; Yurchenko, S. N.; Al-Refaie, A. F.; Clark, V. H. J.; Chubb, K. L.; Conway, E. K.; Dewan, A.; Gorman, M. N.; Hill, C.; Lynas-Gray, A. E.; Mellor, T.; McKemmish, L. K.; Owens, A.; Polyansky, O. L.; Semenov, M.; Somogyi, W.; Tinetti, G.; Upadhyay, A.; Waldmann, I.; Wang, Y.; Wright, S.; Yurchenko, O. P. The 2020 Release of the ExoMol Database: Molecular Line Lists for Exoplanet and Other Hot Atmospheres. *Journal of Quantitative Spectroscopy and Radiative Transfer* **2020**, 255, 107228. <https://doi.org/10.1016/j.jqsrt.2020.107228>.
- (47) Yurchenko, S. N.; Tennyson, J.; Bailey, J.; Hollis, M. D. J.; Tinetti, G. Spectrum of Hot Methane in Astronomical Objects Using a Comprehensive Computed Line List. *PNAS* **2014**, 111 (26), 9379–9383. <https://doi.org/10.1073/pnas.1324219111>.
- (48) Yurchenko, S. N.; Tennyson, J. ExoMol Line Lists – IV. The Rotation–Vibration Spectrum of Methane up to 1500 K. *Monthly Notices of the Royal Astronomical Society* **2014**, 440 (2), 1649–1661. <https://doi.org/10.1093/mnras/stu326>.
- (49) Nikitin, A. V.; Rey, M.; Tyuterev, V. G. An Efficient Method for Energy Levels Calculation Using Full Symmetry and Exact Kinetic Energy Operator: Tetrahedral Molecules. *J. Chem. Phys.* **2015**, 142 (9), 094118. <https://doi.org/10.1063/1.4913520>.
- (50) Amyay, B.; Louvriot, M.; Pirali, O.; Georges, R.; Vander Auwera, J.; Boudon, V. Global Analysis of the High Temperature Infrared Emission Spectrum of ¹²CH₄ in the Dyad (ν₂/ν₄) Region. *The Journal of Chemical Physics* **2016**, 144 (2), 024312. <https://doi.org/10.1063/1.4939521>.
- (51) Thiévin, J.; Georges, R.; Carles, S.; Benidar, A.; Rowe, B.; Champion, J.-P. High-Temperature Emission Spectroscopy of Methane. *Journal of Quantitative Spectroscopy and Radiative Transfer* **2008**, 109 (11), 2027–2036. <https://doi.org/10.1016/j.jqsrt.2008.01.023>.
- (52) Gao, B.; Kass, S.; Campargue, A. Empirical Low Energy Values for Methane Transitions in the 5852–6181cm⁻¹ Region by Absorption Spectroscopy at 81K. *Journal of*

- Molecular Spectroscopy **2009**, 253 (1), 55–63.
<https://doi.org/10.1016/j.jms.2008.09.005>.
- (53) Morino, I.; Uchino, O.; Inoue, M.; Yoshida, Y.; Yokota, T.; Wennberg, P. O.; Toon, G. C.; Wunch, D.; Roehl, C. M.; Notholt, J.; Warneke, T.; Messerschmidt, J.; Griffith, D. W. T.; Deutscher, N. M.; Sherlock, V.; Connor, B.; Robinson, J.; Sussmann, R.; Rettinger, M. Preliminary Validation of Column-Averaged Volume Mixing Ratios of Carbon Dioxide and Methane Retrieved from GOSAT Short-Wavelength Infrared Spectra. *Atmospheric Measurement Techniques* **2011**, 4 (6), 1061–1076. <https://doi.org/10.5194/amt-4-1061-2011>.
- (54) Le, W.; Kass, S.; Campargue, A. Temperature Dependence of the Absorption Spectrum of CH₄ by High Resolution Spectroscopy at 81 K: (I) The Region of the 2v₃ Band at 1.66 Mm. *Journal of Quantitative Spectroscopy and Radiative Transfer* **2010**, 111 (9), 1130–1140. <https://doi.org/10.1016/j.jqsrt.2009.10.019>.
- (55) Campargue, A.; Wang, L.; Kass, S.; Mašát, M.; Votava, O. Temperature Dependence of the Absorption Spectrum of CH₄ by High Resolution Spectroscopy at 81K: (II) The Icosad Region (1.49–1.30μm). *Journal of Quantitative Spectroscopy and Radiative Transfer* **2010**, 111 (9), 1141–1151. <https://doi.org/10.1016/j.jqsrt.2009.11.025>.
- (56) Wang, L.; Mondelain, D.; Kass, S.; Campargue, A. The Absorption Spectrum of Methane at 80 and 294K in the Icosad (6717–7589cm⁻¹): Improved Empirical Line Lists, Isotopologue Identification and Temperature Dependence. *Journal of Quantitative Spectroscopy and Radiative Transfer* **2012**, 113 (1), 47–57. <https://doi.org/10.1016/j.jqsrt.2011.09.003>.
- (57) Votava, O.; Mašát, M.; Pracna, P.; Mondelain, D.; Kass, S.; Liu, A. W.; Hu, S. M.; Campargue, A. Empirical Determination of Low J Values of 13 CH₄ Transitions from Jet Cooled and 80 K Cell Spectra in the Icosad Region (7170–7367 Cm⁻¹). *Journal of Quantitative Spectroscopy and Radiative Transfer* **2014**, 149, 64–71. <https://doi.org/10.1016/j.jqsrt.2014.07.012>.
- (58) Mondelain, D.; Kass, S.; Wang, L.; Campargue, A. The 1.28 Mm Transparency Window of Methane (7541–7919 Cm⁻¹): Empirical Line Lists and Temperature Dependence (80 K–300 K). *Phys. Chem. Chem. Phys.* **2011**, 13 (17), 7985. <https://doi.org/10.1039/c0cp02948c>.
- (59) Ghysels, M.; Vasilchenko, S.; Mondelain, D.; Béguier, S.; Kass, S.; Campargue, A. Laser Absorption Spectroscopy of Methane at 1000 K near 1.7 Mm: A Validation Test of the Spectroscopic Databases. *Journal of Quantitative Spectroscopy and Radiative Transfer* **2018**, 215, 59–70. <https://doi.org/10.1016/j.jqsrt.2018.04.032>.
- (60) Wong, A.; Bernath, P. F.; Rey, M.; Nikitin, A. V.; Tyuterev, V. G. Atlas of Experimental and Theoretical High-Temperature Methane Cross Sections from T = 295 to 1000 K in the Near-Infrared. *ApJS* **2019**, 240 (1), 4. <https://doi.org/10.3847/1538-4365/aad39>.
- (61) Pierre, G.; Hilico, J.-C.; de Bergh, C.; Maillard, J.-P. The Region of the 3v₃ Band of Methane. *Journal of Molecular Spectroscopy* **1980**, 82 (2), 379–393. [https://doi.org/10.1016/0022-2852\(80\)90122-8](https://doi.org/10.1016/0022-2852(80)90122-8).
- (62) Béguier, S.; Liu, A. W.; Campargue, A. An Empirical Line List for Methane near 1μm (9028–10,435cm⁻¹). *Journal of Quantitative Spectroscopy and Radiative Transfer* **2015**, 166, 6–12. <https://doi.org/10.1016/j.jqsrt.2015.07.003>.
- (63) Foltynowicz, A.; Rutkowski, L.; Silander, I.; Johansson, A. C.; Silva de Oliveira, V.; Axner, O.; Soboń, G.; Martynkien, T.; Mergo, P.; Lehmann, K. K. Measurement and Assignment of Double-Resonance Transitions to the 8900–9100- cm^{-1} region.

- }1}\$ Levels of Methane. *Phys. Rev. A* **2021**, 103 (2), 022810.
<https://doi.org/10.1103/PhysRevA.103.022810>.
- (64) Foltynowicz, A.; Rutkowski, L.; Silander, I.; Johansson, A. C.; Silva de Oliveira, V.; Axner, O.; Soboń, G.; Martynkien, T.; Mergo, P.; Lehmann, K. K. Sub-Doppler Double-Resonance Spectroscopy of Methane Using a Frequency Comb Probe. *Phys. Rev. Lett.* **2021**, 126 (6), 063001. <https://doi.org/10.1103/PhysRevLett.126.063001>.
- (65) Ulenikov, O. N.; Bekhtereva, E. S.; Albert, S.; Bauerecker, S.; Niederer, H. M.; Quack, M. Survey of the High Resolution Infrared Spectrum of Methane ($^{12}\text{CH}_4$ and $^{13}\text{CH}_4$): Partial Vibrational Assignment Extended towards $12\,000\text{ cm}^{-1}$. *J. Chem. Phys.* **2014**, 141 (23), 234302. <https://doi.org/10.1063/1.4899263>.
- (66) Albert, S.; Bauerecker, S.; Quack, M.; Steinlin, A. Rovibrational Analysis of the $2\nu_3$, $3\nu_3$ and ν_1 Bands of CHCl_2F Measured at 170 and 298 K by High-Resolution FTIR Spectroscopy. *Molecular Physics* **2007**, 105 (5–7), 541–558.
<https://doi.org/10.1080/00268970601164198>.
- (67) Louvriot, M.; Suas-David, N.; Boudon, V.; Georges, R.; Rey, M.; Kass, S. Strong Thermal Nonequilibrium in Hypersonic CO and CH_4 Probed by CRDS. *J. Chem. Phys.* **2015**, 142 (21), 214305. <https://doi.org/10.1063/1.4921893>.
- (68) Hippler, M.; Quack, M. High-Resolution Fourier Transform Infrared and Cw-Diode Laser Cavity Ringdown Spectroscopy of the $\text{N}_2+2\nu_3$ Band of Methane near 7510 cm^{-1} in Slit Jet Expansions and at Room Temperature. *The Journal of Chemical Physics* **2002**, 116 (14), 6045–6055. <https://doi.org/10.1063/1.1433505>.
- (69) Mandel, S. SMAUG Helps Generate Infrared Spectroscopy Data for Hot Jupiter-Type Exoplanets. *Scilight* **2020**, 2020 (14), 141106. <https://doi.org/10.1063/10.0001091>.

SMAUG experimental setup and its operation

“Experientia est optima rerum magistra”[§]



[§] Experience is the best teacher in all things¹

Contents

2.1 Hypersonic flows	59
2.1.1 Knudsen number	59
2.1.2 Mach number	59
2.1.3 Compressibility	60
2.1.4 Viscosity	60
2.1.5 Isentropic expansion and ideal gas	61
2.1.6 Governing equations	61
2.2 Laval nozzle design	63
2.2.1 Nozzle profile calculation	64
2.2.2 CFD simulations and flow field analysis	68
2.2.3 Isentropic core vs shear-layer	72
2.2.4 2D Pitot probe	74
2.3 SMAUG experimental setup	79
2.3.1 High enthalpy source	80
2.3.2 Cavity Ring-Down Spectrometer	82
2.3.3 Determination of the reservoir temperature	84
2.4 Preliminary study on carbon monoxide	91
2.4.1 Vibrational relaxation	91
2.4.2 Rotational relaxation	92
References	93

2.1 Hypersonic flows

Studying physics at a molecular level in a flow requires a precise characterisation and understanding of the flow properties. In order to have an accurate description of the flow, certain assumptions and clear definitions of the terms to be used are required. The following paragraphs lay out the framework essential to this thesis work.

2.1.1 Knudsen number

In order to investigate the properties of matter a simplification must be introduced. Namely, the concept of the continuum flows whose evolution are described by an average behaviour of molecules instead of describing each molecule as an individual. At the same time, it is vital to ensure that this assumption is correct to apply. The Knudsen number is a dimensionless value, giving information of the ratio between the mean free path (λ) and the respective physical length scale (L) and therefore characterising the different flow regimes as continuum flow ($Kn < 0.01$), slip flow ($0.01 < Kn < 0.1$), nearly free molecular flow ($0.1 < Kn < 10$) and free molecular flow ($1 < Kn$).

The mean free path of the molecules could be delivered from the following equation (2.1):

$$\lambda = \frac{k_b T}{\sqrt{2} \pi d^2 p} \quad 2.1$$

where, k_b – Boltzmann constant, T – temperature, d – particle hard-shell diameter ($d_{CH_4} = 380$ pm) and p – pressure. In case of methane in the hypersonic jet ($T = 39$ K) the mean free path is $\lambda = 1.2 \times 10^{-6}$ m. And considering the nozzle exit ($\varnothing d = 24$ mm) as respective physical length scale the Knudsen number can be delivered:

$$Kn = \frac{\lambda}{L} \quad 2.2$$

and with its value $Kn = 5.2 \times 10^{-5}$ is way below the 10^{-2} which is considered as the upper limit for the continuum flow regime. Throughout this thesis, the studied flows are in the continuum flow regime.

2.1.2 Mach number

The Mach number (M) is a dimensionless variable defined by the ratio of the local flow speed (v) to the local sound speed (a):

$$M = \frac{v}{a} \quad 2.3$$

and it categorises the different regimes of the flow. The denominator refers to the speed of transmission of small pressure disturbances, so called sound waves, along the medium.² It is important to underline that, in the case on an ideal gas, this local variable depends only on the fluid temperature (T) and its specific heat ratio (γ):

$$a = \sqrt{\gamma \cdot r \cdot T} \quad 2.4$$

where r stands for the universal gas constant (R) weighted by the molar mass (\mathcal{M}) of the atom/molecule ($r = R/\mathcal{M}$). In case of Mach number smaller than unity, the flow is called subsonic flow and in practice it means that the propagation of the sound waves is much faster than the fluid particles. This works as a signalling mechanism and therefore the flow can adjust itself instantaneously and in advance before reaching a body. This also implies that no violent and sudden changes could happen to the flow. At Mach number equals to one, it is called a sonic flow and once the Mach number is superior to one, the flow is termed supersonic or hypersonic, as Mach number reaches above five. In these last two cases, the upstream of the flow with respect to a given point remains unresponsive to any changes in the flow at that given point. The fluid particles propagate faster than the sound waves, consequently they have no perception of a body ahead and this conducts to the formation of a shock wave where brusque changes happen to the flow variables: temperature, pressure, density and velocity. Chapter IV of this thesis discusses this phenomenon in details.

From a different point of view, the Mach number can be considered as a ratio between the kinetic energy (characterizable by the velocity (v) of the gas) and the thermal energy of the gas (as the sound speed (a) depends on temperature). Thus, a flow accelerating adiabatically may reach extremely low temperatures associated with very high Mach numbers ($T \rightarrow 0K, M \rightarrow \infty$).

2.1.3 Compressibility

Although all fluids are compressible, that is, by increasing the pressure its density also increases, from a practical point of view these changes in density are sometimes overlooked. A flow is considered incompressible as long as the volumetric flow rate is constant at any cross-section (A): $\dot{Q} = A \cdot v$ and its density-change can be treated as negligible. This is true for liquids and low-speed gas flows around Mach number smaller than 0.3. Conversely, a flow is considered compressible when its density changes with changes in flow velocity. In such a case, only the mass flow rate remains constant at any cross-section: $\dot{m} = \rho \cdot A \cdot v$. Throughout this thesis the flows will be considered as compressible-flows since we are dealing with high speed hypersonic flows.

2.1.4 Viscosity

Despite the fact that there are no flows with zero viscosity, meaning that internal friction between the flow layers is always present, for pragmatic reasons the flow regions are often treated as inviscid ones. In this hypothesis, the shear forces are neglected to greatly simplify the calculations and to obtain preliminary results of the development of the flow field. In this scenario, the simplified Euler equations can be used which do not include the physical energy dissipations, these equations will be presented in the next paragraph. Later, the viscous calculation can deliver the exhaustive flow field characterisation.

The applied viscosity law³ is named after the Australian physicist, William Sutherland, who described the relationship between the dynamic viscosity (μ) and the static temperature (T) in a kinetic theory of the ideal gases:

$$\mu = \frac{C_1 T^{\frac{3}{2}}}{T + C_2} \quad 2.5$$

where, C_1 and C_2 are empirically-derived coefficients.

2.1.5 Isentropic expansion and ideal gas

This thesis concerns the study of isentropic processes which assumes, on one hand, that no heat is added or taken away of the system throughout an expansion, in other words it is an adiabatic expansion (no entropy exchanged with the surroundings). On the other hand, the whole process is considered to be reversible. The latter suggests that the process could be reversed without leaving a trace on the system or the surroundings. This assumption can be made since there is no source of irreversibility through the expansion; there are no chemical reactions, nor molecular dissociations, moreover viscosity effects and thermal diffusion are negligible. Furthermore, all along the studies the gases are considered ideal, implying that neither the heat capacity at constant pressure:

$$c_p = \left(\frac{\partial h}{\partial T} \right)_p = \text{const} \quad 2.6$$

Where h – enthalpy. Nor the heat capacity at constant volume (c_v) depends on temperature:

$$c_v = \left(\frac{\partial u}{\partial T} \right)_v = \text{const} \quad 2.7$$

Where u – internal energy. Therefore, any changes in the enthalpy and state of the gas can be described by the following equations:

$$h = c_p T (+\text{const}) \quad 2.8$$

$$\frac{p}{\rho} = rT \quad 2.9$$

where p – pressure; ρ volumetric mass density; r – gas constant of the considered atom/molecule and T – temperature. The flow region neighbouring the nozzle wall is handled separately, the concept of the boundary layer will be introduced, which deals with thermal conduction and viscous effects.

2.1.6 Governing equations

Two different approaches exist to describe the kinematic motion of the flow.^{4,5} In the Lagrangian specification of the flow field, or material viewpoint, the fluid particle is being surveyed at each point in order to determinate its properties. Conversely, the Eulerian specification, or spatial approach, expresses the flow properties at specific locations in the space through which the fluid flows as time passes. As mentioned above, they do not present any viscous effect on the fluid, nor do they describe the possible thermal conductivity. All things considered, the Eulerian approach is more convenient in this current study as exact boundary conditions can be applied on the system, and a fixed volume can be analysed in a Cartesian coordinate system.

2.1.6.1 Eulerian equations for compressible flows

The following hyperbolic equations describe an inviscid flow and represent the laws of conservation:

Mass conservation:

$$\frac{\partial \rho}{\partial t} + \nabla \cdot (\rho \mathbf{v}) = 0 \quad 2.10$$

Momentum conservation:

$$\frac{\partial \rho}{\partial t} \rho + \rho (\mathbf{v} \cdot \nabla) \mathbf{v} = -\nabla p + \rho \mathbf{g} \quad 2.11$$

Energy conservation:

$$\rho \frac{\partial e}{\partial t} + \rho \mathbf{v} \cdot \nabla e = \nabla (p \mathbf{v}) + \rho \mathbf{g} \cdot \mathbf{v} \quad 2.12$$

where ρ – volumetric mass density; \mathbf{g} – gravitational acceleration; e – energy per unit volume and bold letters represent vectoral quantities. Nevertheless, multiple simplifying assumptions can be introduced to describe the system under study in this thesis, namely, the flow through a nozzle.

To begin with, it operates in a steady state regime, implying that no changes happen over time in the flow characteristics and therefore the flow can be regarded as a stationary flow eliminating all the time dependent elements of the equations. This requires a non-turbulent, or laminar, flow. Another key point is the priming assumption of an isentropic core in the expansion of the Laval nozzle. This can be done with attention to the fact that the thermal diffusion-time from the nozzle wall into the isentropic core is much higher than the characteristic time of the flow. In practice, by the time the heat of the nozzle wall would diffuse into the gas, this latter one could be found already in the pumping system. Lastly, as it is detailed in the following chapter, one of the conditions to develop a supersonic expansion is the presence of overpressure at the input part of the nozzle with respect to the exit pressure. Once the supersonic expansion is established along the z -axis, the axial velocity is much greater than the radial one. Consequently, for the preliminary studies the following rationalised uni-directional equations can be used:

$$\frac{d(\rho v_z)}{dz} = 0 \quad 2.13$$

$$\rho v_z \frac{d(v_z)}{dz} = -\frac{dp}{dz} \quad 2.14$$

$$\rho (\mathbf{v} \cdot \nabla) e = -p \frac{dv_z}{dz} \quad 2.15$$

2.2 Laval nozzle design

The convergent-divergent nozzle that creates a supersonic flow is named a *de Laval* (commonly just Laval) nozzle to honour the Swedish inventor Carl G. P. de Laval who used this configuration for the first time in a steam turbine application in 1888.⁶ Through the twentieth century numerous different scientific fields, without this list being exhaustive, put into application this instrument to study fundamental physics^{7–9} and chemistry^{9–13}, to experimentally verify spectroscopic data bases^{14–22} and to send rockets into space²³.

The instrument is designed to convert the initial total energy of a fluid at rest into kinetic energy. Under adiabatic circumstances, when there is no external heat transfer, the first law of thermodynamics leads to the energy equation (Saint-Venant's equation):

$$h + \frac{v^2}{2} = h_0 = \text{const} \quad 2.16$$

where the specific static enthalpy (h) is the sum of the internal energy (u) and the flow work:

$$h = u + \frac{p}{\rho} \quad 2.17$$

The enthalpy takes into account the work of the external pressure forces responsible for setting the fluid in motion. The “total” or “stagnation” enthalpy h_0 is the fraction of thermal energy of the gas which can be transformed into kinetic energy.

For an ideal gas, equation 2.16 becomes

$$c_p \cdot T + \frac{v^2}{2} = c_p \cdot T_0 \quad 2.18$$

The second law of thermodynamics gives the change of the system's entropy (ds) when a supplementary amount of heat (dq_{rev}) is added reversibly to the system at a certain system temperature (T):

$$ds = \frac{dq_{rev}}{T} \quad 2.19$$

For an ideal gas, equation 2.19 becomes

$$ds = c_p \frac{dT}{T} - r \frac{dp}{p} \quad 2.20$$

Keeping in mind that the medium is an ideal gas and additionally the expansion is an isentropic process, meaning $ds = 0$, the equation (2.20) can be written up to highlight the origin of the evaluation of thermal properties summed up by Poisson's equations:

$$0 = c_p \cdot \ln\left(\frac{T_2}{T_1}\right) - r \cdot \ln\left(\frac{p_2}{p_1}\right) \quad 2.21$$

$$\frac{p_2}{p_1} = \left(\frac{\rho_2}{\rho_1}\right)^\gamma = \left(\frac{T_2}{T_1}\right)^{\frac{\gamma}{\gamma-1}} \quad 2.22$$

Combining equation (2.3), (2.4) and (2.19) derives the relation between the total temperature (T_0) to the static temperature at a given point of the isentropic flow as a function of the local Mach number at that point:

$$\frac{T_0}{T} = 1 + \frac{\gamma-1}{2} M^2 \quad 2.23$$

as well as the relation between the total pressure (p_0) and the static pressure at a given point of the isentropic flow:

$$\frac{p_0}{p} = \left(1 + \frac{\gamma-1}{2} M^2\right)^{\frac{\gamma}{\gamma-1}} \quad 2.24$$

And also, the ratio between the total (ρ_0) and statistic densities:

$$\frac{\rho_0}{\rho} = \left(1 + \frac{\gamma-1}{2} M^2\right)^{\frac{1}{\gamma-1}} \quad 2.25$$

These relationships allow the calculation of the flow properties at a given point of the expansion by solely knowing the local Mach number and the total or, in other words, stagnation values of the variables.

2.2.1 Nozzle profile calculation

In a Laval nozzle, the flow at the throat is sonic, in other words the Mach number is equal to unity. In this case, by respecting the continuity equation and considering that at sonic state the velocity of the gas at the throat is equal to the local sound speed, equations (2.26) and (2.27) can be delivered for the flow passed through the throat:

$$\rho_{th} \cdot v_{th} \cdot A_{th} = \rho \cdot v \cdot A \quad 2.26$$

$$\frac{A}{A_{th}} = \frac{\rho_{th} \cdot a_{th}}{\rho \cdot v} = \frac{\rho_{th} \cdot a_{th} \cdot \rho_0}{\rho \cdot v \cdot \rho_0} \quad 2.27$$

where ρ_0 refers to the stagnation density that remains constant all across the isentropic core. Taking equation (2.25) and applying it to the throat, where sonic conditions apply, the following relation can be retrieved:

$$\frac{\rho_0}{\rho_{th}} = \left(\frac{\gamma+1}{2}\right)^{\frac{1}{\gamma-1}} \quad 2.28$$

And lastly, by combining equation (2.25), with (2.28) and (2.3) the Area-Mach number relation is extracted:

$$\left(\frac{A}{A_{th}}\right)^2 = \left(\frac{\rho_{th}}{\rho_0}\right)^2 \left(\frac{\rho_0}{\rho}\right)^2 \left(\frac{a_{th}}{v}\right)^2 = \frac{1}{M^2} \left(\frac{2}{\gamma+1} \left(1 + \frac{\gamma-1}{2} M^2\right)\right)^{\frac{\gamma+1}{\gamma-1}} \quad 2.29$$

Interestingly, this equation shows that the Mach number of the expansion at any point in the

flow is only a function of the ratio of the cross-section (A) of the duct and the sonic throat (A_{th}). This equation explains the need of a divergent part of the nozzle in order to accelerate the gas at high Mach numbers and demonstrates that the exit flow variables such as Mach number (M_e), pressure (p_e), temperature (T_e) and density (ρ_e) rely solely upon the exit to throat area ratio (A_e/A_{th}).

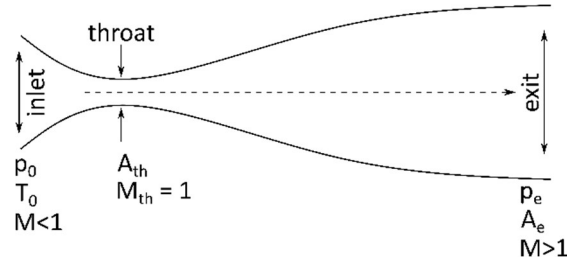


Figure 2.1: Schematic representation of a Laval nozzle indicating the important parameters of the key areas.

Once the desired Mach number and the corresponding area ratio are established, there is only one criterion left to be fulfilled in order to generate the supersonic flow. Namely, an adequate pressure gradient has to be applied along the nozzle in order to accelerate the gas flow. Notably, the exit pressure (p_e) must be maintained lower than the inlet pressure (p_0). For a diatomic gas ($\gamma = 7/5$), Equation (2.24) predicts a maximum of $p_{th}/p_0 = 0.528$ throat to inlet pressure ratio in order to reach the sonic level at the throat and subsequently, a $p_e/p_{th} < 1$ is required for further acceleration of the flow.

To produce a uniform and unidirectional flow downstream of the nozzle exit, a special contoured nozzle profile has to be designed that takes into account not only the area ratio but the shape of the nozzle wall as well. Concurrently, this approach allows control of the gradients of the various flow variables, to overcome the troublesome formation of shock waves in the nozzle divergent section or at the nozzle exit. The gradients of the flow variables are responsible for the disruption of the expansion downstream of the nozzle; therefore, the concept of optimised Laval contoured nozzles was introduced. Scientists confronted these challenges with different approaches. In the late 60's, Rao²⁴ created a method based on the concept of characteristic lines for designing the wall contour. The goal was to obtain the maximum thrust possible by setting the back pressure to zero. Allman and Hoffman²⁵ studied three direct optimisation methods, namely: i) the multidimensional line search, ii) the method of steepest descent and iii) the Newton's method, in order to compare the thrusts developed by the differently obtained nozzle contours. The method of characteristics deconstructed into three steps was used by Atkinson and Smith.²⁶ Firstly, the convergent section is designed up to the throat. The convergent profile is believed to be less critical as no shock waves can form in this subsonic part of the flow. Secondly, the isentropic core is treated within the divergent supersonic section that is divided into three regions from upstream to downstream. They start with a rapid acceleration, followed by a region where the flow behaves as a source flow. This represents a region where the streamlines are linear and radiate out from a source point. The

third region is where the flow is accelerated to the final Mach number, meanwhile the expansion waves are eliminated. In last step in this method, the contour is modified so as to consider the peripheral boundary layer due to viscous effects and the heat transfer originating from friction with the nozzle wall. The importance of matching the exit jet pressure with the expansion chamber pressure is pointed out by Lemos *et al.*²⁷ in order to ensure a good length (at least several nozzle exit diameters) of uniform flow downstream the nozzle exit.

The design of a mini graphite Laval nozzle was decided to improve the original non-LTE experiment developed at the Institut de Physique de Rennes.²² The objective was to overcome the drawbacks inherent to free-jet expansions*, especially the strong convective Doppler line broadening, a consequence of the considerable radial velocity component of the molecules in the jet. Likewise, this new apparatus was planned to reduce the extreme temperature and density gradients specific to free-jets.^{28,29}

2.2.1.1 Profile calculation

The calculation and optimisation of the nozzle contours was carried out through a collaboration with Professor Vinayak and his group at the Indian Institute of Technology Guwahati by using the gradient based steepest descent method.³⁰ Briefly, the procedure iterates in the direction of the negative gradient to approximate the minimum of a function, in our case the overall radial velocity (v_r) component at the nozzle exit. This objective would imply a uniform flow – that is to say non divergent and characterized by a constant Mach number – downstream of the nozzle outlet as the jet is free from any radial component.

The design process was accomplished in two steps. To begin with, the viscous effects were neglected, in essence the mechanical boundary layer forming between the isentropic core and the wall were simply ignored and the thermal exchange between the isentropic core and the wall were disregarded. The solution was computed using Euler's equations and resulted in a preliminary contour.

Next, as a second step, the effects of the boundary layer on the obtained contour were investigated by the means of Computational Fluid Dynamics (CFD) simulations where the Navier-Stokes equations take into account the viscous effects. This was needed to examine the disturbance to the core caused by the flow layers neighbouring the wall.

At the beginning of the process, the input parameters, such as the general dimensions of the nozzle as well as the operating conditions, were declared:

Length (L):	30	mm
Throat radius (R_{th}):	1	mm
Exit Radius (R_e)	12	mm
Stagnation temperature (T_0)	1300	K
Mach number at nozzle exit	9.325	

*"Free-jet" is widely used to denote a supersonic jet exiting a sharp-edged orifice where the gas velocity is sonic and its pressure is far greater than the vacuum chamber pressure. This is the reason why a "free-jet" is also called an under-expanded sonic jet. Note that the gas leaving the Laval nozzle is formally a free-jet. In this manuscript, we reserve the term "free-jet" for flows exiting a sharp-edge sonic orifice, widely used for spectroscopic purposes.

Then, a conical nozzle was discretised by 100 points as shown in figure (2.2) and the local area was calculated at each point:

$$A_i = \pi \cdot y_i^2 \quad 2.30$$

which allowed the calculation of the local Mach number at every x_i slice of the jet. As stated above, equation (2.23) delivers the local temperatures at x_i and these two flow field variables combined with equations (2.3) and (2.4) provide the local velocity (v).

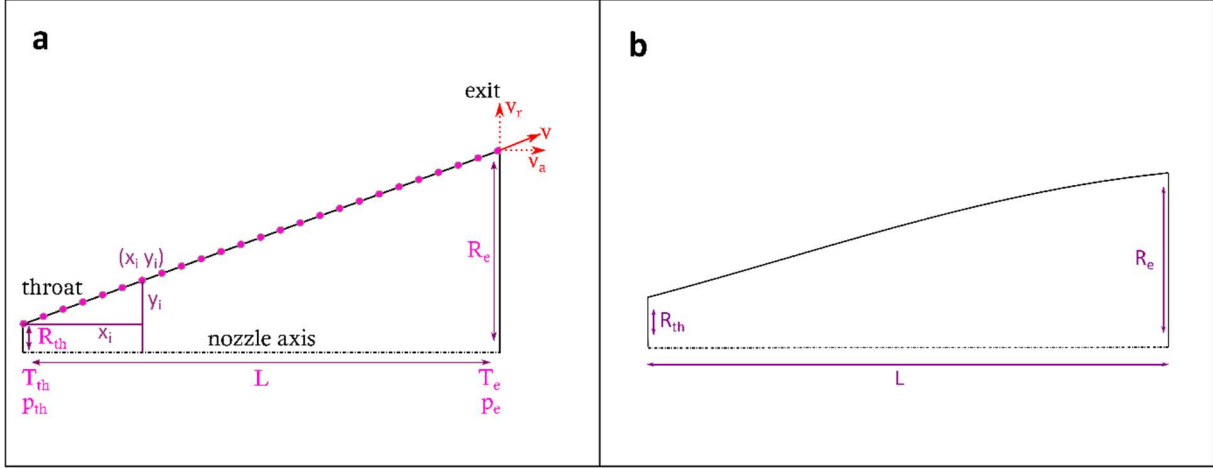


Figure 2.2: Profile design. Panel (a): Initial contour of the nozzle with the input parameters, panel (b) obtained Bezier 15 profile contour

It is important to keep in mind that this velocity is composed of two components: the axial velocity (v_a) parallel to the nozzle axis and the radial velocity (v_r) perpendicular to the nozzle axis, and that their ratio is evaluated from the slope of the tangent. Accordingly, in the first iteration step, it could be simply considered the joining line between the throat and the exit.

This preliminary obtained nozzle contour then went under viscous CFD simulations, assuming compressible-flow and using the axisymmetric laminar Navier-Stokes equations and the total energy equations to compute the flow variables: temperature, pressure, density, *etc.* It must be remembered, these simulations presume the medium, argon, to be an ideal gas. The ANSYS® Fluent commercial solver was used to carry out the simulations, and the viscous effects were treated with the two-term Sutherland's law³, with the solutions considered to be converged at 10^{-5} . The major concern was whether the flow is significantly disturbed by the developing shear layers, the existence of which was neglected through the calculation of the nozzle contour. Figure (2.3) panel (a) shows that the flow is non-uniform as the boundary layer compresses the flow towards the nozzle axis and an undesired oblique shockwave forms at the divergent part of the nozzle. The zero radial velocity component imposed at the nozzle exit seems to be a too severe constraint and the viscous simulations underline the necessity to include the inevitable shear layer effects.

Therefore, the radial velocity component at the nozzle exit was modified and a limit of 1.5 % of the total exit velocity (v) as radial velocity was set as new target function in the

optimisation process. Hence, the newly obtained “Bezier 15” contour was tested again by means of CFD simulations and the stimulating results with the elimination of the oblique shockwave is displayed in panel (b) of figure (2.3).

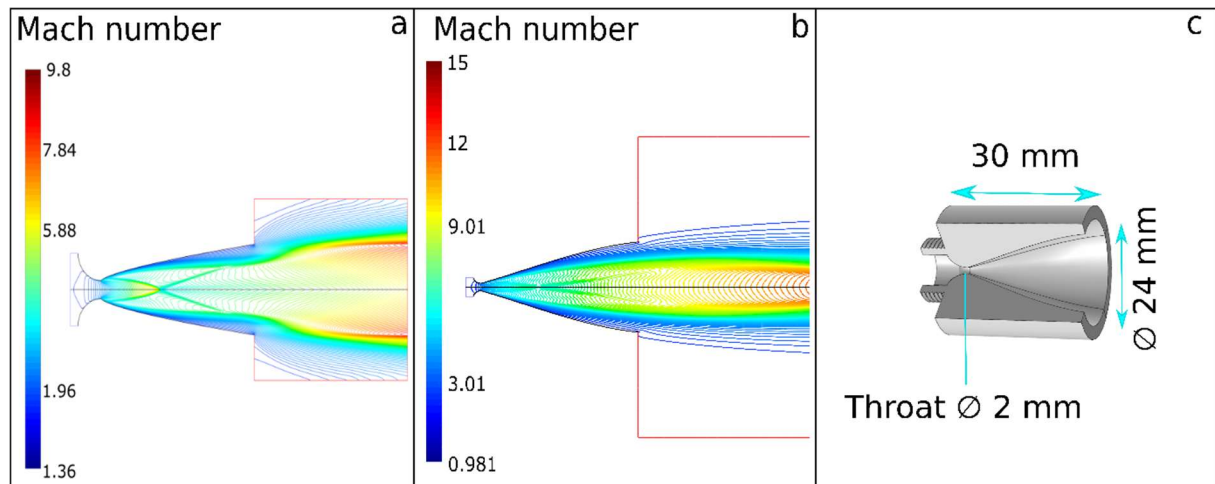


Figure 2.3: Design of an optimised Laval contoured nozzle. Panel (a): CFD simulated Mach number of the preliminary contour obtained by neglecting the viscous effects and by imposing a zero radial exit velocity. Panel (b): CFD simulated Mach number of “Bezier 15” contour leading to a small radial exit velocity. Panel (c): 3D sectional view of the designed Laval graphite nozzle¹⁹

Ultimately, the obtained nozzle contour was manufactured inhouse from isostatic graphite (R6710 grade) which is able withstanding high temperatures. As panel (c) of figure (2.3) shows, the outer side of the convergent part embodies an outer thread which was fabricated in order to allow the proper connection with the High Enthalpy Source (HES), detailed in the following chapter. Finally, figure (2.4) shows the scale of the designed mini graphite Laval nozzle.



Figure 2.4: Manufactured small dimensional, optimised Laval contoured nozzle (Photo credits: Julien Le Bonheur)

2.2.2 CFD simulations and flow field analysis

Prior to the experimental use of the freshly developed Laval nozzle its performance was investigated and verified by axisymmetric CFD simulations, once again using ANSYS Fluent. The numerical simulation envisages to deliver the first insights of the characteristics of the flow field. For the purpose of finding the most adequate region to carry out spectroscopic measurements, the gas flow from the HES to the expansion chamber was simulated at the intended operational conditions, notably a 1300 K reservoir temperature coupled with a 1100

Torr stagnation pressure and an ambient expansion chamber temperature associated with a 0.5 Torr backing pressure. Figure (2.5) demonstrates the simulated temperature flow field downstream of the nozzle exit, and highlights the evolution of the temperature and Mach number along the nozzle axis. The isentropic core of the jet is represented with navy blue and exhibits a remarkably low temperature. This core is surrounded by a hot shear-layer reaching several hundred kelvins. Furthermore, the simulation reveals the occurrence of an oblique shockwave over 60 mm downstream of the nozzle exit, testifying to a quasi-unidirectional flow for over three nozzle exit diameters.

For pragmatic purposes, spectroscopic measurements have to be positioned between the nozzle exit and the formation of the shockwave which induces both recompression and warming of the flow. Moreover, it is crucial to probe the region which has the highest isentropic core/shear-layer ratio with preferably a very low core temperature, therefore a position 20 mm downstream of the nozzle exit was selected. As the lower panels display, the Mach number keeps increasing monotonically from 10 to 18.3 through the expansion. This increase is a direct consequence of the low radial velocity component imposed at the nozzle outlet, causing a slight expansion of the gas. Due to the conservation of the energy, the temperature changes inversely to the Mach number and continuously decreases from 34 K at the nozzle exit down to the remarkably low value of 11.5 K, right before the regular intersection of the oblique shockwaves.

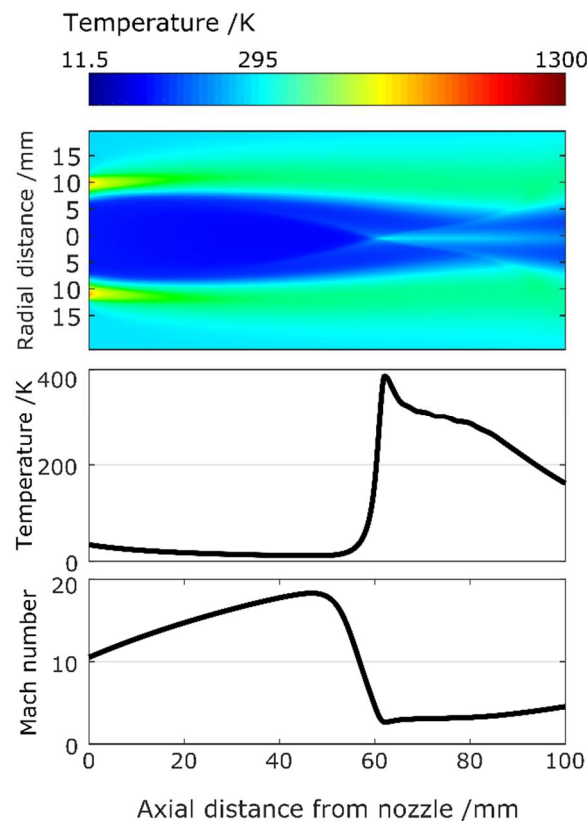


Figure 2.5: CFD simulations of the temperature flow field downstream of nozzle exit (upper panel), evolution of the temperature along the nozzle axis (middle panel) and the corresponding Mach number along the axis.

A leading concern for designing and inserting a Laval nozzle into the SMAUG experimental system was the desire to reduce the radial velocity, pressure, density and temperature gradients. All these factors contribute to problematic line profiles, the so-called

“Batman line shapes”.²⁹ To determine the performance of the nozzle in these latter aspects, the flow field was investigated 20 mm downstream of the nozzle exit in a radial direction and the results are presented in figure (2.6).

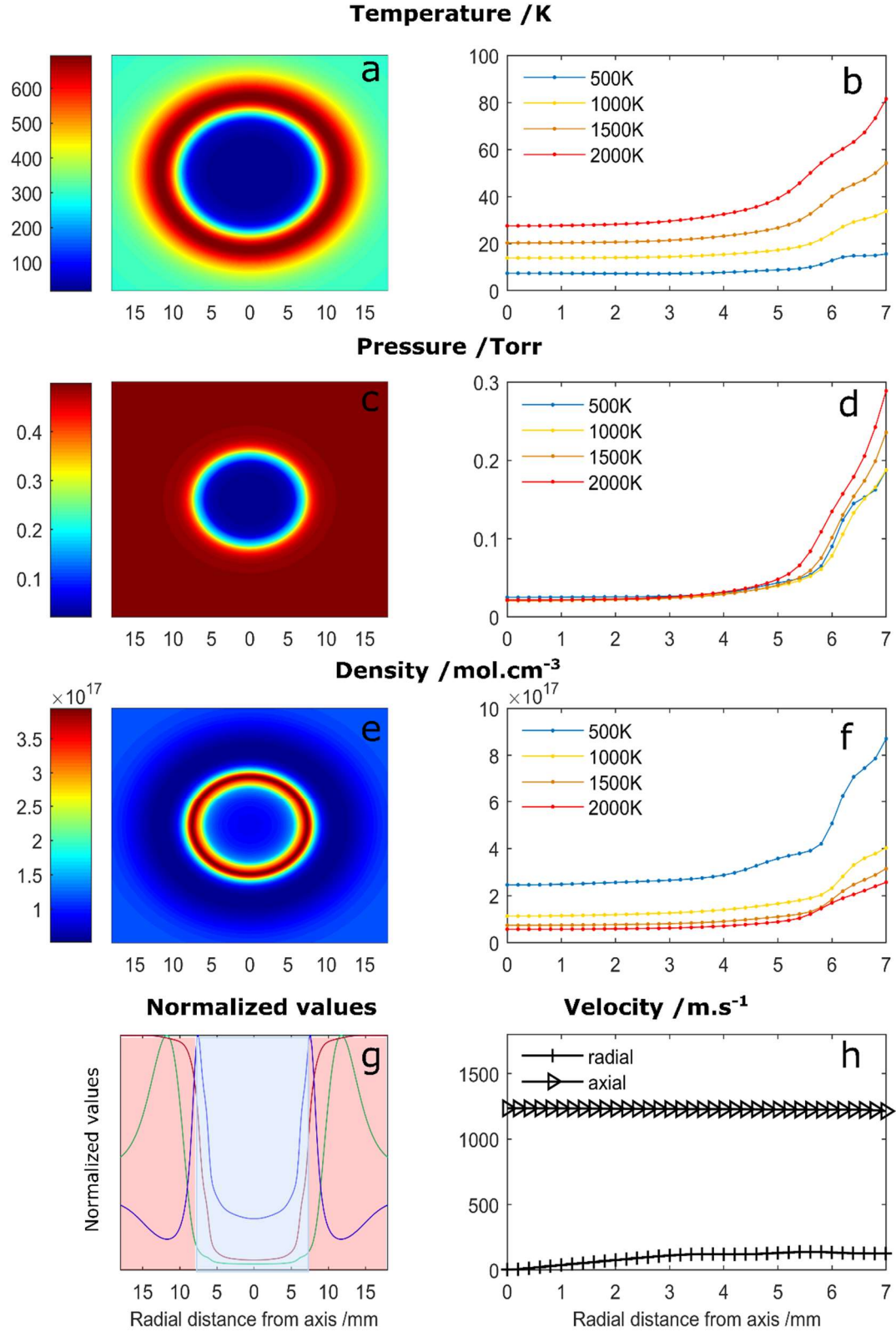


Figure 2.6: Cross-section investigation of the flow field 20 mm downstream of the nozzle exit. Left panels: CFD simulations carried out at a fixed stagnation pressure of 1100 Torr, along with an expansion chamber maintained at ambient temperature and at 0.5 Torr. Right panels: zoom into the isentropic core for different reservoir temperatures. Panels (a) – (b): temperature, panels (c) – (d): pressure, panels (e) and (f): density, panel (g) compares normalised radial temperature (green), pressure (red) and molecular density (blue) values. Panel (h): evolution of the two velocity components from nozzle axis through the isentropic core.

To begin with, panel (a) exhibits the temperature field from which two distinct flow regions can be clearly seen, namely the cold isentropic core and the surrounding hot shear-layers. Panel (b) confirms that the core is indeed free of temperature gradients for over 5 mm from the nozzle axis. Excitingly, panel (b) also unveils that the radial uniformity of the core temperature is maintained, regardless the stagnation temperature of the reservoir. Consequently, the designed nozzle can be tuned to different jet temperatures by merely changing the reservoir temperature.

Afterwards, the unexpectedly low pressure is presented in panel (c). We expected a jet pressure very close to the residual gas pressure of the vacuum chamber, about 0.5 Torr, while the simulations lead to a static pressure about 10 times lower. In fact, the slight radial velocity, 1.5% of the overall exit flow velocity, that was introduced to eliminate the inner shockwave in the nozzle's divergent part, causes the fall of the core's static pressure to 0.05 Torr, an order of magnitude smaller than the expansion chamber pressure. Unlike the variation of the jet temperature, the jet static pressure remains the same, independently of the reservoir temperature, as the stagnation pressure was systematically maintained at 1100 Torr through all the simulations.

Essentially, a direct consequence of the stagnation pressure set at 1100 Torr regardless of the stagnation temperature, is that the static pressure of the core is set at around 0.05 Torr. Therefore, in accordance with the ideal gas law, a lower jet temperature results in a higher concentration of molecules (see panel (f)). Moreover, panel (e) reveals an important augmentation of the jet density in the shear layer. The disadvantage of a dense shear layer is that the CRDS probes the jet along a line of sight and for this reason both flow regions contribute to the integrated absorption spectrum. In summary, for the non-LTE spectroscopic approach, the essential information lies in the isentropic core and the hot gas contribution of the shear layer is rather unwanted. Paragraph (2.2.3) discusses this in detail. Fortunately, after examining the peaks of normalised values of temperature and density, presented in panel (g), a shift of several millimetres can be seen. It is clear that a significant part of the density still corresponds to the cold flow region and therefore will provide a valuable contribution.

Lastly, the examination of the two velocity components are displayed in panel (h). A minor increase of the radial velocity component along the radius can be marked with a maximum value of 130 m.s^{-1} which is still an order of magnitude smaller than the axial velocity component (1230 m.s^{-1}). As a matter of fact, looking at the relation (2.31) describing the Doppler FWHM induced by such a radial velocity (v_r) the line broadening is estimated to be 0.0026 cm^{-1} which corresponds to a Doppler line broadening of static methane maintained at 6 K:

$$\tilde{\nu}_{FWHM} = \frac{\tilde{\nu}}{\left(1 \pm \frac{v_r}{c}\right)} \quad 2.31$$

where $\tilde{\nu}$ – is wavenumber, currently centred at 5885 cm^{-1} and c – is the speed of light.

2.2.3 Isentropic core vs shear-layer

Another key point of the performance of the nozzle is the ratio of the contributions of the different flow regions into the integrated absorption spectrum, as was mentioned above. Thus,

as highlighted in figure (2.7) the respective absorption contribution of the isentropic core (blue) and the surrounding shear layers (pink) were studied through a simulation of the infrared absorption of CO by a numerical procedure, described in detail by Suas-David *et al.*²⁹ Unfortunately, the results shown in panel (a) predict a considerable unwanted hot gas contribution. Despite this, the experimental results in panel (b) show that this contribution is overestimated by nearly a factor of 2.5. The difference is striking when comparing the line intensities for the higher J level transitions (R6 and R7) which are composed mainly by the contribution of the shear-layers.

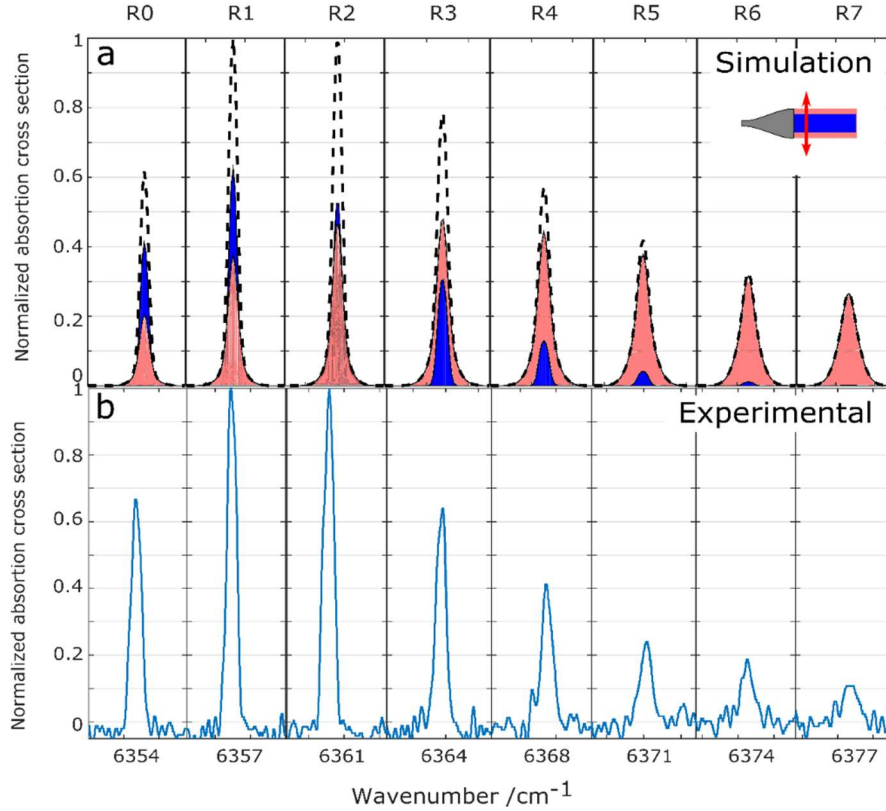


Figure 2.7: Isentropic core and shear-layers contribution to the integrated absorption spectral lines along a line of sight. Panel (a): simulated IR spectra of CO cold band rovibrational absorption lines. Panel (b): experimental lines resulting from the combined contribution of the different flow regions.

Regarding the recorded spectrum, it can be pleasantly seen that there is no sign of the “Batman-shape” (see figure (2.8), reproduced from Ref. 28). The bothersome convective Doppler line broadening of the axisymmetric free-jet was successfully eliminated using the Laval nozzle.

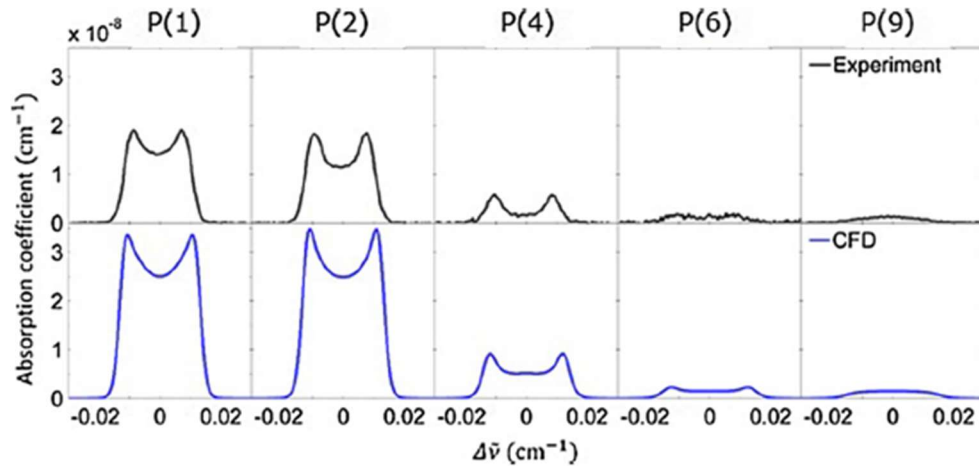


Fig. 5. Comparison of simulated and experimental lines at X3.

Figure 2.8: Representation of the so-called Batman shape lines occurring in the free-jet expansions²⁹

2.2.4 2D Pitot probe

2.2.4.1 Implantation into the experimental environment

Succeeding the numerical characterisation of the generated flow field, the jet was experimentally investigated by Pitot pressure measurements. A Pitot probe³¹, marked in figure 2.9 (1), a metal tube with a small orifice equipped with a pressure gauge, was inserted parallel to the nozzle axis, downstream of the nozzle. Afterwards, a two-dimensional impact pressure mapping procedure was carried out by pulling backwards and moving up and down the reservoir (3) with respect to the fixed Laval nozzle. Between two measuring steps, a proportional–integral–derivative (PID) controller decides whether the measured impact pressure is steady-state and only thereafter proceeds to the next measuring position. Beneficially, the measured data excludes any false values of a non-equilibrated pressure within the small diameter of the probe.

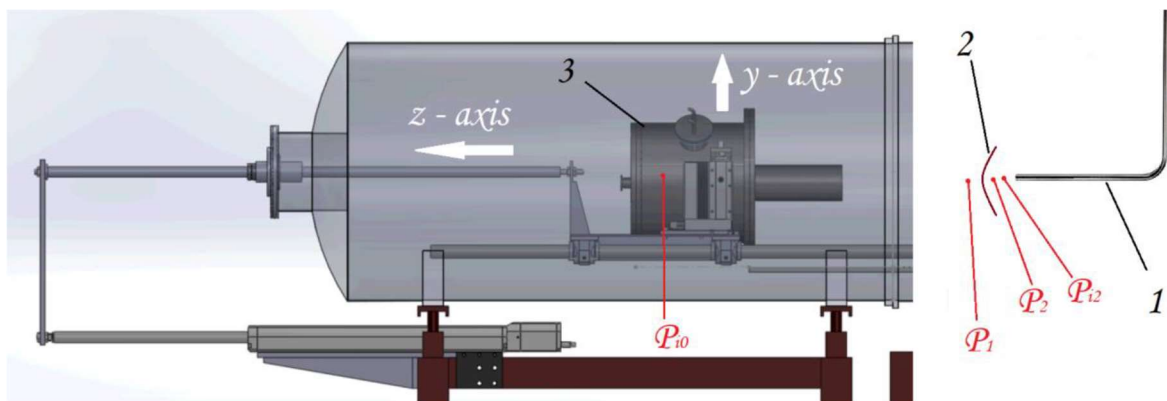


Figure 2.9: Installation of the 2D Pitot probe downstream of the nozzle (schematic reconstruction of the experimental system is taken from the thesis of Suas-David²⁸). 1 – fixed Pitot probe, 2 – impact shockwave, 3 – movable reservoir.

Presuming an isentropic jet and knowing the initial stagnation pressure (p_{i0}) at the reservoir and then measuring the impact pressure (p_{i2}) the Mach number can be retrieved. As

has been demonstrated in the previous paragraphs, once the Mach number and the initial conditions are known every flow variable is derivable.

At first, let us consider an incompressible flow where the flow velocity (v) can be obtained directly from the Bernoulli equation:

$$v = \sqrt{\frac{2}{\rho} p_d} \quad 2.32$$

where $p_d = p_t - p_s$, the dynamic pressure (p_d) is the difference of total pressure (p_t) and the static (p_s). Nevertheless, as it is stated previously, our case is a compressible flow and therefore the equation (2.32) has to be rewritten in a form that considers a variable density as well:

$$v = \sqrt{2c_p T \left(1 - \left(\frac{p_s}{p_t} \right)^{\frac{\gamma-1}{\gamma}} \right)} \quad 2.33$$

Furthermore, the supersonic flow is severely disturbed once the Pitot probe (1) is introduced. To sum up, the formation of a detached normal shockwave (2) in front of the orifice of the metal tube makes the direct application of equation (2.33) invalid. Thus, the effects of the shockwave must be taken into account and incorporated into the calculation. The static pressures upstream (p_1) and downstream (p_2) of the bow shock forming in front of the Pitot probe are linked by the Rankine-Hugoniot relations.³² The ratio p_2/p_1 can be written up in function of the much sought-after Mach number M_1 of the flow:

$$\frac{p_2}{p_1} = \frac{2\gamma}{\gamma+1} M_1^2 - \frac{\gamma-1}{\gamma+1} \quad 2.34$$

while the ratio p_{i2}/p_2 of the measured impact pressure and the pressure downstream of the shock is described by the isentropic equation (2.22), as is the ratio p_{i0}/p_1 of the stagnation pressure and the actual static pressure of the jet upstream of the generated shockwave. Finally, the relation between the measured impact pressure (p_{i2}) and the stagnation pressure is retrieved from

$$\frac{p_{i2}}{p_{i0}} = \frac{p_{i2}}{p_2} \times \frac{p_2}{p_1} \times \frac{p_1}{p_{i0}} \quad 2.35$$

Then, substituting equation (2.35) by (2.24) and (2.34) the Rayleigh pitot-tube formula is introduced³³:

$$\frac{p_{i2}}{p_{i0}} = \frac{\left(\frac{(\gamma + 1)M_1^2}{2 + (\gamma - 1)M_1^2} \right)^{\frac{\gamma}{\gamma - 1}}}{\left(\frac{2\gamma}{\gamma + 1}M_1^2 - \frac{\gamma - 1}{\gamma + 1} \right)^{\frac{1}{\gamma - 1}}} \quad 2.36$$

In conclusion, the above demonstrated measurement process provides the local Mach number (M_1), and thus the flow variables T , v and p , of the flow field at each measured point.

To obtain a good resolution for the mapping process a one-millimetre step size was taken along the nozzle axis as well as along the radial direction. It is important to realise that the above described relationships are only true for isentropic flows, forthwith, once the probe reaches the shear-layer the measured impact pressure will not be useful to derive the Mach number. Because of this, once the probe leaves the core of the hypersonic jet, it measures the only pressure of the expansion chamber ($T_{ch} = 0.5$ Torr) resulting in a misleadingly high Mach number. Therefore, emphasizing the dimensions of the isentropic core obtained by the numerical calculation, the reservoir is elevated only 22 millimetres in radial direction away from the probe's axis.

To avoid systematic measurement errors several principals must be respected. In the first place, even a little deviation of the alignment among the jet streamline and the Pitot tube axis could cause major mistake. An incorrect angle of attack results in a drop in the measured impact pressure, which is derived from the velocity, because the probe only responds to the axial velocity component. Equally important is the geometry of the probe head. An adequate shape would be an aerodynamically rounded curve connecting the inner diameter tube wall with the outer diameter external wall one in order to reduce the induced perturbation to the flow. Despite the fact that this is not the case in our experimental setup, various experimental investigations^{34–37} confirm that as long as the ratio between the inner and outer diameter of the probe is kept below or close to 0.6, the measured impact pressure values contain less than 1% error. Our Pitot tube respects these criteria with a slightly bigger 0.7 ratio.

2.2.4.2 Two-dimensional flow variables mapping

The mapping process was carried out in a hypersonic flow of argon with 1290 Torr of stagnation pressure and a 0.5 Torr backing pressure in the expansion chamber. First of all, the Mach number of the flow was extracted from the measured data using equation (2.36) and the result is presented in figure (2.10). It must be remembered that this procedure is only able to deliver the correct values of the flow variables within the isentropic core and consequently, it could not be applied to characterise the shear-layer, where non-isentropic dissipative effects are present.

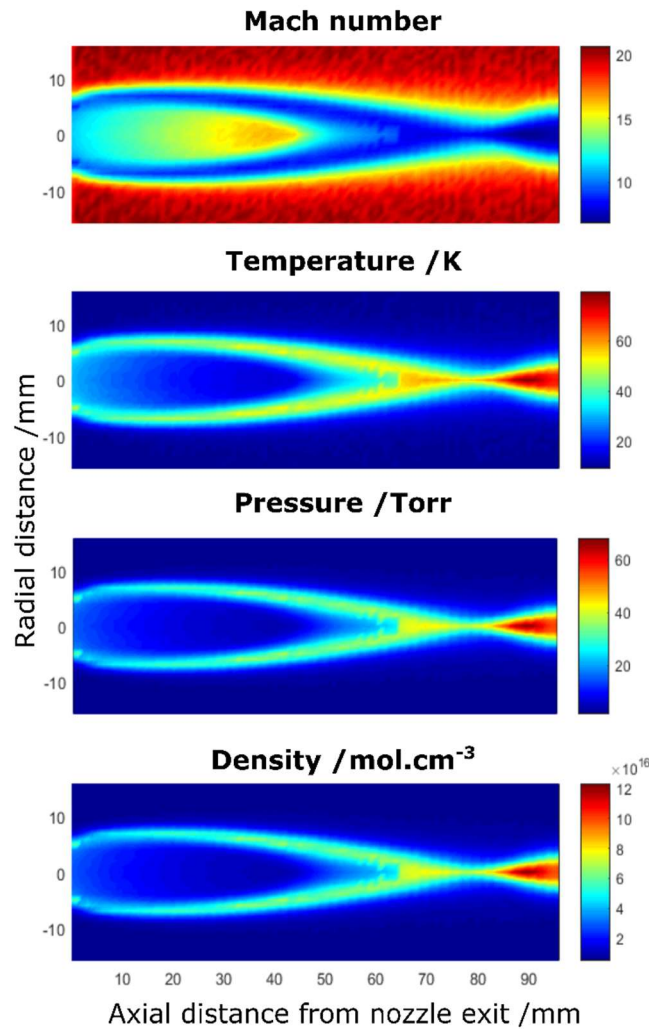


Figure 2.10: Mapping of flow variables extracted from a 2D pitot measurement of a hypersonic argon flow from a Laval nozzle.

The experimentally obtained flow field images are in good agreement with the numerically simulated ones. For example, the forming shockwaves intersect at the same location (~ 70 mm downstream of the nozzle exit, see figure (2.5)) as represented in the direct comparison in figure (2.11). In addition, the radial uniformity of the jet is confirmed together with the monotonic increase of the Mach number along the nozzle axis right up to the occurrence of the shockwave. Finally, despite the fact that this method is not suitable for accessing the Mach number of the shear layer, we can pleasantly notice that shortly after the nozzle exit, the shear-layer is remarkably thin. Henceforth, the numerically chosen position for the spectroscopic studies, 20 mm downstream of the nozzle exit, is confirmed to be the appropriate location to send the laser beam.

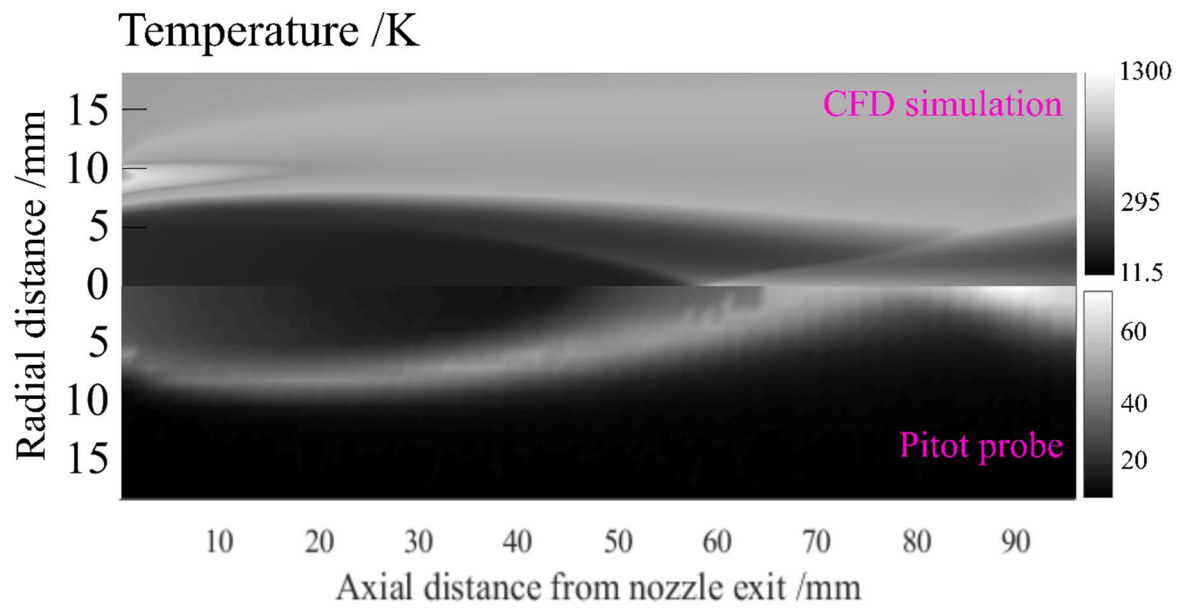


Figure 2.11: Comparison of temperature mapping obtained numerically (upper panel) with the Pitot probe measurement (lower panel)

2.3 SMAUG experimental setup

The following section presents the experimental setup and its performance in terms of rotational and vibrational energy relaxation through a preliminary study carried out with carbon monoxide. As figure (2.12) schematises, the experimental setup is composed of a heating element (HES)^{38,39} that preheats the gas mixture of the carrier gas (argon) and the IR active molecules (CO or methane) before its expansion through the above discussed Laval nozzle. The expansion vacuum chamber is evacuated by a set of roots pumps and eventually the hypersonic jet is probed transversally by means of cavity ring-down spectroscopy (CRDS).

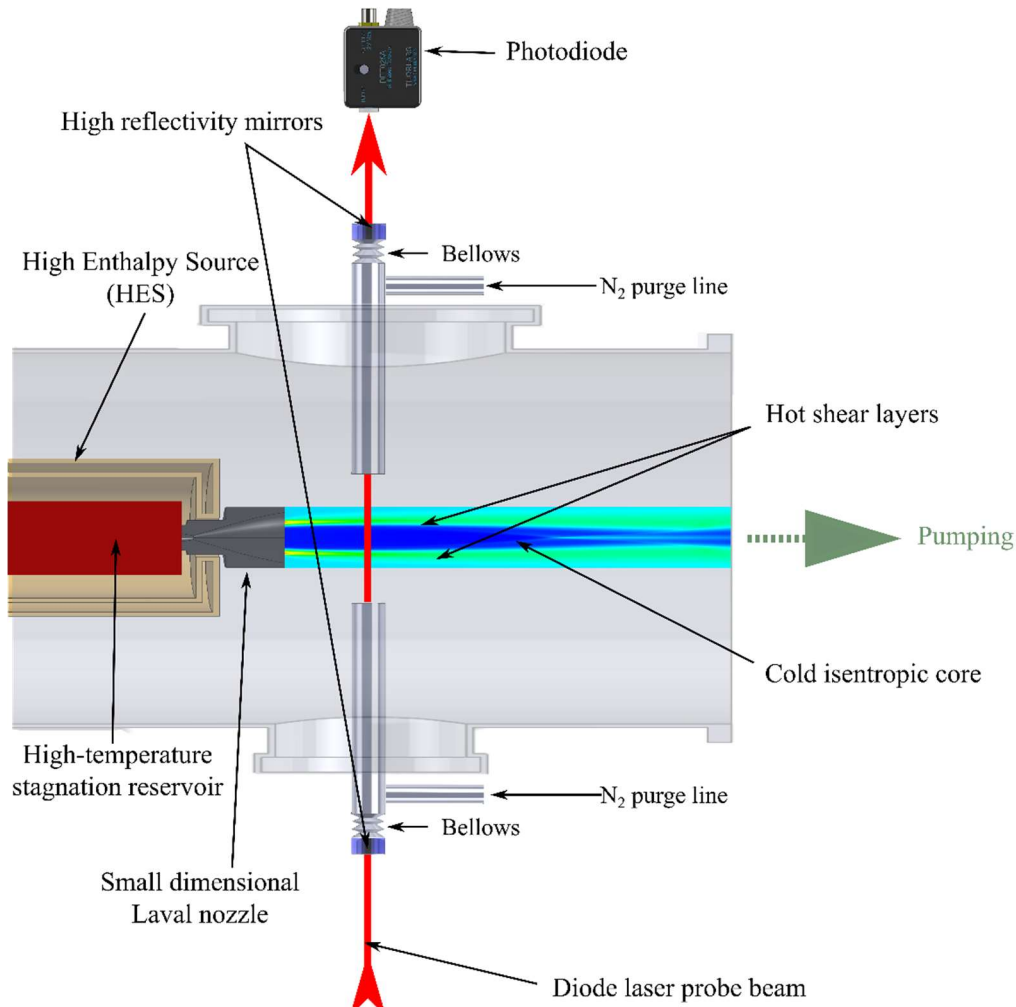


Figure 2.12: Schematic representation of the SMAUG experimental setup

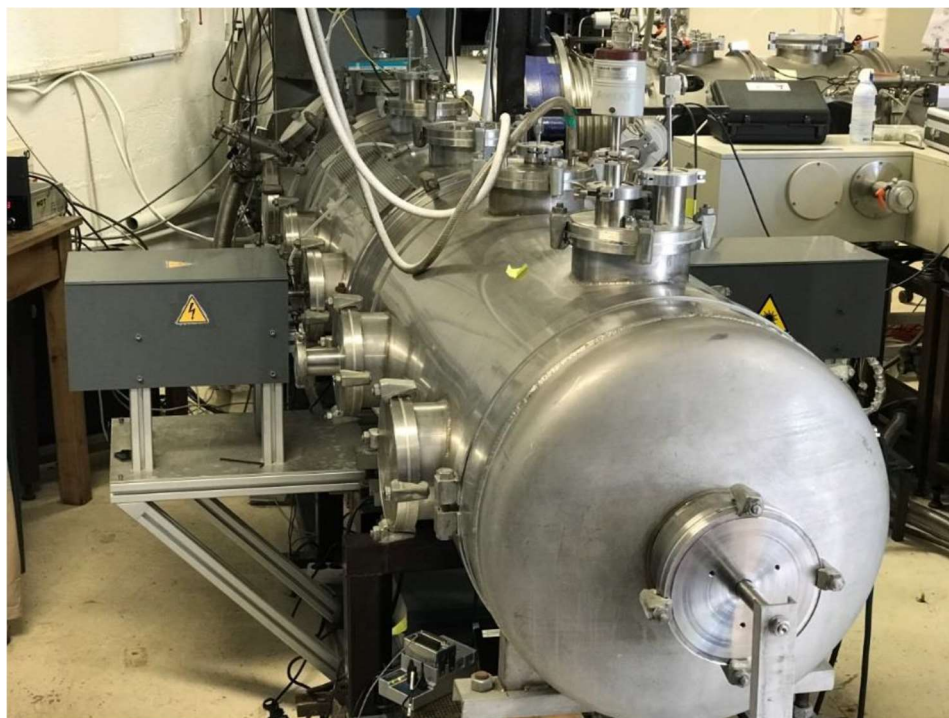


Figure 2.13: Picture of SMAUG

As the photo demonstrates, the experimental setup is composed of a 500 mm diameter stainless steel vacuum chamber that is connected to a pumping system maintaining the setup under low pressure. On the inside, the HES is fixed on a pair of rails that allow horizontal displacement towards, and away from, the optical cavity. This motion is carried out by a computer-controlled servomotor. Moreover, the HES is also placed on two additional servomotors which allow vertical movement. This double movement allows the complete optical investigation of the yz flow field plane.

The system is further equipped with two pressure gauges to continuously derive the pressure values in the HES as well as to report on the expansion chamber conditions. The cavity ring-down spectrometer (in the left and right grey boxes) is mounted on the outer side of the vacuum chamber, on two suspended optical tables.

The required 0.5 Torr constant expansion chamber pressure can be regulated by a built-in butterfly valve (not shown in figure 2.12) capable of adjusting the effective pumping capacity. A significant pumping capacity is needed to ensure the required flowrate (20 standard liter per minute (slm) typically). Accordingly, a pumping system consisting of four separate pumps delivers around $13500 \text{ m}^3 \cdot \text{h}^{-1}$. This arrangement involves a Busch primary pump ($650 \text{ m}^3 \cdot \text{h}^{-1}$), an Alcatel roots pump ($4000 \text{ m}^3 \cdot \text{h}^{-1}$) and two Ruvac Leybold roots pumps ($10000 \text{ m}^3 \cdot \text{h}^{-1}$) connected in parallel.

2.3.1 High enthalpy source

The carrier gas and the IR active molecules were admitted independently into the HES, passing through individual Bronkhorst and MKS mass flow controllers. This gas mixture must then be homogeneously heated up to the desired high temperature. At the heart of the heating element a hollow porous graphite rod (3) is maintained in-between two electrodes (2), as presented in figure (2.14). The graphite (grade R6710) is a fine-grained ISO graphite with an average grain

size of 3 μm and with the ability to withstand high temperature. The in-house manufactured rod has a characteristic size of 200 mm length and 8 mm inner diameter with the porous wall of 3 mm width. Along with its good behaviour at high temperature, another essential characteristic of the material is its electrical resistivity. A resistance value of the graphite rod between 0.15 and 0.3 Ω depending on the temperature, allows, due to the Joule effect, the rod to reach wall temperatures above 1800 K.

The electrodes are part of a circuit supplied by a current generator. The generator is capable of delivering a power of 1600 W, with a corresponding electrical current of 120 A. This value could be extended to 3500 W by dint of a second power supply connected in series, which delivered an additional voltage of 10 V, leading to a maximum electrical current of 153 A through the graphite rod.

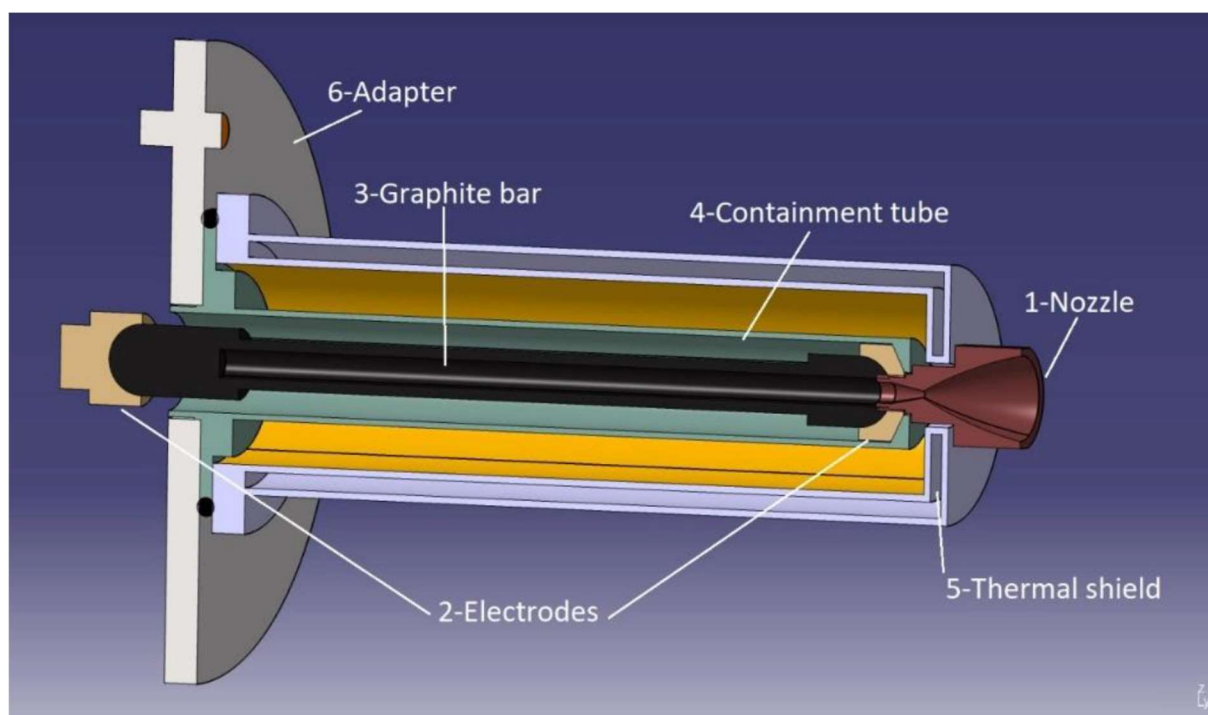


Figure 2.14: Schematic view of the High Enthalpy Source with the mounted Laval nozzle. The graphite rod is maintained between a rear and a front electrode.

The gas flow through the porous wall of the rod is guaranteed by an overpressure in the tantalum containment tube (4) with respect to the open rod cavity which is directly connected to the vacuum chamber through the Laval nozzle. The cavity inside the rod is considered to be the reservoir defining both the stagnation temperature and the stagnation pressure of the molecules before their penetration into the Laval nozzle (1). Most importantly, during the migration process through the hot porous wall the molecules have the opportunity to homogeneously reach a high temperature and consequently populate their rotational and vibrational energy levels in LTE conditions.

As one could imagine, the heated graphite rod and accordingly the surrounding tantalum containment tube emit significant radiation. To ensure the safe operation of the system, a thermal shield is implanted around them, which is in practice a double-walled water-cooled shield. Finally, the specially-designed graphite Laval nozzle is connected by the already-mentioned outer thread to the HES.

One advantage of the HES is to guarantee homogenous heating of the gas. It is well appropriated for studying small hydrocarbons and other highly stable molecules. On the negative side, the use of graphite for the heating element of the system limits the variety of molecules that can be studied. Molecules which contain oxygen would lead, for example, to the destruction by pyrolysis of the graphite rod. Furthermore, due to the axisymmetric design of the system, the expanded flow has axial symmetry giving rise to several inconveniences that will be discussed in chapter III.

2.3.2 Cavity Ring-Down Spectrometer

The cavity ring-down spectrometer was developed by Samir Kassi¹⁵ (LIPhy Grenoble) and implemented to the experimental system by a previous PhD student, Nicolas Suas-David.²⁸ Through the work presented in this thesis, several changes were applied in order to improve the system.

The principle of the method is based on the use of a linear optical cavity consisting of two very high reflectivity mirrors facing each other. A continuous single-mode fiber laser injects through one of the mirrors a pulse of photons into the cavity, the length of which is adjusted in order to obtain a constructive interference system. A photodiode picks up the intensity of photons that escape through the second mirror and that decrease exponentially over time. This decay time (τ_{RD}) is directly related to the absorption coefficient (α) of the molecule:

$$\frac{1}{\tau_{RD}} = \frac{(1 - R) + \alpha L}{\frac{L}{c}} \quad 2.37$$

Where, R - reflexivity coefficient (near to 1), L – pathlength traversed by the laser beam.

The decay time is measured sequentially for each wavelength of the laser to obtain the absorption spectrum of the molecule. In practice, due to the various mechanical vibrations which disturb the device, it is very difficult to stabilize the length of the optical cavity to make it resonant for each wavelength of the laser. This is why one of the mirrors is mounted on a piezoelectric element which makes it vibrate continuously at a frequency of 50 Hz and over a length equivalent to one wavelength, typically. The decay time is thus measured “on the fly”, each time the cavity is resonant.

To reduce the impact of the working environment, the optical tables supporting the optical mounts were removed from their initially fixed-to-the-floor position and mounted to the vacuum chamber. This solution limits the risk of dealignment originating from the deformation that occurs during the evacuation of the air from the expansion chamber. Following the same

path, bellows were implanted in between the high-reflectivity mirrors and the entry of the cavity. These bellows are designed to dampen the vibrations caused by the pumping unit.

Additionally, for a higher resolution spectroscopic result, a new wavelength meter was installed. The HighFinesse/Ångström WS7-60 model is a top-of-the-range instrument with an absolute accuracy of 0.002 cm^{-1} and a wavelength deviation sensitivity of 0.00006 cm^{-1} . Last but not least, its high acquisition frequency of 1.2 kHz is a real advantage for reducing the scanning time and hence allowing a larger number of measurement points to be averaged for a given time period. The laser diode temperature control system has also been improved. They can now be cooled down to -18°C and heated up to $+60^{\circ}\text{C}$ with better stability. The temperature of the diode determines the output wavelength of the laser.

The full description of the optical system can be found in the article by Louvriot *et al.*²² and in the thesis work of Suas-David²⁸. Summarily, the high finesse cavity ($\mathcal{F} > 200\,000$) of the spectrometer relies on the two high-reflectivity ($>99.9987\%$, Layertec) mirrors that are mounted on the specially designed bellows as can be seen in figure (2.12). It is important to realise that the valuable information lies in the $\sim 10\text{ mm}$ isentropic core diameter of the jet located in the centre of the 800 mm long optical cavity. Consequently, the laser beam traversing the experimental system risks to come across a large amount of unwanted absorption due to the static residual gases filling out the expansion chamber. In order to overcome this downside, the two metal tubes, that hold the bellows and therefore the mirrors, are extended right up to either side of the jet. Then, in these tubes a continuous flush of $2 - 4\text{ slm}$ of nitrogen (transparent in the IR range) evacuates any residual gases from the path of the laser beam.

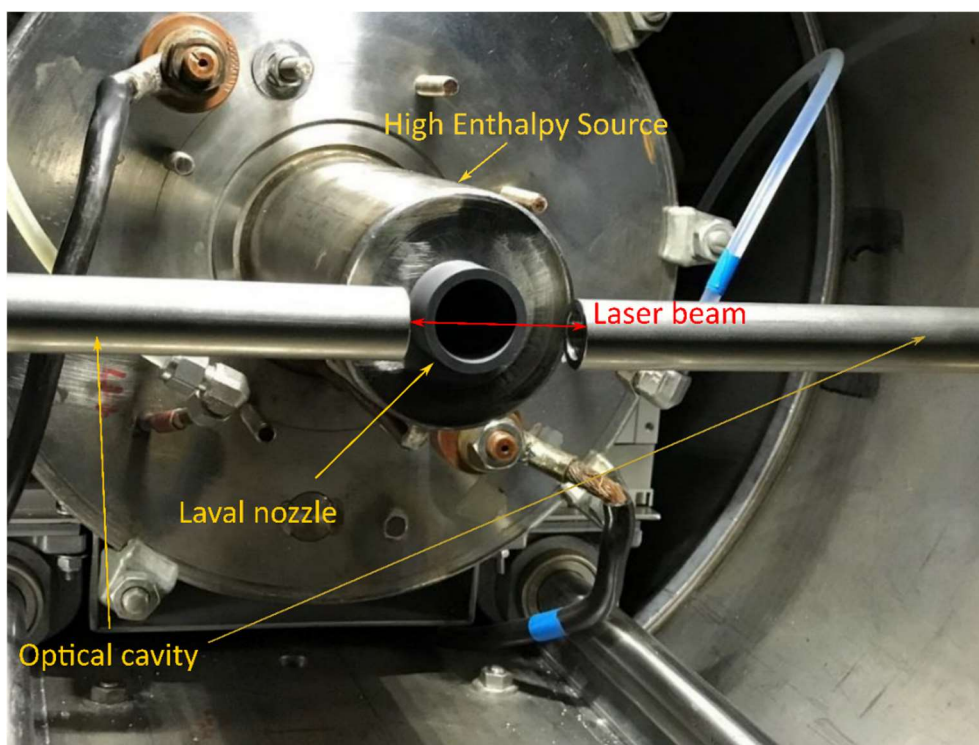


Figure 2.15: Inner view of the expansion chamber. At the back the HES.

The laser light is produced by a series of Distributed Feedback (DFB) diode lasers. These diodes can emit different wavelengths depending on their temperature. Thereupon, they are placed

on a custom Proportional Integral Differential (PID) temperature stabilizer that could vary their temperature from $-18\text{ }^{\circ}\text{C}$ to $60\text{ }^{\circ}\text{C}$ and correspondingly covered a bandwidth of $\sim 30\text{ cm}^{-1}$ per diode. Depending on the manufacturer, a typical optical output of these diodes varies between 5 to 20 mW. The laser beam is divided in two parts: 10% of the signal goes into the wavelength meter and 90% goes toward a radio frequency driven acousto-optic modulator which diffracts the laser beam into the cavity for each ring-down event.

A single lens and two steering mirrors (not present in figure (2.12)) are placed on the optical table immediately at the cavity entry. They regulate the injection of the laser beam and focus it at the isentropic centre of the jet, positioned at the centre of the 800 mm long optical cavity. To obtain a good signal intensity it was essential to align the system into a TEM_{00} mode.⁴⁰

The exit high-reflectivity mirror is resonated by a piezoelectric transducer at 50 Hz which modulates the cavity length in order to ensure the resonance with the instantaneous laser wavelength. The exiting photons are focused via a lens into the photodiode that measures each ring-down decay time. Subsequently, these events are fitted to an exponential decay curve to deliver the absorption coefficient. A typical ring-down time of $120\text{ }\mu\text{s}$ could be routinely obtained, which corresponds to an equivalent of 450 m absorption path length when obtained in $\sim 10\text{ mm}$ isentropic jet core. The ring-down time could be extended up to $200\text{ }\mu\text{s}$ (750 m) when higher reflectivity mirrors were used. These high “equivalent path lengths” are ideal for probing hypersonic expansions which are characterized by inherently low densities and small spatial dimensions.

2.3.3 Determination of the reservoir temperature

The reservoir temperature within the graphite rod, in LTE conditions, is a crucial parameter for carrying out precise and in-depth investigations of the molecules through the expansion, as shown in the previous equations governing flow variables. The exact knowledge of this variable would also allow the accurate characterisation of the various relaxation processes, namely the vibrational and rotational redistribution of the population and its evolution throughout the expansion.

The simple fact that no ascertained method was delivered for a decade to measure this temperature attests to the complexity of the task. The challenge stems from the compact and closed geometry of the HES which is difficult to reach with a temperature probe. Two very different approaches were attempted, both intended to overcome the above-mentioned difficulties. In both cases the experimental setup was run with a pure argon flow.

2.3.3.1 *Attacking from the back door: thermocouple*

In this case, the idea was to reach the cavity of the graphite rod from the back side of the HES. The path is detailed in figure (2.16) highlighting the numerous connections required to ensure the sealing of the different pressure volumes. The advantage of this arrangement is that it does not disturb the development of the hypersonic jet, therefore, in theory, real-time temperature values could be measured continuously along with the recording of the absorption spectrum.

The chosen *type-B* thermocouple maintains a high accuracy and stability in the $600 - 1700\text{ }^{\circ}\text{C}$ temperature region but is very expensive as it is made from 6% rhodium/platinum on the positive side and 30% rhodium/platinum on the negative side. To reduce the costs, only the

first 170 mm that is inside the graphite rod was bought from this material and the rest of the chain was built from cheaper copper. It was possible as only the part entering the graphite rod faces extreme temperatures and the rest is at ambient conditions. Nonetheless, this eliminates the possibility of the direct use of the thermocouple and requires preliminary calibration for accurate results.

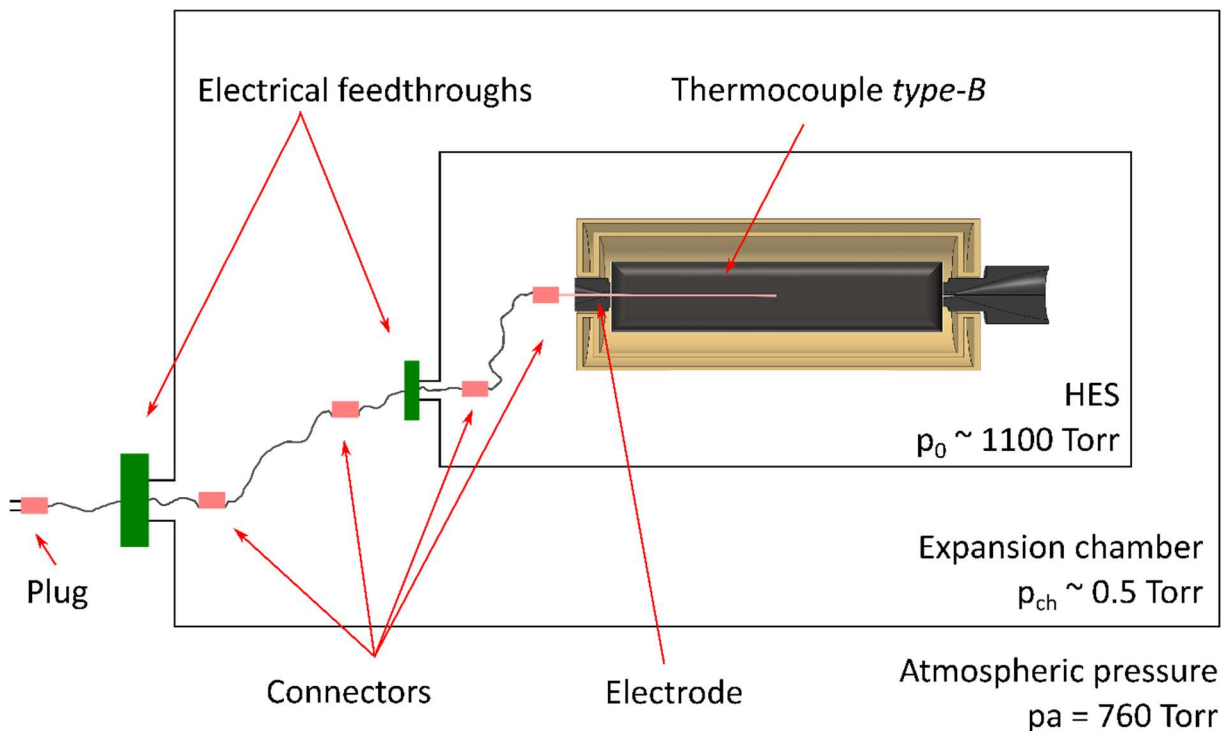


Figure 2.16: Insertion of the Type-B thermocouple into the experimental system

Another key point is the passage of the thermocouple through the rear copper electrode and the small hole drilled in the rear part of the graphite rod. First of all, this passage has to be sealed to ensure that no cold gas could enter into the hollow of the rod, bypassing the porous wall. Secondly, the thermocouple has to be electrically isolated from the heating electrode and the graphite rod. For these reasons, the electrode of the thermocouple was surrounded by a ceramic protective sleeve (DEGUSSIT AL23).

Once the thermocouple chain was constructed, it was placed in an oven next to an etalon thermocouple and heated up to 1600 °C in 50-degree steps. The calibration curve obtained is presented in figure (2.17):

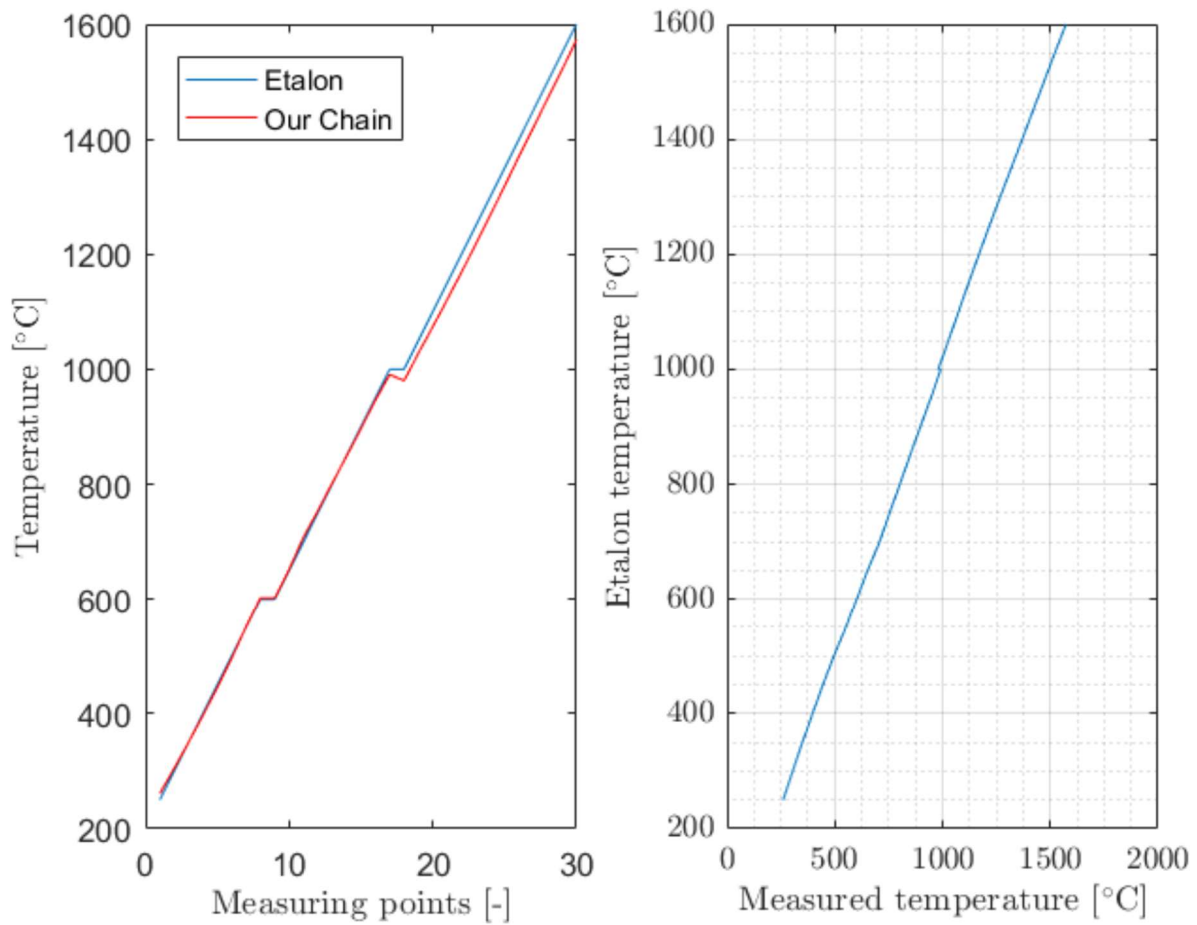


Figure 2.17: Calibration curve of the thermocouple chain

Subsequently, the thermocouple chain was placed into the experimental system and the HES switched on. Figure (2.18) demonstrates two heating processes and the fatal error that occurred at around 500 K in both cases. Supposedly, the increase of the temperature in the graphite rod is associated with an increase of both current and voltage and the appearing spikes on the temperature curve are believed to be a result of electrical discharge between the graphite rod and the head of the thermocouple. After several runs resulting in this critical error, this approach was abandoned.

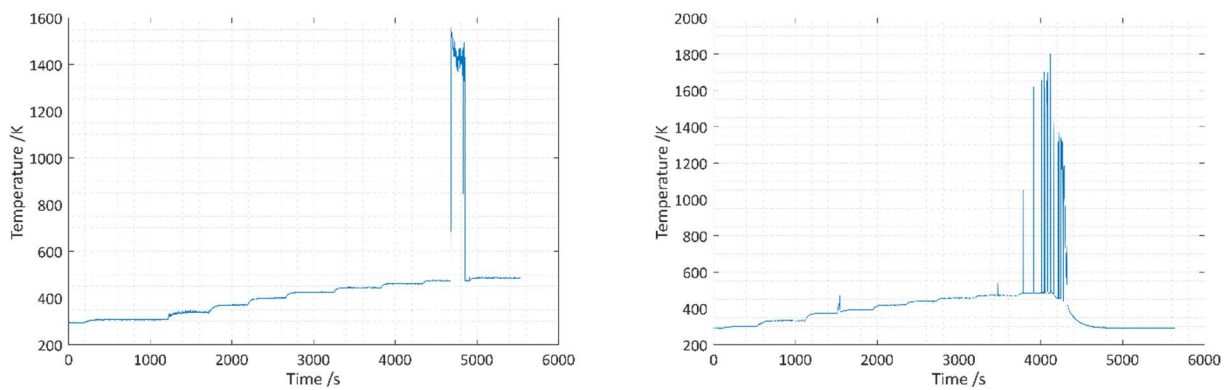


Figure 2.18: Real-time temperature curve measured in the hollow of the graphite rod and the appearance of the peaks corresponding to the electric discharge

Although this setup did not deliver the needed results, as a last attempt the thermocouple chain was inserted into the HES from the expansion side to at least recording some indication of the operation conditions. This approach could not be carried out in real time with spectroscopic measurements, but it could nonetheless give an indicative temperature for notable heating conditions, agreeing with the usual flow rates.

To execute this investigation, the nozzle was dismantled and a graphite cap with two holes was installed in its place. A hole of $\varnothing 2$ mm demonstrates the role of the throat of the nozzle and a second hole of $\varnothing 1$ mm allows the thermocouple to enter the cavity and hold it firmly. This setup has the advantage that it reduces the length of the thermocouple chain as it eliminates the passage from the expansion chamber to the HES and furthermore, the thermocouple could be fixed more steadily, ensuring that it would not touch the wall of the graphite rod. Figure (2.19) represents the recorded temperature values for the different operating conditions. A maximum temperature of 1763 K was obtained for 10 slm of argon and a current of 108 A. Although not measured, a higher temperature can certainly be reached since the generator is able to deliver an intensity which can exceed 150 A.

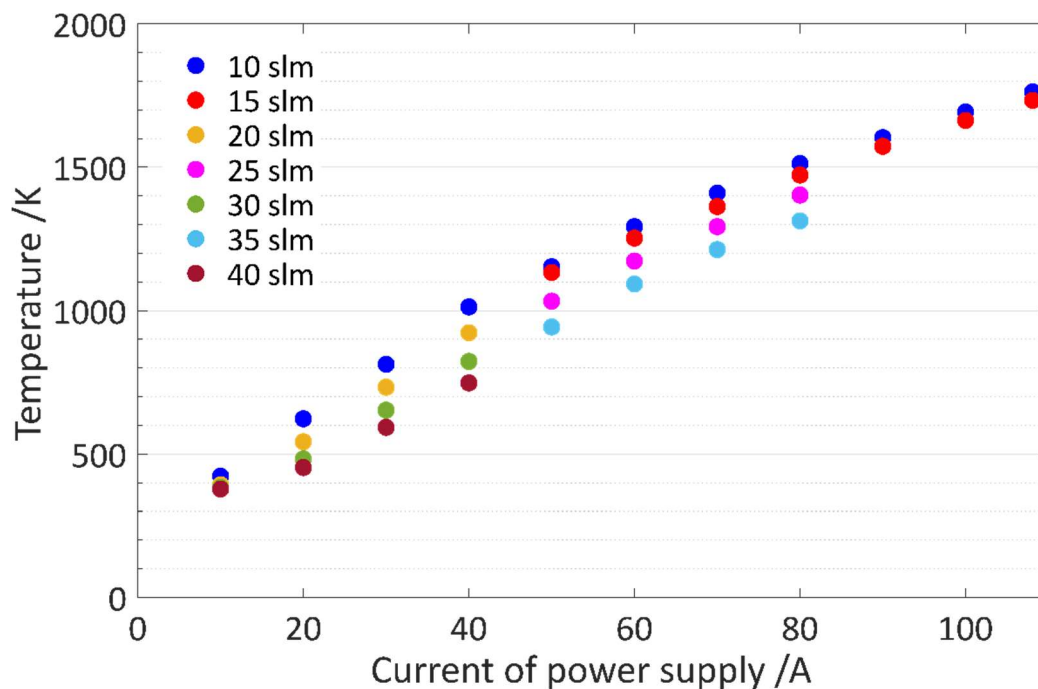


Figure 2.19: Reservoir temperature as a function of supply current for different argon flow rates

2.3.3.2 Attacking from the front door: pyrometer

Whereas the previously discussed thermocouple approach delivered some insight of the reservoir temperature, the main goal, the attempt to deliver continuous temperature values in real-time during spectroscopic measurements failed.

Thereupon, a completely different approach was attempted by inserting an optical pyrometer into the system. The Impac® IGA 6 Advanced pyrometer provides non-contact, short-wave infrared temperature measurement in the range of 600 to 3000 °C. Unfortunately, the apparatus could not be inserted within the low-pressure expansion chamber as its operating environment is ambient temperature and pressure. On the bright side, the infrared

radiation side, the radiation received by the pyrometer can be manually focused over a distance of 210 to 5000 mm, which allows us to build an optical path originating from outside the expansion chamber to the front of the hot reservoir. The device manual prescribes an accurate measuring distance for a given measured spot size, which is the throat area in our case. Thus, the pyrometer should not be more than 688 mm away from the 2 mm diameter nozzle throat. It was decided to mount the pyrometer on a flange located on top of the vacuum chamber (see figure (2.20)). A 45° plane mirror collects and directs the infrared radiation emitted by the graphite rod towards the pyrometer. The mirror is placed in a housing which protects it from the hot flow expanding out from the nozzle. Unfortunately, the placement of the deflecting mirror and its protector blocks the path of the CRDS laser light, meaning no real-time temperature value could be delivered. Nevertheless, this setup was considered adequate for a preliminary enquiry.

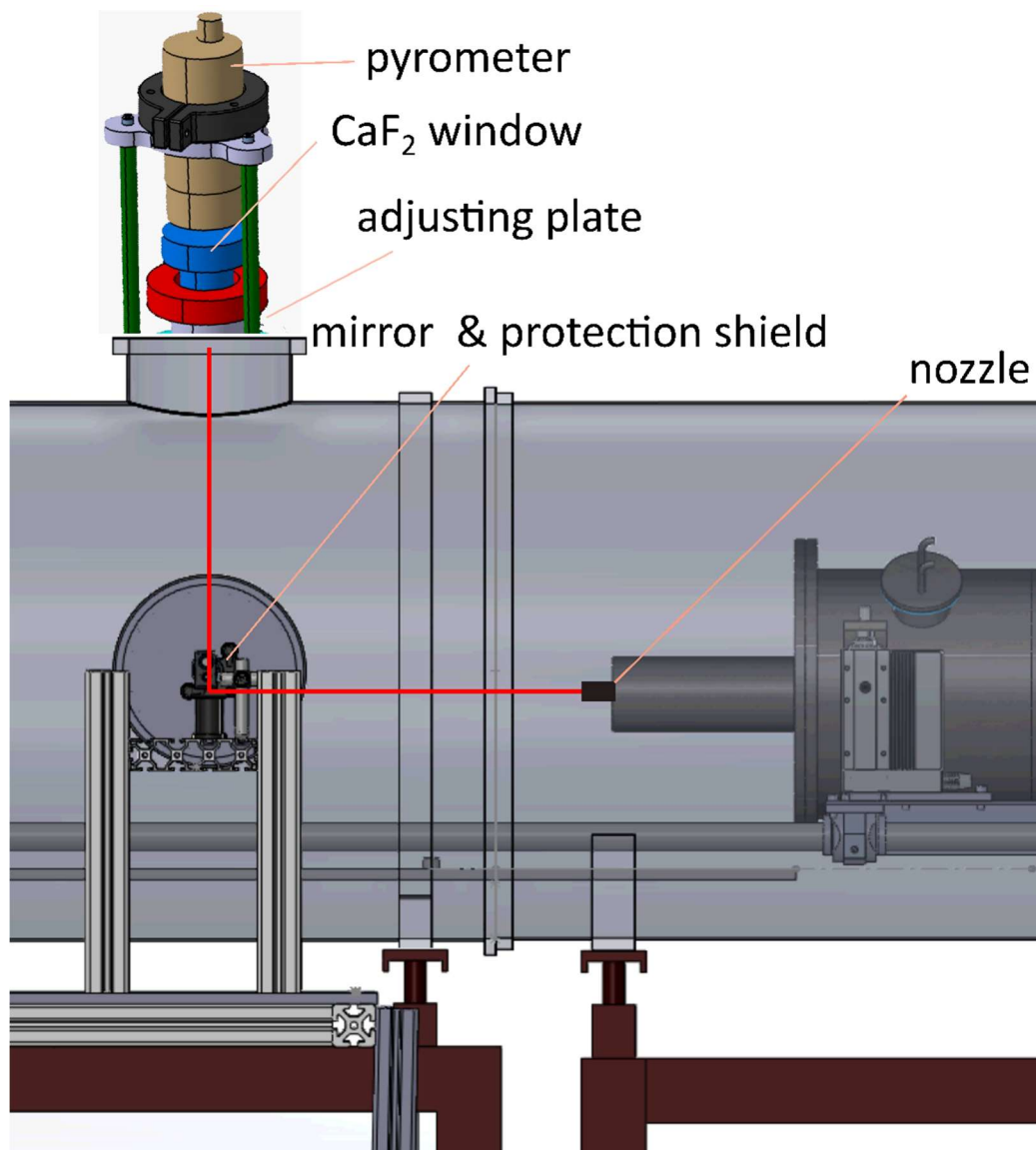


Figure 2.20: Insertion of the pyrometer on the experimental system

The optical adjustment is critical because the pyrometer must collect the radiation emitted by the throat of the nozzle after a deflection of 90° and the successive passage of two small apertures through the mirror's protective housing (see Figure 2.21). Keep in mind that even a small misalignment with respect to the axis of the nozzle would result in an erroneous temperature measurement relating more to the much cooler nozzle wall.

Optical pre-setting is performed at ambient pressure when the expansion chamber is open. Due to mechanical deformations, this initial alignment is partially lost once the pumps are started and the chamber pressure is lowered. To overcome this drawback, a specially designed assembly (see figure (2.20)) allows a minor displacement of the pyrometer in the horizontal plane and enables the recovery of the right optical path.

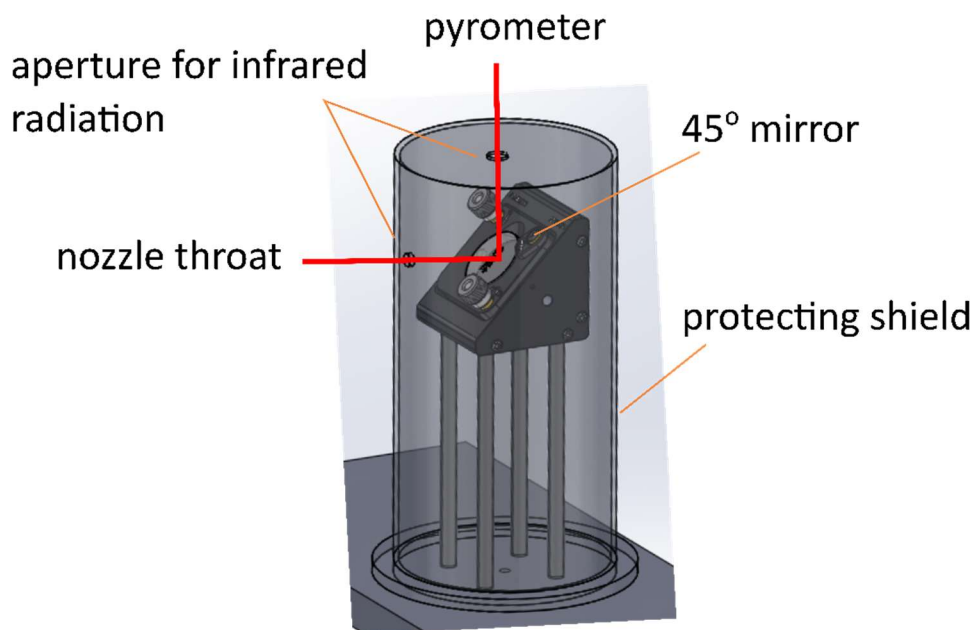


Figure 2.21: Protective housing for the 45° deflection plane mirror

Similar to what was done with the thermocouple, temperature values were measured for a set of discrete operating conditions. Notably, in this case temperature data can be obtained only above 600°C .

Unfortunately, there is a significant temperature difference between the temperatures measured with the pyrometer (figure (2.22)) and those measured by the thermocouple (figure (2.19)) and there is no trustworthy way to prioritize one of the two. The temperatures measured by the pyrometer are systematically lower by about 300 K. This could be explained by the fact that a fraction of the radiation emitted by the walls of the nozzle is collected by the pyrometer despite our precautions.

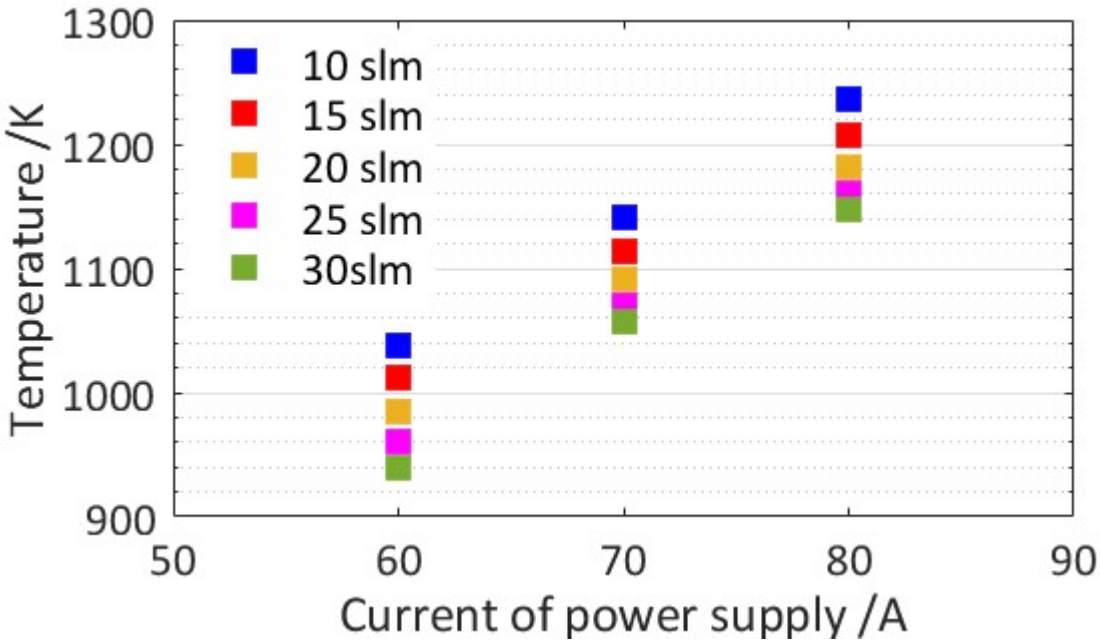


Figure 2.22: Reservoir temperature as a function of the current delivered by the power supply

2.4 Preliminary study on carbon monoxide

The numerical simulations and the above described experimental Pitot probe mapping provided the first insights on the flow structure and Mach number and designated the optimal location along the expansion axis to carry out the spectroscopic measurements. The next step was to test the performance of the experimental system with carbon monoxide molecules admixed in a 5:95 ratio to the argon flow. The objective was to investigate the relaxation of the vibrational and rotational energies in order to confirm that the experimental dispositive indeed corresponds to its vocation and delivers non-LTE spectra.

The choice of the probe molecule is based on the fact that CO is a very well-studied molecule exhibiting a simple infrared spectrum, the line positions of both its cold bands and hot bands are precisely referenced in molecular databases such as HITRAN. This allows a relatively fast examination because instead of scanning the entire spectral region, the sought lines can be recorded directly.

2.4.1 Vibrational relaxation

As previously mentioned, the molecules are heated up under high temperature LTE conditions in order to significantly populate their high vibrational levels. Earlier free-jet studies²² demonstrated that molecular collision events drop as molecules are accelerated to high Mach numbers. As a consequence, the lack of collisions makes it difficult to transfer the vibrational energy of the molecules into rotational or translational energy. However, an expansion through a Laval nozzle instead of a sharp edge orifice results in a more directional jet and a less drastic decrease of the molecular density. Unlike a free-jet, it is possible that in this case the molecules will experience greater vibrational relaxation.

The gas mixture was heated up at around 1400 K at 1010 Torr and the R-branch of the $3 \leftarrow 0$ cold band along with the R-branch of the $5 \leftarrow 2$ hot band were recorded by CRDS. Using the Boltzmann plot method,²² the absorption coefficients of lines issuing from the lower J rotational levels were considered. Correspondingly, a very high vibrational temperature ($T_{vib}^{core} = 1319(125)$ K) could be extracted.

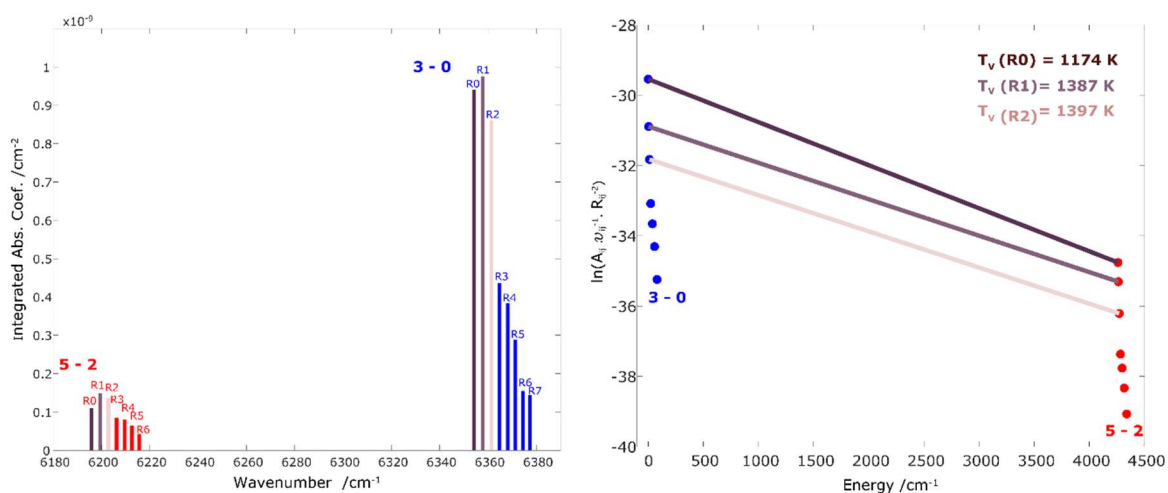


Figure 2.23: Experimental results of CO. Left panel: recorded cold and hot bands. Right panel: Temperature extraction by Boltzmann plot

This high vibration temperature indicates that vibrational relaxation in the isentropic core is inefficient. Next, it must be verified that the rotational energy relaxes effectively so that the experimental setup meets our expectations.

2.4.2 Rotational relaxation

Identically to the study of the vibrational temperature, the Boltzmann-plot method was used once again to retrieve the rotational temperature values and then to describe the rotational relaxation that occurs.

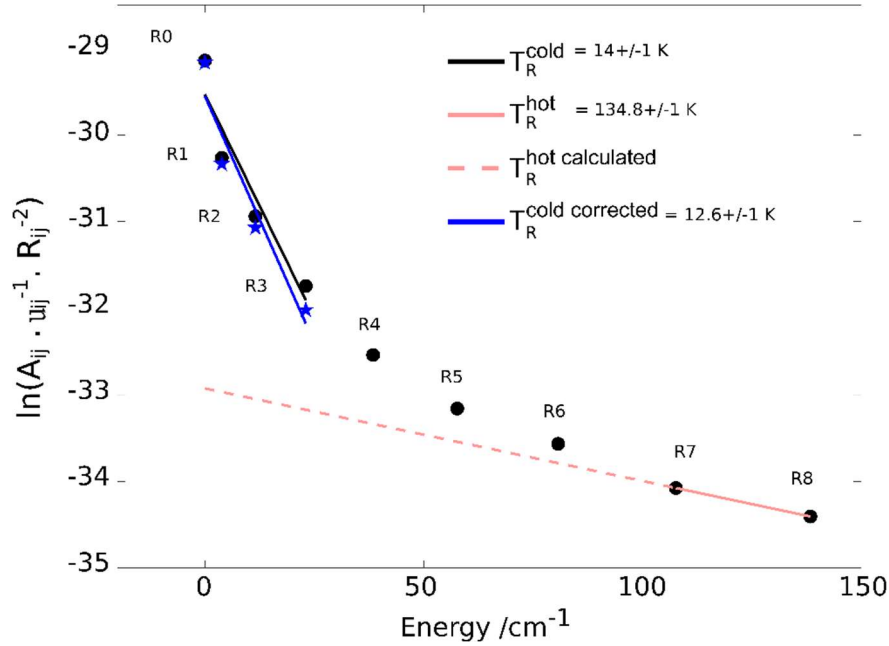


Figure 2.24: Boltzmann plot representing the recorded R-branch of the $3 \leftarrow 0$ cold band. Two different rotational temperatures highlight the two distinct flow regions

Two distinct gradients can be seen in figure 2.24, arising from contributions to the spectrum from regions with different temperatures (cold core and shear layers). The rotational temperature extracted from the first 4 cold transitions ($T_{rot}^{\text{cold}} = 14$ K), corresponding to the cold core, had to be corrected by removing the hot gas contribution of the surrounding shear-layers. This contribution has been described in paragraph (2.2.3) and represented in figure (2.7). The corrected rotational temperature ($T_{rot}^{\text{cold corrected}} = 12.6(1)$ K) of the isentropic core is remarkably similar to that obtained by Pitot probe measurement, confirming a rapid rotational relaxation. In contrast, the extracted rotational temperature of the shear-layer ($T_{rot}^{\text{hot}} = 134.8(1)$ K) is much lower than the 700 K numerically estimated by the CFD simulations. Such a contradiction most likely arises from the fact that T_{rot}^{hot} is an average value integrating the different peripheral layers characterized by very different temperature and density values, as it is shown in figure (2.6).

In conclusion, the SMAUG experimental technique equipped with the custom-designed Laval nozzle described here produces a non-LTE quasi-unidirectional hypersonic flow. Furthermore, the implementation of the nozzle successfully reduces radial temperature and radial density gradients leading to reduced line broadening. This makes it ideally suited for studying the high-energy vibrational modes of more complicated gases such as methane, which will be discussed in the next chapter.

References

- (1) Hoyt, J. K. The Cyclopaedia of Practical Quotationos, English and Latin: With an Appendix Containing Proverbs from the Latin and Modern Foreign Languages ...; Funk & Wagnalls, 1889.
- (2) Speed of Sound <https://www.grc.nasa.gov/www/k-12/airplane/sound.html> (accessed 2021 -05 -02).
- (3) Sutherland, W. LII. The Viscosity of Gases and Molecular Force. The London, Edinburgh, and Dublin Philosophical Magazine and Journal of Science **1893**, 36 (223), 507–531. <https://doi.org/10.1080/14786449308620508>.
- (4) Taub, A. H. General Relativistic Variational Principle for Perfect Fluids. Phys. Rev. **1954**, 94 (6), 1468–1470. <https://doi.org/10.1103/PhysRev.94.1468>.
- (5) Saidi, M. S.; Rismanian, M.; Monjezi, M.; Zendeabad, M.; Fatehiboroujeni, S. Comparison between Lagrangian and Eulerian Approaches in Predicting Motion of Micron-Sized Particles in Laminar Flows. Atmospheric Environment **2014**, 89, 199–206. <https://doi.org/10.1016/j.atmosenv.2014.01.069>.
- (6) de Laval, C. G. P. O. G. P. DE LAVAL. STEAM TURBINE, June 26, 1894.
- (7) Shinobu Tanimura, Yoshiki Okada, and; Takeuchi, K. FTIR Spectroscopy of UF₆ Clustering in a Supersonic Laval Nozzle <https://pubs.acs.org/doi/pdf/10.1021/jp952165d> (accessed 2021 -05 -02). <https://doi.org/10.1021/jp952165d>.
- (8) Abeysekera, C.; Zack, L. N.; Park, G. B.; Joalland, B.; Oldham, J. M.; Prozument, K.; Ariyasingha, N. M.; Sims, I. R.; Field, R. W.; Suits, A. G. A Chirped-Pulse Fourier-Transform Microwave/Pulsed Uniform Flow Spectrometer. II. Performance and Applications for Reaction Dynamics. J. Chem. Phys. **2014**, 141 (21), 214203. <https://doi.org/10.1063/1.4903253>.
- (9) Jiménez, E.; Ballesteros, B.; Canosa, A.; Townsend, T. M.; Maigler, F. J.; Napal, V.; Rowe, B. R.; Albaladejo, J. Development of a Pulsed Uniform Supersonic Gas Expansion System Based on an Aerodynamic Chopper for Gas Phase Reaction Kinetic Studies at Ultra-Low Temperatures. Rev Sci Instrum **2015**, 86 (4), 045108. <https://doi.org/10.1063/1.4918529>.
- (10) Le Picard, S. D.; Tizniti, M.; Canosa, A.; Sims, I. R.; Smith, I. W. M. The Thermodynamics of the Elusive HO₃ Radical. Science **2010**, 328 (5983), 1258–1262. <https://doi.org/10.1126/science.1184459>.
- (11) Rowe, B. R.; Canosa, A.; Heard, D. E. Uniform Supersonic Flows in Chemical Physics: Chemistry Studied Using the CRESU Method Close to Absolute Zero; World Scientific.
- (12) Dupeyrat, G.; Marquette, J. B.; Rowe, B. R. Design and Testing of Axisymmetric Nozzles for Ion-Molecule Reaction Studies between 20 K and 160 K. Physics of Fluids **1985**, 28 pp. 1273–1279.
- (13) Hearne, T. S.; Abdelkader Khedaoui, O.; Hays, B. M.; Guillaume, T.; Sims, I. R. A Novel Ka-Band Chirped-Pulse Spectrometer Used in the Determination of Pressure Broadening

Coefficients of Astrochemical Molecules. *J. Chem. Phys.* **2020**, 153 (8), 084201.
<https://doi.org/10.1063/5.0017978>.

(14) Ferrer, R.; Barzakh, A.; Bastin, B.; Beerwerth, R.; Block, M.; Creemers, P.; Grawe, H.; de Groote, R.; Delahaye, P.; Fléchar, X.; Franchoo, S.; Fritzsche, S.; Gaffney, L. P.; Ghys, L.; Gins, W.; Granados, C.; Heinke, R.; Hijazi, L.; Huyse, M.; Kron, T.; Kudryavtsev, Yu.; Laatiaoui, M.; Lecesne, N.; Loiselet, M.; Lutton, F.; Moore, I. D.; Martínez, Y.; Mogilevskiy, E.; Naubereit, P.; Piot, J.; Raeder, S.; Rothe, S.; Savajols, H.; Sels, S.; Sonnenschein, V.; Thomas, J.-C.; Traykov, E.; Van Beveren, C.; Van Den Bergh, P.; Van Duppen, P.; Wendt, K.; Zadornaya, A. Towards High-Resolution Laser Ionization Spectroscopy of the Heaviest Elements in Supersonic Gas Jet Expansion. *Nature Commun.* **2017**, 8, 14520. <https://doi.org/10.1038/ncomms14520>.

(15) Kass, S.; Campargue, A. Cavity Ring down Spectroscopy with $5 \times 10^{-13} \text{ cm}^{-1}$ Sensitivity. *J. Chem. Phys.* **2012**, 137 (23), 234201. <https://doi.org/10.1063/1.4769974>.

(16) Bernard, D. Etude des émissions thermosphériques des planètes telluriques pour la caractérisation d'exoplanètes, Université de Grenoble, 2014. Thesis.

(17) Hepp, M.; Herregodts, F.; Herman, M. Fourier Transform Infrared Jet Spectroscopy Using a Heated Slit Source. *Chemical Physics Letters* **1998**, 294 (6), 528–532.
[https://doi.org/10.1016/S0009-2614\(98\)00888-4](https://doi.org/10.1016/S0009-2614(98)00888-4).

(18) Hippler, M.; Quack, M. High-Resolution Fourier Transform Infrared and Cw-Diode Laser Cavity Ringdown Spectroscopy of the $\text{N}_2+2\nu_3$ Band of Methane near 7510 cm^{-1} in Slit Jet Expansions and at Room Temperature. *The Journal of Chemical Physics* **2002**, 116 (14), 6045–6055. <https://doi.org/10.1063/1.1433505>.

(19) Dudás, E.; Suas-David, N.; Brahmachary, S.; Kulkarni, V.; Benidar, A.; Kass, S.; Charles, C.; Georges, R. High-Temperature Hypersonic Laval Nozzle for Non-LTE Cavity Ringdown Spectroscopy. *J. Chem. Phys.* **2020**, 152 (13), 134201. <https://doi.org/10.1063/5.0003886>.

(20) Hargreaves, R. J.; Beale, C. A.; Michaux, L.; Irfan, M.; Bernath, P. F. Hot methane line lists for exoplanet and brown dwarf atmospheres. *ApJ* **2012**, 757 (1), 46.
<https://doi.org/10.1088/0004-637X/757/1/46>.

(21) Hilico, J. C.; Baronov, G. S.; Bronnikov, D. K.; Gavrikov, S. A.; Nikolaev, I. I.; Rusanov, V. D.; Filimonov, Y. G. High-Resolution Spectroscopy of (Pentad-Dyad) and (Octad-Pentad) Hot Bands of Methane in a Supersonic Jet. *Journal of Molecular Spectroscopy* **1993**, 161 (2), 435–444. <https://doi.org/10.1006/jmsp.1993.1249>.

(22) Louvriot, M.; Suas-David, N.; Boudon, V.; Georges, R.; Rey, M.; Kass, S. Strong Thermal Nonequilibrium in Hypersonic CO and CH_4 Probed by CRDS. *J. Chem. Phys.* **2015**, 142 (21), 214305. <https://doi.org/10.1063/1.4921893>.

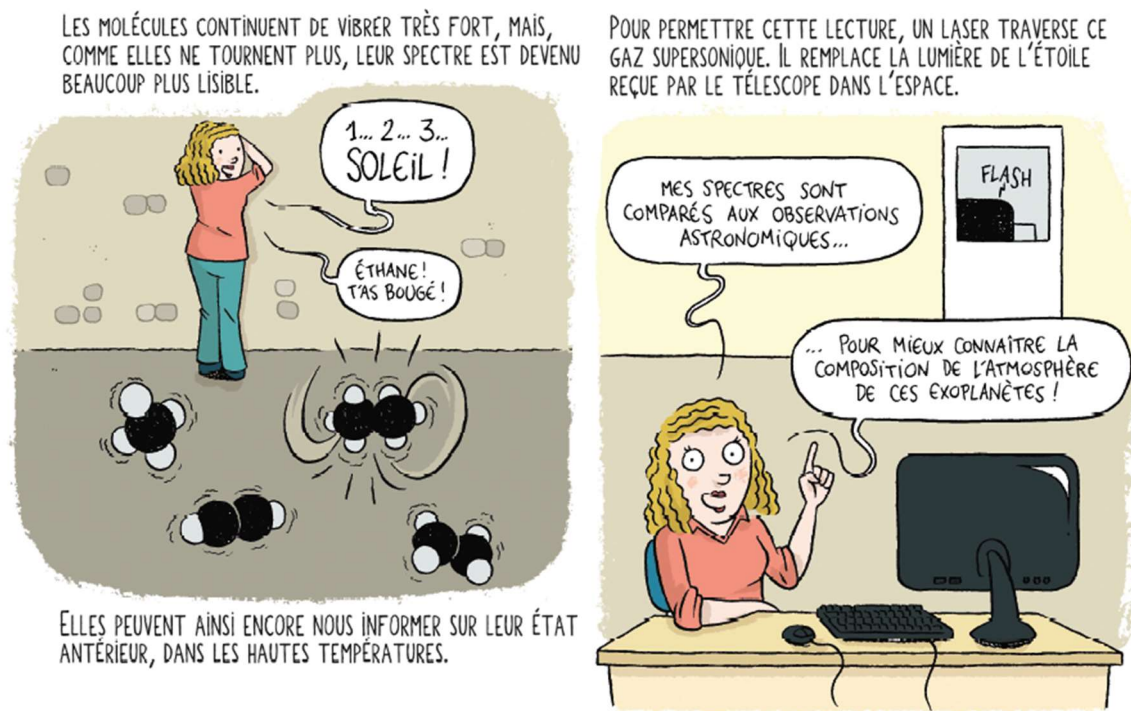
(23) Soukhanovskii, V. A.; Kugel, H. W.; Kaita, R.; Majeski, R.; Roquemore, A. L. Supersonic Gas Injector for Fueling and Diagnostic Applications on the National Spherical Torus Experiment. *Review of Scientific Instruments* **2004**, 75 (10), 4320–4323.
<https://doi.org/10.1063/1.1787579>.

- (24) Rao, G. V. R. Exhaust Nozzle Contour for Optimum Thrust. *Journal of Jet Propulsion* **1958**, 28 (6), 377–382. <https://doi.org/10.2514/8.7324>.
- (25) Allman, J. G.; Hoffman, J. D. Design of Maximum Thrust Nozzle Contours by Direct Optimization Methods. *AIAA* **1981**, 19 (750–751). <https://doi.org/78-1048R>.
- (26) Atkinson, D. B.; Smith, M. A. Design and Characterization of Pulsed Uniform Supersonic Expansions for Chemical Applications. *Review of Scientific Instruments* **1995**, 66 (9), 4434–4446. <https://doi.org/10.1063/1.1145338>.
- (27) Lemos, N.; Lopes, N.; Dias, J. M.; Viola, F. Design and Characterization of Supersonic Nozzles for Wide Focus Laser-Plasma Interactions. *Review of Scientific Instruments* **2009**, 80 (10), 103301. <https://doi.org/10.1063/1.3233895>.
- (28) Nicolas Suas-David. Jets hypersoniques sondés par temps de déclin d’une cavité optique : application à l’astrophysique de laboratoire, Rennes, 2016. Thesis.
- (29) Suas-David, N.; Kulkarni, V.; Benidar, A.; Kassi, S.; Georges, R. Line Shape in a Free-Jet Hypersonic Expansion Investigated by Cavity Ring-down Spectroscopy and Computational Fluid Dynamics. *Chemical Physics Letters* **2016**, 659, 209–215. <https://doi.org/10.1016/j.cplett.2016.06.082>.
- (30) Mathematical Methods for Physicists - 7th Edition <https://www.elsevier.com/books/mathematical-methods-for-physicists/arfken/978-0-12-384654-9> (accessed 2021 -05 -03). Thesis.
- (31) Pitot. Description d’une Machine Pour Mesurer La Vitesse Des Eaux Courantes et Le Sillage Des Vaisseaux. *Histoire de l’Académie Royale des Sciences* **1735**, 363–375.
- (32) Rathakrishnan, E. *Applied Gas Dynamics*; John Wiley & Sons, 2019.
- (33) Shapiro, A. H. The Dynamics and Thermodynamics of Compressible Fluid Flow. In *The Dynamics and Thermodynamics of Compressible Fluid Flow*; 1953; p 153.
- (34) Ower, E.; Pankhurst, R. C.; Pankhurst, R. C. *The Measurement of Air Flow*; Pergamon Press, 1977.
- (35) Matthews, M. L. *An Experimental Investigation of Viscous Effects on Static and Impact Pressure Probes in Hypersonic Flow*, 1958. Thesis.
- (36) Ariaifar, K.; Cochrane, T.; Malpress, R.; Buttsworth, D. Pitot and Static Pressure Measurement and CFD Simulation of a Co-Flowing Steam Jet. *Experimental Thermal and Fluid Science* **2018**, 97, 36–47. <https://doi.org/10.1016/j.expthermflusci.2018.04.004>.
- (37) Al-Doori, G.; Buttsworth, D. Pitot Pressure Measurements in a Supersonic Steam Jet. **2014**. <https://doi.org/10.1016/J.EXPTHERMFLUSCI.2014.05.012>.
- (38) Georges, R.; Thiévin, J.; Benidar, A.; Carles, S.; Amyay, B.; Louvriot, M.; Boudon, V.; Vander Auwera, J. High Enthalpy Source Dedicated to Quantitative Infrared Emission Spectroscopy of Gas Flows at Elevated Temperatures. *Review of Scientific Instruments* **2019**, 90 (9), 093103. <https://doi.org/10.1063/1.5097696>.

- (39) Thiévin, J.; Georges, R.; Carles, S.; Benidar, A.; Rowe, B.; Champion, J.-P. High-Temperature Emission Spectroscopy of Methane. *Journal of Quantitative Spectroscopy and Radiative Transfer* **2008**, 109 (11), 2027–2036. <https://doi.org/10.1016/j.jqsrt.2008.01.023>.
- (40) Lee, J.-C.; Jacobs, S. D.; Gunderman, T.; Schmid, A.; Kessler, T. J.; Skeldon, M. D. TEM₀₀-Mode and Single-Longitudinal-Mode Laser Operation with a Cholesteric Liquid-Crystal Laser End Mirror. *Opt. Lett.*, OL **1990**, 15 (17), 959–961. <https://doi.org/10.1364/OL.15.000959>.

Non-LTE CH₄ spectroscopy

“Absque sudore et labore nullum opus perfectum est”[§]



[§] Without sweat and labour no work is perfected¹

Contents

3.1 The tetradecad spectral region	101
3.2 Recorded spectrum.....	102
3.2.1 Comparison between LTE and non-LTE experimental spectra.....	103
3.2.2 Line broadening	105
3.3 Simulated spectrum	108
3.4 Temperature extraction.....	110
3.4.1 Rotational temperatures	110
3.4.2 Vibrational temperatures	111
3.5 Line identification.....	116
3.6 Conclusion	119
References	120

3.1 The tetradecad spectral region

In Chapter I, it was mentioned that the cold bands of the so-called “tetradecad region” of methane are well studied. The corresponding data is incorporated in the WKMC (Wang, Kass, Mondelain & Campargue) empirical line list (from 5852-7919 cm⁻¹).²⁻⁵ The spectra recorded at 80 K and 296 K allow the analysis and interpretation of observed infrared absorption spectra from the atmosphere of Titan⁶⁻⁸ and other giant planets. However, the transitions corresponding to hot bands, necessary to describe hot astrophysical environments reaching up to 3000 K, such as the atmospheres of hot Jupiters or cool carbon evolved giant stars, remain poorly investigated.

The complexity of the spectrum of methane in its tetradecad region⁹, centred around 1.67 μm (6000 cm⁻¹), has been addressed in detail by Rey *et al.*^{6,10,11} and Cassam-Chenaï *et al.*¹² At high temperature, the lines observed around 1.67 μm come from transitions connecting the ground state (P_0), dyad (P_1), pentad (P_2) and potentially octad (P_3) polyads to higher vibrational states belonging to tetradecad (P_4), icosad (P_5), triacontad (P_6) and tetracontad (P_7) polyads, respectively. The prospective energy structure, with the numerous vibrational sub-levels of the methane molecule, and the difficulties of its investigation are detailed in Chapter I.

In particular, the high-temperature experimental data of methane is essential to constrain *ab initio* variational calculations, from which the theoretical line lists of TheoReTS or Exomol are constructed. Some experimental data, such as the origin of the vibrational bands and the position of the low- J rovibrational energy levels (essentially $J = 0$ or 1), are used to refine the potential energy surface and thus improve the position of the calculated transitions by a factor of about 10. The accuracies reached by TheoReTS are thus approximately 10⁻² to 1 cm⁻¹ for the vibrational energy levels and of the order of 10⁻³ cm⁻¹ for the rotational levels. Non-LTE spectroscopy is therefore a very suitable method in that it precisely reveals information about band origins of highly excited vibrational states (observation of many hot bands) and low- J rovibrational transitions (simplified rotational spectrum).

3.2 Recorded spectrum

After having characterised the performance of SMAUG with CO, the spectroscopic study of more complex molecules, such as methane, under non-LTE conditions can begin.

In the reservoir, 2 slm of CH₄ is mixed with 19 slm of argon at 1040 Torr of stagnation pressure and at around 850(100) K initial temperature, meanwhile the expansion chamber is maintained at 0.5 Torr. The spectral ranges 5884–6003 cm⁻¹, 6005–6073 cm⁻¹, 6120–6140 cm⁻¹, and 6193–6219 cm⁻¹ have been scanned with the available DFB diodes and the recorded spectra are concatenated in panel (a) of figure (3.1).

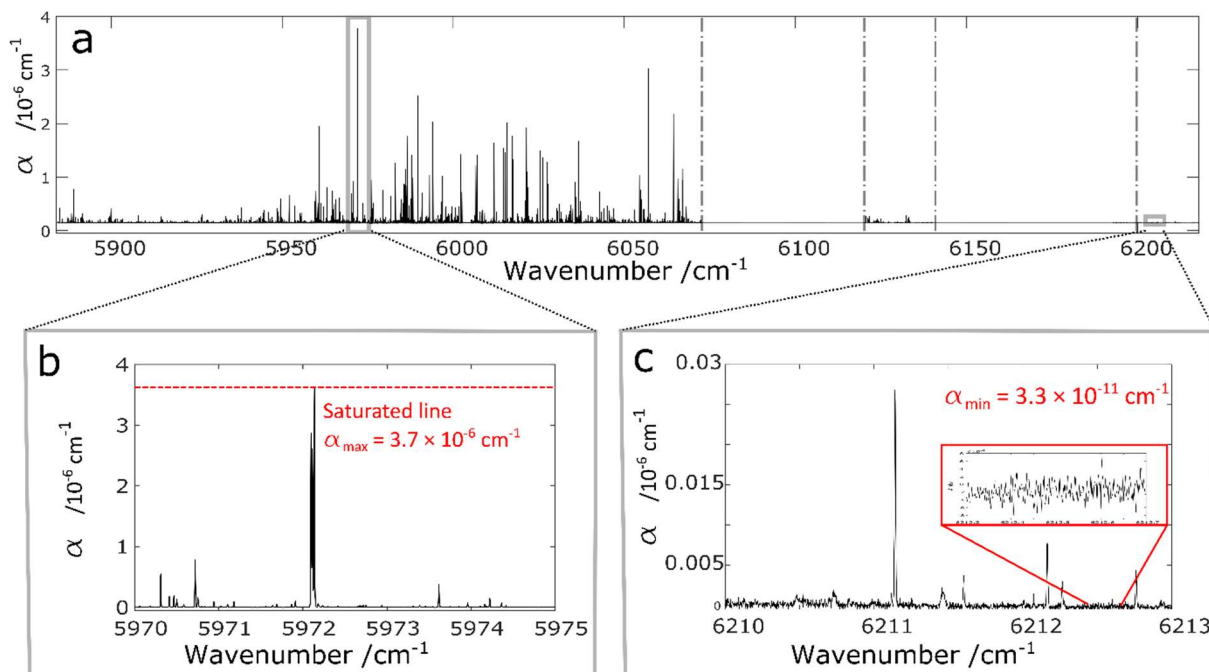


Figure 3.1: Recorded hypersonic non-LTE spectrum of methane. Panel (a): CH₄ spectra over the 5884–6219 cm⁻¹ range and the gaps due to the missing diodes. Panel (b): zoom in of the recorded spectrum to demonstrate a saturated line ($\alpha_{\text{max}} = 3.7 \times 10^{-6} \text{ cm}^{-1}$). Panel (c) reveals the instrumental detection limit defined as the rms of the baseline fluctuations ($\alpha_{\text{min}} = 3.3 \times 10^{-11} \text{ cm}^{-1}$).

As panel (b) highlights, the CRD spectrometer has an upper limit for detecting absorption lines. Specifically, the very intense cold band lines are saturated if they have an absorption coefficient exceeding $\alpha_{\text{max}} = 3.7 \times 10^{-6} \text{ cm}^{-1}$. Therefore, the corresponding line intensities extracted from our fitting procedure are relatively imprecise. From a practical point of view, this saturation effect leads to truncated lines that make it difficult at first glance to compare the experimental spectrum with the spectrum simulated from spectroscopic databases. On the lower side of the dynamic range of the instrument, a detection limit of $\alpha_{\text{min}} = 3.3 \times 10^{-11} \text{ cm}^{-1}$ guarantees the detection of transitions with typical spectral line intensity of $3.7 \times 10^{-29} \text{ cm.molec}^{-1}$ in the hypersonic jet, testifying to a very good experimental sensitivity. To give a rough comparison between the spectroscopic techniques, Fourier-transform infrared spectroscopy (FTIR) has a typical maximum sensitivity of $\sim 10^{-28} \text{ cm.molec}^{-1}$, whereas a state-of-art CW-CRDS spectrometer¹³ can reach the $\sim 10^{-32} \text{ cm.molec}^{-1}$. In summary, a strong dynamic range of around 100,000 should therefore be emphasized for SMAUG.

3.2.1 Comparison between LTE and non-LTE experimental spectra

Two spectra, recorded and provided by the LIPhy laboratory in Grenoble, allow a direct comparison between LTE and non-LTE experimental absorption spectra. In figure (3.2), panel (c) shows the non-LTE hypersonic jet spectrum, meanwhile panels (a) and (b) represent the LTE spectra obtained at 964 K¹⁴ and 81 K^{3,5} respectively.

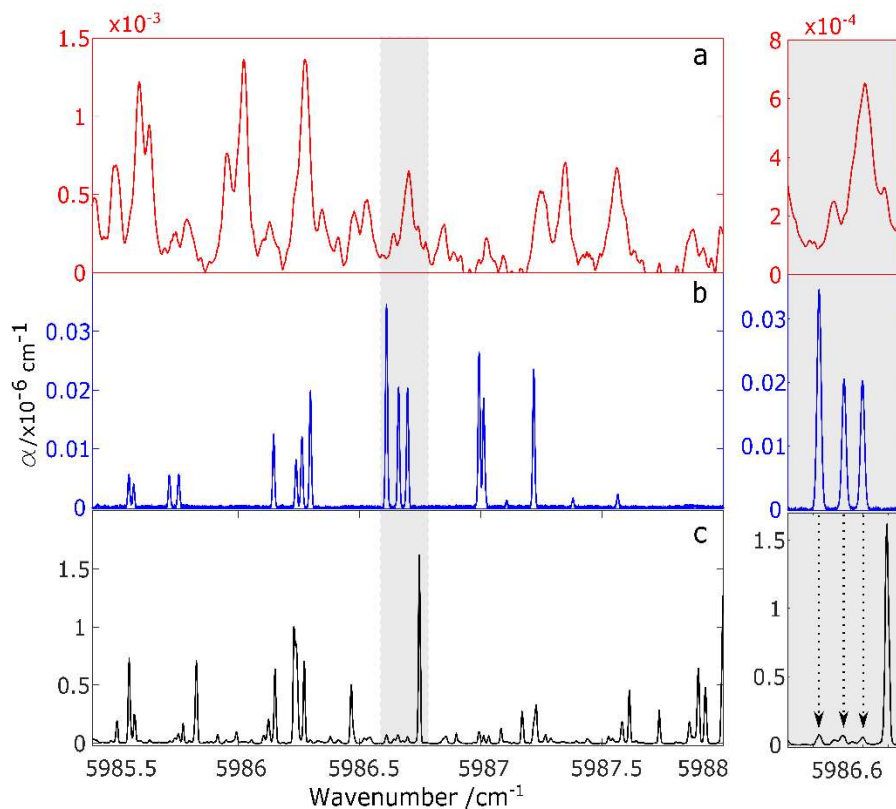


Figure 3.2: Direct comparison of experimental LTE and non-LTE spectra. Panel (a): LTE conditions at 964 K. Panel (b): LTE conditions at 81 K. Panel (c): hypersonic jet non-LTE conditions. Right side: zoomed in to 5986.6 cm⁻¹ to highlight the presence of a hot band transition in our spectrum

One of the most striking differences comes from the considerably broader absorption lines of the 964 K LTE spectrum resulting from both Doppler broadening (FWHM of 0.0334 cm⁻¹ at 964 K) and multiple overlapping transitions. In principle, the information contained in the high temperature static spectrum is extensive and should therefore be considered as a reference spectrum for direct comparison with existing databases.^{6,10,11,15–19} Nevertheless, the determination of the exact line positions requires a problematic post-processing of many unresolved contributions. Conversely, the line narrowing and spectral decongestion observed in the non-LTE spectrum are two strong advantages for a line-by-line identification. However, it remains to be confirmed, as in the former case of carbon monoxide in chapter II, that the lines observed are indeed low-*J* value transitions belonging to different cold and hot bands. In other words, is the methane accelerated by the Laval nozzle vibrationally hot and rotationally cold?

The absorption lines recorded in LTE quasi static conditions at 81 K belong exclusively to cold bands because at such low temperature the population is fully relaxed to the vibrational ground state. In the magnified view of figure (3.2) 3 transitions are shown which are identified

as lines of a Q-branch of the cold band $0020(F_2) \leftarrow 0000(1A_1)$ corresponding to the $^{13}\text{CH}_4$ isotopologue, from left to right: $3(A_1) \leftarrow 3(A_2)$, $3(F_1) \leftarrow 3(F_2)$ and $3(F_2) \leftarrow 3(F_1)$. Comparing the LTE 81 K spectrum with the hypersonic jet spectrum, the appearance of a fourth intense line can be spotted in the non-LTE spectrum which corresponds to the transition $2(F_1) \leftarrow 2(F_2)$ of the hot band $0021(F_1) \leftarrow 0001(F_2)$ of the isotopologue $^{12}\text{CH}_4$ departing from the dyad polyad. This testifies to populated higher vibrational levels and the presence of transitions corresponding to the hot bands.

At the same time, it has to be mentioned that the measured FWHM of the lines in the hypersonic jet is about 0.01 cm^{-1} , which is astonishingly above the value of 0.0052 cm^{-1} corresponding to the simulated radial flow of 130 m.s^{-1} of the isentropic core. The possible reasons for such a broadening are set out in the following section. However, similarly to the recorded spectrum of CO, the obtained CH₄ spectrum contains the contribution of the shear-layers as well. The corresponding transitions issuing from higher- J rotational levels are represented with a broadener lines, with $\text{FWHM} \sim 0.0215 \text{ cm}^{-1}$. Figure (3.3) demonstrates the contributions of the two flow regions: the isentropic core (yellow caption) and the shear-layers (blue caption). The upper trace shows the recorded spectrum, and the lower one exhibits the fitted lines and the reconstructed fitted spectrum. The fitting program used to determine the position and intensity of the lines was provided by LIPhy. The pressure in the isentropic core is sufficiently low (0.05 Torr) to ignore the pressure line broadening and the line shape is essentially Gaussian. However, for better determination of line intensity, a small Lorentzian component has been included in the fit to absorb the effect of the contribution of the warmer shear layer flaring the foot of the line.

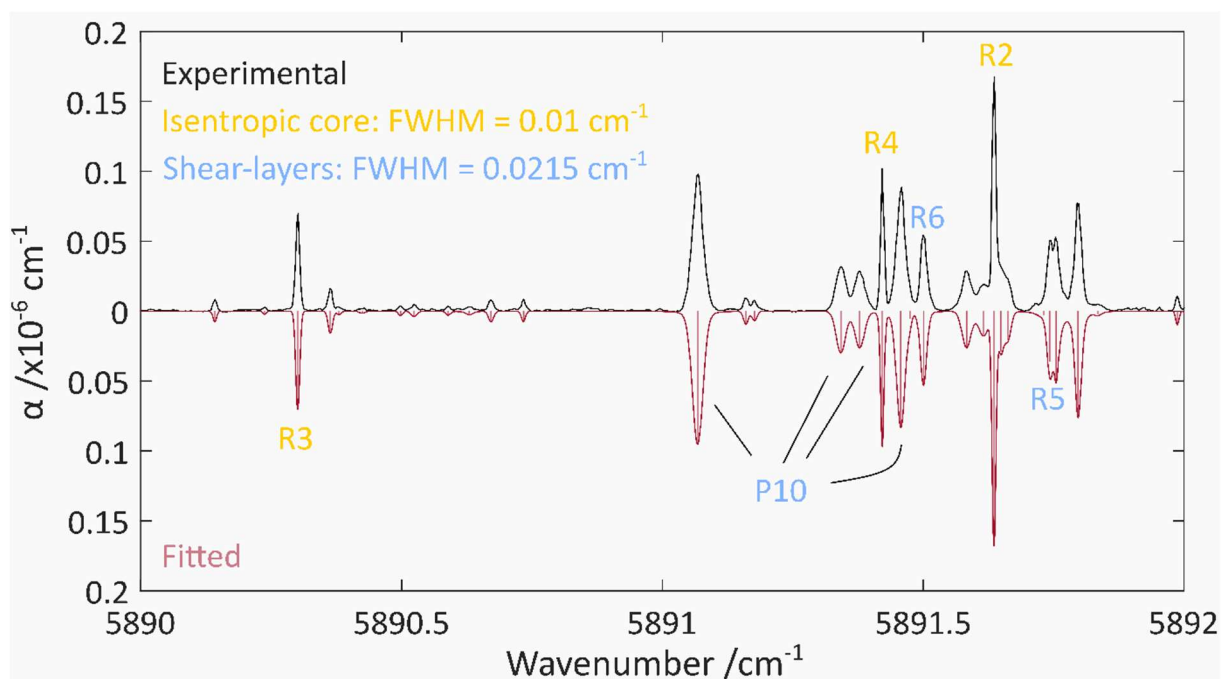


Figure 3.3: Zoom into the experimental non-LTE CH₄ spectrum. Upper trace: recorded spectrum. Lower trace: reconstructed spectrum of the fitted lines. Indication of the two different line shapes emerging from the isentropic core (yellow) and the shear-layers (blue).

3.2.2 Line broadening

As it will be detailed in a next section, the rotational temperature of methane is estimated to be around 39 K, meaning that the translational temperature should be lower or at least equal to this value, thus leading to an expected “thermal” (as opposed to “convective”) Doppler line broadening of 0.0066 cm^{-1} (FWHM at 5885 cm^{-1}). The possible reasons of such a disagreement with regard to the predicted Doppler line broadening and the experimentally measured one are examined hereafter. The thermal Doppler line broadening parameter is retrieved from equation (3.1). The measured value of 0.01 cm^{-1} should correspond to a static gas with temperature (T) of 86 K:

$$\Delta\tilde{\nu}_D = 7.162 \times 10^{-7} \times \tilde{\nu}_0 \sqrt{\frac{T}{M}} \quad 3.1$$

where $M = 16 \text{ g.mol}^{-1}$ is the molar mass of methane.

Four hypotheses have been investigated to explain this surprisingly large line broadening. The first possible culprit is the presence of a more important radial velocity component than the numerically simulated one. To obtain the necessary value of this radial component (v_r) equation (3.2) was used:

$$\tilde{\nu}_{RV} = \frac{c \pm v_r}{c} \times \tilde{\nu}_0 \quad 3.2$$

where c refers to the speed of light. This results in $v_r = 500 \text{ m.s}^{-1}$, this value is significantly higher than that of 130 m.s^{-1} given by the CFD simulations (and leading to a FWHM line broadening of 0.0026 cm^{-1} at 5885 cm^{-1}). It cannot be excluded, but it would be surprising for the simulated radius velocity parameters to disagree by such a large amount, whereas the other simulated parameters tended to be fairly accurate when compared with experimental measurements.

Secondly, a possible misalignment was examined between the jet stream line and the transverse laser beam. In this hypothesis, the numerically simulated axial velocity v_a of 1230 m.s^{-1} was considered and the error was searched in the laser beam’s attacking angle, as it is represented in figure (3.4).

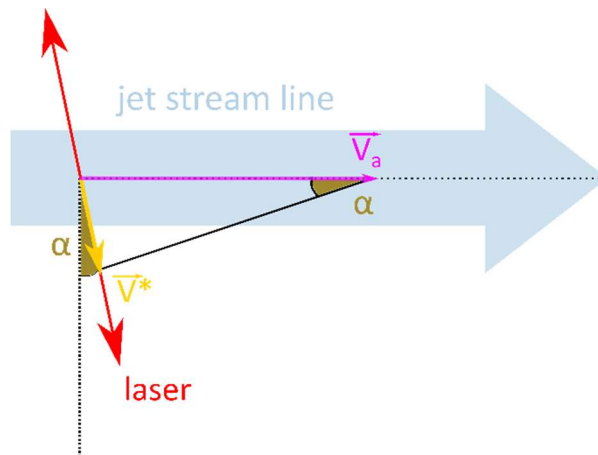


Figure 3.4: Representation of a misaligned laser beam with respect to the jet stream line

The angle (α) that is needed to obtain a line broadening of 0.01 cm^{-1} with the above calculated 500 m.s^{-1} velocity component (v^*) in the plane of the laser beam can be delivered by trigonometry and results in $\alpha = 24^\circ$.

$$\sin(\alpha) = \frac{v^*}{v_a} \quad 3.3$$

Such a huge misalignment is impossible to be carried out in the experimental setup, therefore this cause of line broadening can be ruled out.

A third possible source of line broadening could be the so-called transit broadening that corresponds to the broadening ($\tilde{\nu}_t$) of the line shape due to the effective lifetime of the molecule in the laser path.

$$\Delta\tilde{\nu}_t = 4 \frac{v_a}{d} \sqrt{2 \cdot \ln(2)} \quad 3.4$$

Where v_a – is the axial velocity component of the flow, numerically simulated at 1230 m.s^{-1} and d – corresponds to the laser beam diameter: $\emptyset d = 1 \text{ mm}$ in case of the CRDS in SMAUG. Nevertheless, this phenomenon could be excluded too, as $\Delta\tilde{\nu}_t = 0.00019 \text{ cm}^{-1}$, representing less than 2% of the occurring line broadening.

Finally, the fourth possible option is the presence of significant gas turbulences between the shear-layer and the static gas in the expansion chamber, as well as between the shear layer and the isentropic core. The possibility of turbulent convective motion causing Doppler shift is a well-known occurrence in the domain of astrophysics.²⁰ Despite this, the numerical simulations were carried out under the assumption of laminar flow. This assumption is, however, appropriate as the maximum value of the Reynolds number is below 2500, which is high, yet considered to be within a regime suitable for simulation as a laminar flow:

$$Re = \frac{\rho v_a d}{\mu} \quad 3.5$$

Where, ρ - volumetric mass density, v_a – axial velocity, d - the nozzle exit ($\emptyset d = 24 \text{ mm}$) and μ – the dynamic viscosity calculated according to equation (2.5).

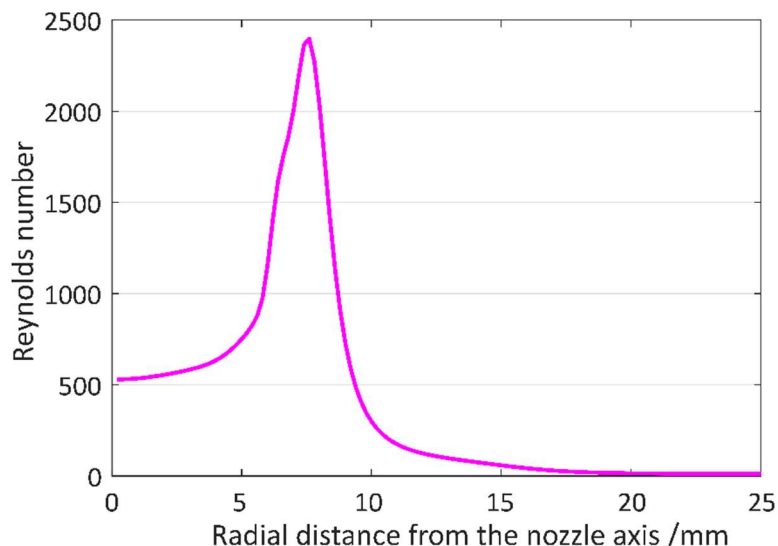


Figure 3.5: Evolution of the Reynolds number along the radial profile 20 mm downstream of the nozzle exit, in the plane of the jet where the CH₄ was recorded.

Nonetheless, to verify this hypothesis, some additional turbulent CFD simulations could be carried out, however, defining the correct turbulent conditions in the simulations is a rather difficult task.

None of these effects considered separately can explain the observed linewidth of 0.01 cm⁻¹. In fact, the origin of this broadening is twofold. One has to consider both a volume of gas at 39 K (FWHM 0.0066 cm⁻¹) and a radial expansion at 130 m.s⁻¹ (FWHM 0.0026 cm⁻¹), so that thermal and convective Doppler effects are cumulative, leading to a predicted FWHM linewidth of 0.0092 cm⁻¹, very close to the experimental value. The additional effects that were mentioned earlier, such as a small misalignment of the CRDS, inaccuracy in the simulated flow parameters and the transit broadening, could also contribute to the observed Doppler FWHM.

3.3 Simulated spectrum

In order to identify lines observed for the first time and not yet reported in empirical line lists, the exact experimental conditions must be first determined by matching a simulation of well-known methane lines to the experimental spectrum. In the course of the simulation of non-LTE spectra, the TheoReTS^{6,10,21} line list was used. This line list provides transitions calculated at 296 K up to the $J = 20$ rotational level, with a cut-off intensity (S_{cut}) of 10^{-32} cm.molecule⁻¹. To simulate both the isentropic core and the shear-layer contributions, the line intensities were manually adjusted to the experimental intensities using equation (3.6). Equation (3.6) converts the theoretical integrated cross section at 296 K into the corresponding non-LTE one (σ_{ij}^{nLTE}):

$$\sigma_{ij}^{nLTE}(T_{\text{rot}}, T_{\text{vib}}) = \sigma_{ij}(T_0) \frac{Q_0(T_0)}{Q_{\text{rot}}(T_{\text{rot}}) \times Q_{\text{vib}}(T_{\text{vib}})} \times \exp \left[\frac{E_i}{kT_0} - \frac{1}{k} \left(\frac{E_i^{\text{vib}}}{T_{\text{vib}}} + \frac{E_i^{\text{rot}}}{T_{\text{rot}}} \right) \right] \times \left[\frac{1 - \exp \left[- \left(\frac{E_f^{\text{vib}} - E_i^{\text{vib}}}{kT_{\text{vib}}} + \frac{E_f^{\text{rot}} - E_i^{\text{rot}}}{kT_{\text{rot}}} \right) \right]}{1 - \exp \left(-c_2 \frac{\tilde{\nu}_{ij}}{T_0} \right)} \right] \quad 3.6$$

Where $Q_0(T_0)$, $Q_{\text{rot}}(T_{\text{rot}})$ and $Q_{\text{vib}}(T_{\text{vib}})$ are the LTE, rotational and vibrational partition functions respectively. Similarly, T_0 , T_{rot} and T_{vib} are the standard and characteristic rotational and vibrational temperatures. E_i describes the lower energy level of the transition, decomposing into a vibrational and a rotational component E_i^{vib} and E_i^{rot} , respectively. Finally, E_f^{vib} and E_f^{rot} represent the two components of the final energy level of the transition and c_2 is the second radiation constant given by $c_2 = \frac{h.c}{k} = 1.4388$ cm.K.

The third term of the equation corresponds to the induced emission term and it was neglected throughout the simulations as its value corresponds to around 0.999 in our temperature conditions for a line centred at 6000 cm⁻¹.

Additionally, the contribution of the isotopologue ¹³CH₄ was considered using integrated absorption cross sections extracted from HITRAN.²² Only transitions departing from the ground state were considered for this isotopologue. Indeed, since its natural abundance is 1.1%, the intensity of the hot bands is too weak to contribute significantly to the experimental spectrum.

As was mentioned previously, due to low static pressure in the jet, there is no need to consider Lorentzian-type broadening. Thus, it was decided to consider a purely Gaussian line shape to simulate the spectrum, although this is not entirely accurate, due to the simultaneous presence of cold and hot gas layers in the line-of-sight, as mentioned above. The simulated absorption coefficient is therefore a sum of Gaussian functions ($g(\nu - \nu_0)$) which were constructed by using the non-LTE line intensities (σ_{ij}^{nLTE}) with the temperature-wise matching FWHM, 0.01 cm⁻¹ and 0.0215 cm⁻¹ for the isentropic core and the shear-layer, respectively. The corresponding densities (n_{IC} and n_{SL}) have been adjusted so as to best match the observed and simulated spectra. Once the correct temperature values and partition functions are established, the exact density values can be easily retrieved by a global adjustment of the calculated line intensities to the experimental spectrum.

Concerning the isotopologue ¹³CH₄, an LTE spectrum was simulated at the rotational temperature of the isentropic core and its intensity has been adjusted to the experimental one

by using an *ad hoc* multiplying factor β . Such factor is needed because the LTE partition function provided by HITRAN is not adapted to our non-LTE conditions. Thus, β contains both the density of the isotopologue $^{13}\text{CH}_4$ and the correction for the partition function.

$$\alpha_{sim}(v) = \sum_{IC} n_{IC} \cdot \sigma_{ij}^{nLTE} \cdot g(v - v_0) + \sum_{SL} n_{SL} \cdot \sigma_{ij}^{nLTE} \cdot g(v - v_0) + \sum_{^{13}\text{CH}_4} \beta \cdot \sigma_{ij}^{LTE}(v - v_0) \quad 3.7$$

The simulated spectrum (pink) is represented in panel (a) of figure (3.6). As explained previously, due to their saturation, the most intense absorption lines are absent from the observed spectrum while they are clearly visible in the simulated one. The axis of the absorption coefficient has been deliberately limited to $\alpha_{max} = 4 \times 10^{-6} \text{ cm}^{-1}$ to facilitate comparison. Below, panel (b) highlights the existence of two different flow regions and their very distinct line broadening characteristics, along with the appropriate simulation of each.

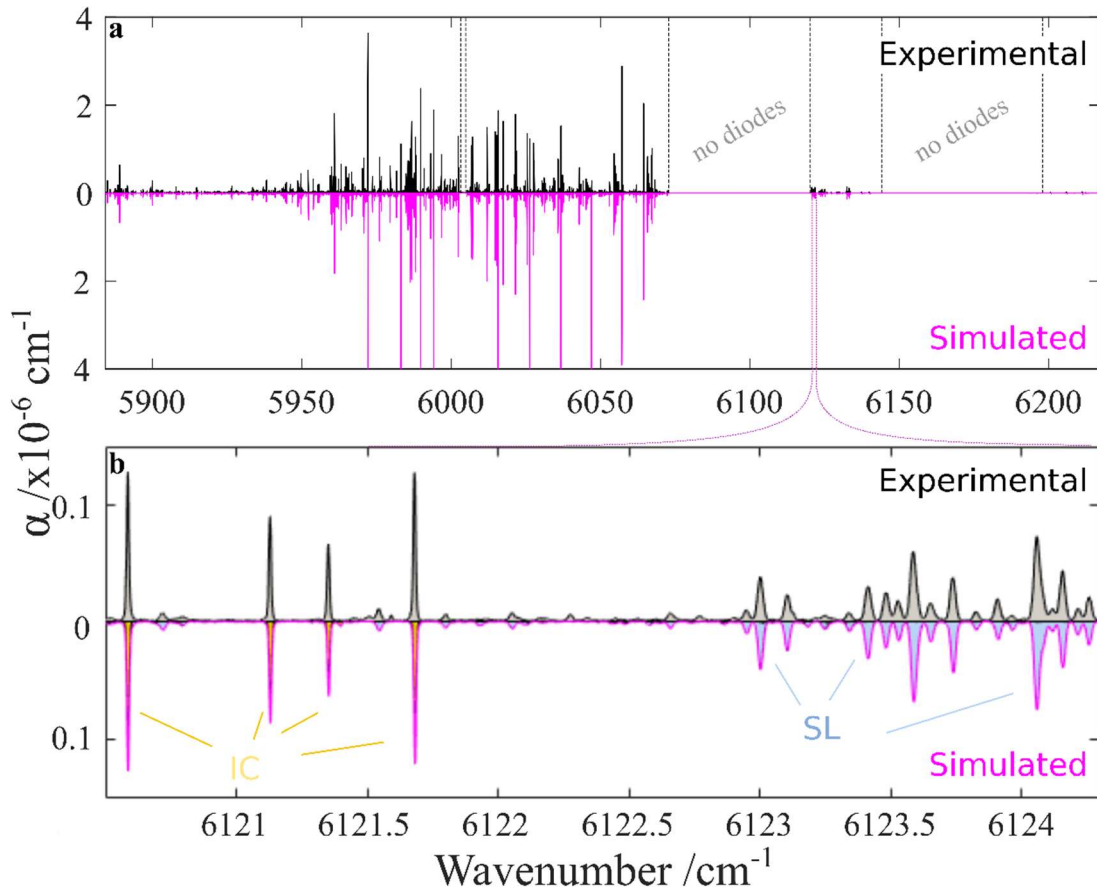


Figure 3.6: Experimental (black) vs simulated (pink) non-LTE hypersonic jet spectrum of methane. Panel (b): part of the spectrum showing the presence of the two distinct flow regions. The yellow lines correspond to the isentropic core (IC) meanwhile the blue ones simulate the contribution of the shear-layer (SL).

3.4 Temperature extraction

To obtain a good agreement between the experimental and simulated spectrum, all the temperatures, i.e. rotational and vibrational, of the different flow regions must be specified. The notion of vibrational temperature is ambiguous here since the vibrational population does not follow Boltzmann's distribution law. As recalled in chapter I, the population ratio between the excited vibrational level and the ground state can be associated with a vibrational temperature unique for each particular level. In principle, it is necessary to define as many vibrational temperatures as there are significantly populated vibrational energy levels.

Secondly, the rotational and non-LTE vibrational partition functions have to be determined. This is an iterative process, in which the rotational temperature (T_{rot}) is initially established and the corresponding rotational partition function ($Q_{rot}(T_{rot})$) is calculated using the Total Internal Partition Sum (TIPS)²³ codes, which were specially extended to high temperatures by Gamache and co-workers. This is followed by the determination of the vibrational temperatures ($T_{vib_{level}}^{flow\ region}$) that serve as the input data for the new TIPS code that differentiates all the vibrational levels and their different symmetries and calculates a non-LTE vibrational partition function ($\tilde{Q}_{vib}(T_{vib})$).

3.4.1 Rotational temperatures

Thankfully, the distribution of population over rotational energy levels follows Boltzmann's law²⁴ and therefore a single rotational temperature is sufficient to describe it. The rotational temperature has been determined from the relative intensities of the absorption lines belonging to a same vibrational band. This approach has the advantage of avoiding the explicit computation of the rotational partition function at this stage of the analysis. From a practical point of view, the ratio between two integrated absorption coefficients is equal to the ratio between two integrated absorption cross sections, so that equation (3.6) leads to:

$$\frac{\alpha^{R0}}{\alpha^{R1}} = \frac{\sigma_{R0}(T_{rot})}{\sigma_{R1}(T_{rot})} = \frac{\sigma_{R0}(T_0) \times \exp \left[\frac{E_{i_{R0}}}{kT_0} - \frac{1}{k} \left(\frac{E_{i_{R0}}^{rot}}{T_{rot}} \right) \right]}{\sigma_{R1}(T_0) \times \exp \left[\frac{E_{i_{R1}}}{kT_0} - \frac{1}{k} \left(\frac{E_{i_{R1}}^{rot}}{T_{rot}} \right) \right]} \quad 3.8$$

Using equation (3.8) for transitions departing from $J = 0, 1$ and 2 energy levels gives the rotational temperature of the isentropic core: $T_{rot}^{IC} = 39(5)$ K, while for transitions $J \geq 7$ the obtained rotational temperature of the shear-layer is: $T_{rot}^{SL} = 375(25)$ K, as demonstrated in figure (3.7). As already indicated above, the experimental system has an instrumental upper limit which saturates the lines that are too intense, in particular the low- J lines of the cold bands. For this reason, the ¹³CH₄ isotopologue was chosen to retrieve the rotational temperature of the isentropic core.

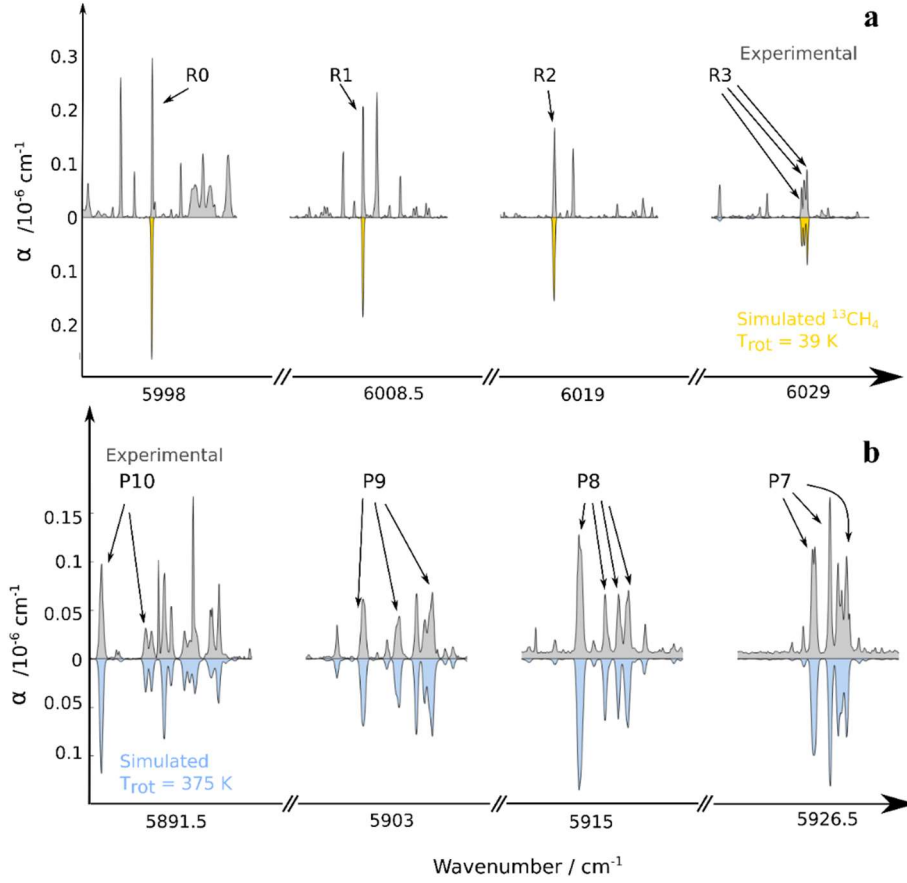


Figure 3.7: Determination of the rotational temperatures. Panel (a): observed spectrum and simulated ¹³CH₄ lines of low-*J* rotational levels used to obtain the rotational temperature of the isentropic core. Panel (b): observed spectrum and simulated ¹²CH₄ lines of higher-*J* rotational levels to extract the rotational temperature of the shear-layer.

3.4.2 Vibrational temperatures

For calculating the vibrational temperatures, the same strategy was continued as with the rotational temperatures, but this time rovibrational transitions starting from an excited level were compared to transitions issuing from the ground state. Applying equation (3.9) for a sufficient number of transitions is assumed to give a reliable vibrational temperature for each vibrational state (ν_i).

$$\frac{\alpha^{GS}}{\alpha^{\nu_i}} = \frac{\sigma(T_0)^{GS}}{\sigma(T_0)^{\nu_i}} \times \frac{\exp \left[c_2 \cdot E_i^{GS} \left(\frac{1}{T_0} - \frac{1}{T_{rot}} \right) \right]}{\exp \left[\frac{c_2 \cdot E_i^{\nu_i}}{T_0} - c_2 \cdot \left(\frac{E_{vib}^{\nu_i}}{T_{vib}} + \frac{E_{rot}^{\nu_i}}{T_{rot}} \right) \right]} \quad 3.9$$

This method works well with the vibrational states of the dyad (P_1 polyad) for which the theoretical line list is sufficiently accurate for direct identification and comparison between calculated and experimental fitted lines. In this way, the dyad polyad in the isentropic core can be described with two vibrational temperatures $T_{\nu_4}^{IC} = 877(100) \text{ K}$ and $T_{\nu_2}^{IC} = 334(21) \text{ K}$, reflecting a much stronger intra-polyad vibrational relaxation than the inter-polyad one. The population of the ν_2 state located at 1533 cm^{-1} partially empties on the first ν_4 state of the polyad located at 1310 cm^{-1} which does not or only slightly relaxes to the GS. These results agree well with the

observation by Bronnikov *et al.*²⁵ and Hilico *et al.*²⁶ It is interesting to note that this non-relaxation from one polyad to another leads to effective vibrational temperatures which can be much higher than the stagnation temperature, which of course contributes to increasing the intensity of the transitions which start from the first state of each polyad.

Contrarily, the shear layer can be described with temperatures $T_{v_4}^{SL} = 797(175)$ K and $T_{v_2}^{SL} = 730(166)$ K. This suggests that the different frictional – and maybe turbulent – processes in the shear-layer, resulting in a higher frequency of molecular collisions compared to the isentropic core, favour vibrational-rotation and vibrational-translation energy transfer between molecules.

To determine a preliminary vibrational temperature associated with the populations of the energy levels of the pentad (P_2 polyad), we looked first at the v_3 transitions identified by Foltynowicz *et al.*²⁷ None of them are observed in our spectrum although they correspond to low- J rotational transitions. Recall from chapter I, the pentad consists of 9 close sub-vibrational levels which facilitates an efficient intra-polyad relaxation. Therefore, the fact that none of the transitions observed by Foltynowicz *et al.* appear in our experimental spectrum sets a maximum vibrational temperature for the v_3 vibrational level at 500 K, as above this temperature the transitions would be detectable in our recorded spectrum.

In parallel, a small number of transitions of the $0030 \leftarrow 0000$ cold band involving the triacontad (P_6 polyad) is reported in the HITRAN database²². The knowledge of the precise position of the final vibrational energy level, in this case the $3v_3$, allows the prediction of precise calculated line positions starting from the pentad and ending on this particular upper energy level. These specific transitions were used to associate a vibrational temperature to the first two vibrational states of the pentad: $T_{2v_4(A1)}^{IC} = 1130(91)$ K and $T_{2v_4(F2)}^{IC} = 860(100)$ K.

Unfortunately, due to the lack of other reliable rovibrational transitions, it was not possible to experimentally determine the vibrational temperature of the other vibrational states of the pentad. It was therefore decided to consider a “local” Boltzmann distribution population within the vibrational energy levels forming the pentad. The population of the different energy levels, and their associated temperature, was thus extrapolated by considering the same intra-polyad relaxation as occurred between the $2v_4(A1)$ and $2v_4(F2)$ states. These assumed temperatures are used as input values for the calculation of the non-LTE vibrational partition function. As a remark, this extrapolation leads to $T_{v_3}^{IC} = 212$ K which is consistent with the limit of 500 K set for the v_3 vibrational level.

Figure (3.8) illustrates the different vibrational population probabilities under LTE conditions in the reservoir heated to 800 K (red) and under the actual non-LTE conditions in the hypersonic jet (blue). The boxes represent the population distribution probabilities along the J rotational levels for the different vibrational levels and their degenerate sublevels. The estimated population percentage is shown in the upper corners.

At 800 K, the population is distributed over more than 30 rotational levels, resulting in a lower percentage of population probabilities for each individual rotational level and therefore relatively weak absorption line intensities. For example, the highest populated rotational level

of the vibrational GS at LTE 800 K is $J_{max} = 7$, which corresponds to 5% of the population probability. In contrast, in case of the hypersonic jet, where the rotational temperature is equal to 39 K, the highest populated rotational level is $J_{max} = 2$, representing more than 20% of the population probability. Henceforth, the strong rotational relaxation in the hypersonic jet not only simplifies the rotational structure of the spectrum, but at the same time provides much more intense absorption lines.

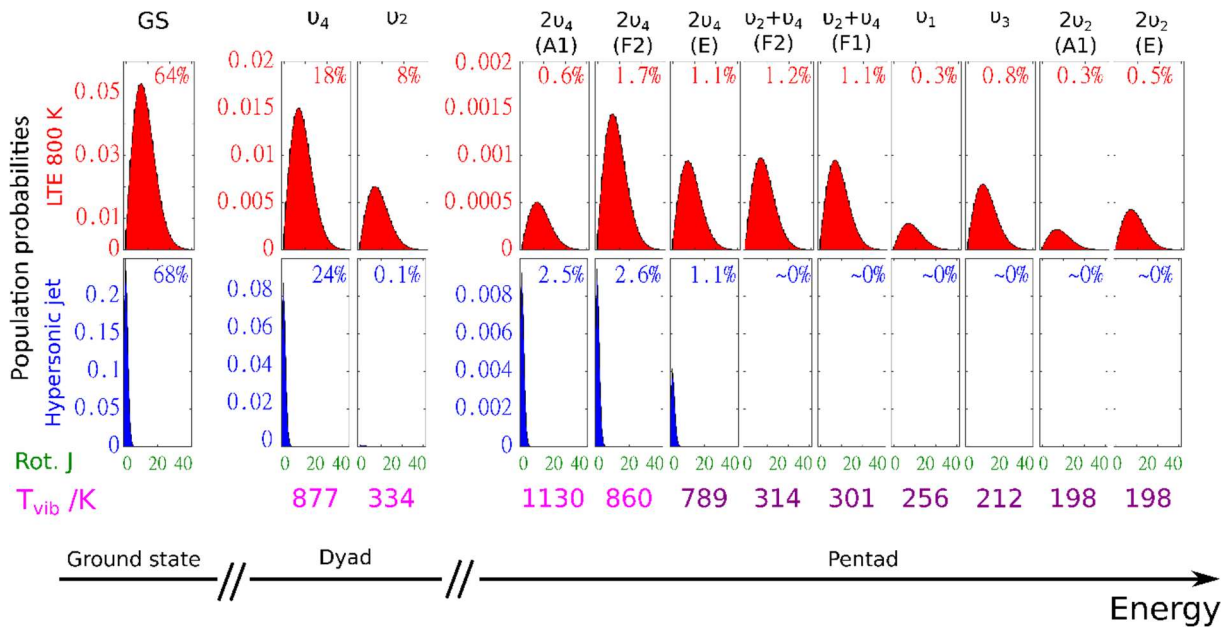


Figure 3.8: Comparing the vibrational and rotational population probabilities between LTE 800 K (red) and hypersonic jet (blue) conditions. The temperatures obtained experimentally (pink) or following hypothesis (purple) are written under each vibrational level.

Another equally important characteristic of the hypersonic jet highlighted in this work is the strong vibrational energy relaxation occurring within the vibrational energy levels of a polyad. This “intra-polyad” relaxation results in the transfer of population from the higher vibrational states towards the lower vibrational ones within the polyad. This phenomenon is represented in figure (3.8), in blue. Thus, the lower v_4 vibrational state of the dyad gathers 24% of the population probability; meanwhile its highest v_2 state basically lost all its population with the corresponding 0.1%. Comparatively, in LTE conditions this ratio is 18% to 8% respectively. Ultimately, looking at the population probability numbers of the pentad, the panels of the hypersonic jet (blue) highlight the severe difference between LTE and non-LTE cases. Considering $2v_4(A1)$, the lowest vibrational state of the polyad, its population probability is more than 4 times higher for the non-LTE hypersonic jet than it would be under LTE conditions. Similarly, on the next $2v_4(F2)$ vibrational level the population probability is 1.4 times greater for the hypersonic jet.

Figure 3.8 clearly shows that the populations of the methane polyads in the reservoir and in the supersonic jet remain almost identical, indicating very low amounts of energy relaxation between polyads. It is as if the population of each polyad moves to the lowest level of each polyad, that is to say, v_4 for the dyad, $2v_4(A1)$ for the pentad, etc. Concerning the inter-polyad relaxation it can be concluded that there is no significant relaxation between the polyads, which is in good agreement with the former observations of Bronnikov *et al.*²⁵

Finally, the temperatures obtained experimentally (pink) or following hypothesis (purple) are displayed in the figure (3.8) and listed in Table 3.1. Remark, the higher vibrational states starting from $4\nu_4(A_1)$ are all assigned with the rotational temperature, 39 K, throughout the calculation of the vibrational partition function.

Table 3.1: Calculated (pink) and extrapolated hypothetical (purple) vibrational temperatures

Polyad	Vib. level	Sym	s.w.	E_i / cm^{-1}	T_v / K
Ground state	0 0 0 0	A1	1	0	
Dyad	0 0 0 1	F2	3	1310.78	877
	0 1 0 0	E	2	1533.34	334
Pentad	0 0 0 2	A1	1	2587.00	1130
	0 0 0 2	F2	3	2614.14	860
	0 0 0 2	E	2	2624.73	789
	0 1 0 1	F2	3	2830.44	314
	0 1 0 1	F1	3	2846.07	301
	1 0 0 0	A1	1	2916.43	256
	0 0 1 0	F2	3	3019.42	212
	0 2 0 0	A1	1	3063.82	198
	0 2 0 0	E	2	3065.19	198
	0 0 0 3	F2	3	3870.50	1195
Octad	0 0 0 3	A1	1	3908.90	900
	0 0 0 3	F1	3	3920.40	838
	0 0 0 3	F2	3	3931.02	789
	0 1 0 2	E	2	4101.64	410
	0 1 0 2	F1	3	4128.92	382
	0 1 0 2	A1	1	4133.17	378
	0 1 0 2	F2	3	4142.77	369
	0 1 0 2	E	2	4151.29	362
	0 1 0 2	A2	1	4161.93	353
	1 0 0 1	F2	3	4223.55	311
	0 0 1 1	F2	3	4319.27	263
	0 0 1 1	E	2	4322.26	262
	0 0 1 1	F1	3	4322.56	262
	0 0 1 1	A1	1	4322.88	262
	0 2 0 1	F2	3	4349.05	252
	0 2 0 1	F1	3	4363.78	246
	0 2 0 1	F2	3	4379.05	241
	1 1 0 0	E	2	4435.17	224
	0 1 1 0	F1	3	4537.55	199
	0 1 1 0	F2	3	4543.86	199
	0 3 0 0	E	2	4592.46	188
	0 3 0 0	A2	1	4595.39	187
	0 3 0 0	A1	1	4595.67	187

The forthcoming figure (3.9) highlights the non-LTE effects through a simulation. In panel (a), the strong rotational and intra-polyad relaxation results in a series of intense P5 transitions starting for the ν_4 (dyad), whereas in LTE conditions they are much less intense. Moreover, according to this figure, the similar intensities of three cold band transitions simulated under both LTE and non-LTE conditions might be surprising. It is simply due to the fact that the ground state population probability is similar in both cases, as there is no significant vibrational relaxation towards the ground state in the hypersonic jet. Another example is given in panel (b). In this small spectral range, the simulated transitions starting from the GS are high- J rovibrational lines, while those starting from the $2\nu_4$ sub-states belonging to the pentad are low- J rovibrational lines. In this second example, the low- J rovibrational lines are magnified in the hypersonic jet, while the high- J rovibrational lines are almost eliminated. As depicted in Fig. 3.8, the rotational population of energy levels with $J > 7$ becomes insignificant.

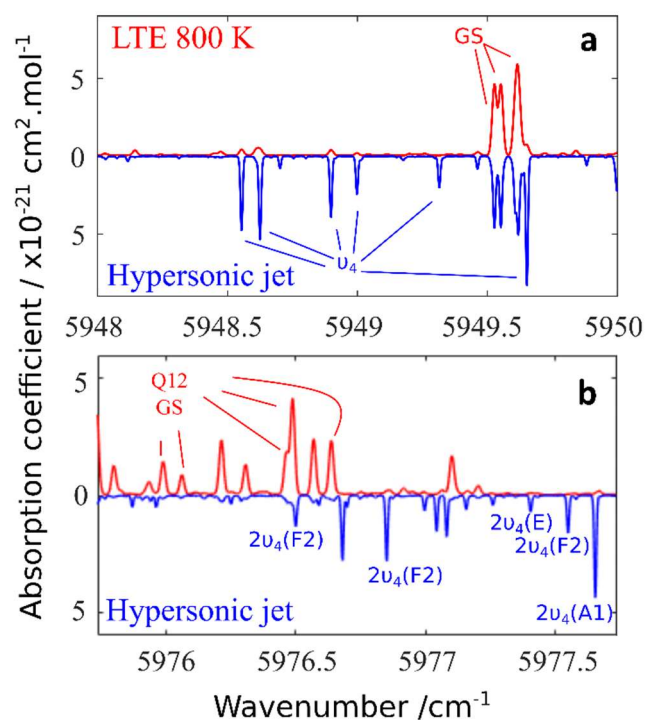


Figure 3.9: Simulated spectrum in LTE 800 K (red) and non-LTE hypersonic jet (blue) spectrum. The lower vibrational states are indicated. Panel (a) emphasizes the ν_4 transitions magnified in the hypersonic jet expansion. Panel (b) displays depopulated high- J rotational levels and the presence of intense lines issuing from the pentad.

3.5 Line identification

For vibrational states of polyads higher than the dyad, theoretical line-lists must be compared with experimental data to validate the upper energy levels of the calculated transitions. The line positions are hence much less accurate than those corresponding to the dyad. Importantly, the calculated *ab initio* line intensities are accurate to within a few percent²¹, which means that once the vibrational temperature is correctly determined, the simulated pattern of the spectrum will match the experimental spectrum in intensity, if not in wavenumber. A previous experimental investigation²⁷ confirmed that the uncertainty of the calculated line positions in the TheoReTS database is $\pm 1 \text{ cm}^{-1}$ at 9000 cm^{-1} , so that it should be possible to find pairs of experimental and simulated peaks with matching intensities within this given wavenumber uncertainty interval.

Following this strategy, we were able to detect in our experimental spectrum a transition starting from the lowest energy vibrational state of the octad. It could be correctly simulated with a vibrational temperature of $T_{3\nu_4(F2)}^{IC} = 1195(80) \text{ K}$ (see Table 3.24.2). This transition is shown in panel (b) of figure (3.10). Once again, in the figure, the pink line corresponds to the simulated non-LTE spectrum. The red, blue and green sticks mark the transitions starting from the $2\nu_4(A1)$, $2\nu_4(F2)$, and $3\nu_4(F2)$ states, respectively. Given the good agreement in intensity between the simulated spectrum and the experimental spectrum, line assignments can be made by matching simulated peaks to equally intense experimental peaks within the uncertainty of the simulated line position. This process results in a new set of hot methane transitions listed in table (3.2).

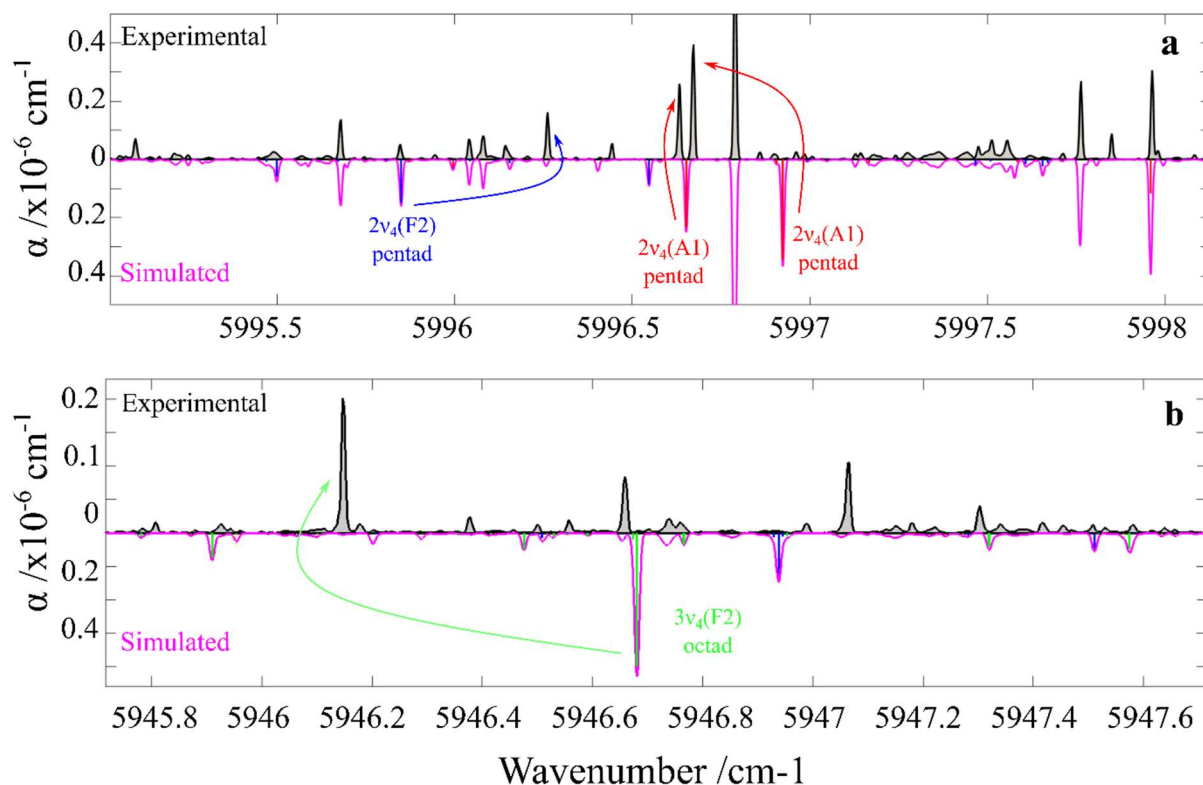


Figure 3.10: Representation of the line assignment process based on the intensity correspondence between observed and simulated lines in an interval of $\pm 1 \text{ cm}^{-1}$ around the simulated line. Panel (a): newly assigned lines issuing from the pentad polyad. Red and blue stick lines correspond to transitions starting from the 2ν₄(A1) and 2ν₄(F2) states of the pentad, respectively. Panel (b): newly assigned line starting from the 3ν₄(F2) state of the octad.

Altogether, 22 possible candidates were identified (see Table 3.2), including 15 transitions issuing from the 2ν₄(A1) lowest vibrational state of the pentad. Three transitions are starting from the next vibrational state of the pentad, 2ν₄(F2). Finally, 4 lines were spotted departing from the octad polyad: three corresponding to the lowest 3ν₄(F2) vibrational state and one to the 3ν₄(F1) vibrational state. All of the reported candidates correspond to low-*J* rovibrational transitions with $J_{\text{max}} = 4$.

Table 3.2: Newly assigned transitions issuing from the pentad and the octad.

$\nu(\text{obs})$ cm-1	$\nu(\text{calc})$ 1 cm-	$\nu(\text{obs-calc})$ cm-1	$S(\text{calc})$ cm/mol	E' cm-1	J'	C'	n'	P'	J''	C''	n''	P''	E'' cm-1	A s-1	vib''	vib'
5944.537	5944.474	0.0635	7.42E-28	2618	1F1	133	6	2F2	1	2	8562	0.436	0.022F2	0.002A1		
5944.677	5944.899	-0.2216	3.81E-28	2618	1E	85	6	2E	1	2	8563	0.335	0.022F2	0.002A1		
5965.059	5964.678	0.3803	2.48E-27	2649	3A1	92	6	3A2	1	2	8613	0.437	0.022F2	0.002A1		
5965.286	5965.204	0.0822	8.42E-28	2618	2E	142	6	2E	1	2	8583	0.448	0.022F2	0.002A1		
5965.323	5965.358	-0.0346	1.31E-27	2618	2F1	206	6	2F2	1	2	8583	0.464	0.022F2	0.002A1		
5965.713	5965.648	0.0645	7.09E-28	2597	1F2	123	6	1F1	1	2	8563	0.379	0.022F2	0.002A1		
5985.829	5985.883	-0.0544	1.10E-27	2597	2F2	217	6	1F1	1	2	8583	0.355	0.022F2	0.002A1		
5996.633	5996.652	-0.019	9.51E-28	2618	3E	197	6	2E	1	2	8615	0.365	0.022F2	0.002A1		
5996.672	5996.924	-0.2521	1.40E-27	2618	3F1	302	6	2F2	1	2	8615	0.358	0.022F2	0.002A1		
6008.554	6008.98	-0.4267	2.56E-27	2649	4A1	134	6	3A2	1	2	8658	0.357	0.022F2	0.002A1		
6021.146	6021.155	-0.008	2.74E-28	2587	1A2	52	6	0A1	1	2	8608	0.0853	0.0212F2	0.002A1		
6194.202	6194.202	0.0003	3.00E-30	2597	1F2	182	6	1F1	1	2	8792	0.00153	0.0121F2	0.002A1		
6195.231	6195.228	0.0025	6.00E-30	2587	1A2	69	6	0A1	1	2	8782	0.00211	1.301F2	0.002A1		
6205.575	6205.574	0.001	8.00E-30	2587	1A2	70	6	0A1	1	2	8793	0.00255	0.0121F2	0.002A1		
6211.603	6211.605	-0.0026	9.00E-30	2597	2F2	321	6	1F1	1	2	8809	0.00308	0.0121F2	0.002A1		
5961.318	5961.425	-0.1066	1.36E-27	2620	1A2	49	6	2A1	1	2	8581	0.486	0.022F2	0.002F2		
5970.308	5970.42	-0.1122	2.28E-27	2620	2A2	67	6	2A1	1	2	8590	0.492	0.022E	0.002F2		
6215.88	6215.879	0.0008	4.70E-30	2649	3F1	460	6	2F2	3	2	8865	0.00151	0.121E	0.002F2		
5909.922	5910.54	-0.6174	2.61E-30	3928	2A2	93	7	3A1	1	3	9839	0.319	0.023E	0.003F2		
5946.148	5946.681	-0.5328	2.28E-30	3872	1A1	55	7	1A2	1	3	9818	0.356	0.023F1	0.003F2		
5960.495	5961.738	-1.2431	3.39E-30	3872	2A1	105	7	1A2	1	3	9833	0.32	0.023F2	0.003F2		
5937.872	5938.331	-0.4587	3.23E-32	4048	4F1	648	7	4F2	10	3	9987	0.00661	0.023F2	0.003F1		

3.6 Conclusion

Through the analysis of the recorded CH₄ non-LTE spectrum, the rotational, intra-polyad and inter-polyad relaxations have been characterised quantitatively. The rotation is well relaxed according to a Boltzmann distribution characterised by a temperature of 39 K. The extracted vibrational temperatures reflect an efficient intra-polyad relaxation that depopulates the high vibrational levels of the polyads, whereas the relaxation between polyads is considerably weaker, which leads to an accumulation of the vibrational population on the first state of each polyad ($\nu_4(A1)$, $2\nu_4(A1)$, $3\nu_4(F2)$, etc.).

At the same time, it is clearly demonstrated that the population of the symmetrically degenerated vibrational levels (e.g. $2\nu_4(A1)$ and $2\nu_4(F2)$ for the pentad) should be described with different vibrational temperatures. They must therefore be distinguished as if they were completely independent vibrational levels.

Based on the determined temperature values, the corresponding rotational and non-LTE vibrational functions could be delivered by the interface NLTE_TIPS_CH4_2021 provided by Gamache *et al.* Knowledge of the partition functions of methane in the isentropic core and shear-layers makes it possible to retrieve the molecular density of each of these flow regions. Thus, it appears that the main contribution comes from the isentropic core with a molecular density of $n_{ic} = 4.95 \times 10^{13}$ molec.cm⁻³, confirming the good sensitivity of the SMAUG apparatus as well as its ability to diagnose hypersonic flows. The shear-layers are effectively characterized by a lower average density of $n_{sl} = 0.887 \times 10^{13}$ molec.cm⁻³, leading to a non-negligible hot gas contribution to the absorption spectrum. A planar de Laval nozzle is currently being designed to increase the absorption path length through the cold isentropic core and maximise the cold gas contribution.

Additionally, many lines recorded in the non-LTE spectrum have yet to be assigned. They most likely belong to hot band transitions starting from vibrational energy levels of the pentad and octad polyads. Future work will consist of systematically assigning them to refine the TheoReTS line list.

In conclusion, SMAUG can produce vibrationally hot and rotationally cold high-resolution infrared spectra of methane. The obtained vibrational temperatures, some above the reservoir temperature, underline the vital features of the experimental setup. Namely, that significant rotational and intra-polyad relaxation ensure the detection of lines corresponding to transitions issuing from pentad and octad by boosting the population in the base vibrations of these polyads. At the same time, these relaxations eliminate a tremendous number of spectral lines from the investigated spectrum and permit the precise analysis of those remaining.

References

- (1) Hoyt, J. K. The Cyclopaedia of Practical Quotationos, English and Latin: With an Appendix Containing Proverbs from the Latin and Modern Foreign Languages ...; Funk & Wagnalls, 1889.
- (2) Campargue, A.; Leshchishina, O.; Wang, L.; Mondelain, D.; Kass, S.; Nikitin, A. V. Refinements of the WKMC Empirical Line Lists (5852–7919cm⁻¹) for Methane between 80K and 296K. *Journal of Quantitative Spectroscopy and Radiative Transfer* **2012**, 113 (15), 1855–1873. <https://doi.org/10.1016/j.jqsrt.2012.05.011>.
- (3) Wang, L.; Mondelain, D.; Kass, S.; Campargue, A. The Absorption Spectrum of Methane at 80 and 294K in the Icosad (6717–7589cm⁻¹): Improved Empirical Line Lists, Isotopologue Identification and Temperature Dependence. *Journal of Quantitative Spectroscopy and Radiative Transfer* **2012**, 113 (1), 47–57. <https://doi.org/10.1016/j.jqsrt.2011.09.003>.
- (4) Le, W.; Kass, S.; Campargue, A. Temperature Dependence of the Absorption Spectrum of CH₄ by High Resolution Spectroscopy at 81 K: (I) The Region of the 2v₃ Band at 1.66 μm. *Journal of Quantitative Spectroscopy and Radiative Transfer* **2010**, 111 (9), 1130–1140. <https://doi.org/10.1016/j.jqsrt.2009.10.019>.
- (5) Campargue, A.; Wang, L.; Kass, S.; Mašát, M.; Votava, O. Temperature Dependence of the Absorption Spectrum of CH₄ by High Resolution Spectroscopy at 81K: (II) The Icosad Region (1.49–1.30μm). *Journal of Quantitative Spectroscopy and Radiative Transfer* **2010**, 111 (9), 1141–1151. <https://doi.org/10.1016/j.jqsrt.2009.11.025>.
- (6) Rey, M.; Nikitin, A. V.; Bézard, B.; Rannou, P.; Coustenis, A.; Tyuterev, V. G. New Accurate Theoretical Line Lists of ¹²CH₄ and ¹³CH₄ in the 0–13400 cm⁻¹ Range: Application to the Modeling of Methane Absorption in Titan's Atmosphere. *Icarus* **2018**, 303, 114–130. <https://doi.org/10.1016/j.icarus.2017.12.045>.
- (7) Coustenis, A.; Achterberg, R. K.; Conrath, B. J.; Jennings, D. E.; Marten, A.; Gautier, D.; Nixon, C. A.; Flasar, F. M.; Teanby, N. A.; Bézard, B.; Samuelson, R. E.; Carlson, R. C.; Lellouch, E.; Bjoraker, G. L.; Romani, P. N.; Taylor, F. W.; Irwin, P. G. J.; Fouchet, T.; Hubert, A.; Orton, G. S.; Kunde, V. G.; Vinatier, S.; Mondellini, J.; Abbas, M. M.; Courtin, R. The Composition of Titan's Stratosphere from Cassini/CIRS Mid-Infrared Spectra. *Icarus* **2007**, 189 (1), 35–62. <https://doi.org/10.1016/j.icarus.2006.12.022>.
- (8) Bailey, J.; Ahlsved, L.; Meadows, V. S. The Near-IR Spectrum of Titan Modeled with an Improved Methane Line List. *Icarus* **2011**, 213 (1), 218–232. <https://doi.org/10.1016/j.icarus.2011.02.009>.
- (9) Nikitin, A. V.; Boudon, V.; Wenger, Ch.; Albert, S.; Brown, L. R.; Bauerecker, S.; Quack, M. High Resolution Spectroscopy and the First Global Analysis of the Tetradecad Region of Methane ¹²CH₄. *Phys. Chem. Chem. Phys.* **2013**, 15 (25), 10071. <https://doi.org/10.1039/c3cp50799h>.
- (10) Rey, M.; Nikitin, A. V.; Babikov, Y. L.; Tyuterev, V. G. TheoReTS – An Information System for Theoretical Spectra Based on Variational Predictions from Molecular Potential Energy and

Dipole Moment Surfaces. *Journal of Molecular Spectroscopy* **2016**, 327, 138–158. <https://doi.org/10.1016/j.jms.2016.04.006>.

(11) Rey, M.; Nikitin, A. V.; Tyuterev, V. G. Theoretical hot methane line lists up to $t = 2000$ K for astrophysical applications. *ApJ* **2014**, 789 (1), 2. <https://doi.org/10.1088/0004-637X/789/1/2>.

(12) Cassam-Chenaï, P.; Rousseau, G.; Ilmane, A.; Bouret, Y.; Rey, M. Application of Quasi-Degenerate Perturbation Theory to the Calculation of Rotational Energy Levels of Methane Vibrational Polyads. *The Journal of Chemical Physics* **2015**, 143 (3), 034107. <https://doi.org/10.1063/1.4926471>.

(13) Kass, S.; Campargue, A. Cavity Ring down Spectroscopy with 5×10^{-13} cm⁻¹ Sensitivity. *J. Chem. Phys.* **2012**, 137 (23), 234201. <https://doi.org/10.1063/1.4769974>.

(14) Ghysels, M.; Vasilchenko, S.; Mondelain, D.; Béguier, S.; Kass, S.; Campargue, A. Laser Absorption Spectroscopy of Methane at 1000 K near 1.7 μ m: A Validation Test of the Spectroscopic Databases. *Journal of Quantitative Spectroscopy and Radiative Transfer* **2018**, 215, 59–70. <https://doi.org/10.1016/j.jqsrt.2018.04.032>.

(15) Yurchenko, S. N.; Tennyson, J. ExoMol Line Lists – IV. The Rotation–Vibration Spectrum of Methane up to 1500 K. *Monthly Notices of the Royal Astronomical Society* **2014**, 440 (2), 1649–1661. <https://doi.org/10.1093/mnras/stu326>.

(16) Tennyson, J.; Yurchenko, S. N.; Al-Refaie, A. F.; Barton, E. J.; Chubb, K. L.; Coles, P. A.; Diamantopoulou, S.; Gorman, M. N.; Hill, C.; Lam, A. Z.; Lodi, L.; McKemmish, L. K.; Na, Y.; Owens, A.; Polyansky, O. L.; Rivlin, T.; Sousa-Silva, C.; Underwood, D. S.; Yachmenev, A.; Zak, E. The ExoMol Database: Molecular Line Lists for Exoplanet and Other Hot Atmospheres. *Journal of Molecular Spectroscopy* **2016**, 327, 73–94. <https://doi.org/10.1016/j.jms.2016.05.002>.

(17) Rothman, L. S.; Gordon, I. E.; Barber, R. J.; Dothe, H.; Gamache, R. R.; Goldman, A.; Perevalov, V. I.; Tashkun, S. A.; Tennyson, J. HITEMP, the High-Temperature Molecular Spectroscopic Database. *Journal of Quantitative Spectroscopy and Radiative Transfer* **2010**, 111 (15), 2139–2150. <https://doi.org/10.1016/j.jqsrt.2010.05.001>.

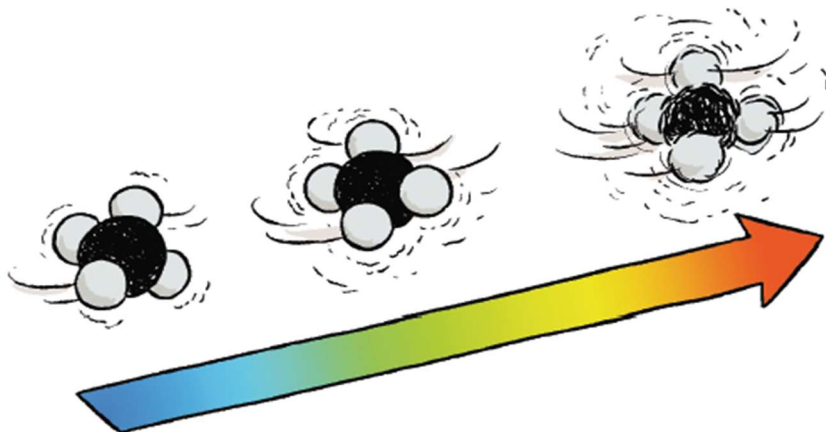
(18) Jacquinet-Husson, N.; Armante, R.; Scott, N. A.; Chédin, A.; Crépeau, L.; Boutammine, C.; Bouhdaoui, A.; Crevoisier, C.; Capelle, V.; Boone, C.; Poulet-Crovisier, N.; Barbe, A.; Chris Benner, D.; Boudon, V.; Brown, L. R.; Buldyreva, J.; Campargue, A.; Coudert, L. H.; Devi, V. M.; Down, M. J.; Drouin, B. J.; Fayt, A.; Fittschen, C.; Flaud, J.-M.; Gamache, R. R.; Harrison, J. J.; Hill, C.; Hodnebrog, Ø.; Hu, S.-M.; Jacquemart, D.; Jolly, A.; Jiménez, E.; Lavrentieva, N. N.; Liu, A.-W.; Lodi, L.; Lyulin, O. M.; Massie, S. T.; Mikhailenko, S.; Müller, H. S. P.; Naumenko, O. V.; Nikitin, A.; Nielsen, C. J.; Orphal, J.; Perevalov, V. I.; Perrin, A.; Polovtseva, E.; Predoi-Cross, A.; Rotger, M.; Ruth, A. A.; Yu, S. S.; Sung, K.; Tashkun, S. A.; Tennyson, J.; Tyuterev, V. G.; Vander Auwera, J.; Voronin, B. A.; Makie, A. The 2015 Edition of the GEISA Spectroscopic Database. *Journal of Molecular Spectroscopy* **2016**, 327, 31–72. <https://doi.org/10.1016/j.jms.2016.06.007>.

- (19) Ba, Y. A.; Wenger, C.; Surleau, R.; Boudon, V.; Rotger, M.; Daumont, L.; Bonhommeau, D. A.; Tyuterev, V. G.; Dubernet, M.-L. MeCaSDa and ECaSDa: Methane and Ethene Calculated Spectroscopic Databases for the Virtual Atomic and Molecular Data Centre. *Journal of Quantitative Spectroscopy and Radiative Transfer* **2013**, 130, 62–68. <https://doi.org/10.1016/j.jqsrt.2013.05.001>.
- (20) Löhner-Böttcher, J.; Schmidt, W.; Schlichenmaier, R.; Steinmetz, T.; Holzwarth, R. Convective Blueshifts in the Solar Atmosphere - III. High-Accuracy Observations of Spectral Lines in the Visible. *A&A* **2019**, 624, A57. <https://doi.org/10.1051/0004-6361/201834925>.
- (21) Rey, M.; Nikitin, A. V.; Tyuterev, V. G. Accurate Theoretical Methane Line Lists in the Infrared up to 3000 K and Quasi-Continuum Absorption/Emission Modeling for Astrophysical Applications. *ApJ* **2017**, 847 (2), 105. <https://doi.org/10.3847/1538-4357/aa8909>.
- (22) Rothman, L. S.; Gordon, I. E.; Babikov, Y.; Barbe, A.; Chris Benner, D.; Bernath, P. F.; Birk, M.; Bizzocchi, L.; Boudon, V.; Brown, L. R.; Campargue, A.; Chance, K.; Cohen, E. A.; Coudert, L. H.; Devi, V. M.; Drouin, B. J.; Fayt, A.; Flaud, J.-M.; Gamache, R. R.; Harrison, J. J.; Hartmann, J.-M.; Hill, C.; Hodges, J. T.; Jacquemart, D.; Jolly, A.; Lamouroux, J.; Le Roy, R. J.; Li, G.; Long, D. A.; Lyulin, O. M.; Mackie, C. J.; Massie, S. T.; Mikhailenko, S.; Müller, H. S. P.; Naumenko, O. V.; Nikitin, A. V.; Orphal, J.; Perevalov, V.; Perrin, A.; Polovtseva, E. R.; Richard, C.; Smith, M. A. H.; Starikova, E.; Sung, K.; Tashkun, S.; Tennyson, J.; Toon, G. C.; Tyuterev, V. G.; Wagner, G. The HITRAN2012 Molecular Spectroscopic Database. *Journal of Quantitative Spectroscopy and Radiative Transfer* **2013**, 130, 4–50. <https://doi.org/10.1016/j.jqsrt.2013.07.002>.
- (23) Laraia, A. L.; Gamache, R. R.; Lamouroux, J.; Gordon, I. E.; Rothman, L. S. Total Internal Partition Sums to Support Planetary Remote Sensing. *Icarus* **2011**, 215 (1), 391–400. <https://doi.org/10.1016/j.icarus.2011.06.004>.
- (24) López-Puertas, M.; López-Valverde, M. A.; Taylor, F. W. Studies of Solar Heating by CO₂ in the Upper Atmosphere Using a Non-LTE Model and Satellite Data. *Journal of the Atmospheric Sciences* **1990**, 47 (7), 809–822. [https://doi.org/10.1175/1520-0469\(1990\)047<0809:SOSHBC>2.0.CO;2](https://doi.org/10.1175/1520-0469(1990)047<0809:SOSHBC>2.0.CO;2).
- (25) Bronnikov, D. K.; Kalinin, D. V.; Rusanov, V. D.; Filimonov, YU. G.; Selivanov, YU. G.; Hilico, J. C. Spectroscopy and non-equilibrium distribution of vibrationally excited methane in a supersonic jet. *Journal of Quantitative Spectroscopy and Radiative Transfer* **1998**, 60 (6), 1053–1068. [https://doi.org/10.1016/S0022-4073\(97\)00210-0](https://doi.org/10.1016/S0022-4073(97)00210-0).
- (26) Hilico, J. C.; Baronov, G. S.; Bronnikov, D. K.; Gavrikov, S. A.; Nikolaev, I. I.; Rusanov, V. D.; Filimonov, Y. G. High-Resolution Spectroscopy of (Pentad-Dyad) and (Octad-Pentad) Hot Bands of Methane in a Supersonic Jet. *Journal of Molecular Spectroscopy* **1993**, 161 (2), 435–444. <https://doi.org/10.1006/jmsp.1993.1249>.
- (27) Foltynowicz, A.; Rutkowski, L.; Silander, I.; Johansson, A. C.; Silva de Oliveira, V.; Axner, O.; Soboń, G.; Martynkien, T.; Mergo, P.; Lehmann, K. K. Measurement and Assignment of Double-Resonance Transitions to the 8900–9100 cm⁻¹ Levels of Methane. *Phys. Rev. A* **2021**, 103 (2), 022810. <https://doi.org/10.1103/PhysRevA.103.022810>.

Post-shock spectroscopy

“Non progredi est regredi.”[§]

EN EFFET, LES MOLÉCULES NE SONT PAS INERTES : PLUS LA TEMPÉRATURE MONTE, PLUS ELLES VIBRENT ET TOURNENT SUR ELLES-MÊMES.



AUTANT DIRE QUE, DANS CETTE ZONE À PLUS DE 2 000 °C, C'EST TRÈS AGITÉ. LES ROTATIONS DONNENT UNE VISION FLOUE DE CE QU'IL SE PASSE.

[§] To not go forward is to go backward.¹

Contents

4.1 Status report.....	127
4.2 Normal shock waves	128
4.2.1 Hugoniot equation.....	130
4.2.2 Experimental flow field for post-shock spectroscopy.....	131
4.3 Experimental setup	132
4.4 CFD simulations and flow field analysis of the shock layer.....	134
4.5 Experimental characterisation of the shock	137
4.5.1 Location of the shock front	137
4.5.2 Evolution of the rotational and vibrational temperatures trough the shock	138
4.6 Methane post-shock spectroscopy	143
References	146

4.1 Status report

The non-LTE results presented in chapter III reveal valuable information about hot bands involving the lowest vibrational states of the first polyads of methane located in the $\sim 1300 - 4000 \text{ cm}^{-1}$ range and the vibrational energy states of the upper polyads in the $\sim 8500 - 10000 \text{ cm}^{-1}$ range. The accurate positions of these upper energy levels are essential for refining the potential energy surface on which *ab initio* variational theoretical models are based, and therefore to improve the precision of calculated line lists.

However, due to a lack of population on the highest vibrational states within each polyad, the non-LTE approach cannot provide insight into the hot band transitions originating from these states. Furthermore, while the simplified rotational structure is a very convenient approach to accessing precise line positions and facilitating their identification, it is clear that non-LTE conditions eliminate a huge number of transitions from the spectrum, which can be perceived as a loss of information.

An original experimental approach has been developed to access these missing transitions. The so-called post-shock spectroscopy is described in the following chapter.

4.2 Normal shock waves

Probing hot gases in the temperature range of 1500 K is challenging due to the sensitive optical elements of the cavity, mainly the two high-reflectivity mirrors. In the HES the wall of the porous graphite rod is heated up to 2000 K, which excludes the possibility of mounting the optical elements onto its walls, as they would melt immediately. Furthermore, these temperature values are accompanied by significant mechanical stress and could give place to undesired leaks. Therefore, the goal was to create a stationary shockwave in the middle of the expansion chamber where a cavity could be built around it.

In chapter II, it has been already stated that in a hypersonic flow, the fluid particles propagate faster than sound waves and for this reason they have no notion of any obstacle in front of them. Consequently, when the particles hit an unexpected body and reflect back from it, they merge with the following incident particles and a compression front develops in the flow field.² Even though the thickness of this detached shock wave is only a few molecular mean free path-lengths^{3–5}, the flow undergoes abrupt changes as it passes through. Specifically, the hypersonic flow suddenly becomes subsonic and the narrow shock region is characterised with pronounced pressure, temperature and density gradients, meanwhile the transport of momentum and energy is significant.

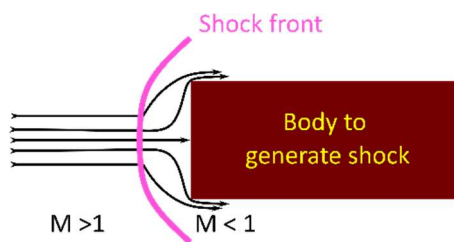


Figure 4.1: Occurrence of normal shock and the representation of the shock front

It is essential to understand that upstream of the shock front, the flow has no information on the presence of the shock, while downstream of the front, in the so-called shock layer, the flow becomes subsonic so that the streamlines adjust to the presence of the body. This shock wave is established once the first particles hit the body and then remains steady as long as the upstream flow conditions remain stable.

The passage of the gas through a shock wave is considered adiabatic because heat is neither given nor removed from the flow. On the other hand, the crossing of this non-equilibrium region should not be an isentropic process. Indeed, inside the shock, complex processes can occur (molecular dissociation, ionization, chemical reactivity, *etc*). Moreover, the large change in flow properties over a very small distance is responsible for an intense viscous stress and heat transfer causing irreversibility on the system.

In chapter II, the characteristic Knudsen number was derived validating the continuum-flow hypothesis. The properties of the flow variables can then be modelled downstream of the shock wave by considering the flow as continuous. However, to take into account the very strong gradients which characterize the thermodynamic variables through the shock wave, it is convenient to assimilate the shock wave to a thin spatial region of discontinuity through which the flow parameters change instantaneously from the upstream state, where there is no

prediction of the upcoming front, into the downstream state where all the changes have already occurred.

To determinate the exact flow properties downstream of the shock, similar conservation equations have to be used as the ones describing the flow field within a hypersonic flow. The continuity of mass:

$$\rho_1 v_1 = \rho_2 v_2 \quad 4.1$$

as well as the conservation of the momentum:

$$p_1 + \rho_1 v_1^2 = p_2 + \rho_2 v_2^2 \quad 4.2$$

and the energy under adiabatic circumstances:

$$h_1 + \frac{1}{2} v_1^2 = h_2 + \frac{1}{2} v_2^2 \quad 4.3$$

apply to the gas as it traverses the shock.

Assuming that the flow field could be considered as a continuum and, furthermore, as an ideal gas, the following two equations can be written:

$$\frac{p}{\rho} = rT \quad 4.4$$

representing the equation of state and at the same time, the enthalpy can be given as:

$$h = c_p T + \text{const} \quad 4.5$$

Similarly to the Rayleigh formula¹ used through the Pitot probe measurements in chapter II, the total pressure ratio upstream (p_{01}) and downstream (p_{02}) of the shock can be described as a function of the Mach number (M_1) upstream from the shock²:

$$\frac{p_{02}}{p_{01}} = \left(1 + \frac{2\gamma}{\gamma+1} (M_1^2 - 1) \right)^{-\frac{1}{\gamma-1}} \left(\frac{(\gamma+1)M_1^2}{(\gamma-1)M_1^2 + 2} \right)^{\frac{\gamma}{\gamma-1}} \quad 4.6$$

And consequently, the ratio between the static pressures downstream (p_2) and upstream (p_1) from the shock can be delivered:

$$\frac{p_2}{p_1} = 1 + \frac{2\gamma}{\gamma+1} (M_1^2 - 1) \quad 4.7$$

This ratio suggests that the static pressure always increases through the shock, as the Mach number (M_1) upstream of the shock is larger than unity. Following this path, the static temperature ratio downstream (T_2) to upstream (T_1) from the shock front can also be written as a function of the upstream Mach number:

$$\frac{T_2}{T_1} = 1 + \frac{2(\gamma-1)}{(\gamma+1)^2} \frac{\gamma M_1^2 + 1}{M_1^2} (M_1^2 - 1) \quad 4.8$$

indicating that the static temperature downstream of the shock is always greater than the upstream temperature.

Remark, the total temperature does not change across the shock wave as the process is adiabatic ($T_{01} = T_{02} = \text{const.}$).

Finally, the evolution of the density can be described with equation (4.9):

$$\frac{\rho_2}{\rho_1} = \frac{(\gamma + 1)M_1^2}{(\gamma - 1)M_1^2 + 2} \quad 4.9$$

once again, pointing out that the gas is denser downstream (ρ_2) of the shock wave than it was upstream (ρ_1) as $\gamma > 1$ and $M_1 > 1$.

4.2.1 Hugoniot equation

Once it is understood that the static pressure value rises across the shock wave, a different view of the shock can be introduced. In fact, it can be regarded as a “thermodynamic device” which performs compression work on gas and therefore the change in flow properties can be provided by exclusively thermodynamic variables excluding any reference to the Mach number. Taking equation (4.1) describing the continuity of the mass, it can be written:

$$v_2 = v_1 \left(\frac{\rho_1}{\rho_2} \right) \quad 4.10$$

and substituting equation (4.10) into momentum conservation equation (4.2) it can be solved to:

$$v_1^2 = \frac{p_2 - p_1}{\rho_2 - \rho_1} \left(\frac{\rho_2}{\rho_1} \right) \quad 4.11$$

The same can be carried out regarding:

$$v_2^2 = \frac{p_2 - p_1}{\rho_2 - \rho_1} \left(\frac{\rho_1}{\rho_2} \right) \quad 4.12$$

Next, the energy conservation through the shock can be described as:

$$e_1 + \frac{p_1}{\rho_1} + \frac{v_1^2}{2} = e_2 + \frac{p_2}{\rho_2} + \frac{v_2^2}{2} \quad 4.13$$

Where e is the energy per unit volume and the values of v_1^2 and v_2^2 can be substituted by the expression delivered in equation (4.11) and (4.12). The result is:

$$e_2 - e_1 = \frac{p_1 + p_2}{2} \left(\frac{1}{\rho_1} - \frac{1}{\rho_2} \right) \quad 4.14$$

which can be further developed if the volumetric mass values (ρ_1 and ρ_2) are replaced with the specific volumes, V_1 and V_2 respectively:

$$e_2 - e_1 = \frac{p_1 + p_2}{2} (V_1 - V_2) \quad 4.15$$

Equation (4.15) is called the Hugoniot equation² and it is established independently of the nature of the gas considered (i.e. perfect gas, real gas or chemically reacting gas). At the same time, $\frac{p_1 + p_2}{2}$ can be considered as a sort of mean pressure across the shock, therefore the change

in the energy per unit volume can be regarded as the product of the mean pressure across the shock and the change in the specific volumes (V) across the shock.

4.2.2 Experimental flow field for post-shock spectroscopy

Our goal is to create a detached stationary shock wave to probe the gas in the downstream high temperature shock layer. The role of the shock wave is to convert the kinetic energy of the gas back into enthalpy.

Substituting equation (4.5) into (4.3) and assuming that in the reservoir the gas is static ($v_{res}=0$) the Saint-Venant equation can be written as:

$$c_p T_0 = c_p T + \frac{1}{2} v^2 \quad 4.16$$

In other words, the left side of equation (4.16) represents the energy initially given to the system, throughout the HES heating system in our case. On the right-side, the distribution of this energy is represented through an adiabatic expansion. Specifically, it could be stored into thermal energy ($c_p T$) or eventually it could be converted into kinetic energy ($\frac{1}{2} v^2$). All along chapters II and III, the principle was to accelerate the gas ($v \rightarrow v_{max}$), to convert its initial total energy into purely kinetic, in order to brusquely lower its temperature ($T \rightarrow 0$) and to create a strong non-LTE condition.

Conversely, here the objective is to stop the gas ($v \rightarrow 0$) to increase its temperature ($T \rightarrow T_0$). Theoretically, a temperature as high as the initial reservoir temperature could be reached by simply stopping the gas. However, in practice, this situation is only true for the particles hitting the “shock wave generator body” perpendicularly, that is to say the ones precisely located on the nozzle axis. As for the rest of the molecules, they are slowed down but follow another streamline which bypasses the obstacle, without being completely stopped. A certain quantity of their kinetic energy is therefore maintained and their corresponding thermal energy and static temperature remain below the stagnation conditions.

4.3 Experimental setup

Practically speaking, the hypersonic jet created by the Laval nozzle impacts an obstacle inserted perpendicularly to its axis. A detached shock wave forms in front of the obstacle, thus decelerating the flow to subsonic speed and heating the gas in the shock layer between the shock and the physical obstacle. This process has already been used to create high-temperature/high-pressure gas layers irradiated by a powerful infrared laser and further expanded to form high-energy secondary beams.^{6,7} The abrupt changes described above occur in the shock wave, and right on the shock generator body where the gas has zero velocity, the reservoir temperature should be restored. However, as demonstrated in the following paragraph, this initial temperature is only specific to the axial streamline and therefore the spatial domain probed by CRDS cannot be described exclusively with a single temperature but rather with an average temperature which contains the contributions of the different probed flow layers.

A previous study was carried out at the IPR by Suas-David.⁸ In this first trial, a 50 mm diameter plate was placed in a free-jet expansion⁸, however, a large radial velocity component was detected in the direction of the laser which caused, on the one hand, a convective Doppler line broadening and, on the other hand, re-cooling of the probed gas as its kinetic energy became significant once more.

This time, to overcome these drawbacks, instead of a large diameter plate, a cylinder with a diameter corresponding to that of the exit of the hypersonic jet was placed in the flow, 20 mm downstream of the Laval nozzle, as it can be seen in figure (4.2). The goal was to stop the hypersonic jet, but at the same time allow the gas to escape quickly on the edges of the plate while being constantly replaced with a continuous renewal of hot gas. The cylinder is mounted directly onto the HES fixed by a ring and three threaded rods used to adjust the distance between the Laval nozzle exit and the plate. As the entire device can be moved horizontally with an actuator in front of the CRDS laser beam, this configuration has the great advantage of being able to probe different regions of the flow upstream and downstream of the shock wave.

The metal tubes prolonging the optical cavity inside the vacuum chamber are brought quite close to the shock and flushed by a substantial flow of nitrogen ($Q_{N_2} = 4$ slm). The nitrogen flow is to ensure the protection of the high-reflectivity mirrors because this setup has a more significant radial velocity component and a much hotter gas is present on the axis of the laser beam compared to the hypersonic jet setup. Figure (4.3) exhibits the experimental setup in operation with the glowing hot Laval nozzle on the left, and the shock generator stainless steel cylinder on the right, reflecting the radiation of the HES.

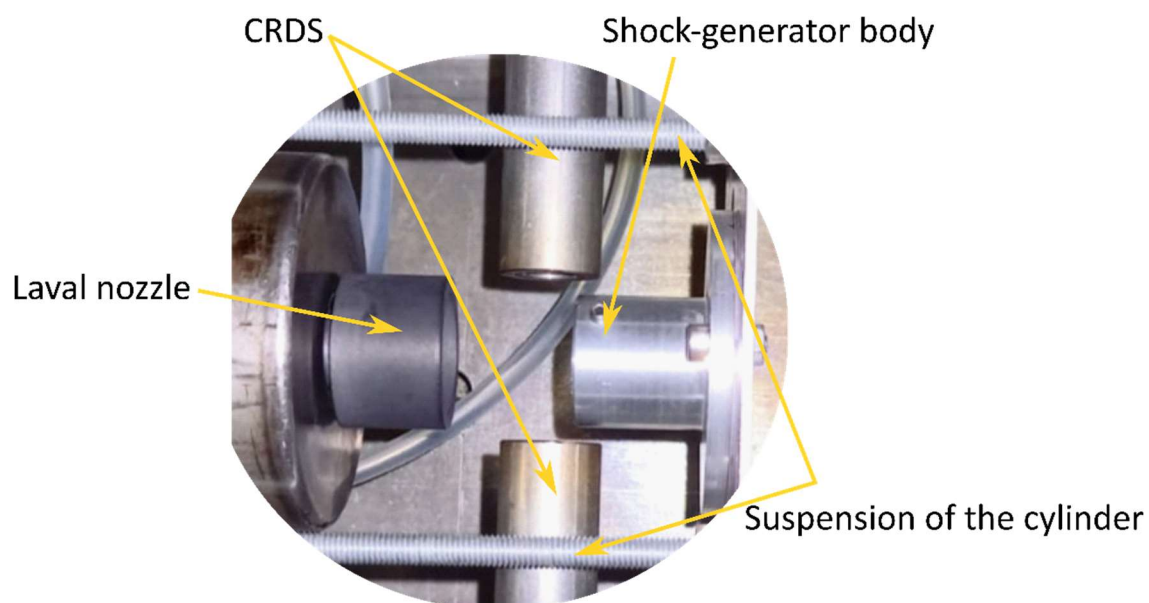


Figure 4.2: Insertion of the suspended cylinder in order to generate the shock

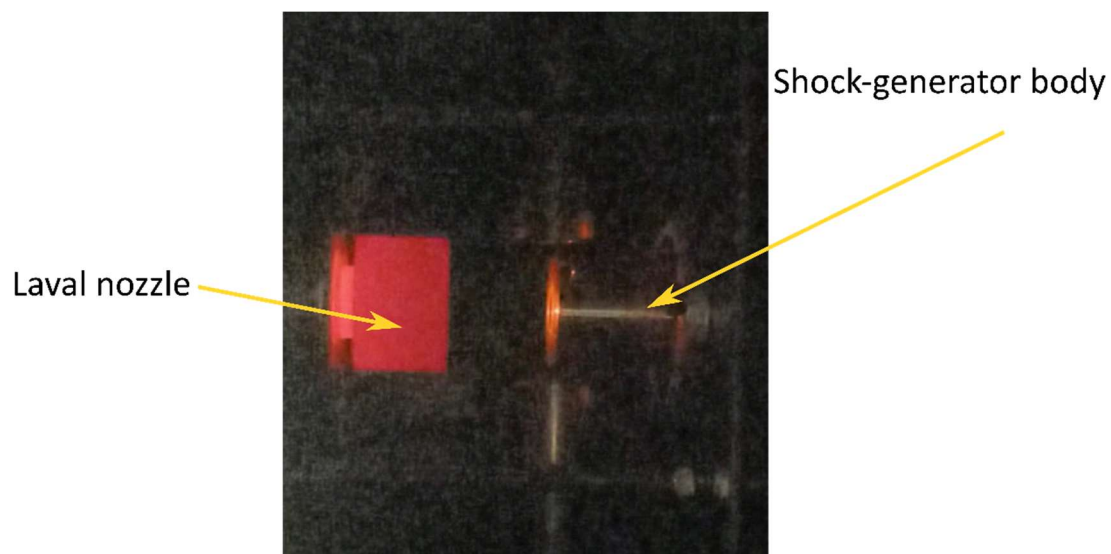


Figure 4.3: Experimental setup during measurements. On the left the glowing graphite Laval nozzle, and on the right the reflection of the hot Laval nozzle and the radiating reservoir graphite rod

4.4 CFD simulations and flow field analysis of the shock layer

The same as for chapter II, the first overview of the properties of the flow field is provided by numerical CFD simulations. By this means, a first estimate of the position, shape and characteristic flow variables of the shock front and shock layer could be studied. Regarding the boundary conditions, the stagnation temperature of argon was set at 1400 K with a stagnation pressure equal to 1500 Torr. The expansion chamber was set at 296 K and 0.5 Torr. The cylinder was defined with a heat-flux, allowing the correct modelling of the heat transfer from the gas to the shock generator body.

In contrast to the laminar simulations performed in chapter II, the realisable $k - \epsilon$ turbulence model was used to ensure the good performance of the viscous simulation. The model includes two additional transport equations that correctly describe the effects of flow turbulence. As suggested in the name of the model, k describes the turbulent kinetic energy, meanwhile ϵ corresponds to the turbulent dissipation term and determinates the scale of the turbulence.^{9,10}

Figure (4.4) demonstrates the obtained simulation results along the jet. The upper panel displays the temperature contour of the flow field between the nozzle exit and the cylinder. About 10 mm downstream of the nozzle exit is the outline of the shock front. Behind the shock, the shock layer is characterised by a high temperature reaching the stagnation temperature of 1400 K, right in front of the shock generator body. In conclusion, to probe the hottest region of the flow, the laser beam, perpendicular to the hypersonic jet, must be positioned as close as possible to the cylinder. Keep in mind, however, that a small portion of cooler gas corresponding to the front (green) region is also probed. This case is the exact opposite of the hypersonic jet scenario with the cold flow region surrounded by a hot shear-layer. The specific contribution of this cooler gas region is studied in figure (4.5).

Accordingly, the lower panel of figure (4.4) shows the evolution of the Mach number (green) and the temperature (red) along the jet axis. It is remarkable how the Mach number drops below unity almost instantly after reaching the front of the shock wave and, correspondingly, the temperature value essentially rises from that front and then continues to increase up to the cylinder.

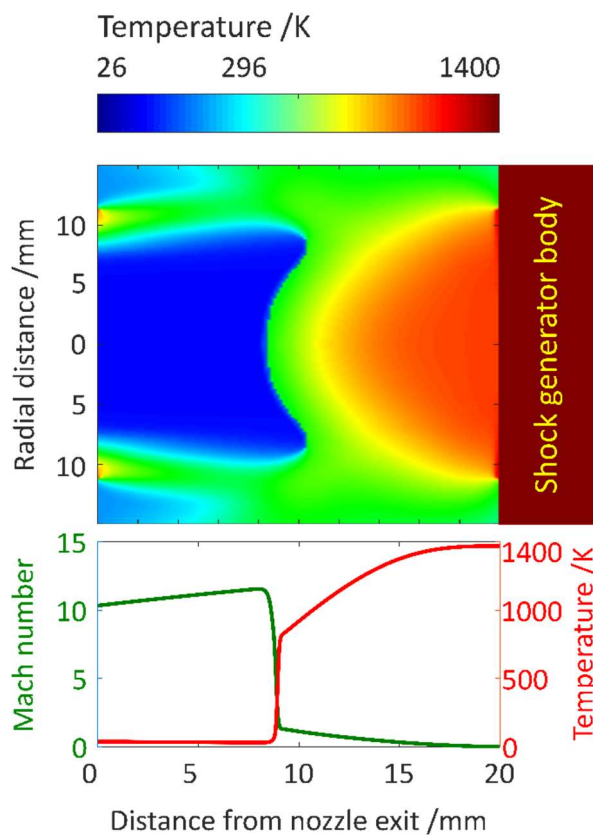


Figure 4.4: CFD simulation of the flow field downstream of the nozzle exit and upstream of the shock generator body. Upper panel: temperature contour. Lower panel: Evolution of Mach number (green) and temperature (red) along the jet axis.

An axial study of the flow helps to locate the position and shape of the shock and, as expected, indicates the most valuable flow region to be probed for spectroscopic measurements, i.e. the closest possible to the shock generator body. Nevertheless, to better characterise the specificities of the region to be probed by the laser, in-depth analysis in the radial direction was carried out 19 mm downstream of the nozzle exit. It is interesting to compare the results of the shock wave simulation with the ones from the hypersonic jet obtained in chapter II (see figure (2.6)).

Panel (a) in figure (4.5) represents the radial distribution of the temperature and highlights the presence of the hot region of the shock whose diameter ($\varnothing d = \sim 20$ mm) is double the one of the isentropic core ($\varnothing d = \sim 10$ mm) of the hypersonic jet. The panel also reveals the existence of cooler surrounding layers of about 500 K. Regarding the radial pressure distribution, panel (b) highlights a much higher pressure in the central region of the shock layer than the one prevailing in the expansion chamber. Accordingly, as panel (c) shows, this high-density region is favourable to spectroscopic measurements. Compared to the isentropic core of the hypersonic jet, the shock layer will provide an interesting signal-to-noise ratio by combining a larger absorption path (20 mm against 10 mm for the isentropic core) with a greater molecular density. Finally, the normalised profiles of the temperature, pressure and density are shown in panel (d). Interestingly, the external cooler part of the front shock is associated with an important drop of the density. Thus, it is expected that the majority of the molecules probed will come from the hot core of the gas, with a minority contribution from the colder outer layers.

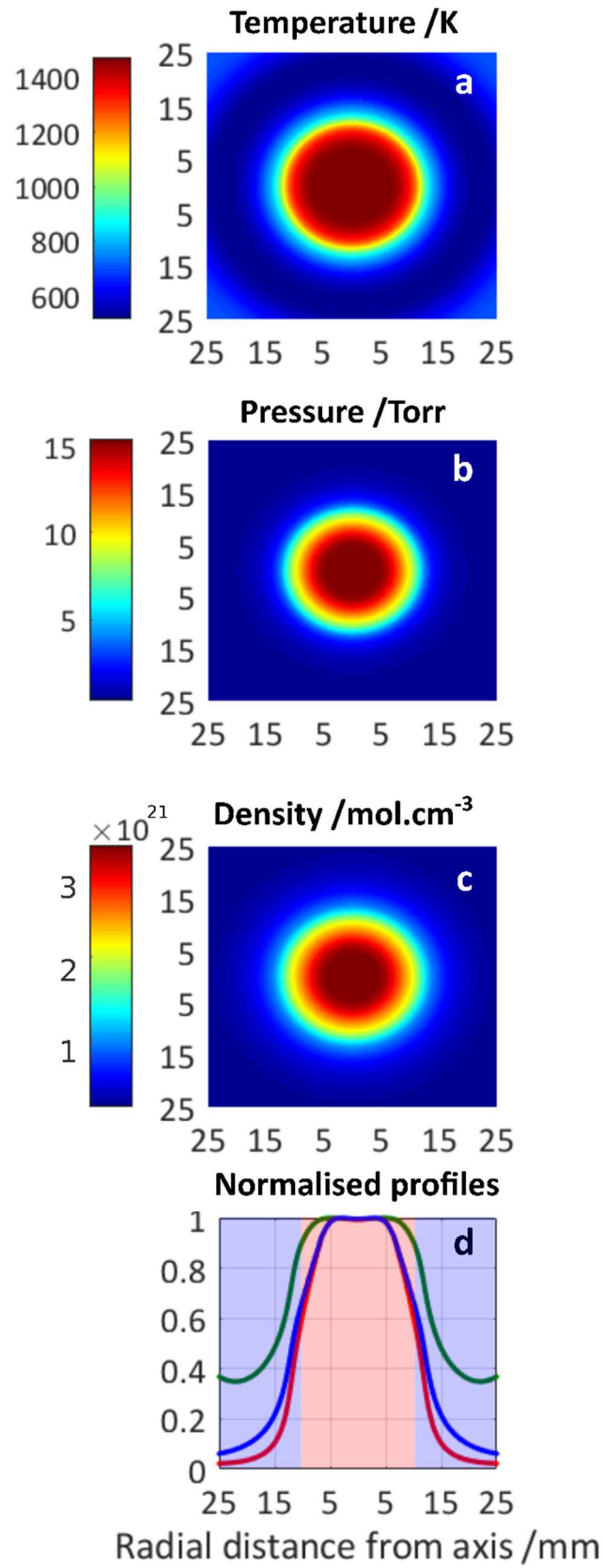


Figure 4.5: Cross section CFD simulation of the shock wave 19 mm downstream of the nozzle exit. Panel (a) represents the temperature radial distribution, panel (b) shows the corresponding pressure values and panel (c) highlights the density properties of the shock. Panel (d) compares the evolution of the temperature (green), pressure (red) and density (blue) curves through their normalised values.

4.5 Experimental characterisation of the shock

4.5.1 Location of the shock front

Following the numerical characterisation of the shock, a preliminary spectroscopic diagnosis was carried out using CO as a tracer molecule. In a first approach, R1 and R9 transitions were recorded by scanning the flow from upstream to downstream of the shock in steps of 1 mm. The R1 transitions are representative of the cold areas of the flow, while the R9 transitions are sensitive to the hot areas.

A flow rate of 19 slm of argon was admixed with 1 slm of CO, while the heating system was set to its maximum current (153 A) and therefore maximum power. The stagnation temperature is estimated to be around 1300 K, and the corresponding stagnation pressure is measured at 1775 Torr, meanwhile the expansion chamber was maintained at 0.5 Torr.

A typical ring-down time of 230 μ s was obtained, leading to equivalent absorption path lengths of 860 and 1720 m through the \sim 10 mm isentropic core diameter of the hypersonic jet and the \sim 20 mm shock layer diameter, respectively. The baselines are systematically adjusted to zero, which means that the absorption caused by the mirror surface is eliminated from each line in order to allow a better qualitative comparison. Figure (4.6) reveals that up to 9 mm away from the obstacle the laser beam passes through the hypersonic jet without interfering with the shock front. At approximately 8 mm from the plate, the change in the R1/R9 intensity ratio indicates a rise in temperature that continues to increase as the laser beam approaches the cylinder. By comparing these results with the CFD simulations, a slight shift of 1 to 2 mm can be spotted in the location of the shock front. This could originate from the inaccurate definition of the position of the cylinder, as well as the imprecise displacement of the HES as the 1 mm difference in resolution is about the limit of the driving servo motors. Of course, this small discrepancy could arise from the numerical calculations as well. Regardless, the quantitative evolution of the extracted translational temperatures from the Doppler linewidths is in good agreement with those simulated by CFD.

Translational temperatures are extracted by fitting the lines with a Doppler line profile, after verifying that the pressure line broadening would be negligible. Indeed, the jet pressure upstream of the shock front is about 0.05 Torr (see chapter II) while the Mach number is about 12 (see figure (4.4)). A static pressure downstream of the shock of about 9 Torr can be easily estimated from equation (4.7), corresponding to partial pressures of 112.5×10^{-4} atm and 5.9×10^{-4} atm for argon and CO, respectively. The default values of the pressure broadening coefficients (HWHM) provided by the HITRAN database ($L_{env} = 0.0600 \text{ cm}^{-1} \cdot \text{atm}^{-1}$ and $L_{self} = 0.0750 \text{ cm}^{-1} \cdot \text{atm}^{-1}$) have been used to calculate a pressure line broadening of 0.0014 cm^{-1} (FWHM), which is relatively small compare to the Doppler line broadening ($\sim 0.027 \text{ cm}^{-1}$ (FWHM) at 1000 K). The measured translational temperature is shown at the bottom of figure (4.6). A value of approximately 60 K is extracted from the hypersonic jet (R1 lines), upstream of the shock front, while a temperature varying between 412 to 1307 K is probed in the shock layer (R9 lines), downstream the shock front. Right at the shock front, 8 mm from the cylinder, two different temperatures of 184 K and 650 K are retrieved from the R1 and R9 lines, respectively. Two reasons can explain the simultaneous presence of these two temperatures. The first is related to the concave shape of the shock layer that develops in front of the cylinder.

As can be seen in figure 4.4, at 8mm from the obstacle, the laser is mainly contained in the thickness of the shock front (green area in the figure) but it also crosses a small distance over part of the external flow still hypersonic (blue area in the figure). The second reason is related to the qualitatively bimodal character of the molecular velocity in the shock that is derived from the distribution functions on either side of the shock and observed by laser induced fluorescence³ or by Raman spectroscopy^{4,5}. This bimodal velocity distribution reflects the abrupt transition between the very different upstream and downstream conditions.

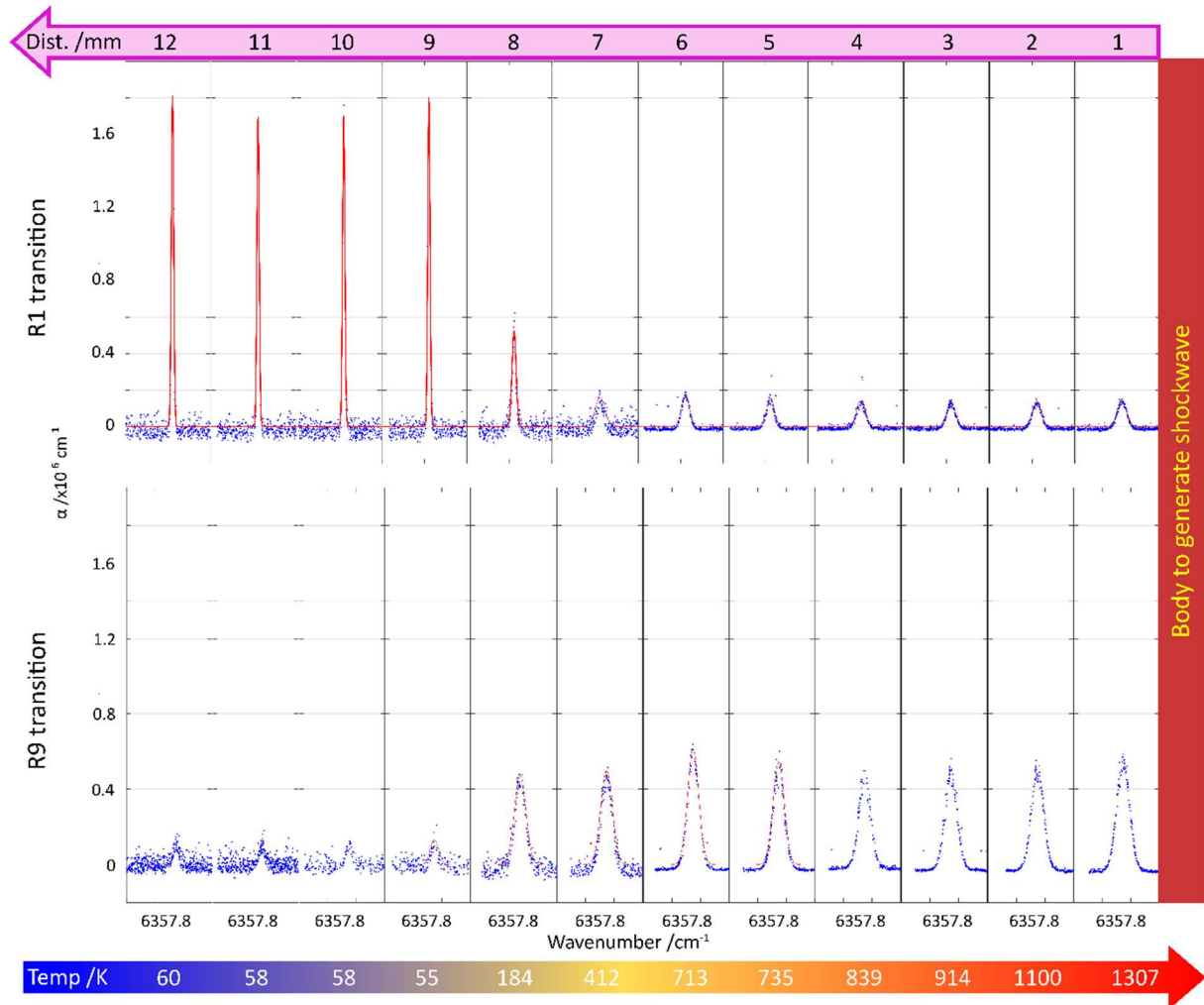


Figure 4.6: Scan through the flow from upstream of the shock front down to the shock generator cylinder. The pink arrow indicates the position in the flow, the upper panel represents the R1 transitions and the lower panel corresponds to the R9 ones. Below, the blue-red arrow reveals the temperatures retrieved from the Doppler linewidths.

4.5.2 Evolution of the rotational and vibrational temperatures through the shock

Once the position of the shock was determined, focus shifted to the evolution of the vibrational and rotational temperature through the shock. A series of spectra were recorded in steps of 1 mm starting from 10 mm from the cylinder. Figure (4.7) shows an example of a recorded spectrum (laser positioned at 6 mm from the cylinder) where a part of the P-branch of the 3-0 cold band and the tail of the R-branch of the 4-1 hot band are missing due to the lack of the

corresponding diode. Nevertheless, as expected, the relatively large observed number of rovibrational lines of the 3-0 R-branch indicates a much higher rotational temperature in the post-shock region than upstream, in the hypersonic jet, where the same R-branch is limited to $J_{max} = 10$.

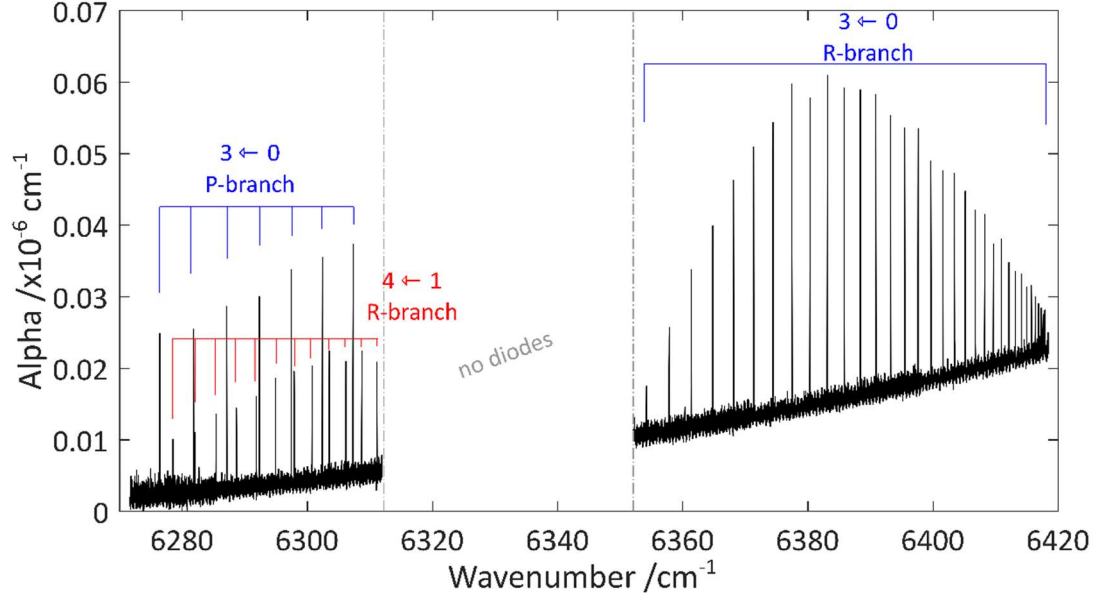


Figure 4.7: CO spectrum recorded in the shock layer at 6 mm from the obstacle. R- and P-branches of the 3-0 cold band and a part of the R-branch of the 4-1 hot band are shown.

Figure (4.8) shows the evolution of the R-branches of the 3←0 cold (blue) and 4←1 hot bands (red) during the variation of the position of the laser. Panels (a) and (b) are relative to the conditions upstream of the shock, where the most intense line corresponds to $J = 2$ and the high- J rotational levels are depopulated and therefore do not contribute to the recorded spectra. Panels (c) to (f) correspond to spectra recorded between 1 and 8 mm from the cylinder, where the laser beam passes through the shock layer. The overall shape of the recorded R-branches is profoundly modified by the significant increase in the rotational temperature. The most intense line shifts progressively towards higher J values and high- J rotational lines become more and more visible, up to R45 in panel (f), as the laser beam approaches the obstacle. At the same time, as evidenced by the increase in the absorption coefficient, the density of the probed molecules gradually increases from the shock wave to the obstacle (from panels (c) to (f)).

These observations nicely confirm the CFD simulations, that is to say a gradual increase in temperature and density as the subsonic flow of the shock layer approaches the obstacle. It therefore seems that the most favorable position of the laser for performing spectroscopy of a hot gas is that which is as close as possible to the obstacle.

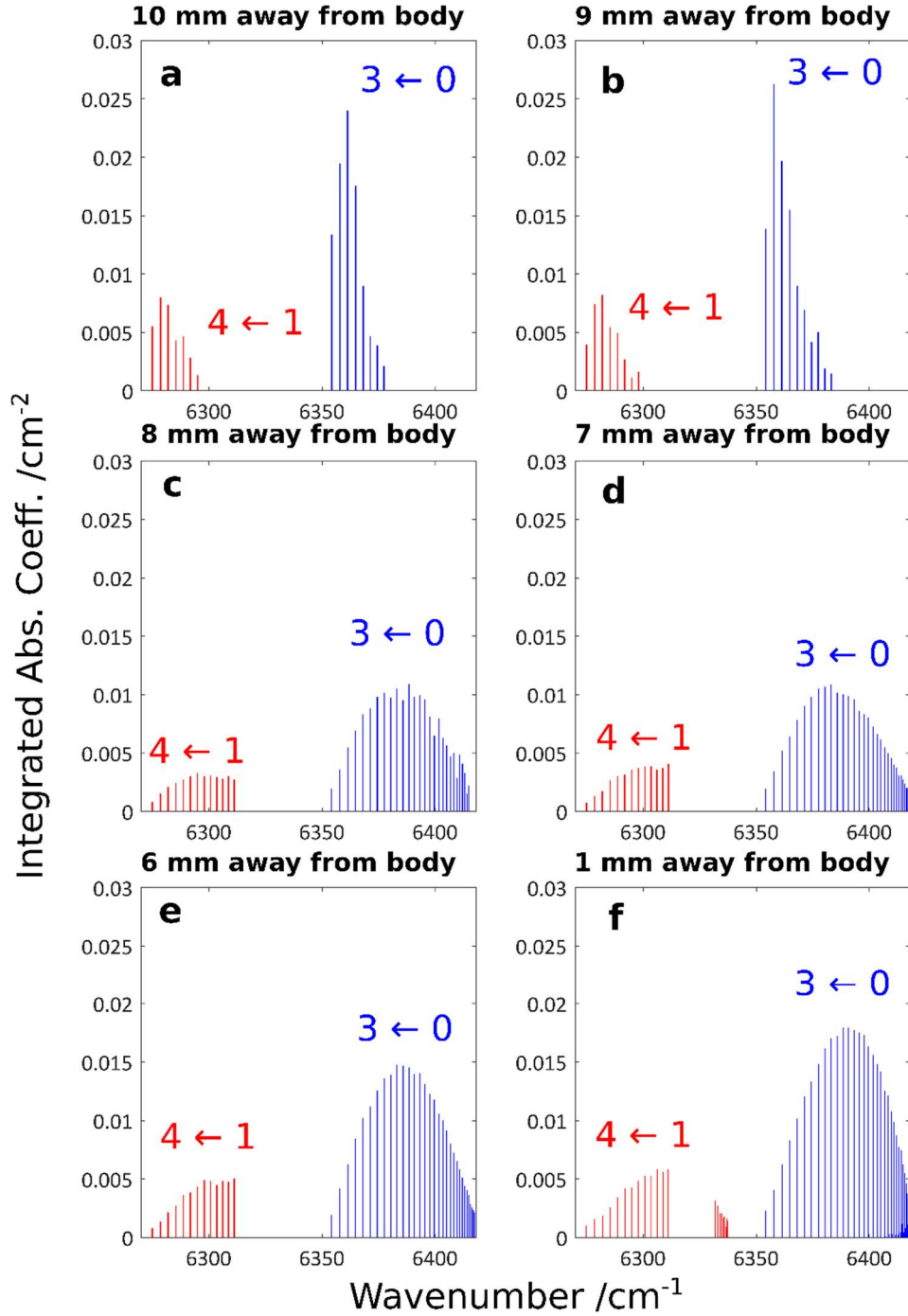


Figure 4.8: CO spectra of the R-branch of the 3←0 cold band (blue) and the R-branch of the 4←1 hot band (red) recorded at different positions of the laser in the flow field, starting upstream from the shock (panel (a)) up to the cylinder (panel (f)).

To determine the rotational and vibration temperatures, a standard Boltzmann plot method was applied (see figure (4.9)). However, this time, the contribution of the shear-layers surrounding the isentropic core has not been removed from the measured integrated absorption coefficients, so that the obtained rotational temperature describing the hypersonic jet is certainly slightly overestimated (according to paragraph 2.4.2, the error made if the absorption coefficients are not corrected for the contribution of the hot gas layer is 1.4 K). The same applies to the shock layer. The contribution of the external part of the shock layer has not

been taken into account, so that the obtained temperature is this time probably slightly underestimated.

The rotational temperatures have been exclusively extracted to the more intense R-branch of the $3 \leftarrow 0$ cold band (blue), while the vibrational temperatures have been extracted from the $J = 0, 1, 2$ rovibrational lines of the $3 \leftarrow 0$ and $4 \leftarrow 1$ vibrational bands. Panel (a) in figure (4.9) represents the temperatures upstream of the shock (10 mm away from the body), unsurprisingly showing a strong non-LTE regime characterised by $T_{rot} = 37(2)$ K and $T_{vib} = 1296(87)$ K. The rotational temperature only slightly increases when the laser beam is brought closer to 1 mm from the shock wave (panel (b), 9 mm away from the body), the vibrational temperature remaining unchanged. The rotational temperature then undergoes a sudden increase as it passes through the shock (panel (c), 8 mm from the body) and continues to increase progressively up to the obstacle (panels (d) to (f)), converging to the vibrational temperature which remains more or less constant, given the measurement uncertainties. This series of measurements shows that the rotational relaxation closely follows the temperature evolution of the translational temperature. However, the vibrational temperature does not relax from the nozzle exit, throughout the hypersonic jet and astonishingly in the shock layer as well remains $T_{vib} \sim 1300$ K. As explained in chapter II, the stagnation (or total) temperature is difficult to measure but it remains probably very close to 1300 K all along the flow field, from the reservoir to the blunt body. Nevertheless, it is surprising to see that the vibrational temperature does not equilibrate with the translational and rotational temperatures despite the significant stagnation pressure close to 10 Torr in the shock layer.

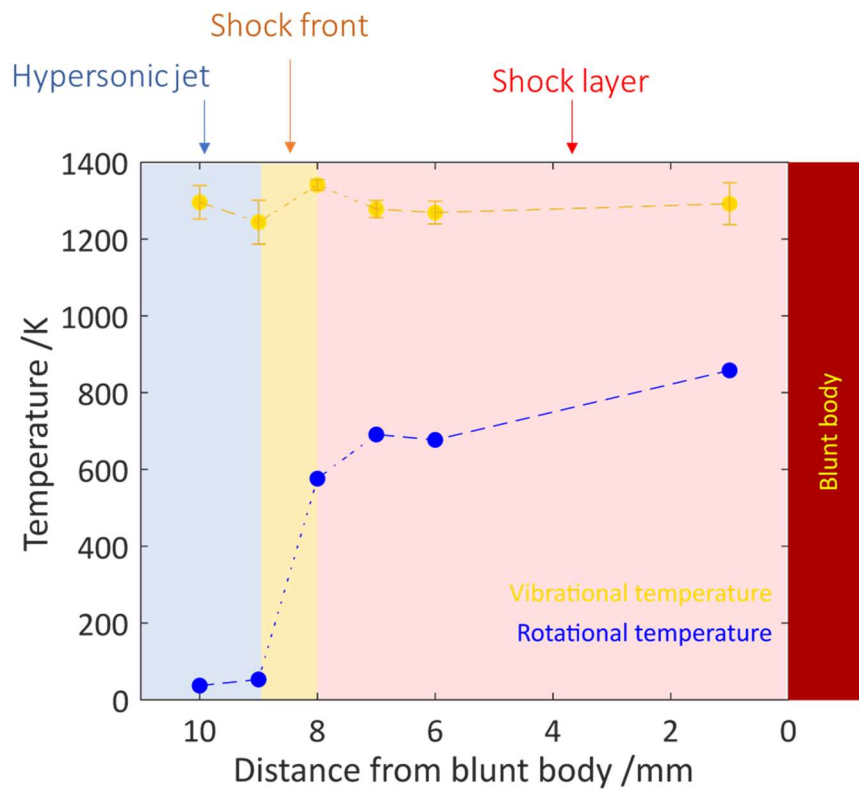


Figure 4.9: Representation of the evolution of the vibrational and rotational temperatures, highlighting the surprising behaviour of the vibrational temperature.

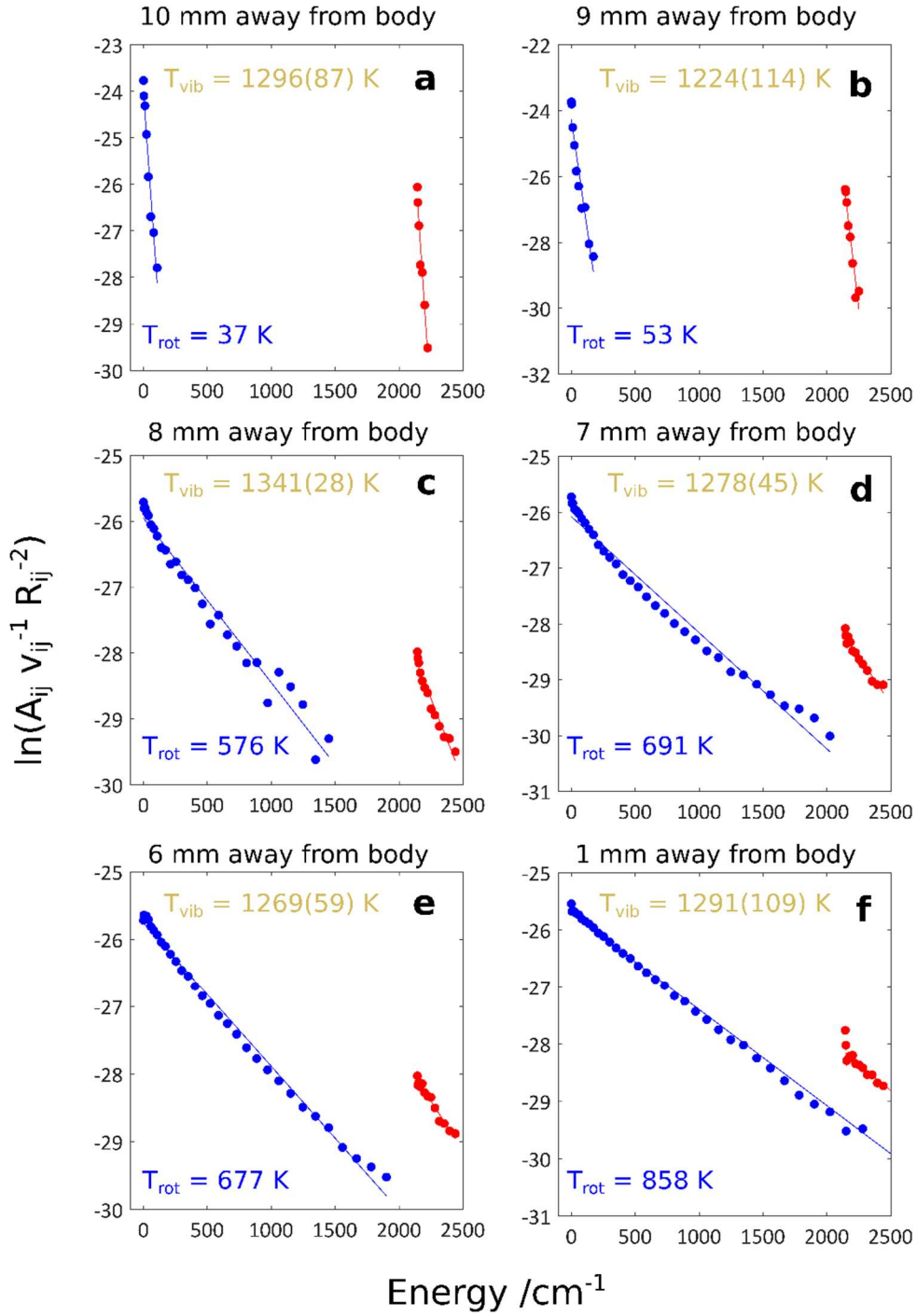


Figure 4.10: Boltzmann plots corresponding to the recorded spectra of figure (4.8).

In conclusion, the CO molecules probed in the post-shock layer are still in a non-LTE regime with $(T_{\text{trans}} = T_{\text{rot}}) < T_{\text{vib}}$. However, they present a much less marked non-equilibrium than in the hypersonic isentropic core ($T_{\text{trans}} \approx T_{\text{rot}} \ll T_{\text{vib}}$). It has thus been demonstrated that the post shock spectroscopy gives access to high- J rovibrational states and high vibrational energy states. This new approach was then applied to the spectroscopy of methane.

4.6 Methane post-shock spectroscopy

The post shock methane spectrum was recorded under two different temperature conditions in the 5877-6216 cm^{-1} spectral range, with a gap between 6139-6183 cm^{-1} due to the lack of the appropriate laser diodes. Firstly, similar to what was done for CO, 19 slm of argon was mixed to 1 slm of CH_4 at a stagnation pressure of 1413 Torr and the pressure in the expansion chamber was set to 0.5 Torr. Later, a second spectrum was recorded with a reduced argon flow of 10 slm which resulted in a higher stagnation temperature and therefore higher post-shock rotational and vibrational temperatures. Datasets recorded under different temperature conditions allow the investigation of the temperature dependence of the recorded lines and facilitate the determination of the position of the hot bands.

The exhaustive analysis of the post-shock methane spectra is still ongoing and the results are being prepared for submission to a peer-reviewed journal. Nevertheless, a preliminary simulation was carried out for a first glimpse of the results. Following the outcome of the CO experiments, non-LTE conditions were considered, thus the rotational and vibrational temperatures were fixed respectively at 850 K and 1000 K. The results show a discrepancy for the lines around 6100 cm^{-1} testifying to the error introduced by attempting to model the spectrum with one single vibrational temperature.

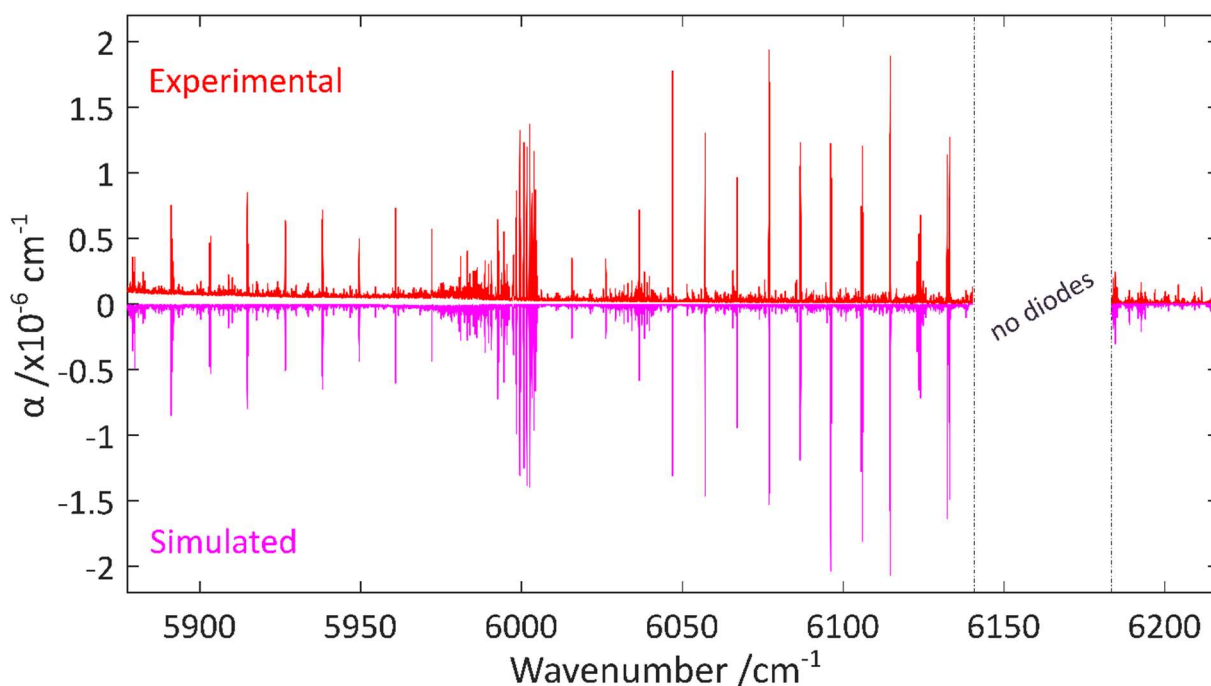


Figure 4.11: Upper panel: experimental post-shock spectrum of 1 slm methane admixed to 10 slm argon. Lower panel: preliminary simulated spectrum at $T_{\text{rot}} = 850 \text{ K}$ and $T_{\text{vib}} = 1000 \text{ K}$.

In chapter III, a part of the 964 K LTE spectrum recorded by the LiPhy laboratory was shown. At this stage of the investigation, this spectrum (green) was compared to the post-shock spectrum of Rennes (red) in figure (4.12). At first glance, only minor differences can be spotted between 6000-6005 cm^{-1} between the two spectra, underlying the slight non-LTE nature of the post-shock spectrum.

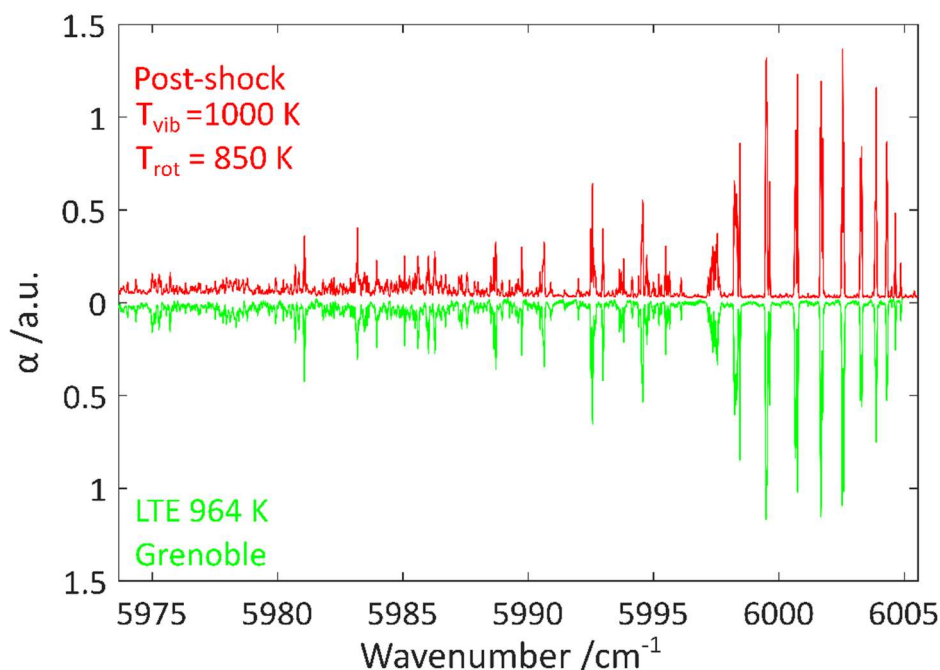


Figure 4.12: Comparison of post-shock spectrum (red) recorded in Rennes with the LTE 964 K spectrum obtained in Grenoble.

Finally, figure (4.13) compares the post-shock spectrum (red) to the hypersonic jet spectrum (black). Panel (a) exhibits the whole spectra and reveals the remarkable difference, such as the increased intensity peaks in the post-shock spectrum corresponding to the high- J rotational states. It has to be remembered that in the hypersonic jet spectrum, the most intense peaks corresponding to the low- J rotational levels of the cold bands are truncated. Panel (b) is a zoom into the two spectra and underlines the key features of the two approaches. In case of the post-shock CRDS approach, the spectrum exhibits a more complex – and more complete – rotational structure and hot bands involving excited vibrational states, but this comes at a price of systematic overlapping transitions and broadener lines. Conversely, the hypersonic jet CRD spectrum results in much narrower peaks, ideal for a precise determination of line positions. However, this spectrum only contains information on low- J rotational energy levels.

In conclusion, post-shock CRD spectroscopy is a new technique that complements hypersonic jet spectroscopy well. The combination of these two approaches has produced valuable spectroscopic data which will unravel the complex structure of the high temperature spectrum of methane.

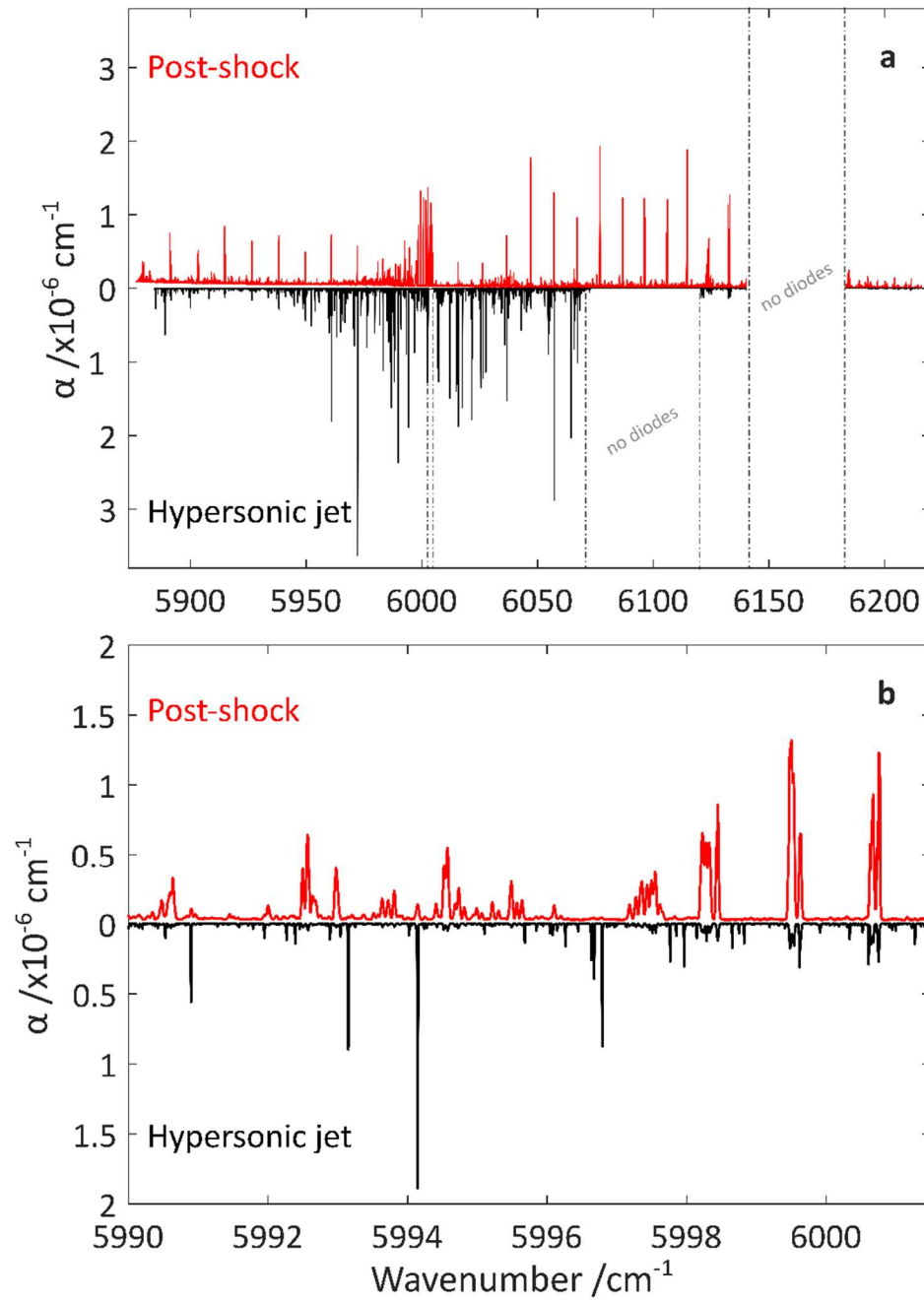


Figure 4.13: Comparison between post-shock spectrum (red) and hypersonic jet spectrum (black). Panel (a): represents the whole recorded spectra. Panel (b): zoomed view

References

- (1) Hoyt, J. K. The Cyclopaedia of Practical Quotationos, English and Latin: With an Appendix Containing Proverbs from the Latin and Modern Foreign Languages ...; Funk & Wagnalls, 1889.
- (2) Rathakrishnan, E. Applied Gas Dynamics; John Wiley & Sons, 2019.
- (3) Pham-Van-Diep, G.; Erwin, D.; Muntz, E. P. Nonequilibrium Molecular Motion in a Hypersonic Shock Wave. *Science* **1989**, 245 (4918), 624–626. <https://doi.org/10.1126/science.245.4918.624>.
- (4) Ramos, A.; Maté, B.; Tejada, G.; Fernández, J. M.; Montero, S. Raman Spectroscopy of Hypersonic Shock Waves. *Phys. Rev. E* **2000**, 62 (4), 4940–4945. <https://doi.org/10.1103/PhysRevE.62.4940>.
- (5) Ramos, A.; Tejada, G.; Fernández, J. M.; Montero, S. Nonequilibrium Processes in Supersonic Jets of N_2 , H_2 , and $N_2 + H_2$ Mixtures: (II) Shock Waves. *J. Phys. Chem. A* **2010**, 114 (29), 7761–7768. <https://doi.org/10.1021/jp1040053>.
- (6) Apatin, V. M.; Makarov, G. N.; Nesterov, V. V. High-Power IR Laser-Induced Acceleration of SF_6 Molecules in a Secondary Pulsed Molecular Beam. *Chemical Physics Letters* **2001**, 347 (1–3), 101–107. [https://doi.org/10.1016/S0009-2614\(01\)01033-8](https://doi.org/10.1016/S0009-2614(01)01033-8).
- (7) Makarov, G. N. Generation of Intense Secondary Pulsed Molecular Beams of High Kinetic Energy Controllable by a Powerful IR Laser. *Chemical Physics* **2003**, 290 (2–3), 137–146. [https://doi.org/10.1016/S0301-0104\(03\)00086-7](https://doi.org/10.1016/S0301-0104(03)00086-7).
- (8) Nicolas Suas-David. Jets hypersoniques sondés par temps de déclin d’une cavité optique : application à l’astrophysique de laboratoire, 2016.Thesis.
- (9) Jones, W. P.; Launder, B. E. The Prediction of Laminarization with a Two-Equation Model of Turbulence. *International Journal of Heat and Mass Transfer* **1972**, 15 (2), 301–314. [https://doi.org/10.1016/0017-9310\(72\)90076-2](https://doi.org/10.1016/0017-9310(72)90076-2).
- (10) Launder, B. E.; Sharma, B. I. Application of the Energy-Dissipation Model of Turbulence to the Calculation of Flow near a Spinning Disc. *Letters Heat Mass Transfer* **1974**, 1, 131–137.

Platypus project

“Tempora mutantur et nos mutamur in illis.”⁵

DU MÉTHANE A ÉTÉ DÉTECTÉ DANS L'ATMOSPHÈRE
DES JUPITERS CHAUDS.



JE VOUDRAIS SAVOIR SI D'AUTRES HYDROCARBURES SONT
ÉGALEMENT PRÉSENTS, ET EN QUELLES QUANTITÉS.

⁵Times are changed, we also are changed with them.¹

Contents

5.1 Platypus project.....	151
5.2 Plasma.....	152
5.3 RF plasma source	153
5.3.1 RF Impedance matching network	153
5.4 Implantation into SMAUG.....	156
5.5 Visualisation of the plasma expansion.....	157
5.6 Preliminary study with carbon monoxide.....	158
5.6.1 Rotational and vibrational temperatures	159
5.7 Conclusion	162
References	163

5.1 Platypus project

Platypus: *“a semiaquatic egg-laying mammal which frequents lakes and streams in eastern Australia. It has a sensitive pliable bill shaped like that of a duck, webbed feet with venomous spurs, and dense fur.”*²

The SMAUG experimental setup coupled with cavity ring-down spectroscopy was of great interest to Professor Christine Charles of the Space Plasma, Power and Propulsion (SP3) laboratory, of the Australian National University (ANU), one of the world specialists in plasma space propulsion. Development of electrothermal mini-thrusters requires technical expertise to characterise the plasma jets, which is a similar process to the characterisation of the SMAUG flows. Such characterisation includes precisely determining the partition of the internal energy into the different degrees of freedom, such as translational, rotational and vibrational energy. The thrusters developed at the ANU are built to power so-called CubeSats³, a standardised satellite form factor of 10x10x10 cm³ and 1.33 kg, which allow efficient access to space studies via numerous possible launch vehicles.⁴ Thousands of small satellites of this type will be launched over the next decade, inducing a space revolution⁵ in the fields of Earth imagery⁶, the internet^{7,8}, navigation⁹ and localization by GPS and weather forecasts.¹⁰

The new collaboration between the research groups at Canberra and Rennes aims to study both applied and fundamental physics via shared expertise founded upon the very similar working principals of SMAUG and plasma thrusters. Investigations on expanding plasmas can help the development of new space thrusters and at the same time deliver new spectroscopic data on strong out-of-equilibrium thermodynamics. This latter application is targeted in this doctoral work to test its ability to contribute to models of exoplanet atmospheres. The joint project consists of the development of a transformed planar Pocket Rocket¹¹, whose nozzle resembles to the beak of a platypus. This plasma source was adapted to be coupled with SMAUG and to produce high-vibrational energy out-of-equilibrium plasma expansions of various molecules which can be then characterised by CRDS.

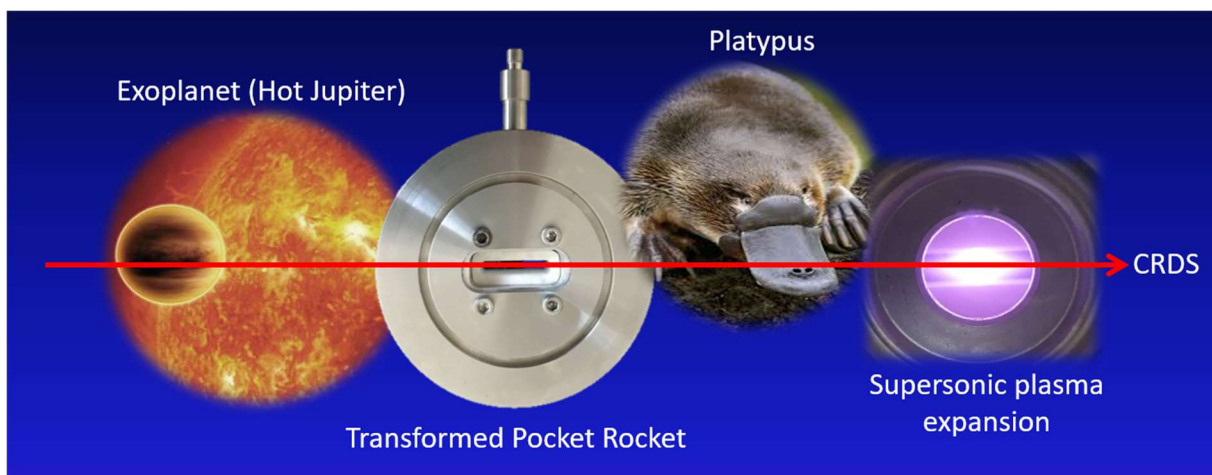


Figure 5.1: Platypus project

5.2 Plasma

Plasma is a quasineutral gas of charged and neutral particles which can be described with a collective behaviour.¹² As the charged particles move around they can generate local negative and positive charge concentrations which produce emerging electrical fields. The movement of these charged particles creates current as well and subsequently magnetic fields are generated. Conversely, these fields influence the motion of the charged particles. Therefore, the term “collective behaviour” refers to the fact that the motion of the particles depends not only on the local conditions and collisions but also on the state of the plasma in a wider zone.

To understand the term quasineutral, first of all the quantity of Debye length (λ_D) has to be introduced:

$$\lambda_D = \left(\frac{\epsilon_0 k T_e}{n e^2} \right)^{\frac{1}{2}} \quad 5.1$$

Where, ϵ_0 - vacuum permittivity, n – number of particles per m^3 , k - Boltzmann constant, T_e - electron temperature and e – electron charge. The Debye length describes the shielding distance in the plasma. In order to be able to call an ionised gas a plasma, this Debye length must be much smaller than the characteristic length (L) of the system. This criterion ensures the quasineutrality, meaning that local charge concentrations or external potentials applied to the system do not create large electric potentials or fields within the system.

This shielding effect can only take place if enough particles ($N_D \gg 1$) are present in the charged cloud. The following equation describes the number of particles in the so-called Debye-sphere:

$$N_D = n \frac{4}{3} \pi \lambda_D^3 \quad 5.2$$

Finally, a third condition must be fulfilled in order to consider a gas a plasma. Namely, the motion of the particles has to be determined by electromagnetic forces rather than hydrodynamic forces. In practice, it means that the product of the frequency of the plasma oscillation (ω) times the mean time (τ) between collisions with neutral atoms must be greater than unity:

$$\omega \cdot \tau > 1 \quad 5.3$$

5.3 RF plasma source

The radiofrequency (RF) plasma source adapted to work with CRDS was based on the “Pocket Rocket” (PR) electro-thermal capacitively-coupled RF plasma thruster operating at 13.56 MHz.¹³ The main difference is the modified outlet section, which has been designed in a rectangular shape, thus the name platypus. This intends to increase the absorption path compared to the original circular aperture, and to reduce the strong Doppler line broadening induced by the jet divergence associated with a circular sonic nozzle.¹⁴

5.3.1 RF Impedance matching network

Using a radiofrequency electrothermal heating element requires a finely tuned network with high quality, low impedance transition lines of a carefully selected length. It ensures the best power transfer from the generator to the plasma chamber. Figure (5.2) represents the schematic chain of this network. At the beginning of the chain, the RF generator with an inbuilt crystal oscillator creates RF waves of 13.56 MHz, which happens to be a commercially permitted broadcast frequency. These waves undergo a huge amplification and then enter the low pass filter, which cuts off the higher frequencies of the output signal. The Standing Wave Ratio (SWR) meter gives information on how much power is transmitted to the plasma chamber by revealing the ratio of the transmitted and reflected amplified signal. The reflected signal does not participate in the plasma creation. Finally, the matching box, using a collection of variable resistors and capacitors, ensures a resonance between the input signal and the plasma chamber. To accomplish its task the capacitance and impedance are tuned to give the maximum power coupling with the plasma chamber. The platypus plasma source has a 30 W maximum output power for generating plasma. Figure (5.3) shows the components of the impedance matching network.

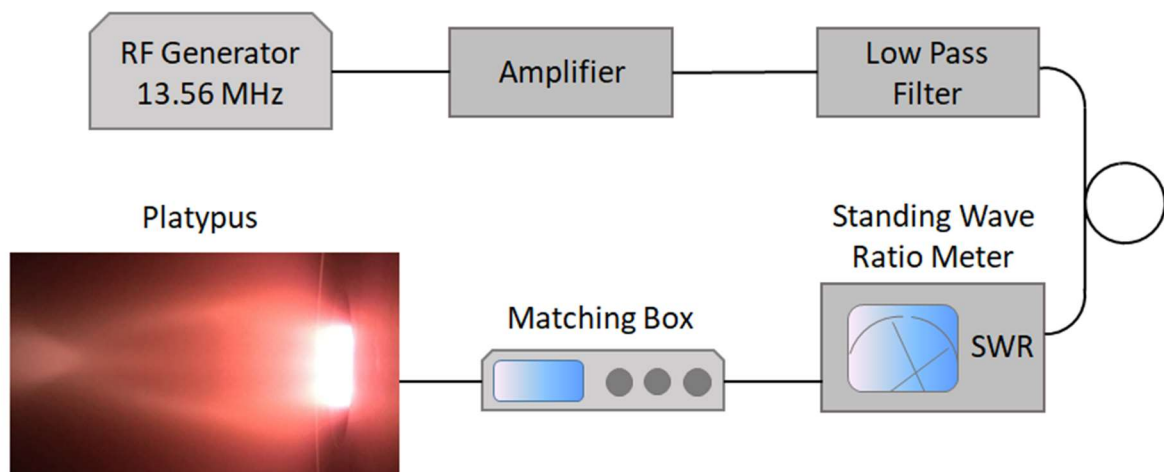
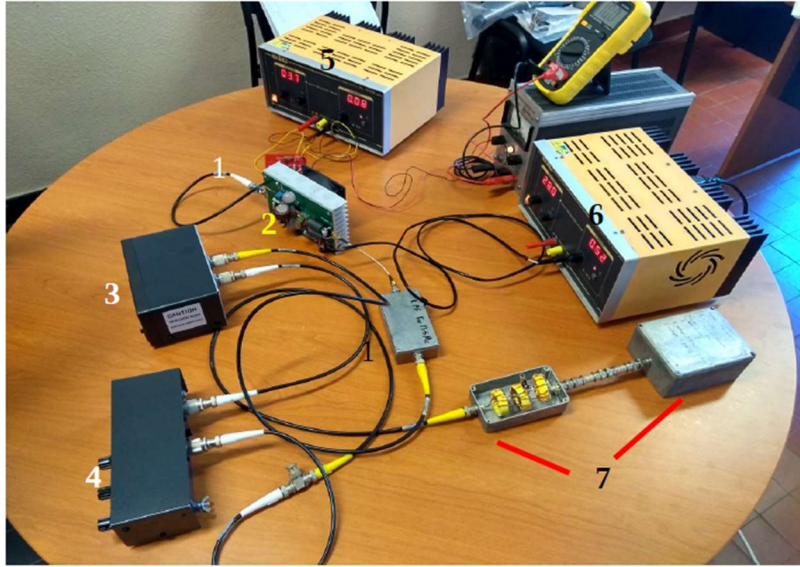


Figure 5.2: Schematic representation of the RF impedance matching network



Components of the plasma source

1. Drive board (red chip)
2. Amplifier
3. Standing wave ratio meter
4. Matching box
5. Power source for drive board
6. Power source for Amplifier
7. Pocket rocket plasma simulator

Figure 5.3: Components of the platypus RF impedance matching network

The goal was to implant the platypus plasma source into SMAUG and to create a supersonic plasma expansion. This new heating source comes with several advantages. First, contrary to the graphite heating element of the HES, the plasma source is not sensitive to molecules containing oxygen and therefore molecules such as water or carbon dioxide could be studied at high temperature using this technique. Another interesting feature of the plasma heating element is the way it excites the gas. Specifically, the vibrational energy levels are already more excited than the rotational levels in the reservoir, before any expansion.¹⁵ Emission spectroscopy of nitrogen plasma revealed a rotational temperature $T_{rot} = 575$ K and a vibrational temperature $T_{vib} = 1500(100)$ K strong out-of-equilibrium condition within the plasma chamber.

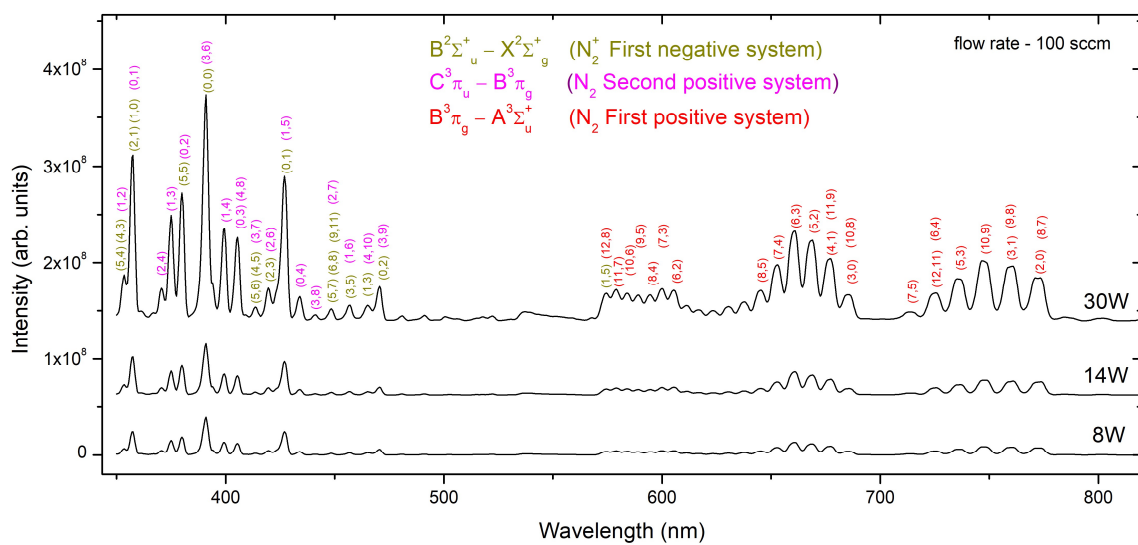


Figure 5.4: Estimation of plasma chamber temperature using LIFBASE Software Spectroscopy Tool. The work was carried out by Vijay Amrut Raj Sunuganty in his Internship report: High temperature molecular spectroscopy.

Passing the plasma into a low-pressure chamber through a supersonic expansion should result a strong non-LTE conditions and provide interesting, vibrationally hot, rotationally cold spectra. Last but not least, the plasma source should be able to overcome the upper reservoir temperature limit of the HES at around 1400 K.

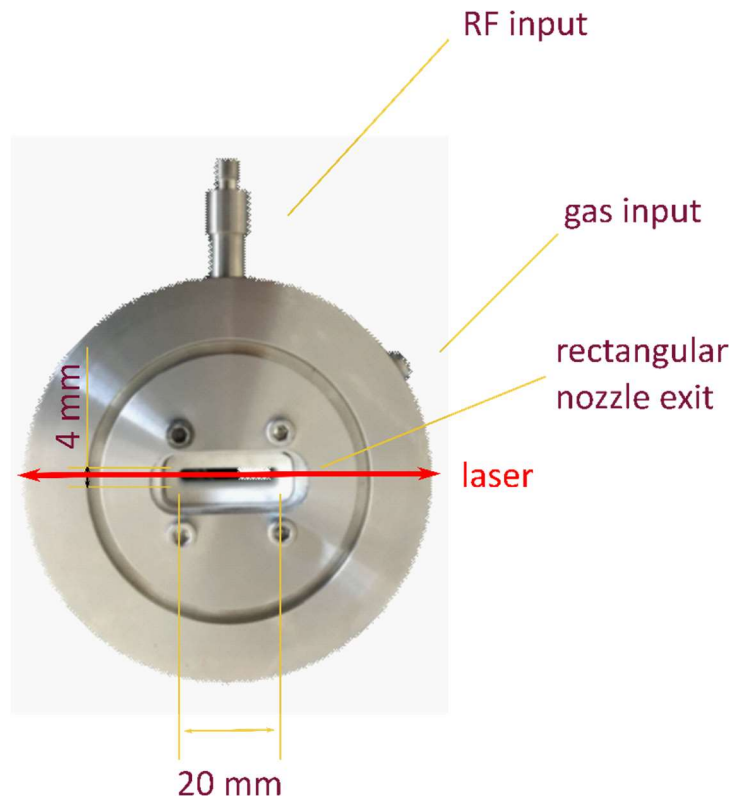


Figure 5.5: The transformed Pocket Rocket into a planar RF plasma source with its adapted rectangular nozzle exit.

5.4 Implantation into SMAUG

The platypus plasma source is designed to replace the HES heating element of SMAUG. A main challenge of the insertion of the developed model into SMAUG was the fact that part of the RF plasma thruster warms up significantly throughout its operation. Therefore, it could not be inserted into the low-pressure chamber directly for the fear of failure of the components due to a lack of cooling.

Therefore, an extra cooling element was made in order to ensure the functioning of the SMA feedthrough. A cylinder has been used to create a space of atmospheric pressure within the vacuum chamber. This cylinder was connected via flexible steel tube to the outer wall of the vacuum chamber. This tube ensures a continuous – all in atmospheric pressure - route for the BNC cables from the power supply to the platypus plasma source.

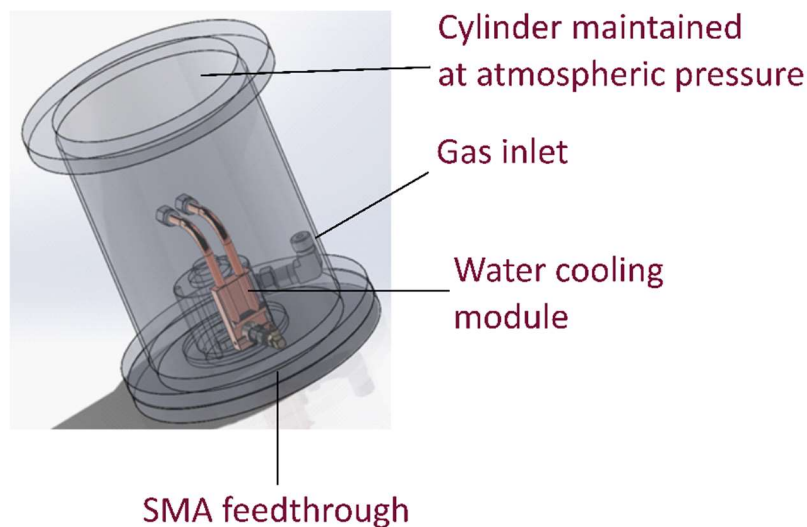


Figure 5.6: Implantation of the platypus plasma source into SMAUG

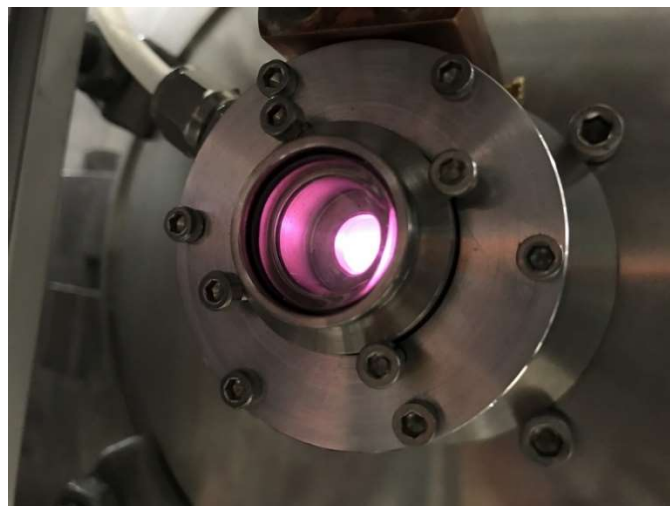


Figure 5.7: Photo of the rear window of the operational platypus plasma source

5.5 Visualisation of the plasma expansion

First of all, it was necessary to verify if the expansion was indeed supersonic. As the rectangular nozzle outlet has an 80 mm^2 area which is enormous compared to the previously used Laval nozzle, where the throat area is equal to 3.14 mm^2 , it was not sure that the necessary critical pressure ratio downstream-upstream of the nozzle throat could be established. The following figure (5.8) demonstrates the visual evidence of the supersonic jet. In panel (a), a 0.5 slm reduced flow rate argon gas expansion is presented which results in a probable subsonic expansion. Conversely, panel (b) exhibits an increased flow rate of 8 slm of argon which results in a supersonic flow. This feature of the plasma jet is justified by the presence of shock diamonds which can only occur in case of an expansion with Mach number greater than unity.¹⁶

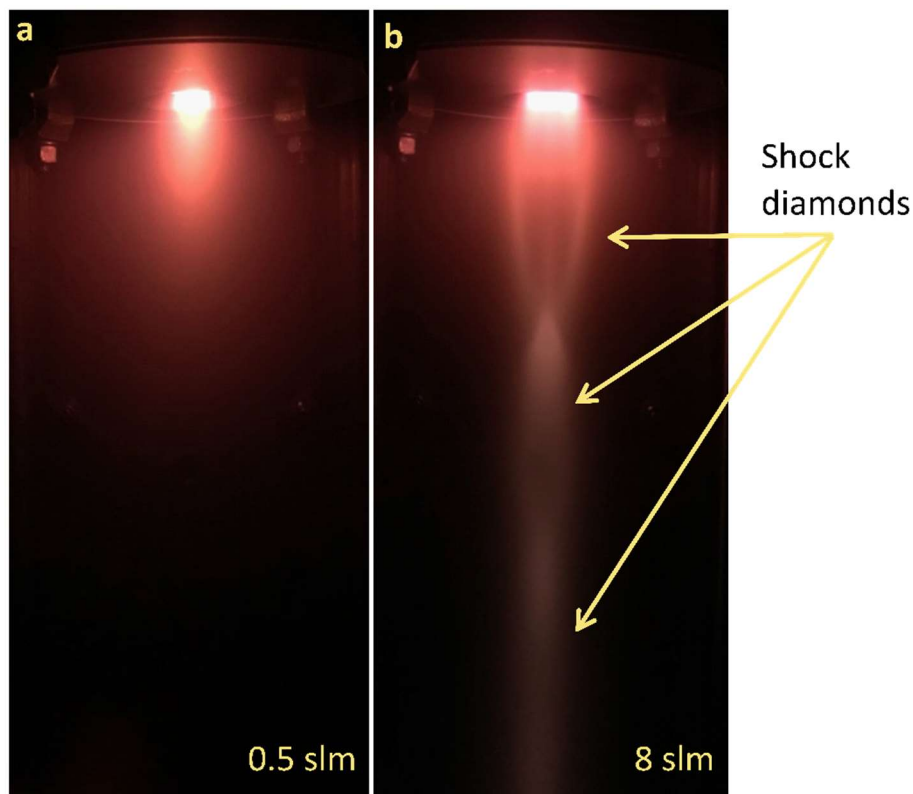


Figure 5.8: Expanding plasma into a low-pressure chamber. Panel (a) represents a subsonic expansion, when a small gas-flow of 0.5 slm argon was expanded through the rectangular outlet. Panel (b) exhibits an increased flow rate of 8 slm argon where the shock diamonds testify for the supersonic characteristic of the flow.

5.6 Preliminary study with carbon monoxide

To characterise the plasma expansion, and to verify the out-of-equilibrium conditions, once again CO was used as a test molecule for spectroscopic study. 0.5 slm of carbon monoxide was admixed with 10 slm of argon and the plasma expansion 20 mm downstream of the nozzle was probed by the CRDS. In this first run, the pressure before the expansion could not be measured, but in the future a pressure tap will allow access to this precious information. The expansion chamber was maintained at 0.05 Torr.

Two sets of R-branch transitions corresponding to the $3 \leftarrow 0$ cold band and to the $5 \leftarrow 2$ hot band were recorded and analysed. Due to the lack of numerical simulations and Pitot measurements, there was no prior understanding of the plasma jet regarding its shape, the Mach number, radial and axial velocity components, *etc.* The increased nozzle outlet section and the absence of the special contoured nozzle profile caused consternation that the “Batman-shaped” lines would return to the spectra.¹⁴ However, it is evident that this phenomenon has been eliminated after analysing the first R0 line corresponding to the $3 \leftarrow 0$ cold band represented in figure (5.9).

Figure (5.9) shows a Gaussian fit over the recorded peak and reveals a remarkably narrow line, with the corresponding FWHM only 0.0056 cm^{-1} . This Doppler width corresponds to a static gas temperature of 41 K. As R0 is only populated in cold flow regions, it contains no information on the potential surrounding hot shear-layers. Consequently, the obtained narrow line suggests that the isentropic core has little radial component.

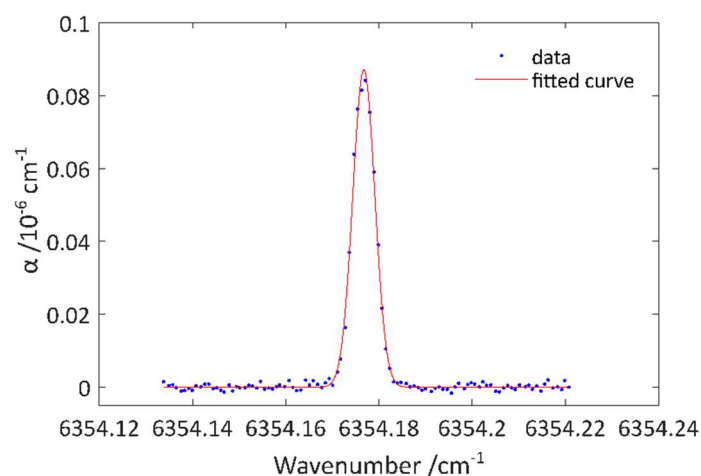


Figure 5.9: Gaussian fit of the R0 line of the 3-0 cold branch revealing a remarkably narrow line (FWHM = 0.0056 cm^{-1}) and a corresponding 41 K static Doppler temperature.

This is not the case for transitions issuing from higher- J rotational levels. Figure (5.10) represents R4 and R5 transitions which both are sensitive not only to the cold contribution of the isentropic core of the plasma jet but the hotter surrounding layers as well. On the left panels the recorded experimental data (blue dots) and a single Gaussian fit (red line) are demonstrated to retrieve higher static temperature values, 51.7 K and 79 K respectively. To distinguish between the two flow regions, the transitions corresponding to higher- J levels had to be fitted with two Gaussians. With this method, the isentropic core has a characteristic temperature of 41(3) K and the shear layers with a 290(10) K, as represented in the right panels of figure (5.10).

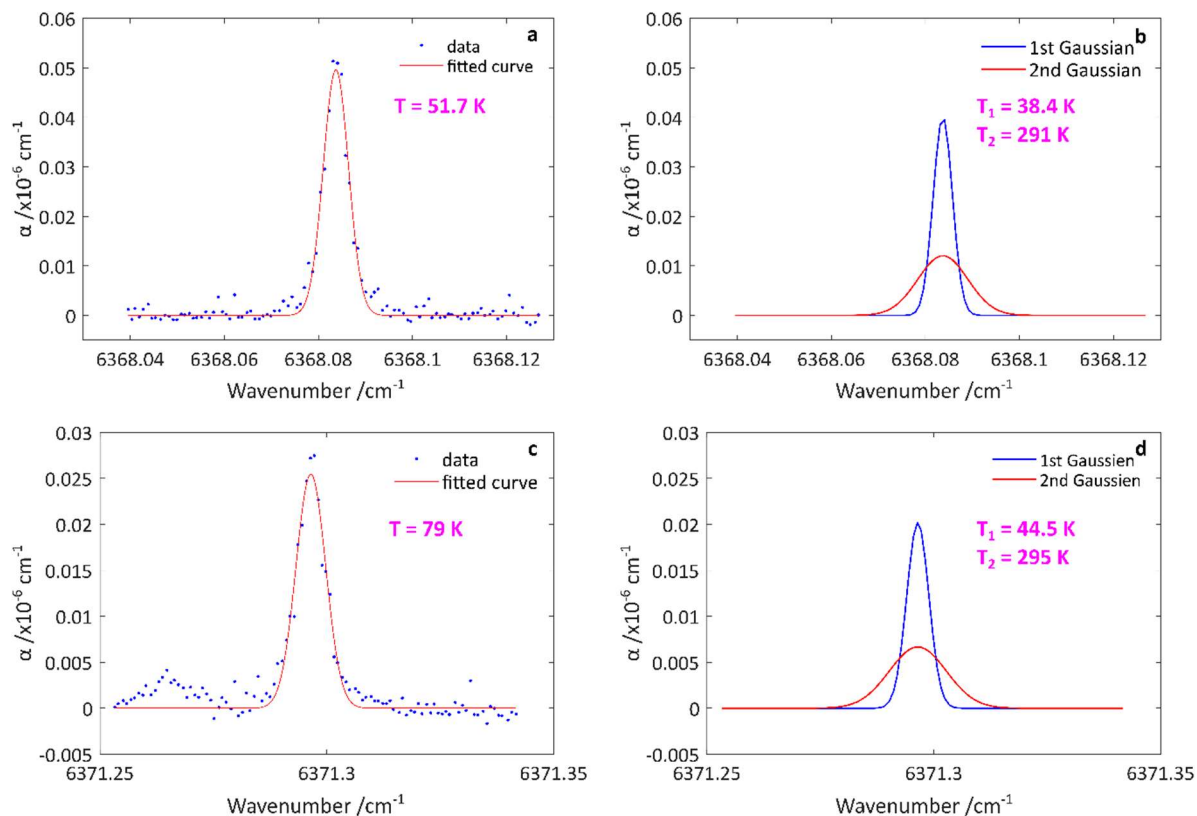


Figure 5.10: Recorded R4 and R5 transitions and the two-Gaussians fitting method to distinguish between the cold isentropic core of the plasma jet and the surrounding shear-layers. Panel (a): recorded R4 data points (blue dots) and the single Gaussian fitted over them (red line). Panel (b): The two-Gaussians method assigns a Gaussian profile for the cold isentropic core (blue) and the hot shear-layers (red). Panel (c): recorded R5 transitions and the corresponding single Gaussian fit. Panel (d): double-Gaussian fit corresponding to the R5 line.

5.6.1 Rotational and vibrational temperatures

Figure (5.11) represents the integrated absorption coefficients corresponding to the recorded $3\leftarrow 0$ cold band (blue) and the $5\leftarrow 2$ hot band (red). The presence of the hot band lines confirms that the high vibrational levels were indeed excited. Conversely, the fact that the most intense lines correspond to $J_{max} = 2$ testifies for a rotationally cold gas.

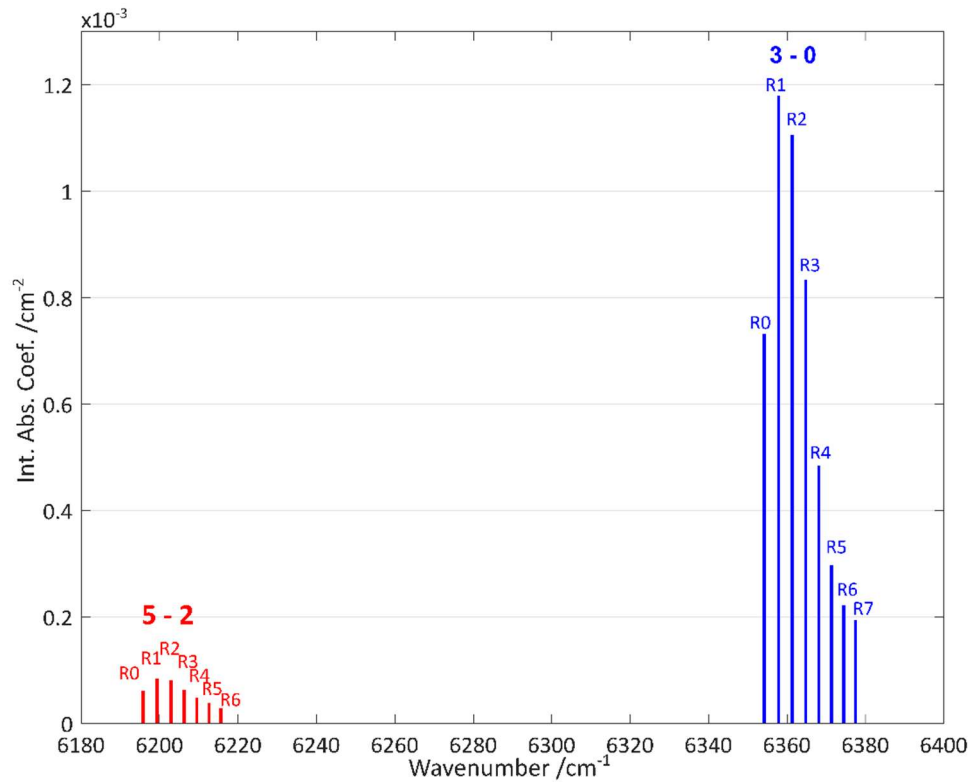


Figure 5.11: Integrated absorption coefficients of the recorded 3-0 cold band (blue) and the 5-2 hot band (red).

The rotational and vibrational temperatures were determined by the usage of the Boltzmann plot method. Figure (5.12) exhibits a remarkably cold rotational temperature of 28(2) K accompanied by an exceptionally high vibrational temperature (over 2300 K) with these results represented in table (5.1). This rotational temperature being below the extracted Doppler temperature of 41(3) K reveals the presence of a small radial component in the isentropic core.

Regarding the different vibrational temperatures, in practice, the values corresponding to the transitions $J = 0, 1, 2$ and 3 and the average retrieved from these temperatures should be considered as the characteristic one. Indeed, they are not perturbed with the contribution of the hot gas from the shear-layer as well as the eventual more significant radial velocity component at the border of the plasma jet and therefore they should deliver a more precise result.

Table 5.1: Vibrational temperatures for each J rotational couples by using the Boltzmann plot method

J level	T_{vib} / K	Average
$R_0 - R_0$	2492	2394 ± 67 K
$R_1 - R_1$	2340	
$R_2 - R_2$	2362	
$R_3 - R_3$	2383	
$R_4 - R_4$	2678	2878 ± 173 K
$R_5 - R_5$	2982	
$R_6 - R_6$	2976	

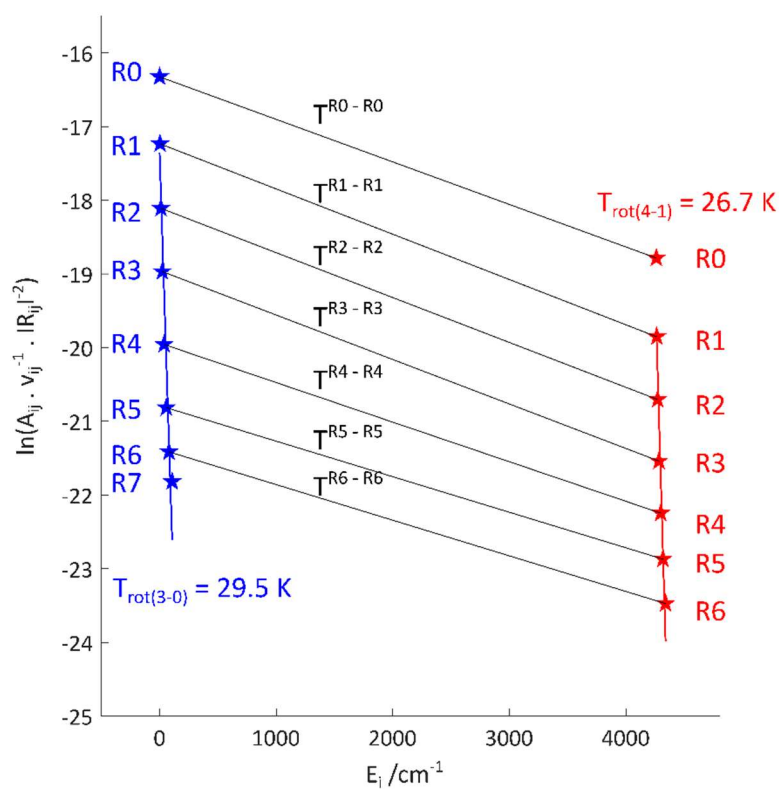


Figure 5.12: Boltzmann-plot of the CO lines recorded in the plasma jet.

5.7 Conclusion

By using carbon monoxide to test our initial assumption, namely that a cold plasma source with a power output of 30 W could deliver a useful out-of-equilibrium plasma jet for spectroscopy, some important results were obtained. In particular, the impressively hot vibrational temperature around 2400 K, combined with a favourably low 28(2) K rotational temperature. Furthermore, it was satisfying to see that the large rectangular nozzle outlet delivers an expansion with high enough density for the CRDS to detect the transitions of CO and at the same time avoid unwanted line broadening.

The future of the platypus project is to follow the same path as the Laval nozzle experiments: to record spectra of vibrationally hot methane. Although, there is a possibility that the methane will partially dissociate in the plasma discharge and would form radicals. Later these radicals could recombine into more complex molecules. The contribution of these new molecules would cause parasitic lines to appear in the absorption spectrum, which would complicate the analysis of the recorded spectra. Despite this, the experimental setup could be used with molecules which had been excluded from study using the HES because of the sensitivity of the graphite heating element. Supplementary development of the platypus source includes upgrading to a newly developed inductively-coupled RF plasma-system which operates at 40.68 MHz¹⁷ instead of the current 13.56 MHz. This new RF source would deliver potentially even higher vibrational temperatures. Alternatively, the shape of the nozzle could be better adapted into a tighter nozzle outlet area, which would result in a higher pressure-ratio downstream-upstream of the throat and accordingly a higher Mach number and lower translational temperature of the plasma jet.

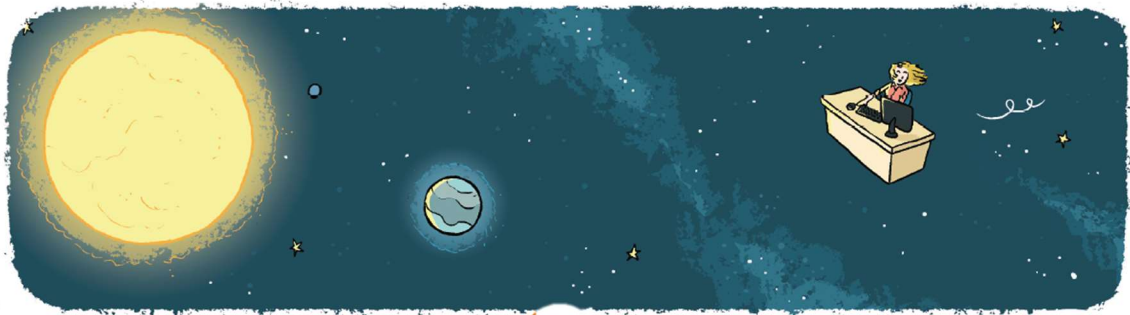
References

- (1) Hoyt, J. K. The Cyclopaedia of Practical Quotationos, English and Latin: With an Appendix Containing Proverbs from the Latin and Modern Foreign Languages ...; Funk & Wagnalls, 1889.
- (2) PLATYPUS | Definition of PLATYPUS by Oxford Dictionary on Lexico.com also meaning of PLATYPUS <https://www.lexico.com/definition/platypus> (accessed May 29, 2021).
- (3) CubeSat <https://www.cubesat.org> (accessed May 29, 2021).
- (4) Lan, W. Document Classification. 34.
- (5) Shkolnik, E. L. On the Verge of an Astronomy CubeSat Revolution. *Nature Astronomy* **2018**, 2 (5), 374–378. <https://doi.org/10.1038/s41550-018-0438-8>.
- (6) Selva, D.; Krejci, D. A Survey and Assessment of the Capabilities of Cubesats for Earth Observation. *Acta Astronautica* **2012**, 74, 50–68. <https://doi.org/10.1016/j.actaastro.2011.12.014>.
- (7) Kak, A.; Akyildiz, I. F. Large-Scale Constellation Design for the Internet of Space Things/CubeSats. In 2019 IEEE Globecom Workshops (GC Wkshps); IEEE: Waikoloa, HI, USA, 2019; pp 1–6. <https://doi.org/10.1109/GCWkshps45667.2019.9024594>.
- (8) Gregorio, A.; Alimenti, F. CubeSats for Future Science and Internet of Space: Challenges and Opportunities. In 2018 25th IEEE International Conference on Electronics, Circuits and Systems (ICECS); 2018; pp 169–172. <https://doi.org/10.1109/ICECS.2018.8617947>.
- (9) Qiao, L.; Glennon, E.; Dempster, A. G.; Chaoui, S. Using Cubesats as Platforms for Remote Sensing with Satellite Navigation Signals. In 2013 IEEE International Geoscience and Remote Sensing Symposium - IGARSS; IEEE: Melbourne, Australia, 2013; pp 852–855. <https://doi.org/10.1109/IGARSS.2013.6721293>.
- (10) Hand, E. CubeSats Promise to Fill Weather Data Gap. *Science* **2015**, 350 (6266), 1302–1303. <https://doi.org/10.1126/science.350.6266.1302>.
- (11) Charles, C.; Tsifakis, D.; Bennet, A.; Boswell, R.; Takahashi, K.; Ando, A.; Braun, W.; Rivas-Davilla, J.; Dudas, E.; Benidar, A.; Rutkowski, L.; Georges, R.; Kassi, S.; Suas-David, N.; Benedicto, J.; Favennec, J.-F.; Rius, E. Laboratory and Space Applications of Expanding Plasmas. In *Laboratory and space applications of expanding plasmas*; Paris, France, 2020.
- (12) Chen, F. F. *Introduction to Plasma Physics and Controlled Fusion*; Springer International Publishing Switzerland, 2018.
- (13) Charles, C.; Boswell, R. W. Measurement and Modelling of a Radiofrequency Micro-Thruster. *Plasma Sources Sci. Technol.* **2012**, 21 (2), 022002. <https://doi.org/10.1088/0963-0252/21/2/022002>.
- (14) Suas-David, N.; Kulkarni, V.; Benidar, A.; Kassi, S.; Georges, R. Line Shape in a Free-Jet Hypersonic Expansion Investigated by Cavity Ring-down Spectroscopy and Computational Fluid Dynamics. *Chemical Physics Letters* **2016**, 659, 209–215. <https://doi.org/10.1016/j.cplett.2016.06.082>.
- (15) Grill, A. *Cold Plasma Materials Fabrication: From Fundamentals to Applications*; Wiley, 1994.
- (16) Rathakrishnan, E. *Applied Gas Dynamics*; John Wiley & Sons, 2019.
- (17) Tsifakis, D.; Charles, C.; Boswell, R. An Inductively-Coupled Plasma Electrothermal Radiofrequency Thruster. *Front. Phys.* **2020**, 8. <https://doi.org/10.3389/fphy.2020.00034>.

Conclusions and perspectives

“Non sum qualis eram”¹

MON TRAVAIL SE FAIT EN COLLABORATION AVEC DES ASTROPHYSICIENS ET DES CHIMISTES THÉORICIENS, QUI ME FOURNISSENT DES PISTES QUE JE PEUX VÉRIFIER COMME SI J'ÉTAIS SUR PLACE, À DES DIZAINES DE MILLIARDS DE KILOMÈTRES !



¹“I am not as I was” - Ernest Dowson

Conclusions

A state-of-art experimental system has been developed and used to produce fundamental information on the hot spectrum of methane, a key molecule in the atmosphere of hot Jupiters, to help the construction of *ab initio* variational theoretical models. Primarily, a new optimised contoured Laval nozzle was designed and manufactured before being implanted into the SMAUG experiment. The goal of this addition was to produce a strong out-of-equilibrium, quasi-unidirectional jet to overcome the drawbacks inherent in free jet expansions. Namely a strong Doppler broadening due to a significant radial velocity component of molecules in the jet and the presence of extreme temperature and density gradients. The performance of the new setup with the nozzle was investigated by means of CFD simulations, 2D Pitot measurements and spectroscopic diagnosis using CO as a tracer molecule. The results demonstrate that the new setup produces a non-LTE quasi-unidirectional hypersonic flow limiting absorption line broadening. The expanded molecules are characterised by high vibrational and low rotational temperatures, thus magnifying the low-*J* rovibrational line intensities of the very many hot bands responsible for the complexity of high temperature infrared spectra of polyatomic molecules.

Next, a non-LTE spectrum of methane was recorded and analysed. After confirming that the non-LTE conditions are also met with this molecule, an in-depth spectroscopic study has been carried out. First of all, the characteristic temperatures were extracted. The cold rotational temperature of 39 K determined with a Boltzmann plot demonstrates effective rotational relaxation and delivers a simplified rotational spectrum structure that allows line-by-line analysis. Regarding the vibrational relaxation, the picture is more complex. Two types of relaxation processes take place in parallel. On one hand, there is a highly efficient intra-polyad relaxation that depopulates the highest vibrational energy levels of each polyad, concentrating the population on the lowest energy levels of each polyad. Conversely, the relaxation between polyads is weak, so that the initial vibrational population remains trapped within each polyad. This phenomenon results in characteristic vibrational temperatures above the reservoir temperature and allows the detection of transitions starting from the pentad and octad. Up to date, 22 new lines have been assigned, however many more lines are yet to be investigated in the recorded spectrum. Further systematic work has to be performed to assign the whole spectrum and to include the newly identified lines in spectroscopic line lists.

In the third part of the thesis, the post-shock CRDS, a novel experimental approach, has been developed to record the high temperature spectrum of methane by probing the gas layer behind a steady shock wave. The shock layer was preliminary investigated by means of CFD simulations and spectroscopic measurements using carbon monoxide as a test molecule revealing conditions close to the LTE conditions. Two spectra of methane were recorded in two different temperature conditions. A preliminary analysis of the methane spectra was performed, showing promising results.

Finally, as a side project to the main SMAUG setup, an alternative heating source was investigated with a view to replacing the HES and to overcome its limitations in terms of the highest achievable temperature as well as the constraint of investigable molecules due to the reactivity of the graphite rod. A collaboration with the SP3 laboratory in Australia provided a

transformed Pocket Rocket plasma source which was installed into SMAUG. The performance of this new technology coupled with the CRDS was investigated by the usage of carbon monoxide molecule once again. The initial results are interesting, since a low rotational temperature of 28 K and a very high vibrational temperature of 2394 K were obtained. This indicates that SMAUG with the pocket rocket could be very useful for future spectroscopic studies.

This thesis focused on the development of experimental approaches to produce high temperature, high-resolution spectral laboratory data and in particular the study of the methane molecule. The accomplished developments and technical innovations contributed to overcome the drawbacks that appeared in the previously investigated free-jet expansion and offered an alternative course to investigate a wider range of molecules than was previously possible. The thesis work successfully delivered unprecedented infrared spectroscopic data of methane and transitions precious to hot radiative transfer models involving the high vibrational energy levels close to 10000 cm^{-1} .

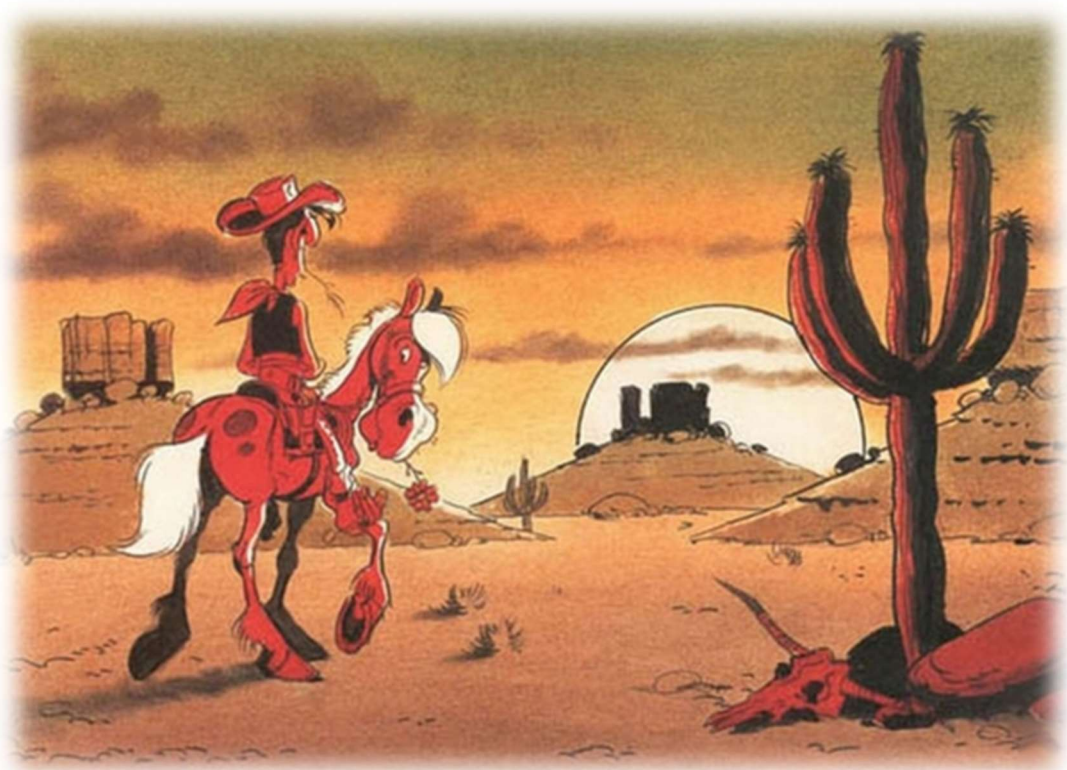
Perspectives

The recorded spectra of methane have yet to be fully investigated and the remaining information will be evaluated in the near future. This thesis was interested in the methane molecule, but SMAUG is ready to receive other hydrocarbons such as acetylene, the presence of which has already been confirmed in the atmosphere of hot Jupiters, or ethylene and ethane which are suspected to be present there.

From a technical point of view, in order to increase the absorption path length of the cold, isentropic part of the cavity, a planar nozzle is currently under development which will be equipped with a new ceramic heating system. This new method of producing a planar jet will considerably reduce the contribution of the shear-layers in the recorded spectrum, therefore facilitating straightforward analysis. At the same time, the sensitivity of the system will grow and transitions which could have been hidden in the current setup will become detectable. Lastly, substituting the graphite heating element with a ceramic one will allow investigations of numerous new oxidizing molecules.

In addition, the platypus plasma source must be explored in future studies. Firstly, the spectrum of methane should be recorded and compared to that recorded using the HES. This future spectrum will contain information on even higher vibrational energy states, involving very high polyads. Alternatively, the transformed Pocket Rocket could contribute to the investigation of the efficiency of miniaturized propulsion systems. Solid fuels provide a high amount of energy in a small volume which through electrothermal heating, such as in the Pocket Rocket, forms a high temperature plasma. The propulsion efficiency relies on optimal conversion of thermal energy into the translational energy of the ionized gas in order to move the satellite. Our collaborating research partners at the ANU in Canberra have already carried out promising early push tests and have high hopes for naphthalene ($C_{10}H_8$) as a plasma source. Naphthalene is the simplest of the polycyclic aromatic hydrocarbons (PAHs) that are thought to be ubiquitous in the interstellar medium and also thought to be partly responsible for the famous diffuse interstellar bands that have intrigued astrophysicists for a century. SMAUG, with its innovative diagnostic system would allow a precise study on how the thermal energy initially imparted to naphthalene by the microwave discharge is distributed into the translational, rotational and vibrational energy levels of the gaseous molecules. Remark that only the translation of the molecules acts on driving the satellite; the energy trapped in the rotation and vibration is unfortunately wasted. Probing plasma flows of naphthalene with CRDS would allow a precise determination of which degrees of freedom the energy of the naphthalene molecules is distributed to during the propulsion phase. Simultaneously, the produced infrared data could be used to model the very complex molecular structure of $C_{10}H_8$ at high temperature.

The End





Annexes


High-temperature hypersonic Laval nozzle for non-LTE cavity ringdown spectroscopy F

Cite as: J. Chem. Phys. **152**, 134201 (2020); <https://doi.org/10.1063/5.0003886>

Submitted: 05 February 2020 . Accepted: 09 March 2020 . Published Online: 01 April 2020

Eszter Dudás, Nicolas Suas-David, Shuvayan Brahmachary , Vinayak Kulkarni, Abdessamad Benidar, Samir Kassi, Christine Charles , and Robert Georges 

COLLECTIONS

 This paper was selected as Featured



View Online



Export Citation



CrossMark

ARTICLES YOU MAY BE INTERESTED IN

[SMAUG helps generate infrared spectroscopy data for Hot Jupiter-type exoplanets](#)

Scilight **2020**, 141106 (2020); <https://doi.org/10.1063/10.0001091>

[A uniform flow-cavity ring-down spectrometer \(UF-CRDS\): A new setup for spectroscopy and kinetics at low temperature](#)

The Journal of Chemical Physics **151**, 244202 (2019); <https://doi.org/10.1063/1.5125574>

[High-resolution infrared spectroscopy of jet cooled CH₂Br radicals: The symmetric CH stretch manifold and absence of nuclear spin cooling](#)

The Journal of Chemical Physics **152**, 134305 (2020); <https://doi.org/10.1063/5.0002165>

Lock-in Amplifiers
up to 600 MHz



Watch



High-temperature hypersonic Laval nozzle for non-LTE cavity ringdown spectroscopy



Cite as: J. Chem. Phys. 152, 134201 (2020); doi: 10.1063/5.0003886

Submitted: 5 February 2020 • Accepted: 9 March 2020 •

Published Online: 1 April 2020



Eszter Dudás,¹ Nicolas Suas-David,^{1,a)} Shuvayan Brahmachary,² Vinayak Kulkarni,² Abdessamad Benidar,¹ Samir Kassi,³ Christine Charles,⁴ and Robert Georges^{1,b)}

AFFILIATIONS

¹Univ Rennes, CNRS, IPR (Institut de Physique de Rennes) - UMR 6251, F-35000 Rennes, France

²Department of Mechanical Engineering, Indian Institute of Technology Guwahati, Guwahati, India

³Université Grenoble Alpes, LIPhy, F-38000 Grenoble, France and CNRS, LIPhy, F-38000 Grenoble, France

⁴Space Plasma, Power and Propulsion Laboratory (SP3), Research School of Physics, The Australian National University, Canberra, ACT 2601, Australia

^{a)}Now at: Leiden Observatory, Laboratory for Astrophysics, NL 2333 CA Leiden.

^{b)}Author to whom correspondence should be addressed: robert.georges@univ-rennes1.fr

ABSTRACT

A small dimension Laval nozzle connected to a compact high enthalpy source equipped with cavity ringdown spectroscopy (CRDS) is used to produce vibrationally hot and rotationally cold high-resolution infrared spectra of polyatomic molecules in the 1.67 μm region. The Laval nozzle was machined in isostatic graphite, which is capable of withstanding high stagnation temperatures. It is characterized by a throat diameter of 2 mm and an exit diameter of 24 mm. It was designed to operate with argon heated up to 2000 K and to produce a quasi-unidirectional flow to reduce the Doppler effect responsible for line broadening. The hypersonic flow was characterized using computational fluid dynamics simulations, Pitot measurements, and CRDS. A Mach number evolving from 10 at the nozzle exit up to 18.3 before the occurrence of a first oblique shock wave was measured. Two different gases, carbon monoxide (CO) and methane (CH_4), were used as test molecules. Vibrational (T_{vib}) and rotational (T_{rot}) temperatures were extracted from the recorded infrared spectrum, leading to $T_{\text{vib}} = 1346 \pm 52$ K and $T_{\text{rot}} = 12 \pm 1$ K for CO. A rotational temperature of 30 ± 3 K was measured for CH_4 , while two vibrational temperatures were necessary to reproduce the observed intensities. The population distribution between vibrational polyads was correctly described with $T_{\text{vib}}^{\text{I}} = 894 \pm 47$ K, while the population distribution within a given polyad (namely, the dyad or the pentad) was modeled correctly by $T_{\text{vib}}^{\text{II}} = 54 \pm 4$ K, testifying to a more rapid vibrational relaxation between the vibrational energy levels constituting a polyad.

Published under license by AIP Publishing. <https://doi.org/10.1063/5.0003886>

I. INTRODUCTION

High-temperature infrared (IR) spectroscopy provides laboratory data that are essential for determining the properties of the atmospheres of Hot Jupiter type exoplanets.^{1–3} Until now, two decades after the discovery of the first exoplanet,⁴ carbon monoxide, carbon dioxide, methane, and water have been directly observed in Hot Jupiter atmospheres by infrared astronomy,⁵ which implies the possibility of a rich chemistry as well as an active photochemistry. Accurate laboratory infrared (IR) spectroscopic data in the temperature range of 500–3000 K for small hydrocarbons, such as acetylene, methane, ethylene, and ethane, are, therefore, believed to be

pivotal to interpret the observed spectra.¹ However, the spectral confusion, characterizing high-temperature local thermal equilibrium (LTE) spectra of polyatomic molecules produced by either absorption⁶ or emission⁷ spectroscopic techniques, greatly complicates the spectral analysis and hampers the development of high-temperature molecular databases.

We have developed a novel approach to produce non-LTE IR spectra, relying on a hypersonic expansion probed by cavity ringdown spectroscopy (CRDS). The Spectroscopy of Molecules Accelerated in Uniform Gas flow (SMAUG) apparatus has been developed to decouple the internal degrees of freedom of polyatomic molecules in order to record vibrationally hot but rotationally and

translationally cold IR spectra, resulting in both a simplified rotational structure and a reduced Doppler-broadening of the absorption lines (see Fig. 1).

Non-LTE processes characterizing rapidly expanding gases have been widely used for spectroscopic purposes. The gasdynamic lasers developed in the 1970s are based on the non-equilibrium distribution of a population of polyatomic molecules such as CO or CO₂.⁸ An expansion in a supersonic nozzle rapidly cools down a gas mixture (e.g., CO₂-N₂-H₂O or CO₂-N₂-He), but as the vibrational relaxation is comparatively slow, this cooling leads to a population inversion resulting in an amplification of the radiative intensity of light emitted by the molecules. From a spectroscopic point of view, such a lasing action triggered by the excitation of water molecules in a supersonic plasma contained in an optical supercavity was used to record rotationally cold spectra of vibrationally excited H₂O⁹ and D₂O¹⁰ in the mid-infrared and far infrared regions, respectively. The rotational and vibrational temperatures associated with the pulsed slit supersonic discharge source were estimated to be 120 K and 2500 K, respectively. A pulsed supersonic planar plasma jet was also used to produce high-resolution infrared cw-CRDS spectra of vibrationally excited HC₄H¹¹ with a rotational temperature of 17 K and vibrational excitation temperatures of 125 K and 570 K, depending on the considered bending vibrations. Vibrationally excited state spectroscopy of NO in a pinhole supersonic plasma was also reported by Bazalgette Courrèges-Lacoste *et al.*¹² with $T_{\text{rot}} < 50$ K and $T_{\text{vib}} = 6700 \pm 700$ K.

Excitation sources besides plasma ones have also been used to produce non-LTE conditions. Intermolecular vibrational energy transfer from ethylene to acetylene was investigated in the 3 μm region by probing a supersonic jet with an IR-IR double resonance technique, producing rotationally cold hot-bands.¹³ Thermally heated nozzles, either axi-symmetric^{14,15} or planar,¹⁶ were

used to supply the preheat gases before their adiabatic cooling in supersonic jet expansions. In close connection with our investigations on infrared spectroscopy of simple hydrocarbons, it is worth mentioning the early study on non-LTE methane by Bronnikov *et al.*¹⁷ They used a thermally heated pulsed slit nozzle to produce non-LTE diode laser spectra of vibrationally excited methane in the 8 μm region. This study highlighted a virtual absence of vibrational relaxation between the different polyads, while a strong vibrational relaxation within the same polyad leads to a redistribution of the populations of the vibrational levels involved.

The tetradecad region of supersonically cooled preheated methane was previously investigated at the Institute of Physics of Rennes (IPR) in a free jet expansion by means of CRDS.¹⁵ A strong decoupling of the internal degrees of freedom ($T_{\text{rot}} = 13$ K and $T_{\text{vib}} = 750$ K) was responsible for the emergence of multiple rotationally cold hot bands in the recorded spectra, which allowed the identification of new transitions connecting highly excited vibrational energy levels. Such a strong non-LTE state is based on fast rotational-translational (R-T) and quite inefficient vibrational-translational (V-T) collisional energy transfers taking place during the adiabatic hypersonic expansion of a thermally preheated gas.¹⁸ Spectra recorded in such conditions exhibit a simplified rotational structure that allows the performance of a line-by-line analysis of the multiple hot bands, characterizing polyatomic molecular spectra, which is unattainable under LTE conditions due to the presence of multiple overlapping transitions.

To improve the original non-LTE experiment developed at the IPR,¹⁵ a mini graphite Laval nozzle, which can withstand high stagnation temperatures, was implemented into the system to overcome the drawbacks inherent to free jet expansion, that is, strong Doppler broadening due to a significant radial velocity component of the molecules in the jet and the presence of extreme temperature and density gradients. Similarly, to record the spectra of exotic isotopes and super-heavy elements, a small Laval nozzle was used with the in-gas laser ionization and spectroscopy (IGLIS) technique to reduce the adverse effect of the Doppler broadening that impedes the detection of transitions with close frequencies.¹⁹

This paper presents the SMAUG apparatus, our approach to produce out-of-equilibrium spectra by coupling a hypersonic jet issued from a mini graphite Laval nozzle with an ultrasensitive CRDS, and its performance based on the analysis of the recorded CO and CH₄ hypersonic-jet spectra.

II. LAVAL NOZZLE DESIGN

A. Profile calculation

In our experiments, the probe laser beam is positioned a few centimeters downstream from the outlet of the nozzle and perpendicular to its axis. Non-divergence of the outlet flow of the nozzle is, therefore, a prerequisite for avoiding gradients in the direction perpendicular to the flow axis, which would complicate the interpretation of the absorption spectrum as a result of transition line broadening of the absorbing species by the Doppler effect. Therefore, the aim was to design a small nozzle profile that provides a non-divergent hypersonic argon flow into a vacuum chamber by connecting its inlet area to the IPR high enthalpy source (HES) capable of reaching gas temperatures up to 2000 K.^{20,21}

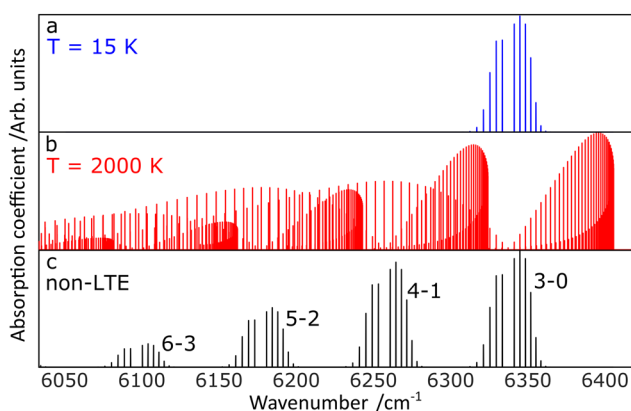


FIG. 1. Spectra of CO simulated at different conditions highlighting the advantage of non-LTE spectroscopy. Panel (a): spectrum simulated at 15 K showing a simplified rotational structure but a lack of information regarding the molecular vibration (total absence of hot bands). Panel (b): spectrum simulated at 2000 K showing overlapping vibrational cold ($3 \leftarrow 0$) and hot ($4 \leftarrow 1$; $5 \leftarrow 2$; $6 \leftarrow 3$) bands, each characterized by a large number of rotational transitions that complicate the spectrum. Panel (c): spectrum simulated in non-LTE conditions $T_{\text{rot}} = 15$ K and $T_{\text{vib}} = 2000$ K, resulting in a simplification of the rotational structure and an easier analysis of the different observed bands.

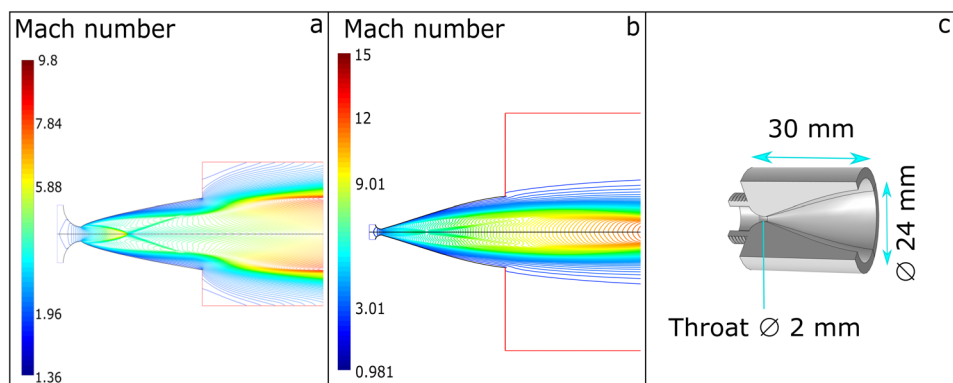


FIG. 2. Argon Laval nozzle design. The CFD simulations were carried out at a stagnation temperature of 1300 K and at a stagnation pressure of 1100 Torr. The expansion chamber was set at 300 K and 0.5 Torr. Panel (a): CFD simulation of the Mach number with a fixed zero transverse nozzle exit velocity. Panel (b): CFD simulation of the Mach number with a transverse nozzle exit velocity set to 1.5% of the magnitude of the total flow velocity. Panel (c): sectional view of the graphite Laval nozzle.

The profile design is carried out in two steps. In the first step, the argon flow was considered to be quasi-one dimensional, steady, inviscid, and fully isentropic. These assumptions help us to use the quasi-one-dimensional nozzle flow relations to determine a preliminary nozzle profile using the steepest-descent optimization method. These calculations made use of the known design parameters for the nozzle flow as reservoir conditions, inlet area, outlet area, and length of the divergent part. Radial velocity minimization was the objective function of this optimization process. Initially, radial velocity at the outlet plane was set to zero to ensure the radial uniformity of the flow, and the final profile was obtained. In the second step of the profile design, this optimum shape was tested through Computational Fluid Dynamics (CFD) simulations based on the Navier–Stokes equations for the viscous flow. The simulation revealed the presence of an oblique shock wave inside the divergent part of the nozzle, causing a recompression of the flow and its subsequent radial expansion at the nozzle exit. [Figure 2\(a\)](#) shows the flow to be non-isentropic and non-uniform. To overcome this problem, the constraint on the radial component of velocity at the nozzle outlet, set in the first step of optimization, was relaxed and set to 1.5% of the total velocity at the nozzle exit. Thus, the obtained nozzle profile was again tested in the second step through CFD simulations, which showed suppression of the oblique shock wave and uniform flow at the nozzle outlet [as shown in [Fig. 2\(b\)](#)]. Following this simulated design, the nozzle was locally machined from isostatic graphite (R6710 grade), which can withstand very high temperatures, and was fixed to the HES via an outer thread on the outside of its convergent part [see [Fig. 2\(c\)](#)]. Our nozzle prototype is characterized by a throat diameter of 2 mm and by an outlet diameter of 24 mm, while the length of its divergent part is 30 mm.

B. CFD simulations and flow field analysis

The performance of the prototype nozzle was first verified by CFD axis-symmetric simulations carried out with the commercial solver ANSYS Fluent. Modeling the gas flow from the nozzle inlet through the expansion gives a first insight into the jet characteristics related to the intended operational conditions. The stagnation or reservoir temperature and pressure were set to the same values as considered in the design process, 1300 K and 1100 Torr, respectively. The expansion chamber was defined to be at ambient

temperature (300 K) and at a low pressure (0.5 Torr). [Figure 3](#) shows the simulated temperature contour and the evolution of the Mach number along the central streamline of the expanding flow, downstream of the nozzle exit. As shown in this figure, the jet consists of a hot shear layer of several hundred kelvins surrounding the cold isentropic core where the maximum temperature is of the order

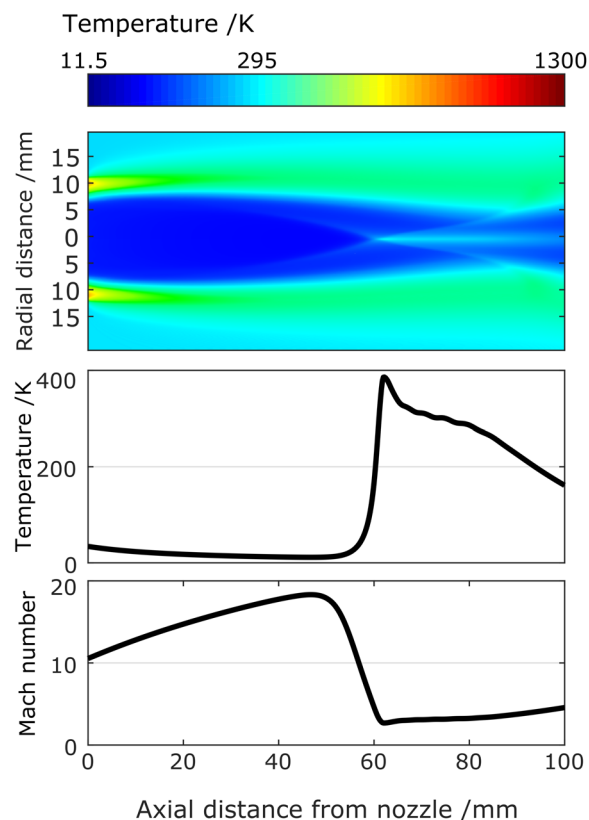


FIG. 3. CFD simulation of the hypersonic jet of argon (stagnation temperature: 1300 K, stagnation pressure: 1100 Torr, and residual pressure: 0.5 Torr). Upper panel: temperature mapping, middle panel: temperature along the jet axis, and lower panel: the Mach number along the jet axis.

of few tens of kelvins. The simulated isentropic core of the jet is quasi-uniform over a distance exceeding 40 mm before an oblique shock wave forms at about 60 mm downstream of the exit. From a practical point of view, it means that the probe laser beam has to

be positioned between the nozzle exit and before the disturbances induced by the oblique shock wave. Interestingly, the Mach number of the flow increases monotonically from 10 at the nozzle exit up to a value of 18.3 right before the occurrence of the oblique shock wave.

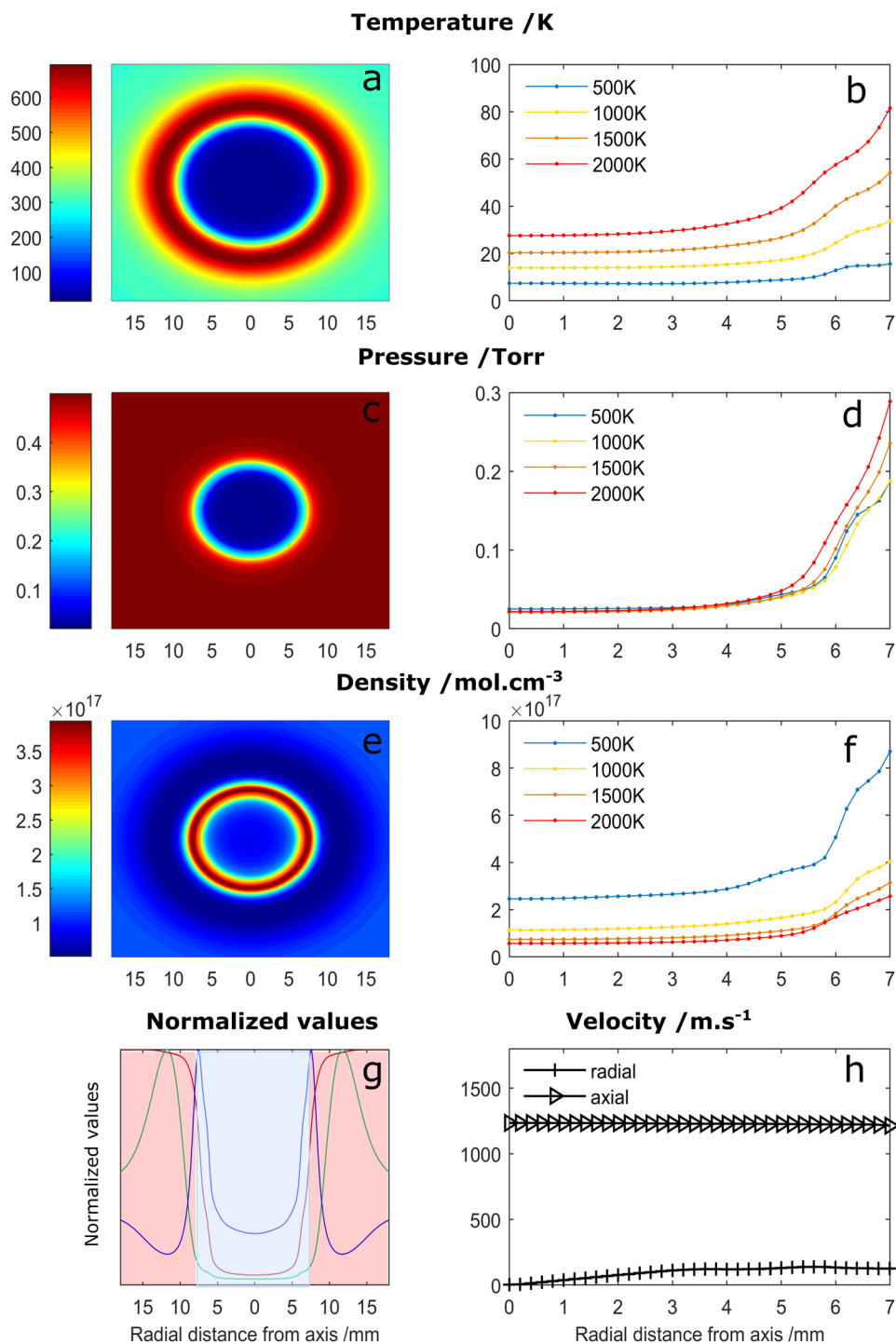


FIG. 4. Cross section CFD simulations of the hypersonic jet of argon 20 mm from the nozzle exit (stagnation pressure: 1100 Torr and residual pressure: 0.5 Torr). Left panels: stagnation temperature fixed at 1300 K. Right panels: zoomed-in view of the isentropic core. Panel (a): temperature cross section. Panel (b): radial temperature. Panel (c): static pressure cross section. Panel (d): radial static pressure. Panel (e): molecular density cross section. Panel (f): radial molecular density. Panel (g): normalized radial temperature (green curve), pressure (red curve), and molecular density (blue curve). The blue zone corresponds to the cold flow zone. Panel (h): evolution of the radial and axial velocity components for a stagnation temperature of 1300 K.

According to the conservation of energy, the temperature follows the inverse trend as that of the Mach number. Therefore, the temperature decreases monotonically from the nozzle exit, where it is at 34 K, before reaching the remarkably low value of 11.5 K in front of the shock wave.

As mentioned earlier, the purpose of designing the Laval nozzle shape was to reduce the radial temperature, density, and pressure gradients. Figure 4 shows the radial flow field obtained from CFD simulations at a distance of 20 mm from the nozzle exit. The temperature contour, shown in panel (a), exhibits two clearly distinct zones of the expansion, viz., the cold isentropic core and the surrounding hotter shear layer. A closer insight of the cold zone [panel (b)] confirms that the core is free of temperature gradients over a radius of about 5 mm. Panel (b) also shows that the core temperature remains uniform, regardless of the initial stagnation temperature. Hence, the jet temperature can be tuned by simply changing the stagnation temperature using the presently designed nozzle profile.

The pressure distribution of the flow is represented in panel (c). The slight radial velocity divergence that was imposed at the nozzle outlet area to eliminate the oblique shockwave within the divergent part of the nozzle is responsible for a jet static pressure of ~ 0.05 Torr that is well below the static pressure of the vacuum chamber (0.5 Torr). Panel (d) shows the pressure distribution in the cold core for different stagnation temperatures varied between 500 K and 2000 K. Unlike the temperature, the static pressure of the cold core does not vary with the initial stagnation temperature because the stagnation pressure was systematically maintained at 1100 Torr in all simulations.

The evolution of the density (i.e., argon concentration) in the jet was also examined [see panel (e)]. The simulation reveals an important increase in the gas density along the jet radius, similar to the gas temperature increase induced by the presence of the shear layers. This can be problematic as CRDS probes the flow along a line of sight, which crosses both the isentropic core and the shear layers, the latter producing an unwanted hot gas contribution to the integrated absorption spectrum. Fortunately, as shown from panel (g), the density and the temperature peaks are shifted by several millimeters so that a significant part of the density corresponds to a very cold flow region. The respective absorption contributions of the cold and hot flow regions [blue and red zones in panel (g)] are simulated in Fig. 5 using a numerical procedure described in Ref. 22. This shows that the hot contribution may not be negligible compared to the cold one. However, the experimental spectrum [panel (b)] shows that the calculated hot gas contribution is clearly overestimated by a factor of almost 2.5. Panel (f) demonstrates the range of achievable molecular densities by setting different initial conditions in the reservoir.

Finally, the axial and radial velocity components are compared in panel (h). A slight increase in the radial component can be observed as a function of the radial distance, but its value (about 130 m/s) remains one order of magnitude smaller than the axial velocity component (1230 m/s). According to the relation

$$\tilde{\nu}' = \tilde{\nu} / \left(1 \pm \frac{v_{\perp}}{c} \right),$$

where c is the speed of light, the Doppler FWHM induced by a radial velocity $v_{\perp} = 130$ m/s is estimated to be 0.0026 cm^{-1} for a line

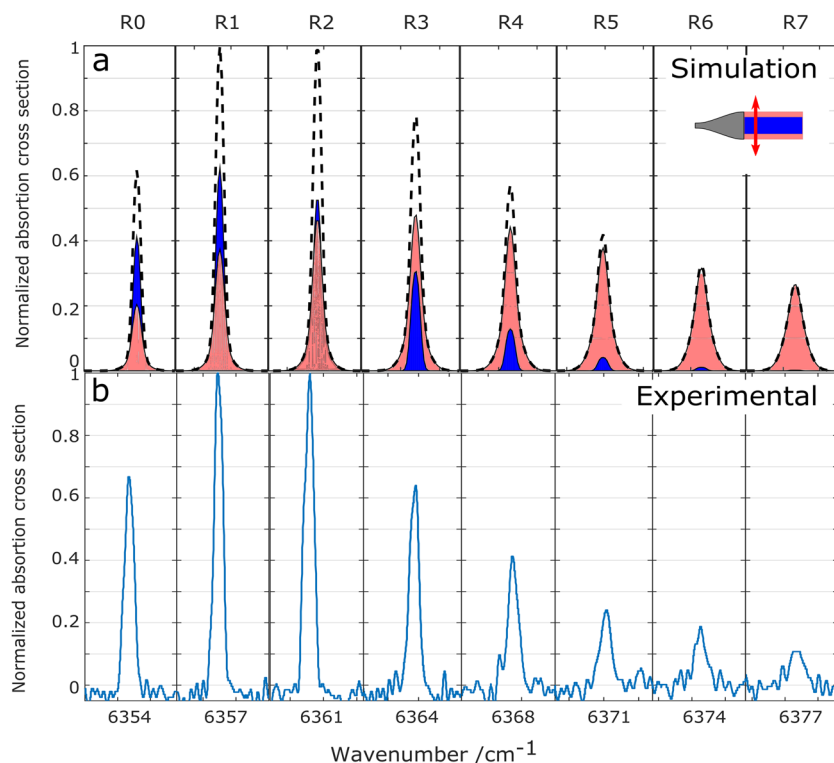


FIG. 5. Absorption contribution of the cold and hot flow regions. Panel (a): simulated IR spectra of the CO $3 \leftarrow 0$ cold band. Blue area: cold flow region, pink area: hot flow region, and dotted line: sum of the cold and hot contributions. Panel (b): experimental results showing the combined hot and cold spectra.

centered at $\tilde{\nu} = 5885 \text{ cm}^{-1}$. For reference, such a line broadening is equivalent to a Doppler FWHM, corresponding to static methane maintained at 6 K.

C. 2D pitot probe

The flow was characterized experimentally by Pitot pressure measurements. A movable Pitot probe was implemented to establish a two-dimensional mapping of the impact pressure of the jet issued from the nozzle. Assuming an isentropic expansion and knowing the stagnation pressure, the Mach number of the flow is extracted from the measured data²³ (see Fig. 6). The velocity, the temperature, the pressure, and the molecular density of the gas are hence calculated from the measured Mach number, the specific heat ratio of argon (fixed to 5/3) and the stagnation conditions (temperature, pressure, and molecular density) using the standard isentropic equations for

an ideal gas.²⁴ It must be noted that this procedure is no longer valid for non-isentropic flows; in particular, it is not suitable for characterizing the shear layers that are sites of non-isentropic dissipative effects. Thus, numerical values relative to the shear layer indicated in Fig. 6 are not realistic.

Figure 6 displays the retrieved values from the Pitot measurements. They agree with the simulation shown in Fig. 3: a regular shock wave intersection is formed at few tens of millimeters ($\sim 80 \text{ mm}$) downstream the nozzle exit, the radial uniformity of the flow is confirmed, and the increase in the monotonic Mach number along the flow axis is also confirmed.

III. HYPERSONIC-JET CRDS

A. Experimental setup

The experimental setup is schematized in Fig. 7; its full description can be found in Ref. 15. Briefly, it is composed of a heating element (the HES)²⁰ used to preheat the argon gas admixed with IR active molecules (CO and CH₄ in the present study) before its expansion through the nozzle in a vacuum chamber evacuated by an ensemble of roots pumps. The hypersonic flow is probed transversally by CRDS.

The carrier argon gas and the CO or CH₄ absorbing species are admitted independently into the HES through mass flow controllers (Bronkhorst and MKS instruments). The HES is mounted on a stainless-steel tank whose position can be adjusted vertically and horizontally using computer-controlled actuators, allowing the CRDS laser to probe any region of the flow.

The laser light is produced by a series of fibered Distributed Feedback (DFB) diode lasers. They are mounted on a custom proportional integral differential (PID) temperature stabilizer that allows the diode temperature to be set from -10°C to 60°C and to produce a bandwidth of 7 nm ($\sim 30 \text{ cm}^{-1}$) per diode. The optical power output of the diodes varies typically between 10 mW and 20 mW, and it is divided in two parts: 90% enters the optical cavity and 10% goes into a fast high-precision wavelength meter (High-Finesse WS7-60 Series). The high-finesse cavity ($\mathcal{F} > 200\,000$) of CRDS relies on two high-reflectivity ($>99.9987\%$, Layertec) mirrors mounted onto bellows that are attached to the end of two stainless-steel tubes. The bellows dampen vibrations caused by the pumping unit. The two tubes are extended on either side of the gas jet in order to reduce the unwanted absorption of the static residual gases filling the expansion chamber. In these tubes, nitrogen is continuously injected at a low flow rate of 2 slm to flush out the IR absorbing gases so that the recorded absorption signal is mainly due to the isentropic core and the shear layers. With the isentropic core diameter being $\sim 10 \text{ mm}$, a typical ringdown time of $120 \mu\text{s}$ corresponds to an equivalent absorption length of $\sim 450 \text{ m}$. A single lens and two steering mirrors (not shown in Fig. 7) fixed onto an optical table adjacent to the cavity entry are used to focus the light beam at the center of the 80 cm long optical cavity and to align the system into the TEM₀₀ mode. At the other end of the optical cavity, the output mirror is installed onto a piezoelectric transducer that resonates at 50 Hz and modulates the cavity length in order to ensure resonance with the instantaneous laser frequency. Each ringdown event is measured by using a photodiode and fitted to an exponential decay curve to retrieve the ringdown time and thus the absorption coefficient.

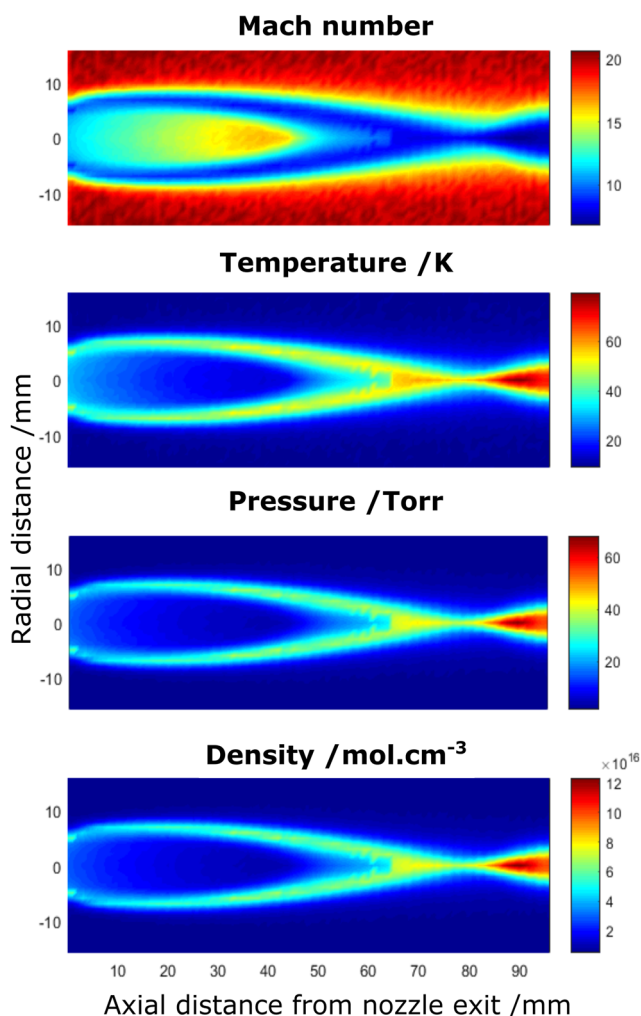


FIG. 6. Mappings extracted from two-dimensional Pitot measurements of a hypersonic flow of argon (stagnation pressure: 1290 Torr, and pressure chamber: 0.5 Torr).

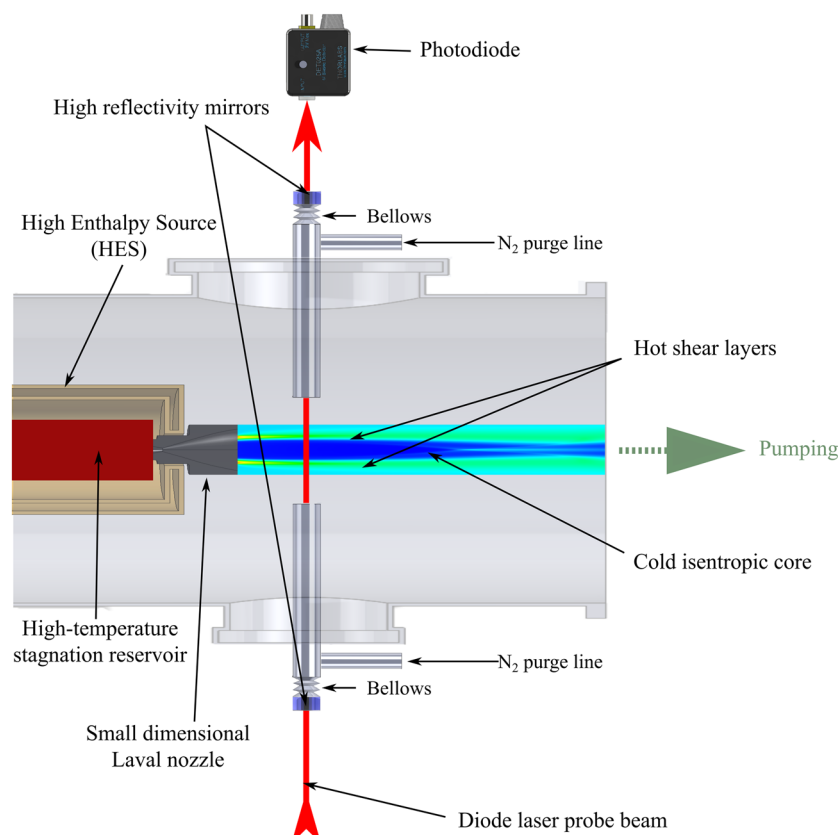


FIG. 7. Schematic of the SMAUG experimental setup showing the main components (from left to right): the HES terminated by the Laval nozzle and the CRDS diagnostic probing the hypersonic flow.

The stagnation and vacuum chamber are measured by using resistive (KELLER, 7500 Torr full scale range) and capacitive (MKS instruments, 10 Torr full scale range) pressure gauges, respectively.

B. Preliminary study on carbon monoxide

The performance of the experimental setup in terms of rotational and vibrational relaxation was first tested with carbon monoxide (CO) molecules. The gas mixture (5% CO in argon) was initially heated up to around 1400 K at 1010 Torr before being expanded into the vacuum chamber maintained at 0.5 Torr. The $3 \leftarrow 0$ cold band and the $4 \leftarrow 1$ and $5 \leftarrow 2$ hot bands were recorded. According to a standard Boltzmann plot method,¹⁵ the rotational temperature of the isentropic core ($T_{\text{rot}}^{\text{core}} = 12 \pm 1$ K) and the surrounding shear layer ($T_{\text{rot}}^{\text{sl}} = 144 \pm 10$ K) were retrieved. Note that the rotational temperature of the isentropic core is very similar to the translational temperature determined by Pitot probe measurements, suggesting a rapid rotational relaxation of CO. The obtained rotational temperature in the shear layer is much colder than the one calculated by CFD simulations (up to 700 K at 20 mm from the nozzle exit, see Fig. 4). Such a discrepancy most probably originates from the fact that the Boltzmann plot method delivers one single value which is integrated over the various probed spatial layers having different temperature and density values [see Fig. 4, panel (g)].

A much higher vibrational temperature ($T_{\text{vib}}^{\text{core}} = 1346 \pm 52$ K) was extracted from the recorded spectra by considering absorption lines of an identical lower J rotational quantum number from different cold and hot vibrational bands. As expected, the sudden drop of molecular collisions in the jet prevents the molecules from relaxing their vibrational energy.

IV. APPLICATION TO NON-LTE SPECTROSCOPY OF METHANE

A. LTE vs non-LTE spectra

The hypersonic spectrum of methane was recorded in the region corresponding to the tetradecad polyad.²⁵ As described by Rey *et al.*,²⁶ the complexity of studying this region lies in the overlapping of several cold bands, ending on the IR active vibrational energy levels of the 14 interacting components of the polyad, and of several hot bands issued from the thermally populated dyad and pentad polyads ending respectively on the poorly studied upper icosad and triacontad polyads.

The stagnation pressure was fixed to 1040 Torr for the stagnation pressure. 2 slm of CH_4 was admixed to 19 slm of argon. The chamber pressure was set to 0.5 Torr. The spectral ranges 5884–6073 cm^{-1} , 6120–6140 cm^{-1} , and 6193–6219 cm^{-1} corresponding to our available laser diodes were systematically examined, giving

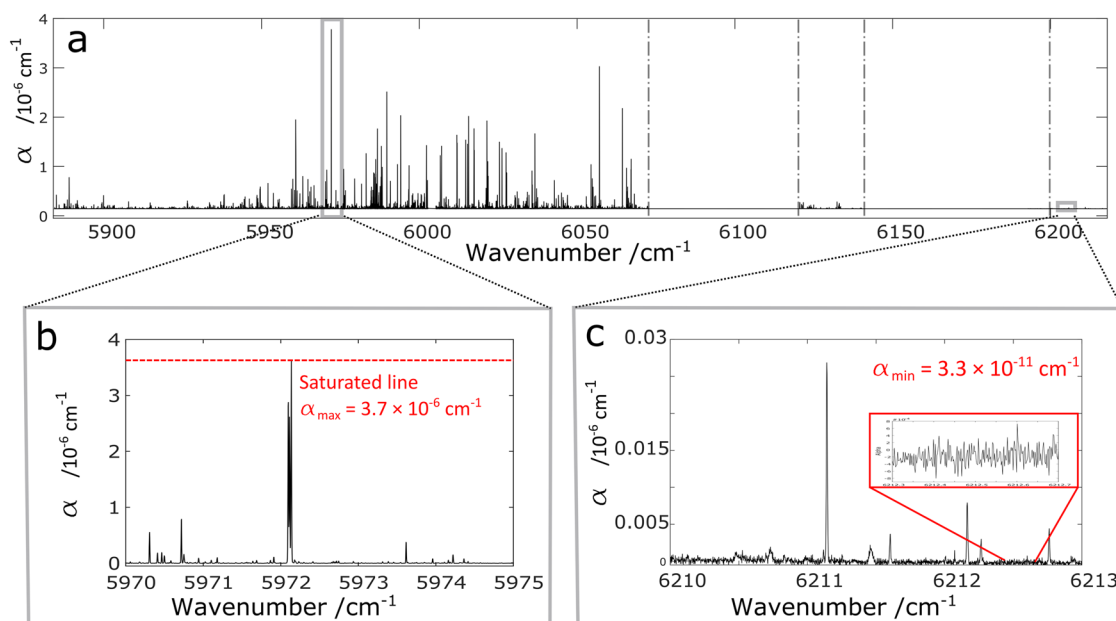


FIG. 8. Panel (a): recorded hypersonic jet CH_4 spectra over the 5884–6219 cm^{-1} range. Panel (b): part of the recorded spectrum showing a saturated line ($\alpha_{\text{max}} = 3.7 \times 10^{-6} \text{ cm}^{-1}$). Panel (c): enlarged view showing the instrumental detection limit ($\alpha_{\text{min}} = 3.3 \times 10^{-11} \text{ cm}^{-1}$).

rise to more than 6300 observed absorption lines (see Fig. 8). As displayed in Fig. 8 [panel (b)], the absorption coefficient α of the strongest absorption lines is beyond the dynamical range of the instrument ($\alpha_{\text{min}} = 3.3 \times 10^{-11} \text{ cm}^{-1}$ and $\alpha_{\text{max}} = 3.7 \times 10^{-6} \text{ cm}^{-1}$).

Figure 9 compares LTE and non-LTE experimental absorption spectra. Panel (c) corresponds to our hypersonic jet spectrum. It greatly differs from the direct absorption spectrum recorded at LIPhy under LTE conditions in a static gas cell maintained at 964 K⁶

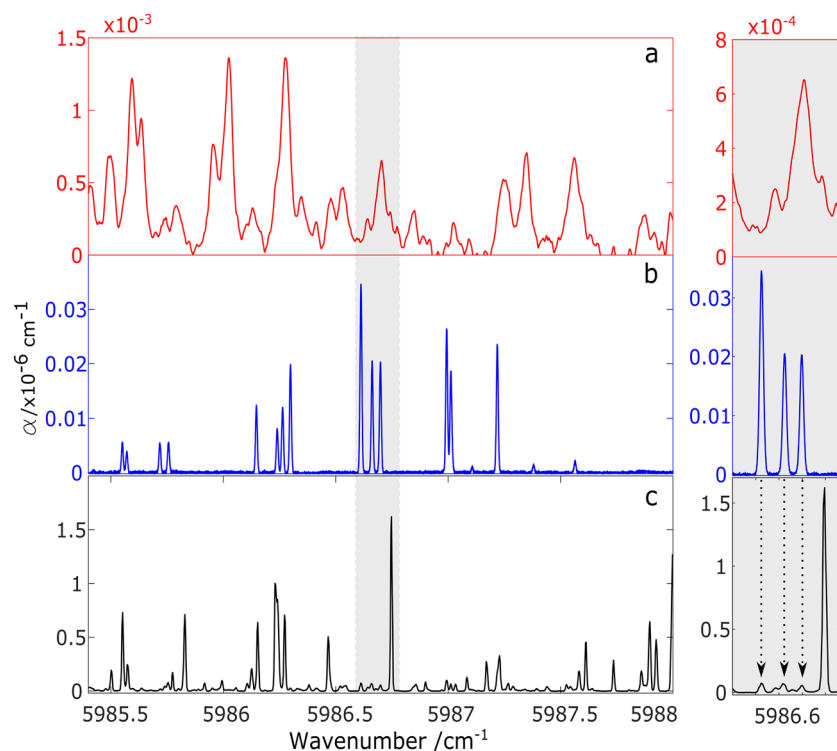


FIG. 9. Left side: Panel (a): laser diode absorption LTE spectrum of CH_4 recorded at LIPhy in static conditions at 964 K. Panel (b): CRDS LTE spectrum of CH_4 recorded at LIPhy in static conditions at 81 K. Panel (c): hypersonic-jet CRDS non-LTE spectrum recorded at IPR. Right side: zoomed-in region around 5986.5 cm^{-1} , highlighting the disappearance of the cold band transitions and the appearance of hot band transitions.

[see Fig. 9, panel (a)]. The considerably broader absorption lines are due to multiple overlapping transitions and a Doppler HWHM of $1.72 \times 10^{-2} \text{ cm}^{-1}$. It is clear that the information contained in the high temperature static spectrum must be considered as a reference spectrum for a direct comparison with the existing databases;^{26–32} however, its analysis relies on a deconvolution of many unresolved contributions that are able to be resolved in our non-LTE spectrum.

In comparison to the high-temperature static spectrum, the hypersonic jet spectrum exhibits remarkably narrow absorption lines with a FWHM of $\sim 0.01 \text{ cm}^{-1}$, however, surprisingly well above the expected value of 0.0026 cm^{-1} estimated from the simulated radial flow velocity of 130 m s^{-1} (see Sec. II). We have no satisfactory explanation to offer for such a discrepancy. The linewidths are comparable to those measured at LIPhy by CRDS in a static gas cell maintained at 81 K ³³ [see panel (b)]. Since at 81 K the population is fully relaxed to the vibrational ground state, the static cold spectrum is composed of absorption lines belonging exclusively to cold bands. In contrast, the cold-band rotational lines are mostly absent from the portion of the hypersonic jet spectrum corresponding to panel (b). Only faint lines can be attributed to transitions originating from the ground vibrational state, suggesting that most of the 6300 observed transitions are actually hot band transitions.

The effect of the non-LTE population distribution on the hypersonic jet spectrum of methane is illustrated in Fig. 10 for which we have simulated a series of three R(0) transitions at different rotational and vibrational temperatures, either under LTE (upper panel) or non-LTE (lower panel) conditions. The R(0) transitions were extracted from the TheoReTS database.^{26–28} They were selected as starting, respectively, from the vibrational ground state ($0301 \leftarrow 0000$), the dyad ($0021 \leftarrow 0001$), and the pentad ($0022 \leftarrow 0002$). The integrated absorption cross sections, $\bar{\sigma}_{ij}$, were calculated at different rotational and vibrational temperatures using the following equation:

$$\bar{\sigma}_{ij}(T_{\text{rot}}, T_{\text{vib}}) = \bar{\sigma}_{ij}(T_0) \frac{Q_0(T_0)}{Q_{\text{rot}}(T_{\text{rot}}) \times Q_{\text{vib}}(T_{\text{vib}})} \times \exp\left[\frac{E_i}{kT_0} - \frac{1}{k}\left(\frac{E_i^{\text{vib}}}{T_{\text{vib}}} + \frac{E_i^{\text{rot}}}{T_{\text{rot}}}\right)\right] \times \left[\frac{1 - \exp\left[-\left(\frac{E_j^{\text{vib}} - E_i^{\text{vib}}}{kT_{\text{vib}}} + \frac{E_j^{\text{rot}} - E_i^{\text{rot}}}{kT_{\text{rot}}}\right)\right]}{1 - \exp\left(-\frac{hc\bar{\nu}_{ij}}{kT_0}\right)}\right], \quad (1)$$

where $\bar{\sigma}_{ij}(T_0)$ is the integrated absorption cross section at $T_0 = 296 \text{ K}$. Q_0 , Q_{rot} , and Q_{vib} are the total, rotational, and vibrational partition functions calculated at the corresponding temperature, respectively; i and j subscripts designate the lower and higher energy states, respectively; k is Boltzmann's constant; h is Planck's constant; and c is the speed of light. The values of Q_{rot} and Q_{vib} were calculated using the Total Internal Partition Sum (TIPS) codes,³⁴ which were specially extended to high temperatures by Gamache and co-workers.

It can be seen from Fig. 10 that an increase in the vibrational temperature promotes the growth of hot-band transitions; of particular interest is the very low rotational temperature characterizing non-LTE hypersonic jets (fixed at 30 K in the present

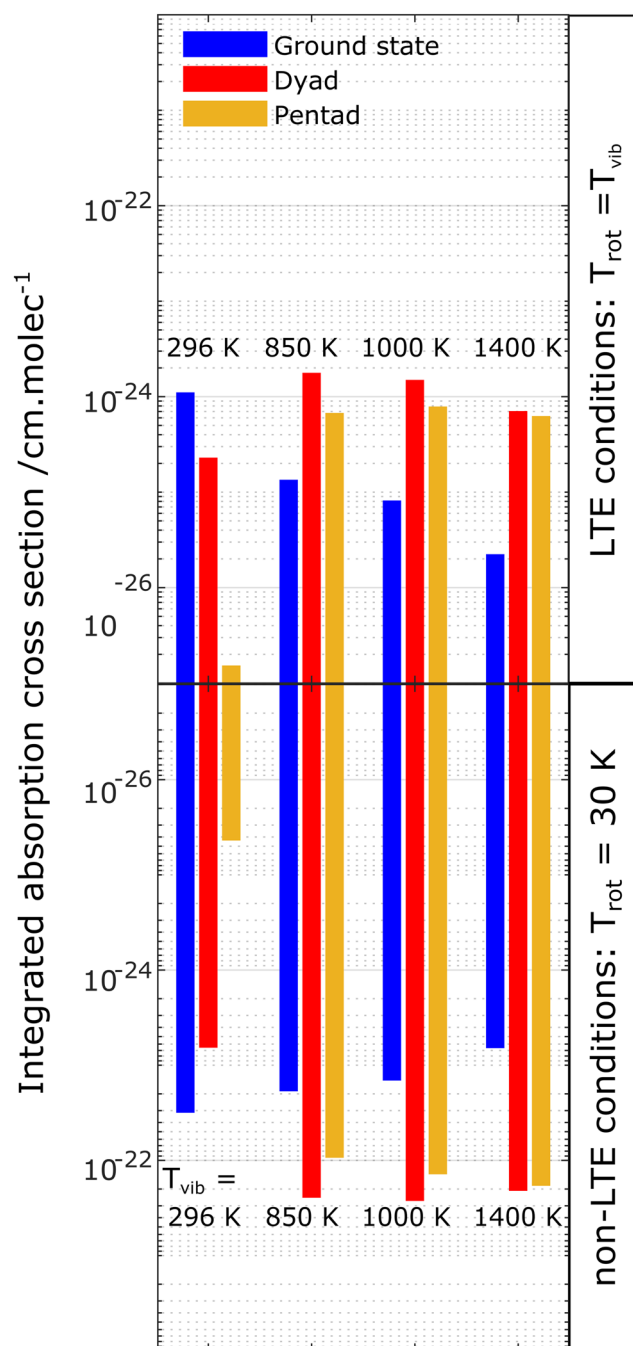


FIG. 10. Evolution of the integrated absorption cross sections at different temperatures of three R(0) transitions of methane starting respectively from the ground state (blue), the dyad (red), and the pentad (ocher). Upper panel: LTE conditions and lower panel: non-LTE conditions (rotational temperature fixed at 30 K).

calculation), which is responsible for magnifying low- J values transitions by more than two orders of magnitude, making our experimental approach well suited for the detection of new hot bands.

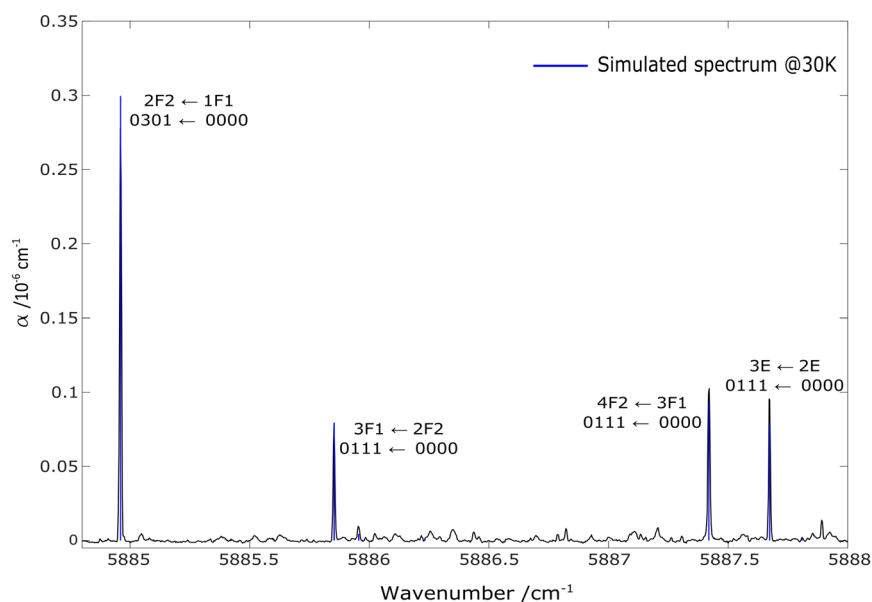


FIG. 11. Determination of the rotational temperature corresponding to the hypersonic jet spectrum of CH_4 using the HITRAN 2012 database.

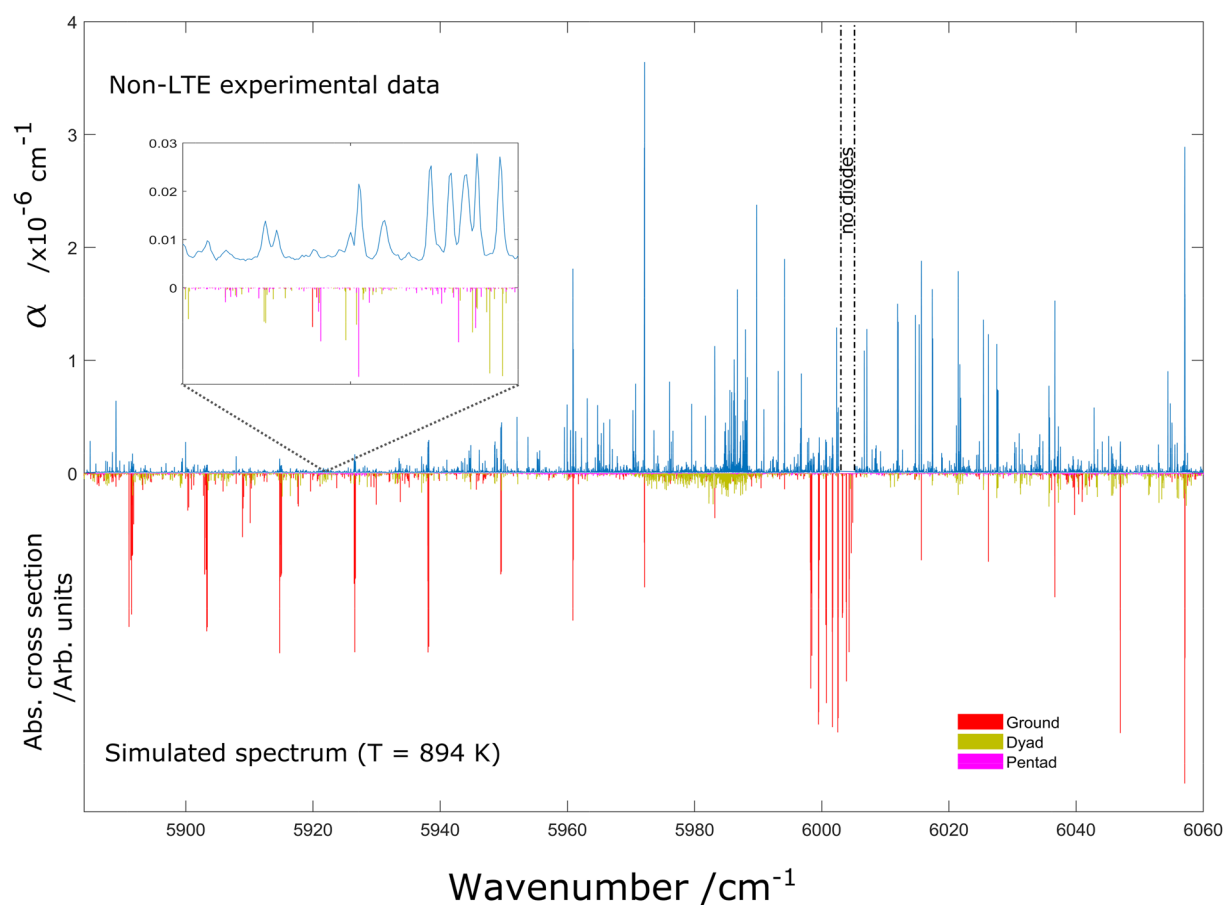


FIG. 12. Comparison between the non-LTE experimental spectrum recorded with SMAUG and a stick spectrum, simulated under LTE conditions at $T = 894\text{ K}$ using the TheoReTS database, where the contributions of the cold and hot bands are represented in different colors. A small region centered at 6005 cm^{-1} could not be studied experimentally due to the lack of the appropriate laser diode. The hot band contribution is clearly magnified in the non-LTE hypersonic spectrum.

B. Temperature extraction

Unlike the simple and the well-studied spectrum of CO to date, the analysis of the more complex tetradecad region of methane is incomplete. The Boltzmann plot method used for CO is more difficult to implement for methane, in particular, for the determination of the vibrational temperature. Hence, the rotational temperature was extracted by a direct iterative comparison of our experimental spectrum with simulations based on the HITRAN 2012 line list.³⁵ By considering only the cold band transitions listed in HITRAN, good agreement was achieved for a rotational temperature of $T_{\text{rot}} = 30 \pm 3$ K (see Fig. 11).

Regarding the vibrational temperature, non-LTE spectroscopy induces a more complex extraction process. Intensities of R(0) lines starting from different initial vibrational energy levels were considered. Their integrated absorption cross section $\tilde{\sigma}_{ij}$ was modeled using Eq. (1), where the rotational temperature was fixed at 30 K. A first “interpolyad” vibrational temperature of $T_{\text{vib}}^{\text{I}} = 894 \pm 47$ K was obtained from the intensity ratio of R(0) lines starting from the vibrational ground state and the ν_4 vibrational energy level of the dyad, thus confirming the weak vibrational relaxation already observed in a planar supersonic expansion of preheated methane.^{17,36} A second “intrapolyad” vibrational temperature of $T_{\text{vib}}^{\text{II}} = 54 \pm 4$ K was obtained when comparing intensities of R(0) transitions starting respectively from the lowest (ν_4) and the highest (ν_2) vibrational energy levels of the dyad, confirming the effective population relaxation between the close vibrational energy levels forming a same polyad.^{17,36}

In Fig. 12, our non-LTE spectrum is compared to a simulation performed in LTE conditions at 894 K ($T_{\text{vib}}^{\text{I}}$) using the TheoReTS database. This comparison highlights the drastic intensity reduction of high- J transitions and the hot band magnification induced by the SMAUG apparatus.

V. CONCLUSION

The performance of the SMAUG setup has been characterized in detail by means of CFD, Pitot probe, and CRDS. Its contoured graphite Laval nozzle can be operated up to 2000 K. As tested with CO and CH₄, it produces a non-LTE quasi-unidirectional supersonic flow limiting absorption line broadening. The expanded molecules are characterized by both high vibrational and low rotational temperatures, thus magnifying the low- J rovibrational line intensities of the very many hot bands responsible for the complexity of high temperature infrared spectra of polyatomic molecules. The SMAUG setup will be extensively used to produce non-LTE infrared spectra of simple hydrocarbons in the frame of the e-PYTHEAS project. A planar Laval nozzle is currently under study in order to increase the absorption path length and to further reduce the radial flow velocity component, leading to an increased experimental sensitivity as well as a better line resolution.

ACKNOWLEDGMENTS

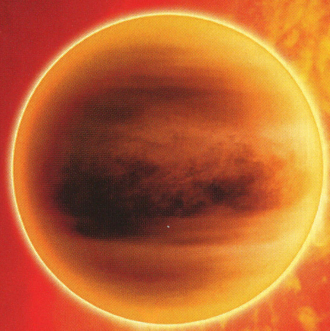
Professor Robert Gamache (University of Massachusetts Lowell) is warmly acknowledged for providing us with a version of the Total Internal Partition Sum (TIPS) codes extended to high temperatures. This work was performed in the frame of the ANR project e-PYTHEAS (Grant No. ANR-16-CE31-0 0 05). The CEFIPRA

project proposal 6005-N. Dr. Jonathan Thiévin (Université de Rennes) is acknowledged for the formatting of experimental data. Mr. Ewen Gallou (Université de Rennes) is acknowledged for his expertise in the manufacture of the graphite Laval nozzle. This work was supported by the Programme National “Physique et Chimie du Milieu Interstellaire” (PCMI) of CNRS/INSU with INC/INP co-funded by CEA and CNES. Dr. Thomas S. Hearne is warmly thanked for his careful reading of this manuscript. We thank Dr. Michaël Rey for stimulating helpful discussion regarding our recorded spectrum of methane. We thank the CNES PERSEUS student program for its financial support.

REFERENCES

- 1 G. Tinetti, T. Encrenaz, and A. Coustenis, “Spectroscopy of planetary atmospheres in our galaxy,” *Astron. Astrophys. Rev.* **21**(1), 63 (2013).
- 2 M. R. Swain, G. Vasisht, and G. Tinetti, “The presence of methane in the atmosphere of an extrasolar planet,” *Nature* **452**(7185), 329–331 (2008).
- 3 P. F. Bernath, “Molecular opacities for exoplanets,” *Philos. Trans. R. Soc., A* **372**(2014), 20130087 (2014).
- 4 M. Mayor and D. Queloz, “A jupiter-mass companion to a solar-type star,” *Nature* **378**(6555), 355–359 (1995).
- 5 M. R. Swain, G. Tinetti, G. Vasisht, P. Deroo, C. Griffith, J. Bouwman, P. Chen, Y. Yung, A. Burrows, L. R. Brown *et al.*, “Water, methane, and carbon dioxide present in the dayside spectrum of the exoplanet HD 209458b,” *Astrophys. J.* **704**(2), 1616–1621 (2009).
- 6 M. Ghysels, S. Vasilchenko, D. Mondelain, S. Béguier, S. Kassi, and A. Campargue, “Laser absorption spectroscopy of methane at 1000 K near 1.7 μm : A validation test of the spectroscopic databases,” *J. Quant. Spectrosc. Radiat. Transfer* **215**, 59–70 (2018).
- 7 E. Czinki, T. Furtenbacher, A. G. Császár, A. K. Eckhardt, and G. Ch. Mellau, “The 1943 K emission spectrum of H₂¹⁶O between 6600 and 7050 cm^{−1},” *J. Quant. Spectrosc. Radiat. Transfer* **206**, 46–54 (2018).
- 8 J. D. J. Anderson, *Gasdynamic Lasers: An Introduction* (Elsevier, 2012).
- 9 E. A. Michael, C. J. Keoshian, D. R. Wagner, S. K. Anderson, and R. J. Saykally, “Infrared water recombination lasers,” *Chem. Phys. Lett.* **338**(4–6), 277–284 (2001).
- 10 E. A. Michael, C. J. Keoshian, S. K. Anderson, and R. J. Saykally, “Rotational transitions in excited vibrational states of D₂O,” *J. Mol. Spectrosc.* **208**(2), 219–223 (2001).
- 11 D. Zhao, K. D. Doney, and H. Linnartz, “High-resolution infrared spectra of vibrationally excited HC₄H in a supersonic hydrocarbon plasma jet,” *J. Mol. Spectrosc.* **296**, 1–8 (2014).
- 12 G. Bazalgette Courrèges-Lacoste, J. P. Sprengers, J. Bulthuis, S. Stolte, T. Motylewski, and H. Linnartz, “Vibrationally excited state spectroscopy of radicals in a supersonic plasma,” *Chem. Phys. Lett.* **335**(3–4), 209–214 (2001).
- 13 J. Oomens and J. Reuss, “Hot band spectroscopy of acetylene after intermolecular vibrational energy transfer from ethylene,” *J. Mol. Spectrosc.* **173**(1), 14–24 (1995).
- 14 J. Dudek, K. Puczk, T. Urbańczyk, and J. Koperski, “High-temperature continuous molecular beam source for aggressive elements: An example of zinc,” *Rev. Sci. Instrum.* **90**(11), 115109 (2019).
- 15 M. Louvriot, N. Suas-David, V. Boudon, R. Georges, M. Rey, and S. Kassi, “Strong thermal nonequilibrium in hypersonic CO and CH₄ probed by CRDS,” *J. Chem. Phys.* **142**(21), 214305 (2015).
- 16 M. Hepp, F. Herregodts, and M. Herman, “Fourier transform infrared jet spectroscopy using a heated slit source,” *Chem. Phys. Lett.* **294**(6), 528–532 (1998).
- 17 D. K. Bronnikov, D. V. Kalinin, V. D. Rusanov, Yu. G. Filimonov, Yu. G. Selivanov, and J. C. Hilico, “Spectroscopy and non-equilibrium distribution of vibrationally excited methane in a supersonic jet,” *J. Quant. Spectrosc. Radiat. Transfer* **60**(6), 1053–1068 (1998).
- 18 P. Wallraff, K. M. T. Yamada, and G. Winnewisser, “Determination of the vibrational temperature of OCS in a supersonic free jet,” *J. Mol. Spectrosc.* **126**(1), 78–81 (1987).

- ¹⁹R. Ferrer, A. Barzakh, B. Bastin, R. Beerwerth, M. Block, P. Creemers, H. Grawe, R. de Groote, P. Delahaye, X. Fléhard *et al.*, “Towards high-resolution laser ionization spectroscopy of the heaviest elements in supersonic gas jet expansion,” *Nat. Commun.* **8**, 14520 (2017).
- ²⁰R. Georges, J. Thiévin, A. Benidar, S. Carles, B. Amyay, M. Louvot, V. Boudon, and J. Vander Auwera, “High enthalpy source dedicated to quantitative infrared emission spectroscopy of gas flows at elevated temperatures,” *Rev. Sci. Instrum.* **90**(9), 093103 (2019).
- ²¹J. Thiévin, R. Georges, S. Carles, A. Benidar, B. Rowe, and J.-P. Champion, “High-temperature emission spectroscopy of methane,” *J. Quant. Spectrosc. Radiat. Transfer* **109**(11), 2027–2036 (2008).
- ²²N. Suas-David, V. Kulkarni, A. Benidar, S. Kass, and R. Georges, “Line shape in a free-jet hypersonic expansion investigated by cavity ring-down spectroscopy and computational fluid dynamics,” *Chem. Phys. Lett.* **659**, 209–215 (2016).
- ²³A. H. Shapiro, *The Dynamics and Thermodynamics of Compressible Fluid Flow* (John Wiley & Sons, 1953), p. 153.
- ²⁴H. Pauly, *Atom, Molecule, and Cluster Beams I: Basic Theory, Production and Detection of Thermal Energy Beams*, Springer Series on Atomic, Optical, and Plasma Physics, Atom, Molecule, and Cluster Beams (Springer-Verlag, Berlin Heidelberg, 2000).
- ²⁵A. V. Nikitin, V. Boudon, Ch. Wenger, S. Albert, L. R. Brown, S. Bauerecker, and M. Quack, “High resolution spectroscopy and the first global analysis of the tetradecad region of methane $^{12}\text{CH}_4$,” *Phys. Chem. Chem. Phys.* **15**(25), 10071 (2013).
- ²⁶M. Rey, A. V. Nikitin, Y. L. Babikov, and V. G. Tyuterev, “TheoReTS—An information system for theoretical spectra based on variational predictions from molecular potential energy and dipole moment surfaces,” *J. Mol. Spectrosc.* **327**, 138–158 (2016).
- ²⁷M. Rey, A. V. Nikitin, B. Bézard, P. Rannou, A. Coustenis, and V. G. Tyuterev, “New accurate theoretical line lists of $^{12}\text{CH}_4$ and $^{13}\text{CH}_4$ in the 0–13400 cm^{-1} range: Application to the modeling of methane absorption in Titan’s atmosphere,” *Icarus* **303**, 114–130 (2018).
- ²⁸M. Rey, A. V. Nikitin, and V. G. Tyuterev, “Theoretical hot methane line lists up to $T = 2000$ K for astrophysical applications,” *Astrophys. J.* **789**(1), 2 (2014).
- ²⁹S. N. Yurchenko and J. Tennyson, “ExoMol line lists—IV. The rotation–vibration spectrum of methane up to 1500 K,” *Mon. Not. R. Astron. Soc.* **440**(2), 1649–1661 (2014).
- ³⁰J. Tennyson, S. N. Yurchenko, A. F. Al-Refaie, E. J. Barton, K. L. Chubb, P. A. Coles, S. Diamantopoulou, M. N. Gorman, C. Hill, A. Z. Lam *et al.*, “The ExoMol database: Molecular line lists for exoplanet and other hot atmospheres,” *J. Mol. Spectrosc.* **327**, 73–94 (2016).
- ³¹L. S. Rothman, I. E. Gordon, R. J. Barber, H. Dothe, R. R. Gamache, A. Goldman, V. I. Perevalov, S. A. Tashkun, and J. Tennyson, “HITEMP, the high-temperature molecular spectroscopic database,” *J. Quant. Spectrosc. Radiat. Transfer* **111**(15), 2139–2150 (2010).
- ³²Y. A. Ba, C. Wenger, R. Surleau, V. Boudon, M. Rotger, L. Daumont, D. A. Bonhommeau, V. G. Tyuterev, and M.-L. Dubernet, “McCaSDa and ECaSDa: Methane and ethene calculated spectroscopic databases for the virtual atomic and molecular data centre,” *J. Quant. Spectrosc. Radiat. Transfer* **130**, 62–68 (2013).
- ³³S. Kass, B. Gao, D. Romanini, and A. Campargue, “The near-infrared (1.30–1.70 μm) absorption spectrum of methane down to 77 K,” *Phys. Chem. Chem. Phys.* **10**(30), 4410 (2008).
- ³⁴A. L. Laraia, R. R. Gamache, J. Lamouroux, I. E. Gordon, and L. S. Rothman, “Total internal partition sums to support planetary remote sensing,” *Icarus* **215**(1), 391–400 (2011).
- ³⁵L. S. Rothman, I. E. Gordon, Y. Babikov, A. Barbe, D. Chris Benner, P. F. Bernath, M. Birk, L. Bizzocchi, V. Boudon, L. R. Brown *et al.*, “The HITRAN2012 molecular spectroscopic database,” *J. Quant. Spectrosc. Radiat. Transfer* **130**, 4–50 (2013).
- ³⁶J. C. Hilico, G. S. Baronov, D. K. Bronnikov, S. A. Gavrikov, I. I. Nikolaev, V. D. Rusanov, and Y. G. Filimonov, “High-resolution spectroscopy of (pentad-dyd) and (octad-pentad) hot bands of methane in a supersonic jet,” *J. Mol. Spectrosc.* **161**(2), 435–444 (1993).



Exoplanètes : ça chauffe au labo

Des chercheurs rennais étudient des planètes très proches de leur soleil, comme sur cette vue d'artiste.

JPL-CALTECH / NASA

ASTRONOMIE À Rennes, la physicienne Eszter Dudàs étudie l'atmosphère brûlante de certaines planètes. Elle n'utilise pas un télescope, mais un caisson sous vide.

Plus de 4 000 exoplanètes ont déjà été repérées¹. La dernière a été découverte en ce début d'année². Mais l'on sait peu de choses sur ces astres qui orbitent autour d'autres étoiles que le soleil. « Nous ne pouvons pas comprendre l'origine et l'évolution d'une planète sans connaître ses composants », explique Robert Georges, astrophysicien à l'Institut de physique de Rennes. Très lointaines, les exoplanètes sont difficiles à étudier... « C'est plus facile d'analyser leur atmosphère, dont les gaz laissent une trace dans la lumière de leur étoile. » Cette signature lumineuse, appelée le spectre, intéresse Eszter Dudàs. Spécialiste en mécanique des fluides, elle prépare une thèse sous la direction de Robert Georges. Les spectres de référence qu'elle produit en laboratoire sont comparés aux observations astronomiques.

Atmosphère à 2 000 °C

Enregistré par un télescope lorsqu'une exoplanète passe devant ou derrière son étoile, le spectre renseigne sur les molécules qui composent son atmosphère. Mais cette signature est difficile à déchiffrer quand la température est très élevée. « Plus le gaz est chaud, plus les molécules vibrent et tournent sur

elles-mêmes, explique Eszter Dudàs. Cela brouille le signal. » C'est le cas pour les exoplanètes étudiées au laboratoire, car elles sont à proximité de leur soleil. Leur atmosphère peut atteindre 2 000 °C ! La première étape consiste à reproduire ces conditions extrêmes, pour étudier le comportement du milieu gazeux.

Dans un caisson sous vide, la chercheuse hongroise fait chauffer, un à un, les gaz supposés présents dans l'atmosphère des exoplanètes. Les molécules s'agitent. Le gaz passe alors dans une petite pièce en graphite, appelée la tuyère. Comme le conduit d'éjection des gaz brûlés d'une fusée, cette structure permet de projeter les molécules à des vitesses supersoniques

1. Les premiers observateurs d'une exoplanète en 1995, Michel Mayor, Didier Queloz et James Peebles, ont reçu le Prix Nobel de physique en 2019.

2. Son nom est TOI 700D.

Eszter Dudàs présente la tuyère qui permet d'accélérer les gaz dans un caisson sous vide (au premier plan).

(plus de 4 500 km/h). La température chute alors à - 260 °C, ce qui bloque la rotation des molécules. Grâce à ce procédé très innovant, le spectre du gaz va devenir lisible.

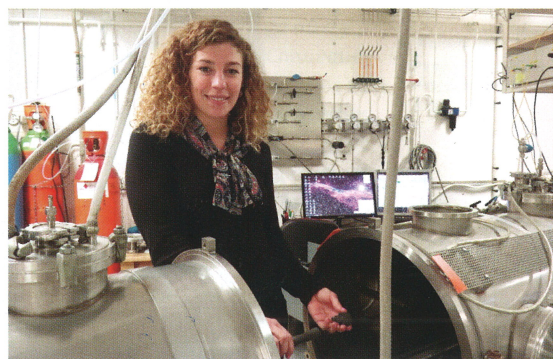
Avec l'Observatoire de Paris

Les chercheurs utilisent un laser infrarouge, pour simuler la lumière de l'étoile. Il traverse le gaz pour sonder les molécules à la sortie de la tuyère. Cela permet d'enregistrer le spectre. Après avoir étudié le méthane, souvent présent sur ces planètes, Eszter Dudàs renouvelle aujourd'hui l'expérience avec l'éthylène. Ses données sont précieuses pour les physiciens théoriciens des universités de Reims et Dijon, qui améliorent ainsi les modèles d'atmosphère. Les planétologues de l'Observatoire de Paris peuvent alors vérifier si ces modèles coïncident avec les observations. Pour se rapprocher un peu plus des exoplanètes... dont le nombre est estimé à plus de 100 milliards dans notre galaxie.

MARION GUILLAUMIN

CONTACTS

Eszter Dudàs, eszter.dudas@univ-rennes1.fr
Robert Georges, robert.georges@univ-rennes1.fr



MARION GUILLAUMIN

OUT-OF-EQUILIBRIUM HYPERSONIC JET SPECTROSCOPY



Eszter Dudás¹, Samir Kassi², Vinayak Kulkarni³, Christine Charles⁴,
Abdessamad Benidar¹, Robert Georges¹

¹ Institut de Physique de Rennes, Université de Rennes 1 - CNRS, France

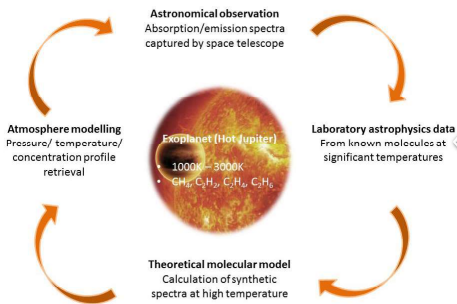
² Laboratoire interdisciplinaire de Grenoble, Université Grenoble Alpes - CNRS, France

³ Indian Institute of Technology Guwahati, Guwahati, India

⁴ Space Plasma, Power and Propulsion laboratory, Australian National University, Canberra, Australia



Introduction



Out-of-equilibrium hypersonic jet spectroscopy

Hypersonic jet

- initially heated up to 2000 K
- sudden drop of molecular collisions
- strong decoupling of the internal degrees of freedom of the molecules
- uniform shape with isentropic core
 - rotational temperature relaxes rapidly
 - vibrational temperature remains very close to the initial one
 - relative high density
 - hot shear layer
 - several hundreds Kelvin

Cavity Ring-Down Spectroscopy

- ultra-sensitive technique
 - 675 m optical path
 - high-finesse optical cavity
- IR spectrum (1.5 μ m range)
- fibred DFB butterfly laser diode
- laser diameter: 0.5 mm
- ring-down time: 180 μ s
- resolution max.: 10^{-4} cm^{-1}

Experimental setup

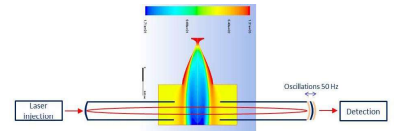


Fig.1: Out-of equilibrium spectroscopy

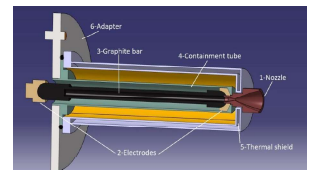
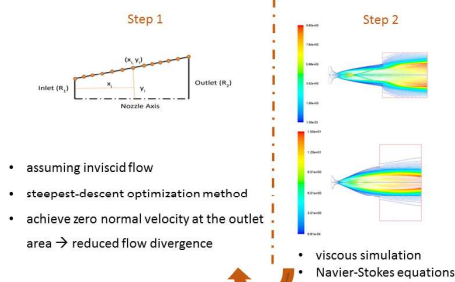


Fig.2: High-enthalpy source

Design of small dimensional de Laval nozzle



Cavity Ring-Down Spectroscopy

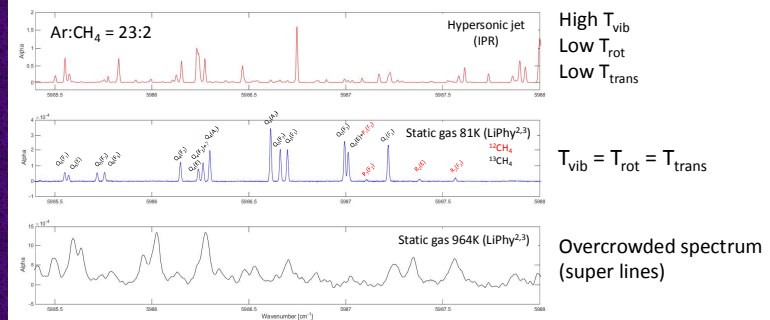
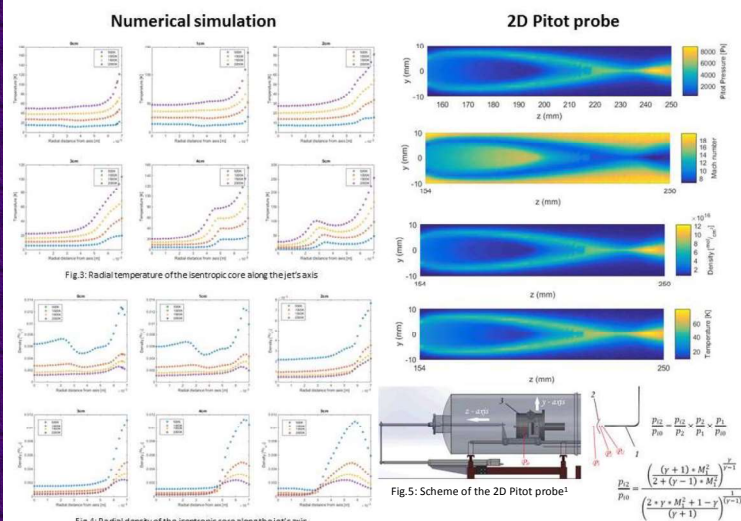


Fig.6: CRD Spectrum of methane

Characterization of the flow



Advantages

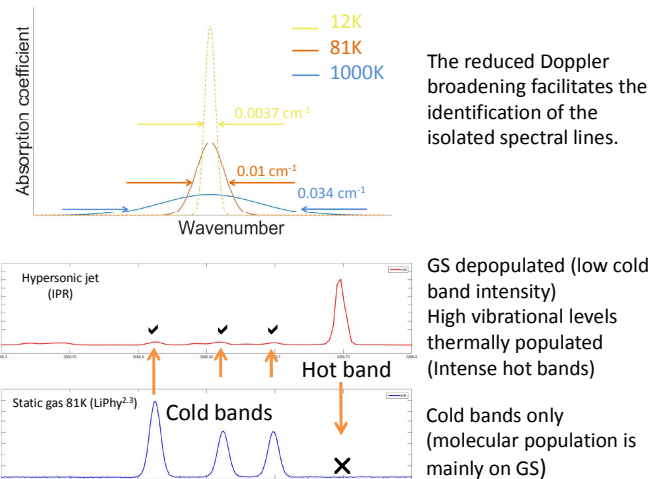
- Low temperature in the isentropic core
- Relatively high density (few 10^{15}cm^{-3})
- Radially uniform core over $\phi 15$ mm
- Tunable initial reservoir temperature and pressure

To be improved

Unwanted shear layer absorption (rotationally hot gas)

Design of a planar nozzle for reducing the shear layer effect and for lengthening the optical path by a factor of 10

Performance



Discussion:

- simplified rotational structure of the hypersonic spectrum (1.5 μ m range)
- without depopulating the highly excited vibrational energy levels whose analysis is really challenging under equilibrium conditions
- in progress: implementation of a planar nozzle

Acknowledgements

The ANR (e-PYTHEAS project) is acknowledged for the PhD grant of ED.
The Technical staff of IPR are warmly thanked for their valuable support.

References

- Suas-David, N., Jets hypersoniques sondés par spectroscopie par temps de déclin d'une cavité optique : application à l'astrophysique de laboratoire. 2016.
- Konefal, M., Ghysels, D., Mondelain, S., Kassi, A., Camargue, The absorption spectrum of 13CH₄ at 80 K and 296 K near 1.73 μ m 2018
- M. Ghysels, S. Vasilchenko, D. Mondelain, S. Béguier, S. Kassi, A. Camargue Laser absorption spectroscopy of methane at 1000 K near 1.75 μ m: A validation test of the spectroscopic databases

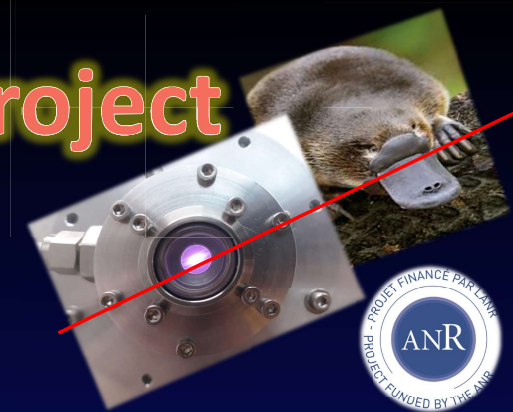
The Platypus exoplanet project

Eszter Dudás¹, Dimitrios Tsifakis², Christine Charles², Rod Boswell², Samir Kassi³, Robert Georges¹

¹Institut de Physique de Rennes, Université de Rennes 1 - CNRS, France

²Space Plasma, Power and Propulsion laboratory, Australian National University, Canberra, Australia

³Laboratoire interdisciplinaire de Grenoble, Université Grenoble Alpes - CNRS, France

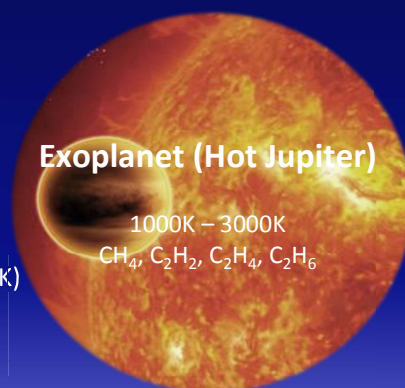


Objectives:

- Modelling the atmosphere of Hot Jupiters
- Identification of the diffuse interstellar bands (DIBs)

Transformed Pocket Rocket

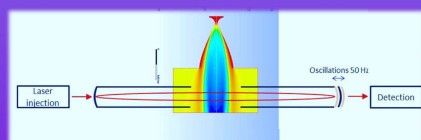
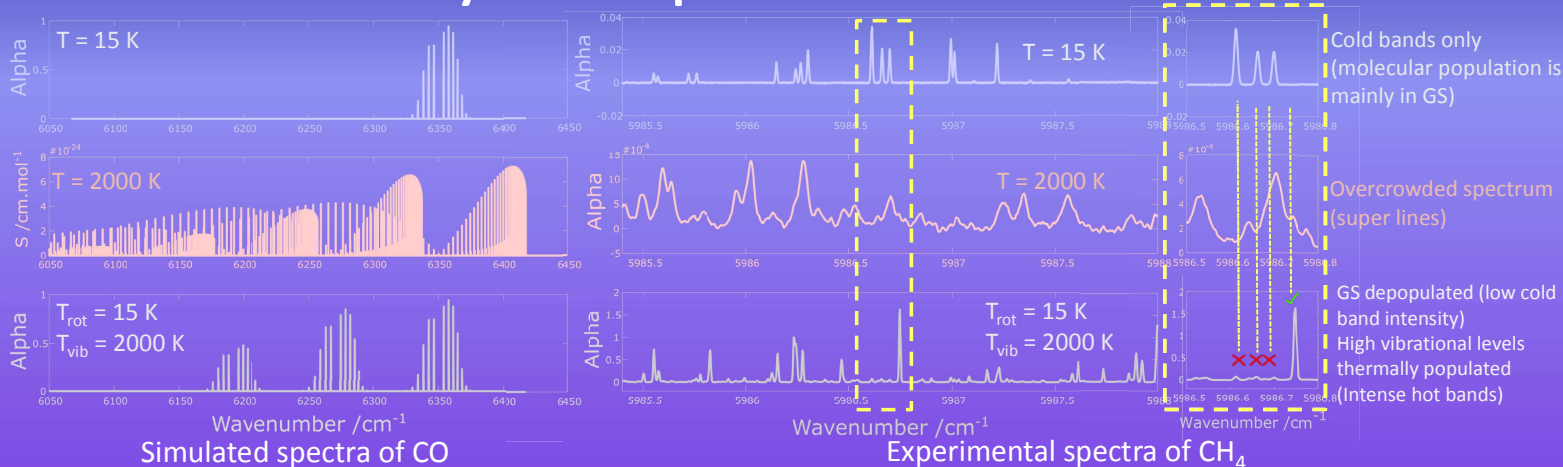
- capacitive electrothermal plasma
- radiofrequency (13.56 MHz) electrothermal thruster (RFETs)
- Power: 30 W
- Supersonic plasma expansion
- High vibrational temperature (several 1000 K)
- Low rotational temperature (several 10 K)



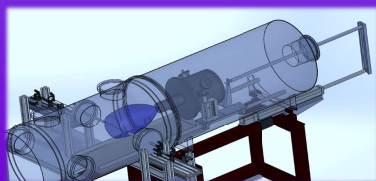
Cavity ring down Spectroscopy

- ultra-sensitive technique
- 675 m optical path
- high-finesse optical cavity
- IR spectrum (1.5 μm range)
- fibered DFB butterfly laser diode
- D_{laser} : 0.5 mm
- $\tau_{\text{Ring-down}}$: 180 μs
- Resolution max.: 10^{-4} cm^{-1}

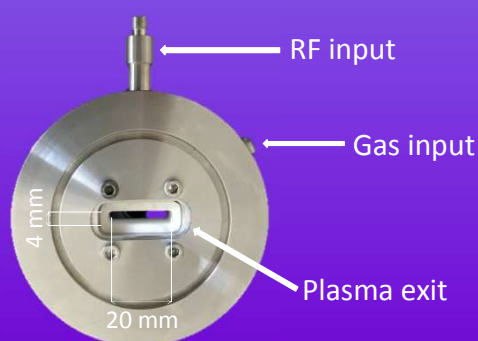
Non Local Thermodynamic Equilibrium – Pocket Rocket – CRDS



Supersonic expansion



Experimental setup



Platypus pocket rocket

Novel geometry:
rectangular cross-section
Large flow rate:
decent signal for CRDS

To do:

- Characterisation of the plasma plume with N_2
- Establishing spectral data of molecules (CH_4) at highly excited vibrational states

Acknowledgements

Special thanks to Christine Charles and the team of Space Plasma Power and Propulsion, ANU. The ANR (e-PYTHEAS project) is acknowledged for the PhD grant of ED. The Technical staff of SP3 and IPR are warmly thanked for their valuable support.

Résumé détaillé

Cette thèse est intégrée au projet e-PYTHEAS (*exo-Planetary high-Temperature Hydrocarbons by Emission and Absorption Spectroscopy*), financé par l'Agence nationale de la recherche. Il vise à mieux connaître la formation d'un certain type d'exoplanètes et leur évolution. Le travail présenté est centré sur le développement d'un nouveau procédé spectroscopique SMAUG (*Spectroscopy of Molecules Accelerated in Uniform Gas flow*) dédié à l'étude des propriétés radiatives des gaz à haute température dans le domaine infrarouge.

En combinant une approche théorique et expérimentale, l'objectif de cette thèse est de modéliser l'atmosphère de planètes géantes gazeuses. Comme la plupart des exoplanètes détectées à ce jour sont très chaudes, il est primordial de connaître les propriétés radiatives à très haute température des gaz qui composent leur atmosphère. En premier lieu, ce sont les propriétés radiatives du méthane, le plus petit des hydrocarbures, qui sont étudiées car sa présence est avérée dans l'atmosphère des planètes extrasolaires de type Jupiter chaud. Pour ce faire, ce travail utilise et perfectionne le dispositif expérimental SMAUG qui simule les conditions astrophysiques extrêmes et produit pour chaque molécule des empreintes infrarouges de référence. Ce manuscrit regroupe des simulations numériques d'écoulement, des mesures expérimentales et des traitements de données poussés. Les données de laboratoire produites alimentent des codes de transfert radiatif permettant d'interpréter la signature infrarouge de ces planètes, et de modéliser leur climat exotique.

Le mémoire est composé de cinq chapitres distincts ainsi que d'une introduction et d'une conclusion. Un article publié dans *J. Chem. Phys.* relatif à une partie de ce travail, ainsi que deux posters, sont placés en Annexe.

Introduction

Cette introduction retrace brièvement l'évolution de nos connaissances au cours des siècles précédents sur le système solaire et les exoplanètes. Elle présente les différentes techniques de détection des exoplanètes et décrit les diverses classes d'exoplanètes, en particulier les Jupiters chauds. Ces exoplanètes orbitent très près de leur étoile si bien que leur atmosphère atteint plusieurs milliers de kelvins. La section suivante expose trois hypothèses qui visent à lever l'ambiguïté quant à l'origine des Jupiters chauds : comment ces planètes géantes gazeuses peuvent-elles exister aussi proches de leurs étoiles hôtes ?

Différentes techniques d'observation permettent d'enregistrer un spectre infrarouge unique de l'atmosphère des exoplanètes dont sont extraites sa température, sa densité et sa concentration caractéristiques. Ces données révèlent également de précieuses informations sur les molécules présentes dans l'atmosphère ; à ce jour neuf espèces ont été confirmées. Enfin, cette introduction présente le projet e-PYTHEAS.

Chapitre I : Spectroscopie infrarouge du méthane

Le premier chapitre introduit la théorie de la spectroscopie rovibrationnelle du méthane, molécule cible de cette thèse. Cette partie expose le regroupement des niveaux vibrationnels de la molécule de méthane en polyades. Elle détaille les conditions relatives à l'équilibre thermodynamique local (ETL) ou au non équilibre thermodynamique local (non ETL) et explique la notion de fonction de partition interne qui donne accès à la probabilité qu'un système occupe un état énergétique donné. La température d'un gaz étant directement liée à la répartition des molécules sur leurs différents niveaux d'énergie, l'intensité d'une transition est donc fortement dépendante de la température du gaz. Ainsi, la méthode du tracé de Boltzmann est une technique couramment utilisée pour extraire les températures moléculaires des spectres infrarouges en comparant les intensités relatives des transitions de rotation-vibration.

Vers la fin de ce chapitre, les différentes bases de données spectroscopiques du méthane sont présentées. À ce jour, de plus en plus de données observationnelles arrivent en provenance de divers environnements spatiaux et atmosphères extraterrestres. Afin d'étudier et d'interpréter ces données, il est essentiel de disposer de listes de raies précises qui peuvent être utilisées comme fichiers d'entrée pour les codes de transfert radiatif qui à leur tour sont utilisés pour modéliser les atmosphères observées ou pour effectuer des mesures de concentration de ces environnements.

Finalement, les précédentes études spectroscopiques infrarouges relatives au méthane obtenues dans des conditions ETL et non ETL sont présentées polyade par polyade.

Chapitre II : SMAUG montage expérimental et son fonctionnement

Le deuxième chapitre commence par une brève introduction aux écoulements hypersoniques et rappelle certaines hypothèses et définitions des notions nécessaires à la caractérisation et la compréhension des propriétés de ce type d'écoulements.

La deuxième section de ce chapitre présente la tuyère de Laval. Elle détaille son principe de fonctionnement et les différentes méthodes pour calculer un profil de tuyère supersonique. Elle décrit en particulier les différentes phases du processus de conception de la tuyère en graphite de petite dimension implantée sur le dispositif SMAUG. L'optimisation du profil de la tuyère est suivie d'une phase de caractérisation numérique de l'écoulement hypersonique créé. L'écoulement est simulé au moyen d'un outil de dynamique des fluides numérique (CFD) et les simulations numériques révèlent bien la présence d'un cœur isentropique froid entouré de couches limites chaudes. Ces investigations numériques permettent d'optimiser la position du laser de sonde dans le jet pour les études spectroscopiques, sachant que le faisceau laser traverse perpendiculairement le jet axisymétrique et se fait par conséquent absorber simultanément par le précieux cœur isentropique froid mais également par les couches limites beaucoup plus chaudes. Néanmoins, il est montré que l'utilisation d'une tuyère de Laval réduit considérablement les gradients de température et de densité caractéristiques de la détente de type jet libre précédemment utilisée au laboratoire.

Une fois validé par ces études numériques, le profil nouvellement conçu a été utilisé pour fabriquer une tuyère de Laval de petite dimension montée sur une source à haute

enthalpie (HES). Le gaz éjecté par la tuyère a été caractérisé expérimentalement sur une nappe 2D par sonde de Pitot. Les cartographies 2D du champ de l'écoulement obtenues expérimentalement sont en bon accord avec celles simulées numériquement. Par exemple, un faisceau d'ondes de choc obliques apparaît au même endroit, à environ 70 mm en aval de la sortie de la tuyère. De plus, l'uniformité radiale du jet est confirmée ainsi que l'augmentation monotone du nombre de Mach le long de l'axe de la tuyère jusqu'à l'intersection des ondes de choc obliques. Une fois la présence d'un cœur isentropique froid confirmée expérimentalement, un spectromètre d'absorption ultrasensible par mesure du temps de déclin d'une cavité (CRDS) a été positionné de sorte à sonder l'écoulement perpendiculairement à son axe. Les performances du montage expérimental en termes de relaxation d'énergie rotationnelle et vibrationnelle ont été caractérisées au travers d'une étude spectroscopique préliminaire réalisée avec du monoxyde de carbone mélangé à de l'argon dans un rapport 5:95. Les spectres confirment une très bonne relaxation rotationnelle des molécules et une relation vibrationnelle quasiment inexistante, ce qui correspond bien à la vocation première du dispositif : la spectroscopie infrarouge non ETL de molécules rationnellement froides et vibrationnellement chaudes.

Le dispositif expérimental est composé d'un élément chauffant (HES) qui préchauffe le mélange gazeux du gaz porteur (argon) et des molécules actives IR (CO ou méthane) avant leur expansion à travers la tuyère de Laval discutée ci-dessus. La chambre d'expansion est évacuée par un ensemble de pompes mécaniques roots et le jet hypersonique est sondé transversalement par le spectromètre CRDS.

La connaissance de la température initiale du réservoir au sein du barreau de graphite, en conditions ETL, est cruciale pour mener des investigations précises et approfondies des molécules dans l'expansion hypersonique. À cette fin, un pyromètre et un thermocouple ont été introduits dans le système afin d'enregistrer la température du réservoir. Cependant, ces deux procédés renvoient un écart de température systématique, si bien que la température du réservoir n'est connue qu'avec une incertitude d'environ 300 kelvins.

En conclusion, la technique expérimentale SMAUG équipée de la tuyère de Laval conçue sur mesure délivre un écoulement hypersonique quasi-unidirectionnel et non ETL. De plus, la mise en œuvre de la tuyère réduit avec succès les gradients radiaux de température et de densité, ce qui limite efficacement l'élargissement des raies de rotation-vibration. Cela rend le dispositif idéal pour simplifier la structure rotationnelle des spectres infrarouges et donc étudier les modes vibrationnels à haute énergie de gaz plus complexes tels que le méthane.

Chapitre III : Non ETL spectroscopie du méthane

Le troisième chapitre expose les résultats extraits du spectre non ETL du méthane dans la région spectrale 1,60-1,67 μm , avec une température initiale avant détente estimée à 850 K. Tout d'abord, le spectre obtenu en jet hypersonique est comparé à deux spectres enregistrés au LIPhy (Grenoble) en conditions ETL à 81 K et 964 K. La comparaison souligne les avantages de l'approche non ETL pour accéder aux états vibrationnels excités du méthane : i) la faible température translationnelle offre une largeur de raie réduite, ii) la forte relaxation

rotationnelle offre un spectre simplifié et enfin iii) la relaxation vibrationnelle inefficace garantit que certains niveaux d'énergie vibrationnels restent effectivement peuplés.

La section suivante du chapitre se penche sur la largeur des raies d'absorption, certes faible mais pourtant supérieure à la valeur attendue en raison de la très faible température de translation ($< 39\text{K}$). Il s'avère que la cumulation des effets Doppler thermique et convectif (dû à la légère divergence du jet) explique bien la valeur expérimentale de la largeur de raie.

La tâche suivante consiste à déterminer les températures de rotation et de vibration caractéristiques afin d'identifier les raies observées pour la première fois et non encore recensées dans les listes de raies empiriques. Grâce à une première analyse du spectre CH_4 non ETL enregistré, les relaxations rotationnelle, vibrationnelle intra-polyades et vibrationnelle inter-polyades ont été caractérisées quantitativement. La rotation est bien relaxée selon une distribution de Boltzmann caractérisée par une température de 39 K . Les températures vibrationnelles extraites reflètent une relaxation intra-polyade efficace qui dépeuple les niveaux vibrationnels élevés de chaque polyade, alors que la relaxation entre niveaux d'énergie appartenant à des polyades différentes est considérablement plus faible, ce qui conduit à une accumulation de la population vibrationnelle sur le premier état de chaque polyade.

Les températures vibrationnelles obtenues, dont certaines supérieures à la température du réservoir en raison de l'accumulation de la population sur le premier état de chaque polyade, soulignent les spécificités essentielles du dispositif expérimental. L'importante relaxation rotationnelle et intra-polyade assure la détection des raies correspondant aux transitions issues de la pentade et de l'octade en augmentant drastiquement la population des états vibrationnels de base de ces polyades. Ces relaxations éliminent d'autre part un nombre considérable de raies du spectre, permettant l'analyse précise de celles restantes.

À la suite d'une analyse préliminaire qui reste à compléter, 22 transitions ont été identifiées, dont 15 transitions issues de l'état vibrationnel le plus bas $2\nu_4(A1)$ de la pentade. Trois transitions partent de l'état vibrationnel suivant de la pentade, $2\nu_4(F2)$. Enfin, 4 raies ont été repérées au départ de l'octade : trois correspondant à l'état vibrationnel $3\nu_4(F2)$ le plus bas et une à l'état vibrationnel $3\nu_4(F1)$. Tous les candidats rapportés correspondent à des transitions rovibrationnelles à faible J avec $J_{\text{max}} = 4$.

Chapitre IV : Spectroscopie post-choc

Une nouvelle technique appelée « spectroscopie post-choc » est décrite dans ce chapitre. En raison du manque de population sur les états vibrationnels les plus élevés au sein de chaque polyade, l'approche non ETL ne peut pas donner un aperçu des transitions des bandes chaudes provenant de ces états. De plus, bien que la structure de rotation simplifiée soit un avantage pour accéder à des positions de raies précises et faciliter leur identification, il est clair que les conditions non ETL éliminent un grand nombre de transitions de haute valeur de J du spectre, ce qui peut être perçu comme une perte d'information. Une approche expérimentale originale complémentaire a été développée pour accéder à ces transitions manquantes.

La première section de ce chapitre présente les notions de base théoriques relatives à la physique des ondes de choc normales car le nouveau procédé expérimental mis en place

consiste à créer une onde de choc détachée stationnaire en amont d'un obstacle placé dans l'écoulement hypersonique. Le rôle de l'onde de choc est de reconvertir l'énergie cinétique du gaz en enthalpie et de sonder la couche de choc pour obtenir le spectre haute température dans des conditions proches de l'ETL.

Des études antérieures utilisant une plaque de 50 mm de diamètre ont révélé certains inconvénients tels qu'une forte composante de vitesse radiale dans la direction du laser qui a provoqué, d'une part, un élargissement de la raie convective Doppler et, d'autre part, un refroidissement du gaz sondé car son énergie cinétique est redevenue significative. Pour pallier ces inconvénients, un cylindre de plus petit diamètre correspondant à celui de la sortie du jet hypersonique a été placé dans l'écoulement, 20 mm en aval de la tuyère de Laval.

Le nouveau dispositif expérimental a une fois de plus été caractérisé au moyen de simulations numériques CFD. Une étude axiale de l'écoulement permet de localiser la position et la forme du choc et indique la zone de l'écoulement la plus intéressante à sonder pour les mesures spectroscopiques, en l'occurrence le plus près possible de l'obstacle générateur de choc. Les simulations numériques révèlent derrière l'onde de choc un champ d'écoulement à haute densité et à haute température prometteur pour la spectroscopie infrarouge.

Suite à la caractérisation numérique du choc, un diagnostic spectroscopique préliminaire a été réalisé en utilisant le CO comme traceur. Ces observations confirment bien les simulations CFD, c'est-à-dire une augmentation progressive de la température et de la densité du gaz au fur et à mesure que l'écoulement subsonique de la couche de choc s'approche de l'obstacle. Il semble donc que la position la plus favorable du laser pour réaliser la spectroscopie d'un gaz chaud soit celle qui est la plus proche possible de l'obstacle. En conclusion, les molécules de CO sondées dans la couche post-choc sont toujours en régime non ETL avec $(T_{\text{trans}} = T_{\text{rot}}) < T_{\text{vib}}$. Cependant, cette couche présente un déséquilibre nettement moins marqué que dans le noyau hypersonique isentropique ($T_{\text{trans}} \cong T_{\text{rot}} \ll T_{\text{vib}}$). Il a ainsi été démontré que la spectroscopie post-choc donne accès à des états rovibrationnels à J élevés et à des états d'énergie vibrationnel excités. Cette nouvelle approche a ensuite été appliquée à la spectroscopie du méthane.

Le spectre du méthane post-choc a été enregistré dans deux conditions de température différentes. Une analyse exhaustive des spectres de méthane post-choc est toujours en cours et les résultats seront publiés dans une revue à comité de lecture.

Chapitre V : Projet Platypus

Le cinquième chapitre révèle un tout nouveau développement instrumental amorcé dans le cadre d'une collaboration avec des chercheurs du laboratoire « Space Plasma, Power and Propulsion » de Canberra, baptisé projet Platypus. Cette nouvelle collaboration s'intéresse à des projets de physique appliquée et fondamentale liés à des plasmas en expansion pour le développement de nouveaux propulseurs spatiaux et la production de nouvelles données spectroscopiques non ETL.

Ce chapitre présente brièvement ce qu'est un plasma avant de décrire la nouvelle source radiofréquence (RF) développée à Canberra à partir d'un prototype de propulseur

spatial miniaturisé (« Pocket Rocket »). L'objectif est de détendre le plasma RF dans la chambre à vide du dispositif SMAUG afin de sonder par CRDS le jet supersonique ainsi créé. Le caractère supersonique de l'expansion est confirmé par la présence visuelle de la structure en diamant des ondes de chocs qui se forment en aval de l'injecteur.

Une fois de plus le CO a été utilisé comme molécule test pour caractériser par spectroscopie le jet de plasma issue de cette source de puissance modérée de 30 W. Le caractère hors d'équilibre du jet a été confirmé, validant notre nouvelle approche pour produire des spectres infrarouges non ETL. Cette source plasma prépare en effet efficacement les molécules dans un état de très fort déséquilibre, comme en témoigne la température vibrationnelle incroyablement chaude mesurée autour de 2400 K, combinée à une température de rotation favorablement basse de 28 K. De plus, il est satisfaisant de constater que la section de sortie importante de l'injecteur rectangulaire délivre bien un jet supersonique, doté de plus d'une densité suffisamment élevée pour que le CRDS détecte les transitions de CO et caractérisé par une vitesse radiale suffisamment faible qui évite l'élargissement indésirable des raies d'absorption.

Conclusions et perspectives

Cette thèse a porté sur le développement de nouvelles approches expérimentales pour produire des données spectrales de laboratoire à haute résolution et haute température, en particulier de la molécule de méthane, molécule clé pour l'atmosphère des Jupiters chauds. Les développements et les innovations techniques apportés ont contribué à surmonter les inconvénients propres au dispositif précédent basé sur l'utilisation d'un jet libre. Ce travail de thèse a fourni des données spectroscopiques infrarouges sans précédent du méthane chaud impliquant des niveaux d'énergie vibrationnelle proches de 10000 cm^{-1} .

L'analyse exhaustive des spectres du méthane produits au cours de ce travail est toujours en cours, elle fera l'objet de publications à venir. Même si cette thèse s'est focalisée sur le méthane, le dispositif SMAUG est prêt à recevoir d'autres hydrocarbures comme l'acétylène dont la présence a déjà été confirmée dans l'atmosphère des Jupiters chauds, ou l'éthylène et l'éthane qui sont fortement soupçonnés d'y être présents.

D'un point de vue technique, afin d'augmenter la longueur du trajet d'absorption des photons de la cavité optique à travers la partie isentropique froide du jet, une tuyère plane actuellement en cours de développement, sera équipée d'un nouveau système de chauffage en céramique. Cette nouvelle méthode de production d'un jet plane réduira considérablement la contribution des couches limites au spectre d'absorption, en simplifiant encore l'analyse. Autre avantage important, la sensibilité du système augmentera, rendant détectables des transitions invisibles par la configuration actuelle. Enfin, le remplacement de l'élément chauffant en graphite par un élément en céramique permettra d'ouvrir l'étude à de nombreuses molécules oxydantes.

Finalement, Platypus, le « Pocket Rocket » modifié, pourrait contribuer à l'étude de l'efficacité des systèmes de propulsion miniaturisés. Les combustibles solides, comme le naphthalène, offrent une grande quantité d'énergie dans un petit volume qui, grâce au chauffage électrothermique, comme dans le Pocket Rocket, forme un plasma à haute

température. L'efficacité de la propulsion repose sur une conversion de l'énergie thermique en énergie de translation du gaz ionisé afin de déplacer des petits satellites de type CubeSat. SMAUG, avec son système de diagnostic innovant permettrait une étude précise sur la façon dont l'énergie thermique initialement conférée au naphthalène par la décharge micro-onde se répartie dans la translation et les niveaux d'énergie de rotation et de vibration des molécules gazeuses qui forment le jet propulsif. Seule la translation des molécules agit sur le pilotage du satellite ; l'énergie piégée dans la rotation et les vibrations sont malheureusement gaspillées.

Titre : Spectroscopie hors équilibre du méthane en jet hypersonique pour la caractérisation des Jupiters chauds

Mots clés : spectroscopie infrarouge ultrasensible, méthane, écoulement hypersonique, exoplanètes, plasma froid

Résumé : Le système expérimental de pointe SMAUG a été développé pour produire des données de référence spectroscopiques infrarouges inédites pour la détection de nouvelles molécules et la reconstruction de la structure verticale de l'atmosphère d'exoplanètes de type Jupiter chaud. Une minituyère de Laval en graphite, connectée à une source de haute enthalpie et couplée à un spectromètre par temps de déclin d'une cavité optique (CRDS), a été développée afin de produire des spectres infrarouges à haute résolution et haute température du méthane dans la région à 1,67 μm . Le dispositif expérimental fonctionne dans deux configurations complémentaires pour accéder aux signatures infrarouges complexes du méthane dans ses états vibrationnels fortement excités. Une détente hypersonique produit un état de très fort déséquilibre thermodynamique moléculaire, associé à des températures vibrationnelles élevées et une température rotationnelle très basse.

Du spectre hors équilibre sont extraites les positions précises des niveaux d'énergie vibrationnels excités qui affinent la surface d'énergie potentielle du méthane et améliorent la précision des modèles théoriques variationnels *ab initio* qui fournissent les listes de raies spectroscopiques à haute température à la communauté des planétologues. Une nouvelle technique CRDS post-choc conduit à des conditions proches de l'équilibre thermodynamique local. Les températures vibrationnelle et rotationnelle élevées atteintes donnent accès à la structure rotationnelle complète des différentes bandes observées, de même qu'aux bandes chaudes vibrationnelles issues des états les plus excités de chaque polyade du méthane. En parallèle, une source plasma radiofréquence de type Pocket Rocket a été adaptée et utilisée comme moyen de chauffage alternatif. Ce travail de thèse a été réalisé dans le cadre du projet ANR e-PYTHEAS qui vise à mieux connaître la formation des exoplanètes et leur évolution.

Title: Non-LTE spectroscopy of methane in hypersonic flow for the characterisation of hot Jupiters

Keywords: infrared ultrasensitive spectroscopy, methane, hypersonic jet, exoplanets, cold plasma

Abstract: A state-of-art experimental system, SMAUG has been developed to produce unprecedented infrared spectroscopic reference data that will help planetologists to detect new molecules and reconstruct the vertical structure of the atmosphere of exoplanets. A specially designed small dimension Laval nozzle connected to a compact high enthalpy source equipped with cavity ringdown spectroscopy (CRDS) is used to produce high-resolution infrared spectra of polyatomic molecules in the 1.67 μm region. The experimental setup can operate according to two complementary working regimes to interpret the complex pattern of highly-excited vibrational states. The hypersonic jet delivers a strong out-of-equilibrium state, in which vibrationally hot and rotationally cold high-resolution infrared spectra was recorded.

The obtained non-Local Thermodynamic Equilibrium (LTE) spectrum of methane provides accurate positions of the upper energy levels to refine the potential energy surface on which *ab initio* variational theoretical models are based. A post-shock CRDS technique results in conditions close to LTE which allow the analysis of a more complex rotational structure and complete information on the excited hot vibrational energy levels. Parallely, through a collaboration, a transformed Pocket Rocket plasma source was developed and implanted into SMAUG to investigate an alternative heating system with more elevated vibrational energy levels. This work was done in the frame of the e-PYTHEAS project that focuses on high-temperature spectroscopy of small hydrocarbons.